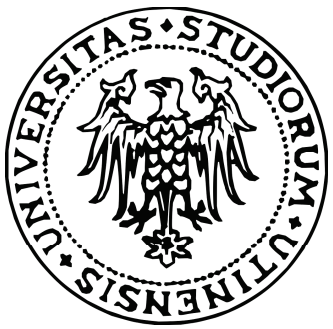

UNIVERSITÀ DEGLI STUDI DI UDINE

Dipartimento Politecnico di Ingegneria e Architettura
Dottorato di Ricerca in Ingegneria Industriale e dell'Informazione

PhD Thesis

MODELING AND OPTIMIZATION OF SINGLE PHOTON AVALANCHE PHOTODIODES FOR X-RAY DETECTION

Alessandro PILOTTO

Supervisor
Prof. Pierpaolo PALESTRI

External Reviewers
Prof. Raphael CLERC
Prof. Alessandro S. SPINELLI

Co-Supervisor
Prof. Luca SELMI

PhD Cycle XXXIII
2021

Abstract

Avalanche Photodiodes (APDs) are electronic devices that transduce a photon flux into an electrical current and provide internal amplification of this current exploiting the impact ionization mechanism. APDs are used as receivers in optical fiber communication links as well as detectors in physics experiments and medical imaging. According to the needs of the target application, they can either be operated below (Linear mode) or above (Geiger mode) their breakdown voltage.

For X-ray detection, APDs fabricated in III-V compound semiconductors, such as GaAs, offer an interesting alternative to SiAPDs, thanks to the short attenuation length at high energies offered by these materials. However, to improve the poor noise performance of APDs fabricated in III-V compounds given by similar electron's and hole's impact ionization coefficients, structures alternative to p-i-n APDs have to be employed. A possible solution is the use of staircase APDs, where heterojunctions between III-V compound semiconductors and their alloys with metals are exploited to enhance the electron to hole impact ionization probability by creating an artificial superlattice.

This thesis aims at proposing models to compute the figures of merit of APDs fabricated in III-V compound semiconductors and operating in Linear mode for the detection of X-rays. Since accurate modeling of impact ionization is key to obtain reliable data from simulations, we present the development of a suite of simulations tools that includes the finite difference and the Random Path Length algorithm implementation of a newly derived nonlocal history dependent impact ionization model and a Full Band Monte Carlo transport simulator. All these models have been validated against experimental results and are thus powerful tools in support of the interpretation of single photon APDs electrical measurements and for the optimization of their performance. These simulation tools have been used to compute the gain, the excess noise factor, the response time, the bandwidth and the jitter of different APD structures, including staircase APDs.

In addition, the Full Band Monte Carlo transport simulator has been employed to assess the basic assumptions, identify the limitations and improve the calibration of nonlocal history dependent impact ionization models. We have found that, even though nonlocal history dependent models give results that are in a satisfactory agreement with experiments, they neglect that after an impact ionization event secondary carriers are generated with non null kinetic energy and that carrier-phonon scattering may lead to electrons and holes that travel for few free flights with velocities that are opposite to the direction of the electric fields. These aspects may become relevant and yield misleading results, in particular for short devices.

Contents

Terminology . . . . . **ix**

List of Figures . . . . . **xiii**

List of Tables . . . . . **xxix**

1 Introduction **1**
1.1 Radiative Generation and Impact Ionization 2
1.2 p-i-n APDs 3
1.3 Figures of Merit of APDs 5
1.3.1 Geiger Mode 6
1.3.2 Linear Mode 6
1.4 Staircase APDs 9
1.5 APDs with Separate Absorption and Multiplication Regions . . 11
1.6 Pulse Shaping 12
1.7 Energy Resolution of an APD 15
1.8 APDs in III-V Compound Semiconductors for X-Ray Detection 17
1.9 Aims and Structure of the Thesis 18

2 Overview of Models for Charge Multiplication in APDs . . . **21**
2.1 The Local Model 21
2.1.1 Gain and Excess Noise Factor 22
2.1.2 Frequency Response 25
2.2 Nonlocal Models 27
2.2.1 Gain and Excess Noise Factor 29
2.2.2 Dead Space Model 31
2.2.3 Model Based on Effective Fields 34
2.2.4 Time and Frequency Response: the Random Path Length Algorithm 36
2.3 Monte Carlo Models 38
2.3.1 Analytical Monte Carlo Simulations 38
2.3.2 Full Band Monte Carlo Simulations 41

3 The Energy Balance History Dependent Model **45**
3.1 Derivation of the Model's Equations 45
3.2 Numerical Solution 48
3.3 Model Calibration 49
3.4 Gain and Excess Noise Factor of APDs featuring Heterojunctions 52

3.4.1 $GaAs/Al_{0.8}Ga_{0.2}As$ SAM-APD . . . 52
3.4.2 $GaAs/Al_xGa_{1-x}As$ Staircase SAM-APD . . . 53
3.5 Optimization of the Noise Performance of Single Carrier Avalanche Photodiodes . . . 55
3.5.1 Derivation of the Equation for the Excess Noise Factor . 56
3.5.2 Numerical Validation with the EBHDM . . . 57
3.6 Optimization of the Noise Performance of $GaAs/Al_xGa_{1-x}As$ Staircase APDs for X-Ray Detection . . . 61
3.6.1 EBHDM results for different number of steps . . . 63
3.6.2 Interpretation based on the Electron and Hole Ionization Probabilities per Step . . . 64
3.7 Summary . . . 67

4 The Improved Random Path Length Algorithm . . . 69
4.1 Time Response, Bandwidth and Jitter . . . 69
4.2 Target Application: Staircase SAM-APD for X-ray Detection . . 70
4.3 Model . . . 71
4.3.1 Carrier Transport in the Absorption Region . . . 71
4.3.2 Carrier Transport in the Multiplication Region . . . 74
4.3.3 Current Induced at the Terminals . . . 74
4.4 Model Verification . . . 77
4.4.1 Performance Analysis of the Multiplication Region of a Staircase SAM-APD for X-Ray Detection . . . 80
4.5 Jitter of the Time Response . . . 83
4.5.1 Case 1: Influence of the Bias Voltage and of the Generation Point . . . 87
4.5.2 Case 2: Effect of impact ionization . . . 89
4.5.3 Case 3: Generation of Multiple Electron-Hole Pairs . . . 90
4.5.4 Case 4: Distributed Electron-Hole Pair Generation . . . 92
4.6 Summary . . . 93

5 Full Band Monte Carlo Simulations of GaAs APDs . . . 95
5.1 Band Structure . . . 95
5.1.1 Density of States . . . 100
5.2 Carrier-Phonon Scattering Rates . . . 101
5.2.1 Acoustic and Nonpolar Optical Phonons . . . 101
5.2.2 Polar Optical Phonons . . . 104
5.2.3 Results . . . 105
5.3 Impact Ionization . . . 107
5.4 The Full Band Monte Carlo Simulator . . . 110
5.4.1 Carriers' Injection and Motion . . . 111
5.4.2 Selection of the Scattering Mechanism and State After Scattering . . . 112
5.4.3 Results . . . 113
5.5 Gain and Excess Noise Factor of Thin GaAs p-i-n APDs . . . 119
5.6 Extraction of the History Dependent Impact Ionization Coefficients with Full Band Monte Carlo Simulations . . . 120

5.6.1 Using $\alpha(x|x')$ and $\beta(x|x')$ from FBMC in the NL-HD Model's Equations . . . 123
5.7 Calibration of the EBHDM based on the Results of FBMC Transport Simulations . . . 125
5.8 Simulation of Conduction Band Steps in GaAs APDs . . . 129
5.9 Summary . . . 135

6 TCAD Simulations and Comparison with Experiments . . . 137
6.1 Dark Current . . . 137
6.1.1 Experimental Characterization . . . 138
6.1.2 TCAD Simulations . . . 140
6.1.3 Simulation of the Collection Efficiency . . . 144
6.2 Simulation of the CV Characteristics . . . 146
6.3 Summary . . . 149

7 Conclusions and Future Work . . . 151
7.1 Future Work . . . 153

Bibliography . . . 155

Acknowledgments . . . 169

Appendices . . . 171

A Solution of the Integral in Eq. 2.15 . . . 173

B Hole's Overlap Integrals . . . 175

C Short Biography . . . 181

D List of Author's Publications . . . 183

Terminology

Abbreviations and Acronyms

APD	Avalanche PhotoDiode
BTE	Boltzmann Transport Equation
DS	Dead Space
EBHDM	Energy Balance History Dependent Model
FBMC	Full Band Monte Carlo
FBZ	First Brillouin Zone
FD	Finite Difference
FWHM	Full Width at Half Maximum
IR	InfraRed radiation
IW	Irreducible Wedge
MBE	Molecular Beam Epitaxy
MQW	Multi Quantum Well
MC	Monte Carlo
NL-HD	Nonlocal History Dependent
PET	Positron Emission Tomography
PDF	Probability Density Function
PSD	Power Spectral Density
QD	Quantum Dot
RC	Resonant Cavity
RPL	Random Path Length
SAM	Separate Absorption and Multiplication
SACM	Separate Absorption, Charge and Multiplication
SiPM	Silicon PhotoMultiplier
SRH	Shockley Read Hall generation/recombination mechanism
TIA	TransImpedance Amplifier
TCAD	Technology Computer Aided Design
UV	UltraViolet radiation

Symbols

a_0	Direct lattice constant of a crystal	m
BW	3dB Bandwidth	Hz

C_D	Detector's capacitance	F
d	Thickness of the intrinsic layer of a p-i-n APD	m
d_e	Electron's dead space	m
d_h	Holes's dead space	m
DoS	Density of States	$\mathrm{eV}^{-1}\mathrm{m}^{-3}$
E	Electric Field	Vm^{-1}
E_A	Activation energy	eV
$E_{eff,e}$	Effective field for electrons	Vm^{-1}
$E_{eff,h}$	Effective field for holes	Vm^{-1}
E_{ehp}	Electron-hole pair creation energy	eV
E_g	Energy gap	eV
E_k	Kinetic energy	eV
E_{ph}	Photon energy	eV
$E_{th,e}$	Threshold energy for electron's impact ionization	eV
$E_{th,h}$	Threshold energy for holes's impact ionization	eV
F	Excess noise factor	
f	Fano factor	
I	Current	A
I_{dark}	Dark current	A
I_{ph}	Photogenerated current	A
L	Attenuation length	m
M	Gain	
m_e	Electron's effective mass	kg
m_h	Hole's effective mass	kg
N_{step}	Number of multiplication steps	
P_e	Electron's impact ionization probability per step	
P_h	Hole's impact ionization probability per step	
SR	Scattering Rate	s^{-1}
T	Temperature	K
t_D	Time delay	s
t_j	Jitter	s
U_{SRH}	SRH generation/recombination rate	$\mathrm{m}^{-3}\mathrm{s}^{-1}$
V	Applied bias voltage	V
V_{rev}	Applied reverse bias voltage	V
V_{br}	Breakdown voltage	V
v_e	Electron's drift velocity	ms^{-1}
v_h	Holes's drift velocity	ms^{-1}
v_{th}	Thermal velocity	ms^{-1}
W	Width of the depletion region	m
Z	Atomic number	
α	Electron's impact ionization coefficient	m^{-1}
β	Hole's impact ionization coefficient	m^{-1}
ΔE_C	Conduction band offset	eV
ΔE_V	Valence band offset	eV
λ	Wavelength	m
λ_e	Electron's energy relaxation length	m

λ_h	Holes's energy relaxation length	m
μ_e	Electron mobility	$m^2V^{-1}s^{-1}$
μ_h	Hole mobility	$m^2V^{-1}s^{-1}$
ν	Frequency	Hz
τ_n	Electron's lifetime	s
τ_p	Hole's lifetime	s
Ψ_0	Built-in potential	V

Physical Constants

c	Speed of light in vacuum	2.99792×10^{8}	ms^{-1}
h	Planck's constant	6.626075×10^{-34}	Js
$\hbar$	Reduced Planck's constant	$h/(2\pi)$	Js
k_B	Boltzmann's constant	1.380649×10^{-23}	JK^{-1}
m_0	Electron rest mass	9.109390×10^{-31}	kg
q	Absolute electron charge	1.602176×10^{-19}	C
ε_0	Vacuum's permittivity	8.854187×10^{-12}	Fm^{-1}

List of Figures

1.1 Electromagnetic spectrum. 1
1.2 a) Radiative generation of an electron-hole pair due to a photon with energy $E_{ph} = h\nu > E_g$. b) Motion of the photogenerated carriers when an electric field is applied. 2
1.3 Representation of impact ionization triggered by electrons (a similar process can be triggered by holes). a) An electron moves inside the conduction band and its kinetic energy grows from 0 at $t = t_0$ to $E_k > E_g$ at $t = t_1$. b) A scattering event transfers the energy E_k to an electron in the valence band, promoting it to the conduction band. 2
1.4 a) Sketch of a reverse biased p-i-n diode, d is the thickness of the intrinsic layer and W is the width of the depletion region. b) Qualitative representation of the electric field profile inside the device of panel a). 4
1.5 Modes of operation of an APD: Linear mode ($|V| < |V_{br}|$) and Geiger mode ($|V| > |V_{br}|$). 5
1.6 Computation of the 3dB bandwidth (BW) of an APD with gain $M = 8 \simeq 18$ dB. The y-axis plots the Fourier transform of the current response to the optical generation of a single electron-hole pair. The lobes above 100 GHz are given by the fact that the current response is similar to a *rect* function in the time domain, which becomes a *sinc* in the frequency domain. 6
1.7 Sketch of an APD connected to a spectrum analyzer through a transimpedance amplifier (TIA). 7
1.8 a) Ratio between the hole and electron impact ionization coefficients for Si [16] (black solid) and GaAs [17] (red dashed) at room temperature. b) Attenuation length in Si (black solid) and in GaAs (red dashed) for photon energies in the range $30 \leq E_{ph} \leq 15000$ eV [14]. 8
1.9 Dependence of the bandgap of $Al_xGa_{1-x}As$ on the Aluminum mole fraction (x). At $x = 45\%$, a transition from direct to indirect bandgap occurs. 9
1.10 Representation of an electron moving from AlGaAs to GaAs. ΔE_C and ΔE_V are the conduction and valence band discontinuities, respectively. 10
1.11 Sketch of the band diagram of a staircase APD. 10
1.12 Excess noise factor for a staircase APD with $N_{step} = 1, 2, 5$ and 12. The computation has been performed using Eq. 1.10 [13]. 11

1.13 a) A UV photon hits an APD: electron-hole pairs are generated only inside region 1, before the multiplication region. b) A X-ray photon hits an APD and, if it is absorbed, it can generate an electron-hole pair in region 1, 2 or 3. 11

1.14 Band diagram of a Separate Absorption and Multiplication APD. 12

1.15 a) Time response of an APD to a single photon with energy E_{ph} that hits the device at $t = 0$. b) Setup of a charge measurement circuit. 13

1.16 Equivalent noise circuit of the charge measurement system of Fig. 1.15b. 13

1.17 Schematic representation of a CR-RC shaping circuit. 14

1.18 a) SAM-APD with a uniform $Al_{0.8}Ga_{0.2}As$ multiplication region for the detection of X-rays at $E_{ph} = 5.9$ keV [8, 25]. b) SAM-APD with a staircase $Al_{0.45}Ga_{0.55}As$/GaAs multiplication region for the detection of X-rays at $E_{ph} = 13.96$ keV [7, 21, 22]. 17

1.19 Energy resolution as a function of the gain for the devices of a) Fig. 1.18a [8, 25] and b) Fig. 1.18b [7, 21] at $E_{ph} = 5.9$ keV and $E_{ph} = 13.96$ keV, respectively. 18

2.1 Electric field profile and motion of carriers inside a p-i-n junction. 22

2.2 Excess noise factor as a function of the gain, in the case of pure electron injection, for $k = 0.01, 0.25, 0.5, 0.75, 1$. 24

2.3 Normalized 3dB bandwidth as a function of the gain, in the case of pure electron injection, for $k = 0.01, 0.05, 0.2, 0.5, 1$. Data taken from [12]. 27

2.4 Comparison between the measured excess noise factor versus gain curves for GaAs p-i-n diodes [23] and the predictions of the local model using the parameters of [17]. 28

2.5 Motion of carriers inside a p-i-n junction in the framework of a nonlocal model: x is the position where a carrier is generated (optically or by impact ionization), while x' is the point where impact ionization occurs. 28

2.6 a) An electron generated in x ionizes in x'. In x' we find the primary electron and a secondary electron-hole pair. b) A hole generated in x ionizes in x'. In x' we find the primary hole and a secondary electron-hole pair. 30

2.7 Comparison between the excess noise factor versus gain curves measured for GaAs p-i-n diodes of different thicknesses (symbols) and the ones obtained with the Dead Space model using the parameters of Tab. 2.1. Data taken from [38]. 32

2.8 Comparison between the experimental impact ionization coefficients for a) electrons and b) holes [17] in GaAs and the ones used in the Dead Space model [38]. 33

2.9 Comparison between the a) gain versus applied voltage and b) excess noise factor versus gain curves measured for GaAs p-i-n diodes of different thicknesses (symbols) and the ones obtained with the nonlocal model based on effective fields using the parameters of Tab. 2.2. Data taken from [36]. 35

2.10 Comparison between the experimental impact ionization coefficients for a) electrons and b) holes [17] in GaAs and the ones used in the history dependent model based on effective fields [36]. 35

2.11 Current waveforms as a function of time for GaAs p-i-n APDs at gains $M = 5$ (black solid line) and $M = 10$ (red dotted line). The thickness of the device is a) $d = 100$ nm, b) $d = 500$ nm and c) $d = 1$ μm. The computation has been performed with the RPL algorithm, using the parameters of [43]. 37

2.12 a) Electron and b) hole drift velocity as a function of the applied electric field in GaAs at $T = 300$ K. Results obtained with analytical Monte Carlo simulations by [48] (red circles) are compared with the experimental results in [50] or with other MC simulations [51]. Data are taken from [48] (black lines). 39

2.13 Comparison between the experimental electron and hole impact ionization coefficients [17] (black solid and dotted lines) and the ones computed with the analytical Monte Carlo simulations of [47] (red circles and blue squares). Data are taken from [47]. . . 39

2.14 Position dependent impact ionization coefficients in GaAs p-i-n diodes of thickness a) $d = 0.1$ μm and b) $d = 1.0$ μm computed by using analytical Monte Carlo simulations. Data are taken from [49]. 40

2.15 Dependence of the a) gain versus applied bias and b) excess noise factor versus gain curves of an $Al_{0.6}Ga_{0.4}As/GaAs/Al_{0.6}Ga_{0.4}As$ APD on the thickness of the GaAs layer. Data are taken from [54]. 41

2.16 Comparison between the a) electron and b) hole scattering rates as a function of the carrier's energy used for GaAs in the Full Band Monte Carlo simulators of [61] (red) and [62] (blue). The solid lines represent the carrier-phonon scattering rates, while the dotted lines are the impact ionization scattering rates. . . . 42

2.17 a) Electron and b) hole drift velocities as a function of the applied field. The results of the Full Band Monte Carlo simulations of [61] (red circles) and [62] (blue squares) are compared with the experimental results of [50] and [64] (black solid lines). . . . 42

2.18 a) Electron and b) hole impact ionization coefficients as a function of the reciprocal of the electric field. The results obtained by the Full Band Monte Carlo simulations of [61] (red circles) and [62] (blue squares) are compared with the experimental results of [17] (black solid lines). 43

2.19 a) Gain versus applied bias voltage and b) excess noise factor versus gain curves for GaAs p-i-n diodes with thickness d = 100 nm (black) and d = 200 nm (red). The experimental results of [66] (filled symbols) and [67] (empty symbols) are compared with the results of the Full Band Monte Carlo simulations of [61] (solid lines). 43

3.1 Spatial discretization of the variables N_e and N_h and indication of the boundary conditions (in red). 48

3.2 a) Gain versus applied bias voltage and b) excess noise factor versus gain curves for GaAs p-i-n diodes with different thickness. The experimental measurements reported in [23] (symbols) are compared with the results of the EBHDM using the parameters of Tab. 3.1 (dotted lines). 49

3.3 Same as Fig. 3.2 but for $Al_{0.2}Ga_{0.8}As$ p-i-n diodes. Experimental data are taken from [36]. 50

3.4 Same as Fig. 3.2 but for $Al_{0.6}Ga_{0.4}As$ p-i-n diodes. Experimental data are taken from [77]. 50

3.5 Same as Fig. 3.2 but for $Al_{0.8}Ga_{0.2}As$ p-i-n diodes. Experimental data are taken from [78, 79]. 51

3.6 Same as Fig. 3.2 but for InAs p-i-n diodes. Experimental data are taken from [20]. 51

3.7 Comparison between simulated (dashed line) and experimental (circles) C-V characteristics at ν = 1 MHz of the SAM-APD in [8] (Fig. 1.18a). 52

3.8 a) Simulated (dotted line) and measured (circles) gain versus voltage and b) excess noise factor versus gain for the SAM-APD reported in [8, 25]. 53

3.9 a) Band diagram at equilibrium of the multiplication region of the device in [7]. b) Comparison between simulated (dotted line) and experimental (circles) C-V characteristics of the staircase SAM-APD in [7] (Fig. 1.18b). 54

3.10 Simulated (dotted line) and measured (circles) a) gain versus voltage and b) excess noise factor versus gain for the staircase APD reported in [7]. Experimental results for plot b are taken from [21]. The structure in [21] slightly differs from the one in [7], but the EBHDM, with the model parameters of Tab. 3.1, gives the same $F(M)$ curve for both of these devices. 54

3.11 Conduction band profile of a staircase structure with N_{step} steps. M_i and F_i are the gain and excess noise factor of each step. . . . 57

3.12 a) Sketch and b) band diagram at equilibrium extracted from TCAD simulations [76] of the staircase SAM-APD reported in [10], along the vertical direction. 58

3.13 a) Gain versus applied voltage and b) excess noise factor versus applied voltage for the staircase SAM-APD reported in [10]. Experimental results from [10] (circles) are compared with the EBHDM (dotted line). 58

3.14 Comparison between the excess noise factor versus gain curves predicted by Eq. 1.10 for $N_{step} = 1$ (solid line), by the EBHDM (squares) and by the Local Model (blue dashed line) for single step staircase structures with different amplitude of the conduction band discontinuity. Experimental data from [10] are also reported (circles). 59

3.15 Gain (a) and excess noise factor (b) as a function of the normalized position $x/\Delta x$ (Δx being the step's length) at which an electron is generated for two staircase structures with ten steps. Solid red line: five steps with $\Delta E_C = 0.17$ eV are followed by five steps with $\Delta E_C = 0.6$ eV. Dashed blue line: five steps with $\Delta E_C = 0.6$ eV are followed by five steps with $\Delta E_C = 0.17$ eV. . 60

3.16 Excess noise factor as a function of the gain for different GaAs/AlGaAs APDs: experimental data for a thick ($d = 1.6\ \mu m$) GaAs p-i-n diode from [23] (•), staircase APDs fabricated by our group [22] (■, ⋇ for the 200 μm and the 600 μm mesa diameters, respectively), a MQW APD with 25 steps [84] (⧫), a MQW APD with 15 steps [85] (**x**) and for the staircase APD of [21] (▲). The dotted lines represent the results obtained with the EBHDM model (same calibration for both devices), while the solid line is Eq. 1.10 [13] (for $N_{step} = 12$ steps). 62

3.17 a) Simulated (EBHDM) gain as a function of the applied bias and b) excess noise factor as a function of gain for a staircase APD like the one in Fig. 1.18b with $N_{step} = 6, 12, 24, 48$ multiplication steps. 63

3.18 Conduction band profile of a 0.55 eV single multiplication step (as for the $Al_{0.45}Ga_{0.55}As/GaAs$ [76]) at fixed total gain ($M = 10$) for staircase APDs with 12 (solid line) and 48 steps (dashed line). 64

3.19 a), b) Electron's impact ionization coefficient $\alpha(0|x')$ and c), d) hole's impact ionization coefficient $\beta(d|x')$ as a function of the ionization point x' in one (a), two (b)(c) or three (d) steps of a $GaAs/Al_xGa_{1-x}As$ staircase APD ($N_{step} = 12$, $M = 5$). $x = d$ is the right-most point of the multiplication region. The location of conduction and valence band discontinuities is highlighted by red dashed lines. 65

3.20 Simulated (EBHDM) a) electron's and hole's ionization probabilities and b) ionization ratio $k_p = P_h/P_e$ as a function of the number of steps at given gain $M = 5, 10, 20$. 66

3.21 Comparison of the excess noise factor as a function of the gain computed by using the EBHDM (solid lines) or by using Eqs. 2.20 and 2.21 with the P_e and P_h from Fig. 3.20a (dashed lines) for a staircase APD like the one in Fig. 1.18 with $N_{step} = 6, 12, 24, 48$ multiplication steps. 66

4.1 Doping profile of the SAM-APD of Fig. 1.18b. The absorption region (thickness $d = d_{abs}$) is separated from the multiplication region ($d = d_{mult}$) by a p-doped δ-layer. The staircase multiplication region of this device features twelve AlGaAs/GaAs steps. In simulations, electron-hole pairs are generated at various x_g points inside the device. 70

4.2 Electron's drift velocity in GaAs as a function of the applied electric field for different values of the effective mass m_e, extracted from the RPL algorithm by using the description of carriers' motion reported in Section 4.3.1. The mobility (the slope of the $v(E)$ curve) is insensitive to the choice of m_e, thus $\mu_e = 8450$ cm^2/Vs in all cases, that is the value inserted in Eq. 4.2 to find τ_s when producing the points in this figure. 72

4.3 a) Electron's drift velocity and b) electron's mobility as functions of the applied electric field in GaAs. The values extracted from TCAD simulations (black circles) are compared with the ones obtained with the RPL algorithm by using $\tau_s \simeq 0.3$ ps, corresponding to $\mu_e = 8450$ cm^2/Vs and $m_e/m_0 = 0.063$ (red crosses). 73

4.4 a) Evolution in time of the PDF of the electron's position (after simulating an ensemble of 10^5 electrons) when the applied electric field is $E = 0$ and $T = 300$ K. b) Comparison between the time dependence of the variance of the PDF of the electron's position for $E = 0$ and $T = 300$ K (black circles) and the one of a Gaussian bell with variance $\sigma^2_{diff} = 2t\mu_e k_b T/q$ (red line), as given by the solution of the diffusion equation [92]. 73

4.5 Conductivity as a function of the position inside the device of Fig. 4.1 (in linear (a) and logarithmic scales (b)) extracted from TCAD simulations [76]. Two bias voltages lower than the breakdown voltage are considered: $V = -28$ V (black solid line) and $V = -32$ V (blue dashed line). 76

4.6 a) Sketch of the SAM-APD of Figures 1.18b and 4.1. Electron-hole pairs are generated at position x_g. b), c) Comparison between the weighting functions $w_i(t)$ extracted by using Eqs. 4.5, 4.6 and nominal d_{abs} and d_{mult} values (symbols) and Eqs. 4.10, 4.11 (lines) at two different positions inside the device ($x = -2.35$ μm in red, that corresponds to a point close to the middle of the absorption region, and $x = 0$ in blue, that corresponds to the coordinate where the multiplication region begins) and at b) $V = -28$ V and c) $V = -32$ V. In plot c), the dotted lines represent the $w_i(t)$ computed using Eqs. 4.5, 4.6, but employing effective values of d_{abs} and d_{mult}. When Eqs. 4.5, 4.6 are used, a constant conductivity inside the absorption region, equal to the value of σ at $x = -d_{abs}/2$ in the TCAD simulation, has been assumed. 77

4.7 a) Gain vs. voltage and b) excess noise factor vs. gain curves for GaAs p-i-n APDs of different thicknesses. The results obtained with the improved RPL algorithm (lines) are compared with the results of the Finite Difference implementation (open symbols, see Section 3.2) and with the experimental data from [23] (filled symbols). 78

4.8 Same as Fig. 4.7, but for the staircase SAM-APD of Fig. 1.18b. Experimental data are taken from [7, 21]. 78

4.9 Comparison between the current waveforms computed with TCAD [76] (dashed lines) and with our algorithm averaging over 10^5 photon-induced generation events (solid lines). The generation of a single electron-hole pair occurs at $x_g = -2.35$ μm a), c) or at $x_g = -0.25$ μm, b), d) and two different bias voltages have been applied: $V = -28$ V a), b) and $V = -32$ V c), d). In these simulations, impact ionization is turned off. Here and in the next figures, the spatial coordinates are the same as in Fig. 4.1. 79

4.10 a) Gain vs. voltage and b) excess noise factor vs. gain characteristics obtained with the improved RPL algorithm for a 1 μm thick GaAs p-i-n APD and for the staircase SAM-APD reported in Fig.1.18b. In the staircase SAM-APD we have an extended voltage range where a gain significantly larger than one that is achieved by the p-i-n diode. 80

4.11 Current waveforms at different gains for the multiplication region of the staircase SAM-APD of Fig. 1.18b obtained with the improved RPL algorithm a) without or b) with hole impact ionization. Carriers move at a constant velocity $v_e = v_h = 10^7$ cm/s so that the transit time across the 1-μm multiplication region is $T_R = 10$ ps. 81

4.12 a) Simulated Gain-bandwidth product of a 500 nm and a 1 μm-thick GaAs p-i-n diodes and of the multiplication region of the staircase SAM-APD of Fig. 1.18b obtained with the improved RPL agorithm (open symbols). Filled symbols: experimental data for a planar [95] and a thin layer [96] separate, absorption, charge and multiplication (SACM), a Multi Quantum Well (MQW) [97], a quantum dot (QD) SACM [98] and a resonant cavity (RC) APDs [99] based on III-V compound semiconductors. b) Same as plot a) in the range $1 \leq BW \leq 20$ GHz. 82

4.13 Simulated current waveforms for a staircase APD like the one in Fig. 1.18b with $N_{step} = 6, 12, 24, 48$ multiplication steps at fixed gain $M = 10$. 82

4.14 Simulated current waveforms, after the convolution with the impulse response function of a CR-RC shaper with time constant $\tau = 1$ μs, for a staircase SAM-APD as the one in Fig. 1.18b with $N_{step} = 6, 12, 24, 48$ multiplication steps at fixed gain $M = 10$. . 83

4.15 Representation of the Crossover Timing method to compute t^*, which is representative of a readout scheme used in time of flight measurements. The original current waveform (a) is subtracted to itself delayed by t_D (b) to obtain a bipolar pulse (c). A trigger is generated at the zero-crossing point t^*. In the inset of panel (a), the procedure is reported in the form of a block diagram. . 84

4.16 a) Sample current waveform for a single generation event and b) the corresponding current power spectral density averaged over $N_{ev} = 10^3$ generation events computed with our algorithm using the complete model described in Section 4.3 (black solid line) or imposing $w_i(x,t) = 0$ for $x < 0$ (red dotted line) for $V = -28$ V and $x_g = -2.35$ μm. A single electron-hole pair is generated per absorbed photon. 86

4.17 Probability Density Functions of t^* for a) $V = -28$ V and b) $V = -32$ V for different t_D. The generation point is $x_g =$ -2.35 μm. $PDF(t^*)$ is the same regardless of the t_D value. . . . 86

4.18 Probability Density Functions of t^* at $V = -28$ V a), b) and at $V = -32$ V c), d) when an electron-hole pair is generated at $x_g = -2.35$ μm a), c) or at $x_g = -0.25$ μm b), d). The PDFs extracted with the RPL algorithm (red solid lines) are compared with a fitted inverse Gaussian distribution (Eq. 4.12, black dashed lines). The delay of the readout of Fig. 4.15 is chosen so that the falling edge of the original current waveform crosses the rising edge of the delayed one, thus: $t_D = 0.5 \cdot d_{mult}/v_e = 7$ ps a), b) or $t_D = d_{mult}/v_e = 14$ ps c), d). Note the different scales of the x-axis and the Dirac's delta like shape of the $PDF(t^*)$ in graph d). Impact ionization is turned off. 88

4.19 a), c), e), g): Sample current waveforms associated to the arrival of a photon that generates one electron-hole pair at $x_g = 0$ when impact ionization is turned on. The applied voltage is $V = -28$ V. Since impact ionization is a stochastic process, the gain m is not the same for all events: $m = 1$ in a) and b), $m = 2$ in c) and d), $m = 6$ in e) and f) and $m = 83$ in g) and h). Plots b), d), f), h) report the difference between the current waveform and its delayed version when the delay is $t_D = d_{mult}/v_e = 14$ ps. The first zero-crossing point is highlighted with a red dot. . . . 89

4.20 Probability Density Function of t^* after the arrival of $N_{ev} = 10^5$ photons, when the bias voltage is $V = -28$ V. Single electron-hole pairs are generated at the beginning of the multiplication region ($x = 0$). $t_D = d_{mult}/v_e = 14$ ps. 90

4.21 a) Distribution of the number of generated electron-hole pairs in GaAs for a photon with energy $E_{ph} = 500$ eV according to [25]. b) Probability Density Functions of t^* considering 10^3 times the process of the arrival of a photon and the random generation of electron-hole pairs, at $x_g = 0$ in the device of Fig. 4.1. $E_{ph} =$ 125, 500 or 2000 eV (black solid line, red dashed line and blue dotted line respectively). Impact ionization is turned on, the applied voltage is $V = -28$ V. $t_D = d_{mult}/v_e = 14$ ps. 91

4.22 Comparison between the Probability Density Functions of t^*, extracted with the extended RPL after the arrival of $N_{ev} = 10^3$ photons, when multiple electron-hole pairs are generated at $x_g = -4.25$ μm (black solid line), $x_g = -2.35$ μm (red dashed line), $x_g = 0$ (green dashed-dotted line) or when the generation follows the profile given by Eq. 1.8 (blue dotted line). The applied bias voltage is $V = -28$ V and impact ionization is turned on. The delay of the readout circuit of Fig. 4.15 is $t_D = d_{mult}/v_e = 14$ ps. 92

5.1 a) First Brillouin Zone and b) Irreducible Wedge of the Face-Centered Cubic reciprocal lattice. The symmetry points are indicated in plot b). 96

5.2 Comparison between the Band Structure of GaAs computed by employing the Empirical Pseudopotential Method, including Spin Orbit Interaction, by using the code of [104] with the parameters of Tabs. 5.1 and 5.2 (red lines), and the one calculated by [105] (black circles). 99

5.3 Comparison between the Γ valley of GaAs, along the $[1, 0, 0]$ direction, computed in this work by using the EPM with the parameters of Tabs. 5.1 and 5.2 and the analytical dispersion relation of Eq. 2.79 with the parameters of Tab. 5.3. 100

5.4 Comparison between the GaAs Density of States computed by using our code (red line) and the ones calculated by [60] (black circles), [105] (blue squares) and [62] (magenta triangle-downs). 100

5.5 Carrier-phonon scattering rates for a) holes and b) electrons as functions of energy. Our results (red lines), obtained by using the parameters in Tab. 5.4 and $\Delta E = 4$ meV, are compared with the calculations of [60] (black circles), [105] (blue squares), [61] (green triangle-ups) and [62] (magenta triangle-downs). . . . 106
5.6 Schematic representation of the impact ionization mechanism for a *hot* electron in a direct bandgap semiconductor. The primary electron (1) in the conduction band interacts with an electron in the valence band (4). The process ends with two secondary electrons in the conduction band (2, 3) and a secondary hole in the valence band (4). 107
5.7 a) Electron and b) hole impact ionization scattering rates in GaAs as a function of energy. Our results (red lines), obtained by using the Constant Matrix Element approximation [112], are compared with the scattering rates computed by other authors [105, 113, 114]. 109
5.8 Secondary carriers' energy distributions for a ionizing electron with kinetic energy (a) 4 eV or (b) 6 eV. Positive energy refers to electrons and negative energies to holes. The computation has been performed by using Eqs. 5.35 and 5.36 with the constant matrix elements of Tab. 5.4. $\Delta E = 4$ meV and $ndiv = 20$. . . . 110
5.9 Same as Fig. 5.8 but for hole-initiated impact ionization. 110
5.10 Schematic representation of the selection of the state after scattering with the rejection algorithm. 113
5.11 a) Electron velocity v_e and b) hole velocity v_h versus electric field (E) curves in GaAs at $T = 300$ K. FBMC results (red crosses) are compared with experimental data [50, 64, 115, 116] (solid lines). 114
5.12 Electron's and hole's average energies as functions of the applied electric field. Results of our FBMC simulations (red crosses and (blue plus signs) are compared with the results of [60] (black filled and open squares). 114
5.13 a) α and b) β versus the reciprocal of the electric field in GaAs at $T = 300$ K. FBMC (Eq. 5.45 (red crosses) or Eq. 5.46 (blue solid line)) is compared with experiments [17] (black solid) and with α and β used in [69] (black dotted line). 115
5.14 $PDF(l_e)$ at different electric fields. The red solid lines represent Eq. 5.48. The magenta dashed line is the electron's dead space (d_e) computed by using Eq. 2.60 with $E_{th,e} = 2.69$ eV (see Fig. 5.22b). 116
5.15 Same as Fig. 5.14, but secondary electrons are generated with null kinetic energy in FBMC simulations. 116
5.16 $PDF(l_h)$ at different electric fields. The red solid lines represent Eq. 5.48. The magenta dashed line is the hole's dead space (d_h) computed by using Eq. 2.61 with $E_{th,h} = 3.12$ eV (see Fig. 5.24b). 118

5.17 Same as Fig. 5.16, but secondary holes are generated with null kinetic energy in FBMC simulations. 118

5.18 Sketch of the simulation domain employed in this work to compute the gain and the excess noise factor in thin GaAs APDs. . 119

5.19 a) M versus V_{rev} and b) F versus M curves for GaAs p-i-n APDs. FBMC (solid lines) is compared with experiments [23] (symbols). A built-in voltage $\Psi_0 = 1.2$ V has been assumed [117]. 120

5.20 Discretization of the intrinsic region of a p-i-n diode with a mesh with uniform spacing Δx. x is the point where a carrier is generated, optically or by impact ionization, and x' is the point where it ionizes. Electrons move from left to right with average velocity v_e (while holes move from right to left with average velocity v_h and x and x' are inverted). 120

5.21 $\alpha(x|x')$ extracted from FBMC simulations by using Eq. 5.53 in a 100 nm-thick GaAs p-i-n APD with electron injection from the left side at $V_{rev} = 5.5$ V (black) and $V_{rev} = 6.6$ V (red). a) $x = 0$, b) $x = 50$ nm. A built-in voltage $\Psi_0 = 1.2$ V has been assumed [117]. 122

5.22 a) α (empty symbols) and α^* (filled symbols) versus $1/E$ extracted from FBMC simulations of GaAs p-i-n diodes by using Eq. 5.45 and Eq. 5.53 (plateau for $x' \gg x$), respectively. b) Electron's dead space d_e versus $1/E$ extracted, point by point, with Eq. 5.49 from the α and α^* of Fig. 5.22a with Eq. 5.49. The blue dotted line in plot b is the least squares linear fit of the d_e values, giving a slope $E_{th,e}/q = 2.69$ V. The same parameter inserted in Eq. 5.49 gives the blue dotted line in plot a. 122

5.23 $\beta(x|x')$ extracted from FBMC simulations by using Eq. 5.53 in a 100 nm-thick GaAs p-i-n APD with hole injection from the right side at $V_{rev} = 5.5$ V (black) and $V_{rev} = 6.6$ V (red). a) $x = 100$ nm, b) $x = 90$ nm. A built-in voltage $\Psi_0 = 1.2$ V has been assumed [117]. 123

5.24 Same as Fig. 5.22, but for the hole's impact ionoization coefficient β. The the least squares linear fit of the d_h values in plot b) (blue dotted line) has slope $E_{th,h}/q = 3.12$ V. 123

5.25 Comparison between the a) M and b) F versus V_{rev} curves for GaAs p-i-n diodes obtained with the FBMC (circles) or by using the NL-HD model's equations described in Section 3.2 with $\alpha(x|x')$ and $\beta(x|x')$ extracted from FBMC simulations as inputs (crosses). A built-in voltage $\Psi_0 = 1.2$ V has been assumed [117]. 124

5.26 Same as Fig. 5.25 but, after an impact ionization event, secondary electrons and holes are generated with null kinetic energy. 124

5.27 Comparison of the excess noise factor as a function of the gain computed with FBMC simulations (solid lines) or by using the NL-HD model's equations described in Section 3.2 with $\alpha(x|x')$ and $\beta(x|x')$ extracted from FBMC simulations as input (symbols) for GaAs p-i-n APDs of different thickness. a) Secondary carriers are generated with an inital energy determed with the selectrion rules described in Section 5.4.2. b) Secondary carriers are generated with null kinetic energy. The values of M and F in plots a) and b) are the same reported in Figs. 5.25 and 5.26, respectively. A built-in voltage $\Psi_0 = 1.2$ V has been assumed [117]. 125
5.28 Fitting of the values of a) α^* and b) β^* as a function of the reciprocal of the electric field extracted from FBMC simulations (and reported in Figs. 5.22a and 5.24a) by using Eqs. 2.72 and 2.73, respectively, with the parameters of Tab. 5.6. 126
5.29 Comparison of the electron's impact ionization coefficient $\alpha(0|x')$ extracted from FBMC simulations (black solid line) with the one computed using the EBHDM (Eq. 2.72) with an energy dependent relaxation length $\lambda_e(x|x')$ (Eq. 5.54, blue dashed line) for devices with different thickness and at different bias voltages: a) $d = 100$ nm, $V_{rev} = 6$ V; b) $d = 200$ nm, $V_{rev} = 9$ V; c) $d = 500$ nm, $V_{rev} = 17$ V. The built-in voltage is $\Psi_0 = 1.2$ V [117]. 127
5.30 Same as Fig. 5.29, but for the hole's history dependent impact ionization coefficient $\beta(d|x')$. 128
5.31 $\alpha(0|x')$ for a 100 nm-thick GaAs p-i-n diode when hole impact ionization is turned off. FBMC (black solid line) is compared with the EBHDM described in Chapter 3 either with $\lambda_e = 18$ nm (red dotted line) or λ_e from Eq. 5.54 (blue dashed line) and with the Dead Space model (DS) [35], when d_e is taken from Fig. 5.22b (green dashed-dotted line). A built-in voltage $\Psi_0 = 1.2$ V has been assumed [117]. 128
5.32 Same as Fig. 5.31, but for $\beta(d|x')$. Electron's impact ionization is turned off. 129
5.33 Schematic representation of how conduction band steps have been simulated in this thesis. The initial electron is injected with energy ΔE_C in the simulation domain, that extends from $x = 0$ to $x = d$. An electric field is applied along the x direction, to ensure that all the carriers exit from the simulation domain. . 130
5.34 a) Gain and b) excess noise factor as functions of the applied electric field in a 50 nm thick device when an electron with initial $\Delta E_C = 0$ eV (black), 0.3 eV (red) or 0.5 eV (blue) is injected at $x = 0$. The results obtained with FBMC simulations (circles) are compared with the results of the NL-HD model's equations described in Section 3.2 when $\alpha(x|x')$ and $\beta(x|x')$ extracted from FBMC simulations are taken as input. 131

5.35 Same as Fig. 5.34, but for a 100 nm thick device. 131

5.36 Gain variation (ΔM) as a function to the electron's injection energy (ΔE_C) w. r. t the case $\Delta E_C = 0$ eV in a a) 50 nm or in a b) 100 nm thick device. 132

5.37 Comparison between the excess noise factor as a function of the gain per step calculated by using Eq. 1.10 with $N_{step} = 1$ (black solid line), $F = 2-1/M$ (black dashed line), which is Eq. 2.19 in the $k = \beta/\alpha \to 0$ limit, and the results of FBMC simulations of 100 nm thick GaAs conduction band steps at different applied electric fields (symbols). For a given electric field, the increase of the gain is achieved by increasing the electron's injection energy. 132

5.38 $\alpha(0|x')$ for a 100 nm-thick GaAs conduction band steps of different amplitude and at different values of the applied electric field. FBMC (black solid line) is compared with the EBHDM either with $\lambda_e = 18$ nm (red dotted line) or λ_e from Eq. 5.54 (blue dashed line). 133

5.39 Comparison between a) the gain and b) the excess noise factor as a function of the applied electric field and for different values of ΔE_C computed with the FBMC simulator (circles and solid lines) and with the EBHDM by using constant λ_e and λ_h (crosses and dotted lines) or $\lambda_e(x|x')$ and $\lambda_h(x|x')$ from Eq. 5.54 (plus signs and dashed lines). 134

6.1 Dark current as a function of the applied reverse bias voltage V_{rev} for a subset of APDs. The breakdown voltage of the devices (V_{br}) is around 38 V. The APD active area is circular, with diameter 400 μm. 138

6.2 Experimental IV curves of a representative APD for different operating temperatures T. 138

6.3 Breakdown voltage as a function of temperature. The positive temperature coefficient is a signature of the avalanche multiplication process. 139

6.4 Arrhenius plots of the dark current for several V_{rev} values. Curves show the expected exponential behavior down to low temperatures where they start to deviate from Eq. 6.1 likely because a temperature independent dark current component enters into play. 139

6.5 Activation energy as a function of the appiled reverse bias voltage, V_{rev}, extracted from the Arrhenius plots in Fig. 6.4. E_A is rather independent of the V_{rev} value and close to $E_g/2$. 140

6.6 Arrhenius plots simulated for $V_{rev} = 20$ V assuming constant τ_n and τ_p and variable trap energy depth E_T. 141

6.7 Arrhenius plots simulated with $\tau_n = \tau_p$ as in Eq. 6.8, and with $E_T = E_i$. Simulations now reproduce the experiments for different V_{rev}. A power-law temperature dependence is assumed to model the lifetimes (Eq. 6.8, $\tau_{300K} = 0.39$ ns, $\alpha = 6.06$). At low T, the experiments deviate from the linear behavior most likely because of a temperature-independent component not included in simulations. 142

6.8 SRH generation/recombination function along the device depth. $x = 0$ corresponds to the p-doped δ-layer position that separates the absorption and multiplication regions. Note that carrier generation ($U_{SRH} < 0$) occurs in the small bandgap GaAs layers of the multiplication region. $V_{rev} = 20$ V. $\tau_n = \tau_p = \tau_{300K} = 0.39$ ns, $\alpha = 6.06$. 142

6.9 Simulated IV curves with $\tau_n = \tau_p$ as in Eq. 6.8. Simulations well reproduce the experiments, except at low T, when a temperature independent leakage component most likely arises in the measurements. 143

6.10 Typical experimental capacitance–voltage curves (symbols) of the measured APDs. The TCAD simulation for nominal parameter values (line) is reported for comparison. 143

6.11 Electron density n calculated in absorption layer at different instants (t) after the generation of an electron-hole pair (in the middle). After the generation, carrier diffuse all over the absorption layer, due to the negligible electric field in the region. Then, without the SRH process (a), electrons can exit the region only through the multiplication layer on the right. With SRH (b), instead, electrons partly recombine before reaching the multiplication layer. Area of the device is 1 μm^2. 144

6.12 Simulated current collected at the n-type contact as a function of time after the generation of an electron-hole pair in the middle of the absorption layer. The current is simulated including (red) or not (black) the SRH generation/recombination. At $V_{rev} = 28$ V, the SRH process causes the loss of 45% of the photo–generated charge. 145

6.13 Collection efficiency as a function of the position inside the absorption layer where the photo–generation takes place. If the electron–hole pair is generated closer to the multiplication region ($x > 4.5$ μm), the collection efficiency is larger. 146

6.14 Dose of the p-doped δ-layer that separates the absorption and the multiplication region of the staircase SAM-APD of Fig. 1.18b. The dose is computed with Eq. 6.9 since a Gaussian doping profile has been assumed in the TCAD simulations [76]. 147

6.15 Capacitance as a function of the reverse bias voltage obtained with TCAD simulations [76] for different $FWHM$ values of the dose of the p-doped δ-layer (see Fig. 6.14). 147

6.16 Schematic representation of the absorption and multiplication regions' contributions to the total capacitance of the staircase SAM-APD of Fig. 1.18b. 148
6.17 Experimental (symbols) and simulated (red lines) capacitance versus applied reverse bias voltage curves of the staircase SAM-APD of Fig. 1.18b for different doses of the p-doped δ-layer. The dose is a) 1.3×10^{12} cm^{-2}, b) 1.6×10^{12} cm^{-2} and c) 2.5×10^{12} cm^{-2}. 148
6.18 Conduction band profiles near the end of the absorption region extracted from TCAD simulations [76] of the staircase SAM-APD of Fig. 6.18 at differnt bias voltages: a) $V_{rev} = 10$ V, b) $V_{rev} = 20$ V, c) $V_{rev} = 25$ V. The dose of the p-doped δ-layer is 1.3×10^{12} cm^{-2} (blue), 1.6×10^{12} cm^{-2} (red) or 2.5×10^{12} cm^{-2}. Notice that in plot c) the blue curve is not visible beacuse it is out of scale. 149

7.1 Schematic representation of the simulation tools developed in this thesis. Each model is suited to analyze different feature sizes and times scales. 152

B.1 Hole-phonon scattering rate as a function of the carrier energy. The deformation potentials of Tab. B.1 have been used and the hole's overlap integrals have been computed as in [124]. Our results (red solid line) have been compared with the results of [114] (black circles). 175
B.2 Hole's drift velocity as a function of the applied electric field in bulk GaAs at $T = 300$ K when the hole-phonon scattering rate is the one of Fig. B.1. FBMC results have been compared with the experimental results of [64, 115, 116] (black, blue and brown solid lines, respectively). 176
B.3 Hole's impact ionization a) scattering rate as a function of the carrier energy and b) impact ionization coefficient as a function of the reciprocal of the electric field. The results have been obtained by multiplying by 3 the matrix element $T_{ii,h}$ of Tab. 5.5. In plot a) our results (red solid line) have been compared with the computations of [113, 114] (black circles and triangles, respectively), while in plot b) FBMC results (red crosses) have been compared with experiments (black solid line)[17]. 177
B.4 a) M versus V_{rev} and b) F versus M curves for GaAs p-i-n APDs when the hole's overlap integrals have been compued as in [124] and the matrix element $T_{ii,h}$ of Tab. 5.5 has been multiplied by 3. FBMC (solid lines) is compared with experiments [23] (symbols). A built-in voltage $\Psi_0 = 1.2$ V has been assumed [117]. 177
B.5 Same as Fig. B.4, but the matrix element $T_{ii,h}$ of Tab. 5.5 has been multiplied by 50. 178
B.6 Same as Fig. B.3, but the results for when the matrix element $T_{ii,h}$ of Tab. 5.5 is multiplied by 50 are also reported (blue solid line). 178

B.7 Squared modulus of the hole's overlap integrals $\mathcal{I}(n_1, n_2; \vec{k_1}, \vec{k_2})$ by using Eq. 5.15, with the wavefunctions given as output of the solution of the EPM Hamiltonian (Eq. 5.4). For each plot, the wavevector of the initial state is fixed ($\vec{k_1} = \Gamma$), while the band index n_1 goes from the highest valence band ($VB4$) in plot a) to the lowest one ($VB1$) in plot d). The final state $(n_2, \vec{k_2})$ is chosen along the $[1, 0, 0]$ direction and the overlap integral is computed only if $|E(n_2, \vec{k_2}) - E(n_1, \vec{k_1})| \leq 33$ meV, which is the maximum phonon energy in GaAs (Eq. 5.18 with the parameters in Tab. 5.4). The dotted magenta line is the result of the Rigid Ion approximation (Eq. 5.29). 179

List of Tables

2.1 Parameters for the computation of the impact ionization coefficients and of the dead space lenghts using the Dead Space model [38]. 32
2.2 Parameters for the computation of the impact ionization coefficients in the nonlocal model base on effective fields [36]. 35

3.1 Model parameters for GaAs, $Al_{0.2}Ga_{0.8}As$, $Al_{0.6}Ga_{0.4}As$, $Al_{0.8}Ga_{0.2}As$ and InAs used in the EBHDM to fit experimental results for the gain versus applied bias and excess noise factor versus gain measurements. 51
3.2 Comparison between the excess noise factor obtained with the EBHDM and the one calculated using Eq. 3.21 for staircase structures with different number of steps and conduction band discontinuities with different amplitudes. 60

5.1 Empirical Pseudopotential parameters for GaAs used in the code of [104]. 98
5.2 Spin Orbit Interaction parameters for GaAs used in the code of [104]. 98
5.3 Band structure parameters for bulk GaAs. 99
5.4 Deformation potentials and other parameters used for the computation of the carrier-phonon scattering rates in GaAs. 106
5.5 Constant Matrix Elements used for the computation of the hole's and electron's impact ionization scattering rates in GaAs. 109
5.6 EBHDM model parameters for GaAs calibrated on the results of FBMC simulations. 126
5.7 Values of the parameters A_λ and B_λ to insert into Eq. 5.54 to compute the electron's energy dependent relaxation length $\lambda_e(x|x')$. 127

B.1 Deformation potentials used for the computation of the hole-phonon scattering rates in GaAs when the hole's overlap integrals have been computed as in [124]. 176

Chapter 1

Introduction

Studying the interaction of an electromagnetic wave (or, in other words, due to the discrete nature of light, of photons) with other objects is of extreme importance in our daily life. In astronomy, radio waves are used to discover new planets, stars and galaxies. In telecommunications, infrared (IR) and ultraviolet (UV) light are exploited for data transmission in optical fiber links. In medicine, X- and γ-rays are used for the diagnosis of fractures, tumors and other diseases. In addition, in physics and material science experiments, new properties can be analyzed by observing the behavior of a material when it is irradiated by a photon flux.

The energy of a photon (E_{ph}) is linked to the frequency (ν) and wavelength (λ) of the electromagnetic wave by the relation

$$E_{ph} = h\nu = \frac{hc}{\lambda}, \tag{1.1}$$

where h is the Planck's constant and c is the speed of light.

The realization of new generations light sources able to work on the short wavelength side of the spectrum (see Fig. 1.1), such as advancements in synchrotrons and Free Electron Lasers, requires the development of detectors able to resolve high energy photons, so that new phenomena, down to the atomic scale, can be observed. For instance, energies in the order of 1 keV corresponds to $\lambda \simeq 1.2$ nm.

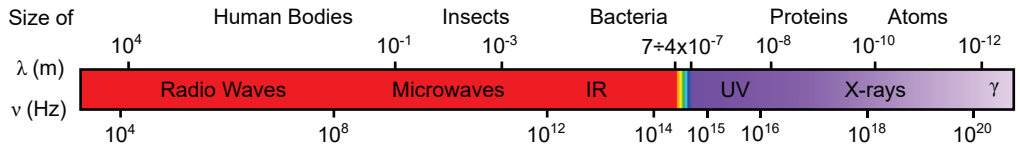

Figure 1.1: Electromagnetic spectrum.

In this thesis, we will focus on the modeling of solid state detectors for high energy photons and in particular of a specific type of detector used for the analysis of X-ray photons (100 eV $\leq E_{ph} \leq$ 200 keV), the Avalanche Photodiode (APD). In this Chapter, we review the working principles of APDs to understand the trade-offs at the basis of their design, while different modeling

methodologies will be discussed and applied in the following ones. A detailed description of the structure of this thesis is provided in Section 1.9.

1.1 Radiative Generation and Impact Ionization

Avalanche Photodiodes are electronic devices that transduce a photon flux into an electric current and that provide intrinsic amplification of this current. To do so, two generation/recombination mechanisms of semiconductor materials are exploited: radiative generation and impact ionization.

When a photon hits a semiconductor, its energy E_{ph} is transferred to an electron that populates the valence band of the material. If the photon's energy is larger than the bandgap of the semiconductor (E_g), then the electron in the valence band may be promoted to the conduction band, leaving a hole in the valence band: a new electron-hole pair is, thus, created (see Fig. 1.2a). This mechanism is called *radiative generation*. If an electric field $E(x)$ is now applied to the semiconductor, then carriers will move, with their respective velocities (v_e for electrons and v_h for holes) according to the direction of the field (Fig. 1.2b), inducing a current at the contacts (the so-called *photogenerated current, I_{ph}*).

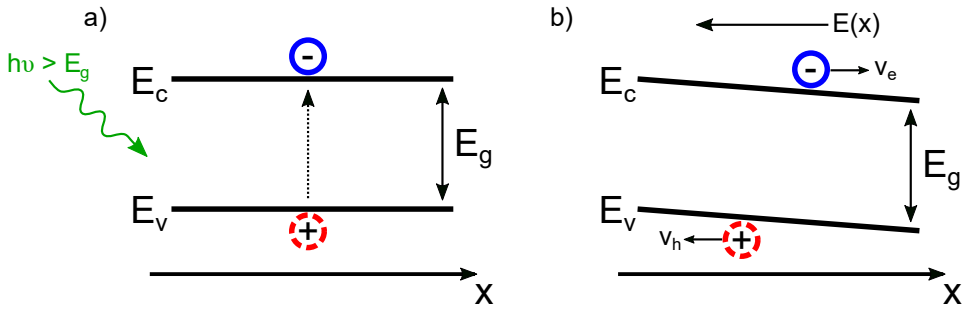

Figure 1.2: a) Radiative generation of an electron-hole pair due to a photon with energy $E_{ph} = h\nu > E_g$. b) Motion of the photogenerated carriers when an electric field is applied.

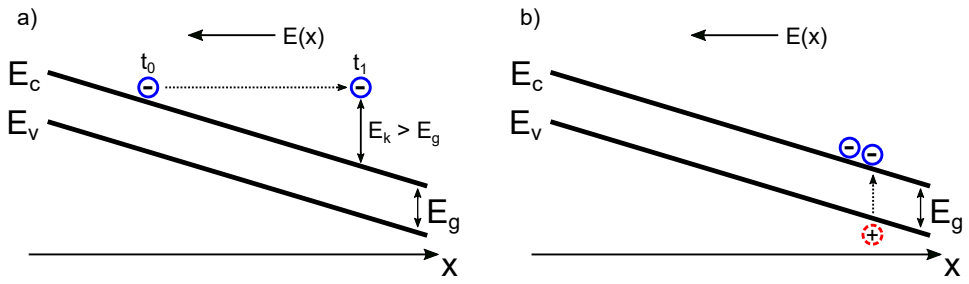

Figure 1.3: Representation of impact ionization triggered by electrons (a similar process can be triggered by holes). a) An electron moves inside the conduction band and its kinetic energy grows from 0 at $t = t_0$ to $E_k > E_g$ at $t = t_1$. b) A scattering event transfers the energy E_k to an electron in the valence band, promoting it to the conduction band.

Figure 1.3a shows that, when a strong electric field is applied, a *primary* electron moving in the conduction band can acquire a kinetic energy $E_k > E_g$. A scattering event, denoted as *impact ionization*, may now transfer E_k to an electron in the valence band, creating a new *secondary* electron-hole pair (see Fig. 1.3b). The primary electron loses its kinetic energy and falls at the bottom of the conduction band. This mechanism is responsible for the amplification of I_{ph}, since, as shown in Fig. 1.3, starting from a single electron in the conduction band we end up with two electrons in the conduction band and a hole in the valence band. Indeed a sequence of generation events will generate a bunch of secondary carriers, thus increasing appreciably the current from its original value. This process is also called *avalanche multiplication* and, like impact ionization, it occurs also for holes moving inside the valence band. Avalanche multiplication is quantified by the so-called *multiplication factor*, M_e, defined as the ratio of the total (electron) current density to the injected starting electron current.

Finally we remind that impact ionization is a stochastic process and, thus, it is a source of noise. This is an important aspect in view of APD detectors development, usually quantified in terms of the r.m.s. of the multiplication current. Impact ionization depends on the device geometry, the bias configuration and the semiconductor material at the microscopic level. Impact ionization is quantified through the impact ionization coefficients, α for electrons and β for holes, that are the reciprocal of the average distances between two consecutive ionizing events. As it will be clear in the following, it is also useful to define $k = \beta/\alpha$ [1].

1.2 p-i-n APDs

The simplest structure of an APD is a reverse biased p-i-n junction (Fig. 1.4a). The electric field inside the depletion region is responsible for both the separation of the photogenerated electron-hole pairs and the amplification of I_{ph}. The width of the depletion region is given by

$$W = \sqrt{\frac{2\varepsilon}{q}\left(\frac{1}{N_A} + \frac{1}{N_D}\right)(\Psi_0 - V) + d^2} \simeq d, \tag{1.2}$$

where ε is the permittivity of the material, q is the electron's charge, N_A and N_D are the acceptor and donor dopants concentrations, Ψ_0 is the junction's built-in potential, V is the applied voltage and d is the thickness of the intrinsic layer. This means that, since W depends mainly on the geometric parameter d, the maximum electric field inside the device,

$$E_{max} = \frac{\Psi_0 - V}{W} \simeq \frac{\Psi_0 - V}{d}, \tag{1.3}$$

is a function of the geometry of the structure and of the applied voltage. As qualitatively shown in Fig. 1.4b, the electric field profile is uniform along the

whole depletion region as long as N_A and N_D are constant and the hole's and electron's densities, p and n, are therein negligible.

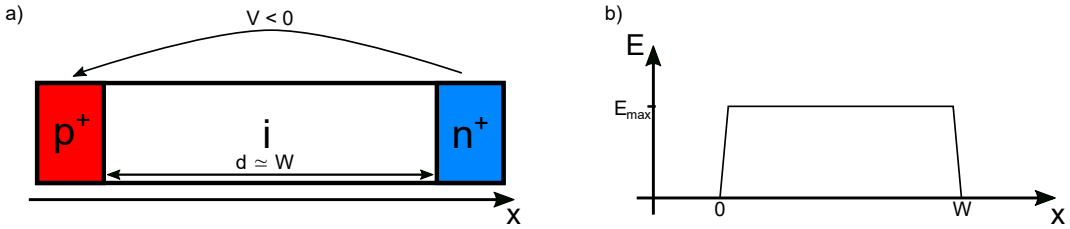

Figure 1.4: a) Sketch of a reverse biased p-i-n diode, d is the thickness of the intrinsic layer and W is the width of the depletion region. b) Qualitative representation of the electric field profile inside the device of panel a).

The region of the APD where impact ionization occurs (i. e. the intrinsic layer in the case of a p-i-n APD) is called *multiplication region*.

Two different modes of operation can be implemented with this device (see Fig. 1.5):

- *Geiger Mode*: the applied voltage is larger, in modulus, than the breakdown voltage ($|V| > |V_{br}|$). A photon that hits the device generates electron-hole pairs that trigger the avalanche multiplication with multiplication factors exceeding 10^5. An external quenching circuit interrupts the avalanche only when the output current reaches a defined threshold. A short current pulse is thus generated upon arrival of the photon. An APD operating in Geiger mode is, thus, a *binary* device, since the amount of charge at the output of the device is independent of both E_{ph} and the number of incident photons. The very high charge amplification ($\sim 10^6$ [2]) makes these devices suited for the detection of single photons. Geiger mode APDs are typically used for timing measurements, such as in time-of-flight experiments, like PET scanners [2, 3] and lidars [4]. Photon counting is possible at low fluxes or using pixellated detectors [5]. Silicon PhotoMultipliers (SiPMs) represent the state of the art for APDs operating in Geiger mode [2].

- *Linear Mode*: the applied voltage is smaller, in modulus, than the breakdown voltage ($|V| < |V_{br}|$). A photon that hits the device generates electron-hole pairs that trigger the avalanche multiplication but the applied voltage is not high enough to sustain the positive feedback, so that, after the occurrence of few impact ionization events, the multiplication ends autonomously. The amplitude of the current at the output of the APD is proportional to E_{ph}, since the number of generated electron-hole pairs is a function of the photon's energy (via the so-called quantum yield), and on the number of incident photons. For this reason, APDs in linear mode are used for experiments where it is important to determine the energy of incident photons (such as spectroscopy) [6, 7, 8]. APDs in linear mode are also widely used as receivers in optical fiber communication links [9, 10].

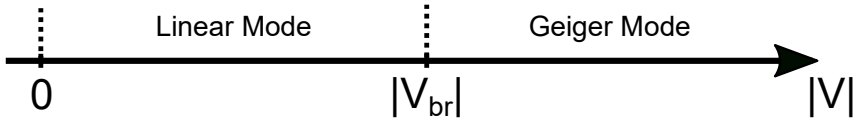

Figure 1.5: Modes of operation of an APD: Linear mode ($|V| < |V_{br}|$) and Geiger mode ($|V| > |V_{br}|$).

In this thesis we will always consider APDs working in the Linear regime, but, for completeness, some details about APDs operating in Geiger mode are also provided.

1.3 Figures of Merit of APDs

To evaluate the performance of APDs and to understand the main trade-offs that are at the basis of the design and fabrication of these devices, it is important to know which are the figures of merit to look at. Here, a brief list for APDs operating either in Geiger or in Linear mode is reported:

- Dark current (I_{dark}). It is the current measured, at a given operating voltage, at the contacts of the APD with no photon flux impinging. It originates from thermal generation of carriers and/or band-to-band tunneling. Beside being a source of noise, it sets a limit for the minimum I_{ph} that can be detected.

- Photogenerated current (I_{ph}). It is the current that flows into the device when it is exposed to the photon flux that has to be resolved. I_{ph} should be significantly larger than I_{dark}.

- Gain. It is the ratio between the current measured at the contacts and the photogenerated current ($M = I/(I_{ph} + I_{dark}) \simeq I/I_{ph}$ if $I_{ph} \gg I_{dark}$). Essentially M coincides with the multiplication factor of the depletion region.

- 3dB bandwidth (BW). It is the frequency at which the Fourier transform of the output current is attenuated by 3dB. A large BW indicates a fast response time of the APD. An example is reported in Fig. 1.6, obtained with a model that will be explained later in this thesis.

- Detector's capacitance (C_D). It depends on the device area, on the permittivity of the materials used for its fabrication and on the thickness of the depletion region. As it will be shown in Section 1.7, the value of C_D affects the energy resolution of the APD.

- Collection efficiency. Ratio between the number of photogenerated carriers that contribute to the output signal and the total number of photogenerated carriers (i.e. that includes carriers that are photogenerated but recombine and do not contribute to the current).

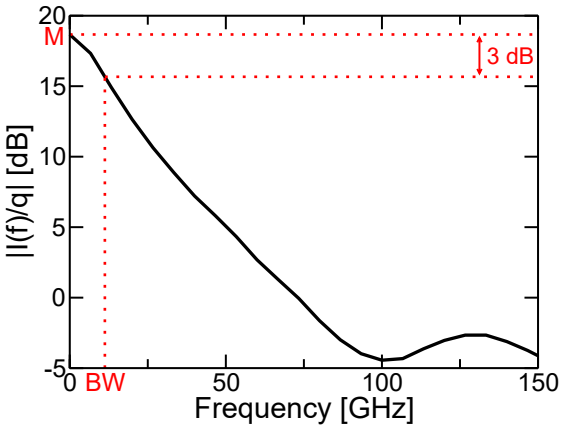

Figure 1.6: Computation of the 3dB bandwidth (BW) of an APD with gain $M = 8 \simeq 18$ dB. The y-axis plots the Fourier transform of the current response to the optical generation of a single electron-hole pair. The lobes above 100 GHz are given by the fact that the current response is similar to a *rect* function in the time domain, which becomes a *sinc* in the frequency domain.

1.3.1 Geiger Mode

In this Section, some useful figures of merit of APDs operating in Geiger Mode are listed [11]:

- Jitter (t_j). It is defined as the statistical fluctuation of the time interval between the photon arrival and the output pulse leading edge. It can be measured as the variance, or equivalently, as the full-width half-maximum of the temporal variation in the avalanche breakdown pulses resulting from an incident photon beam.

- Dead Time. Time, due to accumulation of charge in the active region of the device, during which the APD is not responsive. It depends on the time needed to quench avalanche multiplication and to reset the device.

- Dark Count Rate. Rate, per second, at which avalanche multiplication is triggered by the dark current (i. e. internal generation of electron-hole pairs) and not by a photogenerated carrier.

- Afterpulsing. False detection, caused by secondary peak pulses that originate from carriers released by traps in the semiconductor that were filled by the primary current peak.

1.3.2 Linear Mode

In this Section, the figure of merit that quantifies the noise in APDs operating in Linear mode is introduced.

If the contribution of the dark current to the noise is neglected, two noise sources can be identified. The first one, given by I_{ph}, relates to the discrete nature of the photon arrival and of the electric charges: the photogenerated

current I_{ph} will give a "shot noise" contribution to the total current noise power spectrum. This can be modeled with a Poisson statistics [1], hence

$$S_{ii,shot} = 2qI_{ph}. \tag{1.4}$$

The second noise source, instead, relates to the gain, that is, to avalanche multiplication. In fact, as reported in Section 1.1, carrier amplification occurs via impact ionization, that is a stochastic process and comes with an associated multiplication noise. Hence, the gain, M, can be represented by the random variable m, so that:

$$M = \frac{I}{I_{ph}} = \langle m \rangle, \tag{1.5}$$

where the angular brackets indicate the ensemble average.

The figure of merit that measures the contribution of the multiplication noise to the total noise power spectrum is:

- Excess Noise Factor ($F \geq 1$). It indicates how much the power spectrum of the noise of the device differs from the power spectrum of pure shot noise. By definition [6],

$$F \equiv \langle m^2 \rangle / M^2. \tag{1.6}$$

The noise power level measured when we connect an APD to a spectrum analyzer (Fig. 1.7) is then obtained combining Eq. 1.4 with Eqs. 1.5 and 1.6, that is:

$$S = 2qI_{ph}M^2FBR_L, \tag{1.7}$$

where B and R_L are, respectively, the instrument bandwidth and impedance.

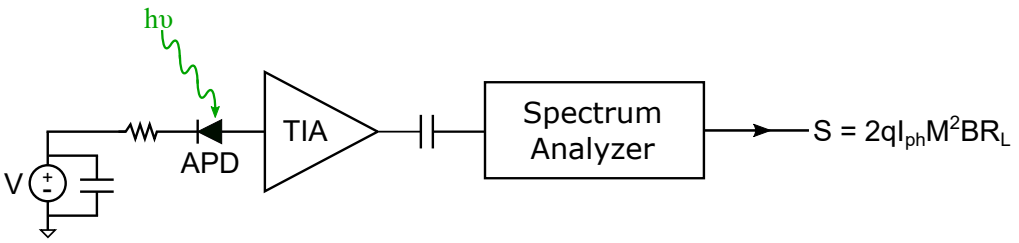

Figure 1.7: Sketch of an APD connected to a spectrum analyzer through a transimpedance amplifier (TIA).

It has been demonstrated that a low F and a high gain-bandwidth product can be achieved only if the impact ionization probability of one type of carriers is way greater than the one of the carrier with opposite charge, that means that the ratio between the impact ionization coefficients $k = \beta/\alpha$ has to be far from unity [1, 12].

In Silicon $\alpha \simeq 20\beta$ [13] at electric fields $|\vec{E}| \ll 300$ kV/cm [6] (see Fig. 1.8a and, therefore, this material is suitable for the realization of APDs operating in the Linear mode (SiAPDs) with good performance. However, the following considerations have to be made:

- Silicon has a small bandgap ($E_g = 1.12$ eV). Since the intrinsic concentration and, thus, the dark current, go as $exp(-E_g/2k_bT)$, cooling of SiAPDs at $T = -20$ °C or even at $T = -90$ °C [6] is fundamental to achieve a low I_{dark}, in order to limit its contribution to the total noise and obtain a good energy resolution (see Section 1.7).

- According to the Beer-Lambert's law, the intensity of a photon flux that is transmitted through a material is an exponential decaying function of the distance (x) and of the attenuation length (L) [8], namely

$$\Phi = \Phi_0 exp\left(-\frac{x}{L}\right). \tag{1.8}$$

  L is a function of the photon energy E_{ph} and is a property of the material where the photon is transmitted. The small atomic number of Silicon ($Z_{Si} = 14$) is responsible for large attenuation lengths at high photon energies [14]. For instance, the attenuation length is about $5 \div 6$ nm for UV photons with $E_{ph} \simeq 7.29$ eV (i. e. $\lambda = 170$ nm) [15], while for X-ray photons with $E_{ph} = 6$ keV, $L \simeq 30$ μm [15]. At $E_{ph} = 15$ keV, instead, $L \simeq 442$ μm (see Fig. 1.8b). A large attenuation length requires p-i-n structures with large W and this translates into a low bandwidth.

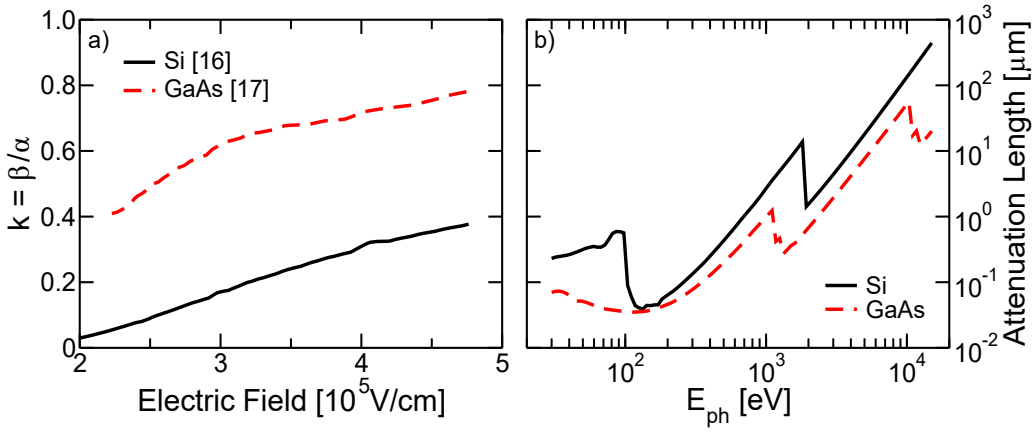

Figure 1.8: a) Ratio between the hole and electron impact ionization coefficients for Si [16] (black solid) and GaAs [17] (red dashed) at room temperature. b) Attenuation length in Si (black solid) and in GaAs (red dashed) for photon energies in the range $30 \leq E_{ph} \leq 15000$ eV [14].

For these reasons, SiAPDs are not recommended for applications at room temperature and in harsh environments (e. g. space applications) and for the detection of photons at high energies, such as X-rays, since this would require the fabrication of very thick and, consequently, very slow devices [7, 18].

III-V compound semiconductors represent a valid alternative for the fabrication of X-ray detectors. In fact, materials such as GaAs have a higher atomic number ($Z_{Ga} = 31$, $Z_{As} = 33$) and a larger bandgap ($E_g = 1.42$ eV) with respect to Silicon. This corresponds to remarkably smaller attenuation

lengths for a given photon's energy (at, e. g., $E_{ph} = 15$ keV, $L \simeq 20$ μm in GaAs, see Fig. 1.8b) and opens also the possibility to work at higher operating temperatures (i. e. room temperature). However, the main drawback of III-V compound semiconductors is that, for most of them, $k = \beta/\alpha \simeq 1$ [13] (see Fig. 1.8a for GaAs), thus, in principle, APD fabricated in III-V compounds show a higher F and a smaller gain-bandwidth product than SiAPDs.

1.4 Staircase APDs

One of the main advantages of III-V compound semiconductors is the possibility to perform *bandgap engineering*. In fact, the energy gap of a III-V material can be modulated by creating alloys between the semiconductor and a metal (e. g. Aluminum). Figure 1.9 shows the value of E_g of $Al_xGa_{1-x}As$ as a function of the Aluminum concentration [19]; it is worth noting the transition from direct to indirect bandgap taking place at $x = 45\%$.

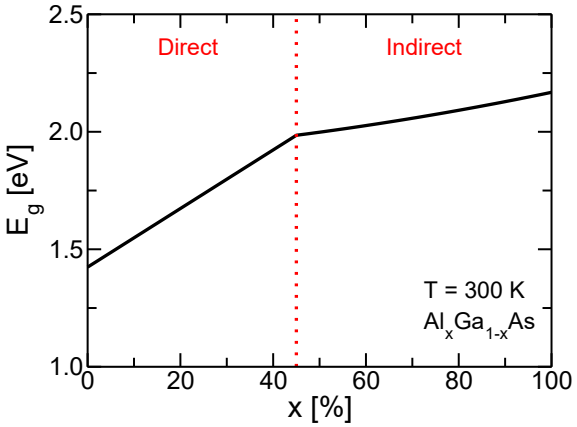

Figure 1.9: Dependence of the bandgap of $Al_xGa_{1-x}As$ on the Aluminum mole fraction (x). At $x = 45\%$, a transition from direct to indirect bandgap occurs.

Consequently, heterojunctions between a III-V-metal alloy and a III-V compound semiconductor with a matched lattice constant, as in the case of AlGaAs/GaAs, can be exploited to artificially enhance the electron's impact ionization probability with respect to the one of holes. In fact, as schematically reported in Fig. 1.10, when an electron moves from AlGaAs to GaAs, it crosses a conduction band discontinuity ΔE_C that adds its energy to the kinetic energy E_k. On the other hand, when a hole moves from GaAs to AlGaAs, it encounters a valence band discontinuity ΔE_V that is opposite to its direction of motion, hence ΔE_V is subtracted from the kinetic energy of the hole.

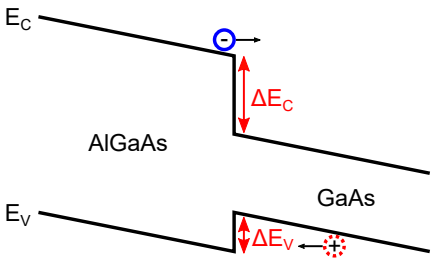

Figure 1.10: Representation of an electron moving from AlGaAs to GaAs. ΔE_C and ΔE_V are the conduction and valence band discontinuities, respectively.

For this reason, [13] proposed the fabrication of APDs with the multiplication region constituted by the periodic repetition, for N_{step} times, of abrupt AlGaAs/GaAs heterojunctions; linear grading of the Al mole fraction is used to pass from the material with a smaller bandgap (GaAs) to the one with a larger gap (AlGaAs). Owing to the configuration of its band diagram, [13] called this device *staircase* APD (see Fig. 1.11).

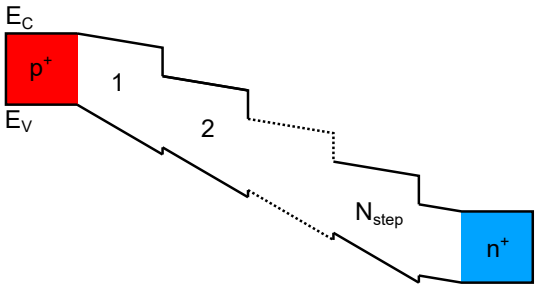

Figure 1.11: Sketch of the band diagram of a staircase APD.

In [13], it is also demonstrated that if hole impact ionization is completely suppressed and electron impact ionization occurs only when the carrier crosses a conduction band discontinuity, then the gain and the excess noise factor in a staircase APD can be computed, respectively, as

$$\langle M \rangle = (1 + P_e)^{N_{step}} \tag{1.9}$$

$$F(N_{step}, P_e) = 1 + \frac{(1 - P_e)\left[1 - (1 + P_e)^{-N_{step}}\right]}{1 + P_e}, \tag{1.10}$$

where P_e is the electron impact ionization probability at each heterojunction.

Figure 1.12 shows the excess noise factor of a staircase APD as a function of N_{steps}, computed using Eq. 1.10. It is worth noting that, under the assumptions reported above, in staircase APDs it is possible to achieve a noiseless multiplication ($F = 1$) only when $P_e = 1$, that means that electrons undergo an impact ionization scattering event every time they cross a conduction band discontinuity. In fact, in this case carrier multiplication is no longer a random process.

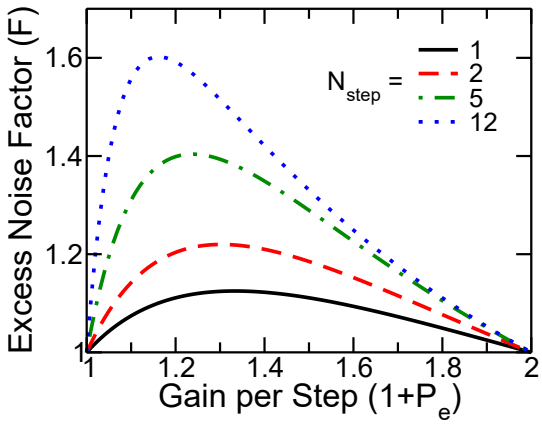

Figure 1.12: Excess noise factor for a staircase APD with $N_{step} = 1, 2, 5$ and 12. The computation has been performed using Eq. 1.10 [13].

Staircase APDs are nowadays used both in optical fiber communication links [10], where also III-V compunds with small bandgaps and an intrinsic low $k = \beta/\alpha$ can be exploited (like InAs alloys [20]) and for X-ray detection [7, 21, 22].

1.5 APDs with Separate Absorption and Multiplication Regions

As discussed in Section 1.3.2, the depth at which a photon can be absorbed has an exponential dependence (Eq. 1.8) on the attenuation length L (see Fig. 1.8b).

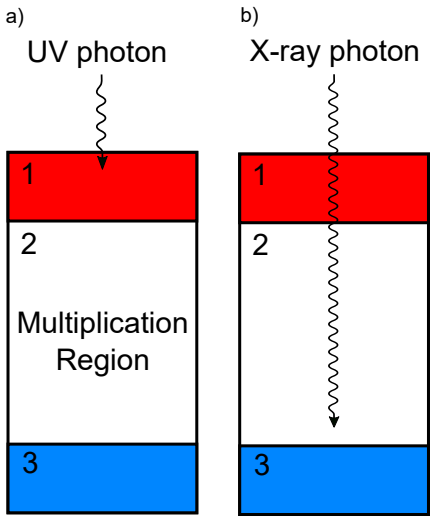

Figure 1.13: a) A UV photon hits an APD: electron-hole pairs are generated only inside region 1, before the multiplication region. b) A X-ray photon hits an APD and, if it is absorbed, it can generate an electron-hole pair in region 1, 2 or 3.

The location where photons are absorbed has a huge influence on the gain and on the excess noise factor of the APD [8, 23]. This can be easily understood by looking at Fig. 1.13. In fact, in a Silicon device, a UV photon will be absorbed in the first few nm of region 1, generating all the electron-hole pairs before the multiplication region so that all undergo the same multiplication process (Fig. 1.13a). On the other hand, in the same device, an X-ray photon can be absorbed in region 1, 2 or even region 3, generating electron-hole pairs that can be fully, partially or not amplified (Fig. 1.13b). As it will be discussed in Section 1.7, this non-uniformity of the gain gives a relevant contribution (σ_U^2) in worsening the energy resolution of the device.

A possible solution to reduce the gain non-uniformity is the fabrication of Separate Absorption and Multiplication (SAM) APDs (see Fig. 1.14).

The aim of the absorption region, whose thickness is designed according to the energy of the radiation that has to be detected, is to absorb most of the impinging photons, so that electron-hole pairs are generated before the multiplication region and get amplified by it in the same manner. The electric field in the absorption region in very low (to avoid unwanted multiplication and band-to-band generation), so that carriers move mostly by diffusion. The applied bias voltage falls, instead, almost entirely on the multiplication region, that is responsible for the carrier amplification. Electric separation between the absorption and the multiplication regions is obtained by means of a thin p^--doped charge sheet layer (also called δp-layer [7]).

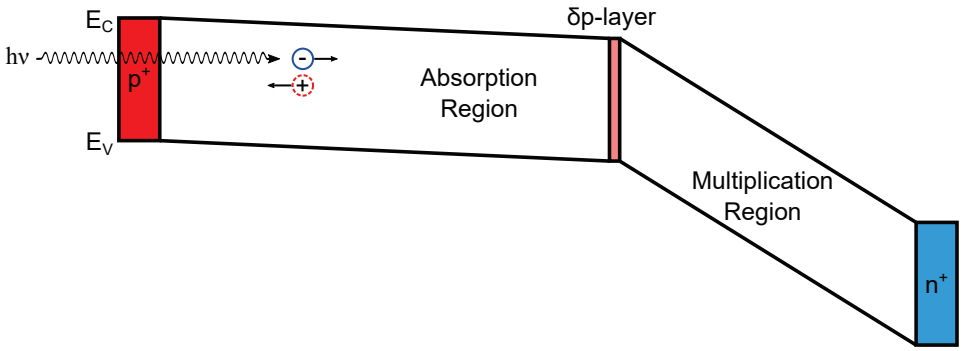

Figure 1.14: Band diagram of a Separate Absorption and Multiplication APD.

Another advantage of SAM-APDs is that almost *pure* unipolar injection of only one carrier type (electrons) can be achieved, that means that only one type of carrier is injected in the multiplication region. This is beneficial for the excess noise factor [7, 8, 23].

SAM-APDs are nowadays used for both optical fiber links [10, 24] and X-ray detection [7, 8, 21, 22, 25].

1.6 Pulse Shaping

In many applications that involve X-ray detection, such as X-ray spectroscopy, the aim of the experiment is the accurate measure of the charge available at

the detector output, that is proportional to E_{ph} [26] (see Fig. 1.15a). The processing of the signal that comes out from a detector is called *pulse shaping* and consists of an integrator followed by an appropriate filter, called *shaper*, as shown in Fig. 1.15b.

Of course, pulse shaping comes with an associated electronic noise, whose relevance depends on the detector capacitance and on the time available for the measurement of a single event [26], that affects the accuracy of the charge measurement. In the following, we will demonstrate that an optimum shaping filter exists, in the sense that it exists a design that minimizes the noise power at the output of the shaper.

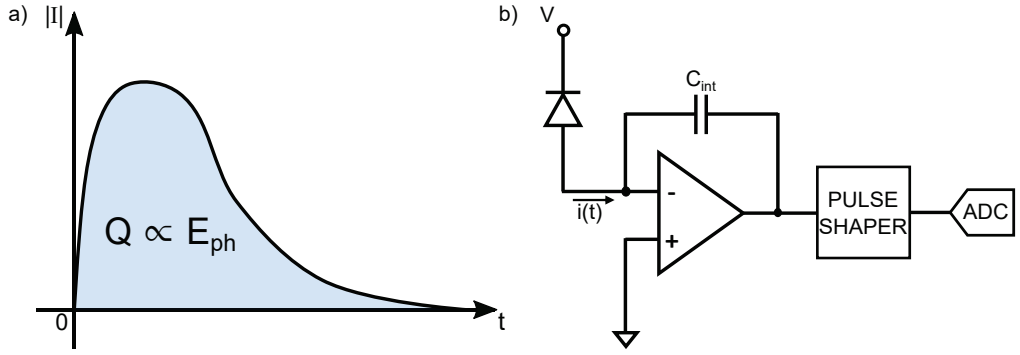

Figure 1.15: a) Time response of an APD to a single photon with energy E_{ph} that hits the device at $t = 0$. b) Setup of a charge measurement circuit.

If we denote as Q the charge at the output of APD, C_D the detector capacitance, C_i the preamplifier input capacitance, $G_{ee}(\omega)$ and $G_{ii}(\omega)$ the power spectra of the equivalent voltage and current noise generators, respectively, $H(j\omega)$ the transfer function of the shaping filter and as $X(j\omega) = Q$ the Fourier trasform of the input signal $x(t) = Q\delta(t)$ (i.e. the time response of the APD is much faster than the readout time constant), then the equivalent noise circuit can be represented as in Fig. 1.16 [26].

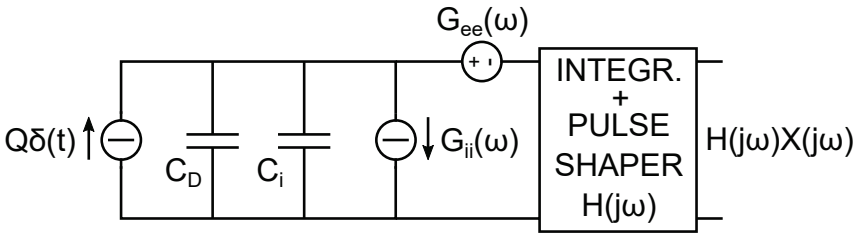

Figure 1.16: Equivalent noise circuit of the charge measurement system of Fig. 1.15b.

As described in [26], for the applications of our interest the two generators $G_{ee}(\omega)$ and $G_{ii}(\omega)$ can be considered uncorrelated. We write them as:

- $G_{ee}(\omega) = a_1 + a_2/|\omega|$; a_1 is a white noise term and accounts for thermal noise in the channel of the field-effect devices of the preamplifier, while

the term $a_2/|\omega|$ is the contribution of the $1/f$ noise. For the sake of simplicity, we can neglect the effect of a_2 and, thus, consider G_{ee} independent of ω [26].

- $G_{ii}(\omega) = b_1(\omega) + b_2(\omega)$; $b_1(\omega)$ accounts for the leakage current in the transistors of the preamplifier, while $b_2(\omega)$ is the contribution due to the shot noise associated to the dark current of the APD. b_1 and b_2 are independent of ω and, thus, also G_{ii} does not depend on the frequency.

Several shaping circuits can be found in the literature [26]. Here, we will focus on the CR-RC scheme reported in Fig. 1.15b, that is commonly used in X-ray spectroscopy [25].

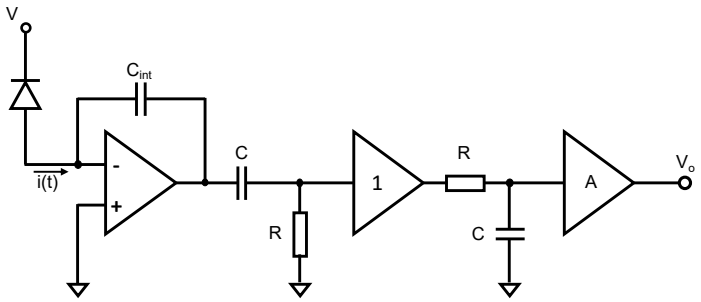

Figure 1.17: Schematic representation of a CR-RC shaping circuit.

The transfer function of the filter in Fig. 1.17, in the frequency and time domains, can be written as

$$H(j\omega) = \frac{A}{C_{int}}\tau_s \left(\frac{1}{1+j\omega\tau_s}\right)^2 \Rightarrow h(t) = \frac{A}{C_{int}}\frac{t}{\tau_s} exp\left(-\frac{t}{\tau_s}\right)\Theta(t), \qquad (1.11)$$

where A is a suitable gain, $\tau_s = RC$ is the filter's time constant and $\Theta(t)$ is the Heaviside step function.

The noise resulting from the dark current of the APD and from the readout electronics can be derived as in [27]. Firstly, the expression for power of the current noise is extracted from the Norton equivalent circuit of the noise generators at the input of the readout (Fig. 1.16):

$$P_{noise} = \int_0^{+\infty} G_{ii}(\omega)|H(j\omega)|^2 df + \int_0^{+\infty} G_{ee}(\omega)\omega^2 C_{tot}^2 |H(j\omega)|^2 df, \qquad (1.12)$$

where $C_{tot} = C_D + C_i$. The expression for $|H(j\omega)|$ in Eq. 1.11 can be now substituted in Eq. 1.12 and, since, as previously discussed, $G_{ii}(\omega)$ and $G_{ee}(\omega)$ can be considered independent of ω, the solution of Eq. 1.12 yields

$$P_{noise} = \frac{A^2}{8C_{int}^2}\left(G_{ii}\tau_s + G_{ee}\frac{C_{tot}^2}{\tau_s}\right). \qquad (1.13)$$

The value of τ_s ($\tau_{s,opt}$) that minimizes P_{noise} and the corresponding $P_{noise,opt}$ can be found by minimization of Eq. 1.13, namely

$$\frac{\partial P_{noise}}{\partial \tau_s} = 0 \Rightarrow \tau_{s,opt} = C_{tot}\sqrt{\frac{G_{ee}}{G_{ii}}} \Rightarrow P_{noise,opt} = \frac{A^2}{4C_{int}^2} C_{tot}\sqrt{G_{ee}G_{ii}}. \qquad (1.14)$$

For X-ray spectroscopy, $\tau_{s,opt}$ is in the order of few μs [25].

On the other hand, the signal at the output of the filter ($w(t)$) is given by the convolution between the input signal $Q\delta(t)$ and the filter's impulse response function $h(t)$. Hence

$$w(t) = h(t) * Q\delta(t) = \frac{QA}{C_{int}} \frac{t}{\tau_s} exp\left(-\frac{t}{\tau_s}\right) \Theta(t) \tag{1.15}$$

The maximum value of the output signal w_{max}, can be found by differentiation of Eq. 1.15

$$\frac{\partial w(t)}{\partial t} = 0 \Rightarrow w_{max} = \frac{QA}{eC_{int}} = \frac{qE_{ph}MA}{eE_{ehp}C_{int}}, \tag{1.16}$$

where e is the Euler's constant. In Eq. 1.16 it has been made explicit that $Q = qME_{ph}/E_{ehp}$, where q is the electron charge, E_{ph} is the photon energy, M is the APD gain, E_{ehp} is the average energy required for the creation of a single electron-hole pair in the material used for the fabrication of the detector.

The noise, expressed in eV^2, resulting from the dark current of the APD and from the electronic readout can be finally computed as:

$$\sigma_N^2 = E_{ph}^2 \frac{P_{noise}}{w_{max}^2} = \frac{1}{8} \left(\frac{eE_{ehp}}{qM}\right)^2 \left(G_{ii}\tau_s + G_{ee}\frac{C_{tot}^2}{\tau_s}\right) \tag{1.17}$$

The multiplication by E_{ph} in Eq. 1.17 is necessary to translate in energy the output, expressed in V, of the readout of Fig. 1.17.

1.7 Energy Resolution of an APD

To compute the energy resolution of an APD, several sources of uncertainty have to be taken into account [15]:

- σ_S^2: the statistical fluctuations of the number of electron-hole pairs generated per incident photon and of the gain of the APD.
- σ_U^2: the non-uniformity of the gain (see Section 1.5).
- σ_N^2: noise resulting from the dark current of the APD and from the readout electronics (see Section 1.6).

These noise sources are all independent, hence the total variance is the sum of the single contributions:

$$\sigma^2 = \sigma_S^2 + \sigma_U^2 + \sigma_N^2. \tag{1.18}$$

Following [6], the statistical fluctuation of the APD gain can be computed as

$$\sigma_{APD}^2 = \langle m^2 \rangle - M^2 = M^2 \frac{\langle m^2 \rangle - M^2}{M^2} = M^2 (F - 1). \tag{1.19}$$

The effects of the stochastic natures of carrier generation and avalanche multiplication can be combined exploiting the fact that these two processes are independent, thus the final variance scaled by M^2, in eV^2, is

$$\sigma_S^2 = E_{ehp}^2 \frac{M^2\sigma_{ehp}^2 + N\sigma_{APD}^2}{M^2} = E_{ehp}^2 \left[\sigma_{ehp}^2 + N(F-1)\right], \tag{1.20}$$

where N is the average number of electron-hole pairs generated by a photon with energy E_{ph}.

When we consider X-ray detection, the variance associated to the process of carriers generation is [6, 15]

$$\sigma_{ehp}^2 = Nf, \tag{1.21}$$

where f is the Fano factor. Consequently, σ_S^2 becomes

$$\sigma_S^2 = N(f + F - 1)E_{ehp}^2 \tag{1.22}$$

The energy resolution is usually expressed as the *full width at half maximum* ($FWHM$), which is related to the variance by the relation $FWHM = 2\sqrt{2ln(2)}\sigma \simeq 2.35\sigma$. The intrinsic energy resolution of an APD expressed in eV is, thus,

$$FWHM_{int} \simeq 2.35\sqrt{\sigma_S^2 + \left(\frac{\sigma_U}{M}\right)^2} \simeq 2.35E_{ehp}\sqrt{\frac{E_{ph}(f+F-1)}{E_{ehp}} + \left(\frac{\sigma_U}{M}\right)^2}, \tag{1.23}$$

where it has been made explicit that $N = E_{ph}/E_{ehp}$. As mentioned in Section 1.5, the non-uniformity of the gain is an important aspect to consider in the case of X-ray detection. For this reason, σ_U^2 is included in Eq. 1.23.

Exploiting the analysis performed in Section 1.6, it is now possible to compute the energy resolution ($FWHM$) accounting also for the contribution of σ_N^2. In fact, the current at the output of the APD is given by

$$I = MI_{dark,p} + I_{dark,n} + MI_{ph}. \tag{1.24}$$

where $I_{dark,p}$ is the dark current that originates in the region before the multiplication region (i. e. region 1 of the devices in Fig. 1.13) and, thus, gets multiplied, while $I_{dark,n}$ is the dark current that originates after the multiplication region (i. e. region 3 in Fig. 1.13) and does not suffer the avalanche multiplication [15]. For this reason, the power spectrum of the equivalent noise generator G_{ii} can be written as

$$G_{ii} = 2q(I_{dark,n} + I_{dark,p}M^2F). \tag{1.25}$$

On the other hand, the power spectrum of the voltage noise current source can be modeled with an equivalent resistance R_{eq} [15], hence

$$G_{ee} = 4k_BTR_{eq}, \tag{1.26}$$

where k_B is the Boltzmann constant and T is the temperature.

By substituting Eqs. 1.25 and 1.26 in Eq. 1.17 we get

$$\sigma_N^2 = \left(\frac{eE_{ehp}}{qM}\right)^2 \left[\frac{k_B T R_{eq} C_{tot}^2}{2\tau_s} + \frac{q\tau_s}{4}\left(I_{dark,n} + I_{dark,p} M^2 F\right)\right]. \tag{1.27}$$

Finally, the total energy resolution is given by

$$FWHM^2 \simeq FWHM_{int}^2 + \left(2.35\frac{eE_{ehp}}{qME_{ph}}\right)^2 \left[\frac{k_B T R_{eq} C_{tot}^2}{2\tau_s} + \frac{q\tau_s}{4}\left(I_{dark,n} + I_{dark,p} M^2 F\right)\right], \tag{1.28}$$

where $FWHM_{int}$ is given by Eq. 1.23. From Eq. 1.28, we can notice that it exists an optimum gain M_{opt} that allows to obtain the best energy resolution. M_{opt} can be found by setting $\partial FWHM^2/\partial M = 0$. In Section 1.8, we will see how the choice of M affects the energy resolution by looking at two practical examples from the literature [7, 25].

1.8 APDs in III-V Compound Semiconductors for X-Ray Detection

Many different architectures have been proposed for the fabrication of avalanche photodiodes in III-V compound semiconductors for the detection of X-rays: from simple p-i-n diodes [18, 28, 29, 30] to SAM-APDs featuring a uniform [8, 25] or a staircase [7, 21, 22] multiplication region.

For the reasons reported in Section 1.3.2, $Al_xGa_{1-x}As$, with different concentration of Al, is the most used for the realization of such devices. The p-i-n APDs in [18, 28, 29, 30], for instance, exploit the large bandgap of $Al_{0.8}Ga_{0.2}As$ ($E_g = 2.09$ eV) and feature a 100-nm thick multiplication region. The best energy resolution achieved is $FWHM = 1.47$ keV for the detection of ^{55}Fe photons ($E_{ph} = 5.9$ keV), at room temperature.

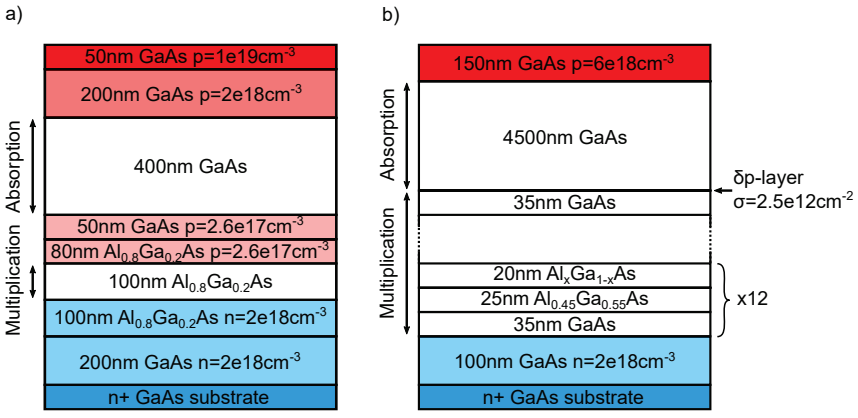

Figure 1.18: a) SAM-APD with a uniform $Al_{0.8}Ga_{0.2}As$ multiplication region for the detection of X-rays at $E_{ph} = 5.9$ keV [8, 25]. b) SAM-APD with a staircase $Al_{0.45}Ga_{0.55}As$/GaAs multiplication region for the detection of X-rays at $E_{ph} = 13.96$ keV [7, 21, 22].

To improve the energy resolution of $Al_{0.8}Ga_{0.2}As$ devices, [8, 25] realized a SAM-APD that consists of a 400-nm GaAs intrinsic absorption region, separated from the 100-nm intrinsic $Al_{0.8}Ga_{0.2}As$ multiplication region by a 130-nm p-doped GaAs/$Al_{0.8}Ga_{0.2}As$ charge sheet layer. The 300-nm n-doped $Al_{0.8}Ga_{0.2}As$/GaAs layer between the multiplication region and the n^+ GaAs substrate avoids the depletion of the substrate when a bias voltage is applied. A schematic representation of the structure is shown in Fig. 1.18a. The best energy resolution for the detection of X-ray photons at $E_{ph} = 5.9$ keV achieved with this device is $FWHM = 1.08$ keV, at room temperature and with a gain $M = 3.6$ [8, 25] (see Fig. 1.19a).

A staircase SAM-APD, based on $Al_{0.45}Ga_{0.55}As$/GaAs heterojunctions, was instead proposed in [7, 21, 22] for the detection of X-rays at $E_{ph} = 13.96$ keV. The architecture of the APD, sketched in Fig. 1.18b, consists of a 4.5-μm i-GaAs absorption region, separated from the multiplication region by a δ-p doping with dose $\sigma = 2.5 \times 10^{12}$ cm^{-2}. The multiplication region is the periodic repetition of a structure composed by a 20-nm linearly graded i-$Al_xGa_{1-x}As$ (x from 0 to 0.45), a 25-nm i-$Al_{0.45}Ga_{0.55}As$ and a 35-nm i-GaAs layers. The total length of the this region is $\simeq 1$ μm. Finally, a 200-nm n-GaAs layer is placed between the n^+-GaAs substrate. The best energy resolution that was obtained at room temperature is $FWHM = 0.9$ keV for a gain $M = 4.1$ [7] (see Fig. 1.19b).

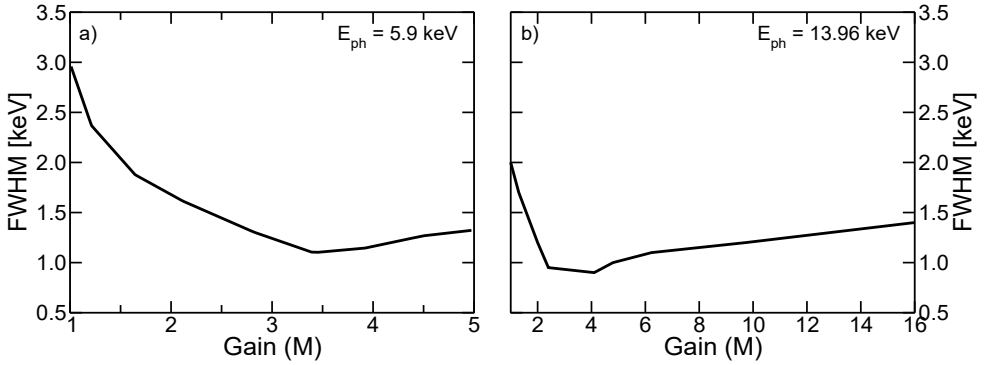

Figure 1.19: Energy resolution as a function of the gain for the devices of a) Fig. 1.18a [8, 25] and b) Fig. 1.18b [7, 21] at $E_{ph} = 5.9$ keV and $E_{ph} = 13.96$ keV, respectively.

1.9 Aims and Structure of the Thesis

The aim of this work is the development of a set of simulation tools for the study of the figures of merit (gain, excess noise factor, response time, bandwidth and jitter) of Avalanche Photodiodes fabricated in III-V compound semiconductors used for X-ray detection and operating in Linear mode, with particular focus on the GaAs/AlGaAs staircase SAM-APD of Fig. 1.18b.

An overview of the existing models for impact ionization is provided in Chapter 2, from the simple *Local model* to more complex approaches such as *Analytical* and *Full Band* Monte Carlo transport simulators.

The derivation and the implementation with a Finite Different scheme of a new nonlocal history dependent impact ionization model are described in Chapter 3. The model is then used to compute the gain and the excess noise factor of p-i-n and staircase APDs fabricated with different III-V compound semiconductors and to optimize the design of staircase APDs in terms of number of conduction band steps.

The Random Path Length implementation of the nonlocal history dependent model described in Chapter 3 is presented in Chapter 4. The algorithm describes carriers' drift and diffusion as well as multiplication and is used to compute the response time, the bandwidth and the jitter of APDs with different structures.

The development, the implementation and the calibration for GaAs of a Full Band Monte Carlo transport simulator (FBMC) are presented in Chapter 5. The FBMC is used to compute the gain and the excess noise factor of thin GaAs APDs, to analyze some major limitations of nonlocal history dependent impact ionization models and to improve the calibration of the model described in Chapter 3. The FBMC is also employed to compute M and F in GaAs APDs with conduction band discontinuities.

Experimental characterization and DC, AC and time dependent TCAD analyses of GaAs/AlGaAs staircase APDs are performed in Chapter 6. TCAD simulations calibrated on experiments are used to predict the dark current and the collection efficiency of the device fabricated by CNR-IOM (Trieste) in the framework of a PRIN project coordinated by the University of Udine.

Finally, conclusions are drawn in Chapter 7.

Chapter 2

Overview of Models for Charge Multiplication in APDs

Accurate modeling of impact ionization is fundamental to extract reliable information from simulations of Avalanche Photodiodes and to understand how changes in the device structure affect the figures of merit. In this Chapter, we review the main models for charge multiplication that have been developed and employed in the past by other authors, from the analytical *Local Model* to more complex numerical models based on *Full Band Monte Carlo* transport simulators.

2.1 The Local Model

The main assumption of the *local* impact ionization model is that the impact ionization generation rate and, thus, the electron and hole ionization coefficients ($\alpha(x)$ and $\beta(x)$), depend on variables at the same location x. In particular $\alpha(x)$ and $\beta(x)$ are functions of the electric field $E(x)$ following the Chynoweth's law [31]:

$$\alpha(x) = A_e exp\left[-\left(\frac{E_{ce}}{E(x)}\right)^{\gamma_e}\right] \tag{2.1}$$

$$\beta(x) = A_h exp\left[-\left(\frac{E_{ch}}{E(x)}\right)^{\gamma_h}\right]. \tag{2.2}$$

The coefficients $A_{e,h}$, $E_{ce,h}$ and $\gamma_{e,h}$ are chosen in order to reproduce experimental measurements of multiplication currents in p-i-n diodes.

The device structure assumed in the following is the one shown in Fig. 2.1. The p-i-n diode depletion region extends from $x = 0$ to $x = W$; electrons are swept by the electric field from left to right and move at constant average velocity v_e, while holes move from right to left with uniform average velocity v_h. If an electron-hole pair is injected at $x = 0$, pure electron injection is achieved (as opposed to pure hole injection, that takes place when the injection occurs at $x = W$).

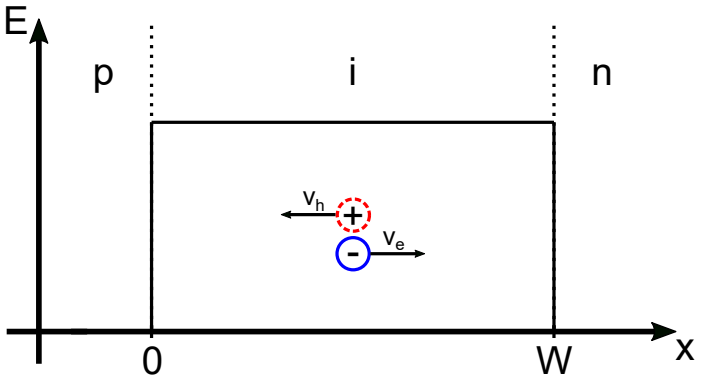

Figure 2.1: Electric field profile and motion of carriers inside a p-i-n junction.

Under these circumstances, the electron and hole continuity equations can be written as:

$$\frac{1}{v_e}\frac{\partial J_e(x,t)}{\partial t} = \alpha(x)J_e(x,t) + \beta(x)J_h(x,t) + qG_{opt}(x,t) + \frac{\partial J_e(x,t)}{\partial x} \tag{2.3}$$

$$\frac{1}{v_h}\frac{\partial J_h(x,t)}{\partial t} = \alpha(x)J_e(x,t) + \beta(x)J_h(x,t) + qG_{opt}(x,t) - \frac{\partial J_h(x,t)}{\partial x}, \tag{2.4}$$

where $J_e(x,t)$ and $J_h(x,t)$ are, respectively, the electron and hole conduction current densities and $G_{opt}(x,t)$ is the optical generation rate, induced by photons absorbed at location x and time t in the APD.

2.1.1 Gain and Excess Noise Factor

The expressions for the gain, $M(x)$, and the excess noise factor, $F(x)$, in the framework of the local model can be derived directly from the transport equations (Eqs. 2.3, 2.4) but, for the sake of simplicity, instead of the current densities $J_e(x,t)$ and $J_h(x,t)$, we will use as unknowns the corresponding fluxes $\phi_e(x,t) = -J_e(x,t)/q$ and $\phi_h(x,t) = J_h(x,t)/q$.

In steady-state conditions, current conservation implies

$$\phi = \phi_e(x) + \phi_h(x) = const. \tag{2.5}$$

$$\frac{d\phi}{dx} = 0 \Rightarrow \frac{d\phi_e(x)}{dx} = -\frac{d\phi_h(x)}{dx} = \alpha(x)\phi_e(x) + \beta(x)\phi_h(x) + G_{opt}(x) \tag{2.6}$$

Equation 2.5 can be rewritten as $\phi_h(x) = \phi - \phi_e(x)$, thus

$$\frac{d\phi_e(x)}{dx} = [\alpha(x) - \beta(x)]\,\phi_e(x) + \beta(x)\phi + G_{opt}(x). \tag{2.7}$$

The solution of 2.7 yields

$$\begin{aligned}\phi_e(x) = &\int_0^x [\beta(x')\phi + G_{opt}(x')]\, exp\left(-\int_0^{x'} [\alpha(x'') - \beta(x'')]\, dx''\right) dx' \\ &\cdot exp\left(\int_0^x [\alpha(x') - \beta(x')]\, dx'\right).\end{aligned} \tag{2.8}$$

Hence, the total flux $\phi = \phi_e(W)$ ($\phi_h(W) = 0$, since we are injecting an electron-hole pair at x) can be expressed as

$$\phi = \frac{\int_0^W G_{opt}(x) exp\left(\int_x^W \left[\alpha(x') - \beta(x')\right] dx'\right) dx}{1 - \int_0^W \beta(x') exp\left(\int_{x'}^W \left[\alpha(x'') - \beta(x'')\right] dx''\right) dx'} = \int_0^W G_{opt}(x) M(x) dx, \tag{2.9}$$

where

$$M(x) = \frac{exp\left(\int_x^W \left[\alpha(x') - \beta(x')\right] dx'\right)}{1 - \int_0^W \beta(x') exp\left(\int_{x'}^W \left[\alpha(x'') - \beta(x'')\right] dx''\right) dx'}. \tag{2.10}$$

The gain in the case of pure electron ($M(0)$) or hole ($M(W)$) injection can be easily derived from Eq. 2.10.

$$M(0) = \frac{1}{1 - \int_0^W \alpha(x') exp\left(-\int_0^{x'} \left[\alpha(x'') - \beta(x'')\right] dx''\right) dx'} \tag{2.11}$$

$$M(W) = \frac{1}{1 - \int_0^W \beta(x') exp\left(\int_{x'}^W \left[\alpha(x'') - \beta(x'')\right] dx''\right) dx'}. \tag{2.12}$$

It is also worth noting that $M(x)$ can be expressed as a function of $M(W)$ using the following relation

$$M(x) = M(W) exp\left(\int_x^W \left[\alpha(x') - \beta(x')\right] dx'\right). \tag{2.13}$$

Each generation term in Eqs. 2.3, 2.4 ($\alpha\phi_e$, $\beta\phi_h$, G_{opt}) acts as a source of shot noise. Knowing that M is transfer function of the system under consideration, we can write the current noise spectral density as

$$S_i = \int_0^W 2q^2 \left[\alpha(x)\phi_e(x) + \beta(x)\phi_h(x) + G_{opt}(x)\right] M^2(x) dx \tag{2.14}$$

and, by substituting Eq. 2.6 into Eq. 2.14, we obtain

$$S_i = 2q^2 \int_0^W \frac{d\phi_e(x)}{dx} M^2(x) dx. \tag{2.15}$$

Equation 2.15 can be solved integrating by parts (see Appendix A), which leads to

$$\begin{aligned} S_i &= 2q^2 \left\{ \int_0^W G_{opt}(x) M^2(x) \left[2 + \frac{2\int_0^W \beta(x') M^2(x') dx'}{M(x)} - \frac{M^2(W)}{M(x)} \right] dx \right\} \\ &= 2q^2 \int_0^W G_{opt}(x) M^2(x) F(x) dx, \end{aligned} \tag{2.16}$$

where

$$F(x) = 2 + \frac{M(W)\left[2\int_0^W \beta(x')exp\left(2\int_{x'}^W [\alpha(x'') - \beta(x'')]\,dx''\right)dx' - 1\right]}{exp\left(\int_0^W [\alpha(x') - \beta(x')]\,dx'\right)}. \tag{2.17}$$

Finally, under the assumption of constant electric field, that implies $\alpha(x) = \alpha$ and $\beta(x) = \beta$, it is useful to express the gain and the excess noise factor as a function of $k = \beta/\alpha$ [1, 32]. In case of pure electron injection we can write

$$M(0) = M = \frac{(\alpha - \beta)\,exp\,[(\alpha - \beta)\,W]}{\alpha - \beta exp\,[(\alpha - \beta)\,W]} = \frac{1 - k}{exp\,[\alpha\,(k - 1)\,W] - k} \tag{2.18}$$

$$F(0) = F = kM + (1 - k)\left(2 - \frac{1}{M}\right) \tag{2.19}$$

Figure 2.2 shows the excess noise factor as a function of the gain for different values of k. Low values of F can be obtained only if $k \ll 1$ [1]. It is also worth nothing that, in the limit $k \to 0$, $F = 2 - 1/M$, which sets a lower limit $F = 2$ for the excess noise factor at high gains.

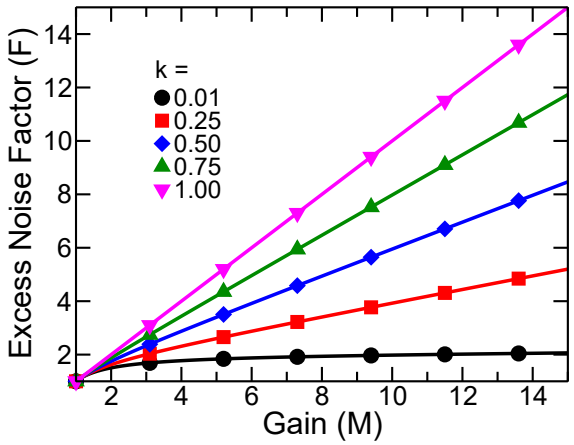

Figure 2.2: Excess noise factor as a function of the gain, in the case of pure electron injection, for $k = 0.01, 0.25, 0.5, 0.75, 1$.

Considering that the noise in staircase APDs is largerly influenced by hole impact ionization in the constant electric field regions between consecutive steps, the local model can be used to derive analytic expressions for the gain and the excess noise factor in staircase APDs including hole impact ionization. For example, in case of pure electron injection [32] proposes:

$$M(P_e, P_h, N_{step}) = \frac{(1 + P_e)^{N_{step}}(1 - k_p)}{(1 + k_p P_e)^{N_{step}+1} - k_p(1 + P_e)^{N_{step}+1}} \tag{2.20}$$

$$\begin{aligned} F(P_e, P_h, N_{step}) =& 1 + \frac{(1 - 1/M)(1 - k_p)}{2 + P_e(1 + k_p)} \\ & \times \left\{-P_e + 2\frac{1 - k_p P_e^2}{1 + k_p P_e}\left[M k_p \frac{1 + P_e}{1 - k_p} + \frac{1}{1 + P_e}\right]\right\}, \end{aligned} \tag{2.21}$$

where P_e is the electron impact ionization probability at each step (see Section 1.4), N_{step} is the number of steps,

$$P_h = \int_0^L \beta(x)dx - 1 \tag{2.22}$$

is the hole impact ionization probability in the layer of length L between two steps and $k_p = P_h/P_e$. As demonstrated in [32], in the limit $k_p \to 0$, Eqs. 2.20, 2.21 coincide with Eqs. 1.9, 1.10 in Section 1.4 [13].

2.1.2 Frequency Response

The frequency response of a p-i-n APD will be derived as a particular case of the analysis performed in [33]. Assuming a uniform electric field in the depletion region ($\alpha(x) = \alpha$, $\beta(x) = \beta$), in the Laplace domain the transport equations (Eqs. 2.3 2.4) can be written in matrix form as

$$\frac{\partial}{\partial x}\mathbf{I}(x,s) = \mathbf{A}(s)\mathbf{I}(x,s) + G_{opt}(s)\mathbf{Q}, \tag{2.23}$$

where

$$\mathbf{I}(x,s) = \begin{bmatrix} I_e(x,s) \\ I_h(x,s) \end{bmatrix} \tag{2.24}$$

$$\mathbf{A}(s) = \begin{bmatrix} (s/v_e - \alpha) & -\beta \\ \alpha & (\beta - s/v_h) \end{bmatrix} = \begin{bmatrix} a_{11} & a_{12} \\ a_{21} & a_{22} \end{bmatrix} \tag{2.25}$$

$$\mathbf{Q} = \begin{bmatrix} -q \\ q \end{bmatrix} \tag{2.26}$$

and $s = j\omega = j2\pi\nu$ (ν is the electronic signal frequency).

We will consider the case of pure electron injection, corresponding to a current having the shape of a Dirac's delta injected at $x = 0$, thus, with reference to the scheme proposed in Fig. 2.1, the boundary conditions that have to be applied to the differential equation in Eq. 2.23 are

$$I_e(0,s) = q \tag{2.27}$$

$$I_h(W,s) = 0 \tag{2.28}$$

The solution of Eq. 2.23 is

$$\mathbf{I}(x,s) = exp\left[\mathbf{A}(x,s)\right]\mathbf{I}(0,s) + \mathbf{G}(x,s), \tag{2.29}$$

where

$$exp\left[\mathbf{A}(x,s)\right] = \begin{bmatrix} A_{11}(x,s) & A_{12}(x,s) \\ A_{21}(x,s) & A_{22}(x,s) \end{bmatrix} \tag{2.30}$$

$$\mathbf{G}(x,s) = G_{opt}(s)\int_0^x exp\left[\mathbf{A}(x-x',s)\right]\mathbf{Q}dx' = \begin{bmatrix} G_1(x,s) \\ G_2(x,s) \end{bmatrix} \tag{2.31}$$

$$A_{11}(x,s) = \frac{\lambda_2 e^{\lambda_1 x} - \lambda_1 e^{\lambda_2 x} + a_{11}\left(e^{\lambda_2 x} - e^{\lambda_1 x}\right)}{\lambda_2 - \lambda_1} \tag{2.32}$$

$$A_{12}(x,s) = \frac{a_{12}\left(e^{\lambda_2 x} - e^{\lambda_1 x}\right)}{\lambda_2 - \lambda_1} \tag{2.33}$$

$$A_{21}(x,s) = \frac{a_{21}\left(e^{\lambda_2 x} - e^{\lambda_1 x}\right)}{\lambda_2 - \lambda_1} \tag{2.34}$$

$$A_{22}(x,s) = \frac{\lambda_2 e^{\lambda_1 x} - \lambda_1 e^{\lambda_2 x} + a_{22}\left(e^{\lambda_2 x} - e^{\lambda_1 x}\right)}{\lambda_2 - \lambda_1} \tag{2.35}$$

$$G_1(x,s) = \frac{qG_{opt}(s)}{\lambda_2 - \lambda_1}\left[(a_{11} - a_{12} - \lambda_2)\frac{e^{\lambda_1 x} - 1}{\lambda_1} + (-a_{11} + a_{12} + \lambda_1)\frac{e^{\lambda_2 x} - 1}{\lambda_2}\right] \tag{2.36}$$

$$G_2(x,s) = \frac{qG_{opt}(s)}{\lambda_2 - \lambda_1}\left[(a_{21} - a_{22} + \lambda_2)\frac{e^{\lambda_1 x} - 1}{\lambda_1} + (-a_{21} + a_{22} - \lambda_1)\frac{e^{\lambda_2 x} - 1}{\lambda_2}\right] \tag{2.37}$$

and $\lambda_{1,2}$ are the eigenvalues of the matrix $\mathbf{A}(s)$ (Eq. 2.25)

$$\lambda_{1,2} = \frac{(a_{11} + a_{22}) \pm \sqrt{(a_{11} + a_{22})^2 - 4(a_{11}a_{22} - a_{12}a_{21})}}{2}. \tag{2.38}$$

Since $I_e(0,s)$ and $I_h(W,s)$ are given by the boundary conditions (Eqs. 2.27, 2.28), $I_h(0,s)$ can be derived from Eq. 2.29 as

$$I_h(0,s) = \frac{I_h(W,s) - A_{21}(W,s)I_e(0,s) - G_2(W,s)}{A_{22}(W,s)}. \tag{2.39}$$

Finally the impulse response in the Laplace domain is given by the Ramo's theorem [34]

$$\begin{aligned} I(s) &= \frac{1}{W}\int_0^W \left[I_e(x,s) + I_h(x,s)\right] dx \\ &= \left[A_{11}(s) + A_{21}(s)\right] I_e(0,s) + \left[A_{21}(s) + A_{22}(s)\right] I_h(0,s) + G_1(s) + G_2(s), \end{aligned} \tag{2.40}$$

where $A_{11}(s)$, $A_{12}(s)$, $A_{21}(s)$, $A_{22}(s)$, $G_1(s)$ and $G_2(s)$ are, respectively, the integrals over x of $A_{11}(x,s)$, $A_{12}(x,s)$, $A_{21}(x,s)$, $A_{22}(x,s)$, $G_1(x,s)$ and $G_2(x,s)$.

The study of Eq. 2.29 at different values of α and $k = \beta/\alpha$ allows us to extract the 3dB bandwidth of the APD as a function of the gain (see Section 1.3). By assuming $v_e = v_h = v$, [12] demonstrated that, if we denote $M = M(\omega = 0)$ and $M > 1/k$, we can write

$$M(\omega) \simeq \frac{M}{\sqrt{1 + \omega^2 M^2 T_{tr,eff}^2}}, \tag{2.41}$$

where $T_{tr,eff} = NkT_{tr}$ is the effective transit time, $T_{tr} = W/v$ is the actual transit time across the multiplication region and N is a number that varies

slowly between 1/3 and 2 as k goes from 1 to 10^{-8} [12]. Figure 2.3 shows the 3dB bandwidth as a function of the gain for different values of k, we notice that the constant gain-bandwidth product implied by Eq. 2.41 decreases as k approaches unity.

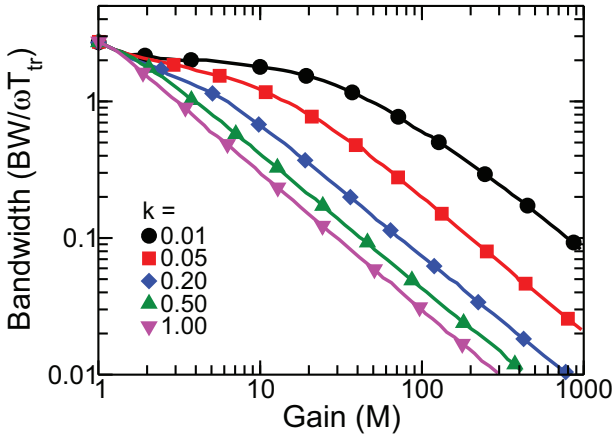

Figure 2.3: Normalized 3dB bandwidth as a function of the gain, in the case of pure electron injection, for $k = 0.01, 0.05, 0.2, 0.5, 1$. Data taken from [12].

Interestingly, as detailed in [33], the local model can be used also to study the frequency response of staircase APDs by considering N_{step} layers where uniform conditions can be assumed, so that, given the boundary conditions in Eqs. 2.27, 2.28, Eq. 2.23 can be solved for each stage of the device by exploiting recursion.

2.2 Nonlocal Models

In principle, the position where a carrier is generated, optically or by impact ionization, plays a significant role in determining its ionization probability. In fact, a carrier that starts its path with almost zero kinetic energy has to travel a certain distance, often referred to as *dead space* ($d_{e,h}$ for electron and holes respectively [35]), before gaining an energy that is sufficient for impact ionization.

As stated in Section 2.1, the local model assumes that, at position x, the electron and hole impact ionization coefficients depend only on the value of the local electric field at the same location ($E(x)$). It is clear that this hypothesis is valid only if the width of the multiplication region and the distances over which the electric field varies are much longer than the dead space.

Modern technologies for the device fabrication, such as Molecular Beam Epitaxy (MBE), allow to control the thickness of the different layers that form an APD almost at a nanometric scale. This translated into the fabrication of p-i-n APDs with very thin intrinsic region [36, 37, 38], of APDs where heterojunctions are exploited to induce steep variations of the electric field profile [24] and of staircase APDs with steps that have lengths of few tens of

nm [7, 21, 22]. To study the behavior of these devices, models that include in the computation of the impact ionization probability the information of both the point where the carrier is generated and the point where impact ionization occurs have been developed. These models are called *nonlocal* or *history dependent* models.

The importance of including the nonlocality principle in the computation of the the ionization probability for the study, for instance, of short p-i-n diodes is visible in Fig. 2.4. In fact, while the local model, using the parameters of [17], predicts an increase of the excess noise factor for a given gain as the thickness of the diode shortens, experimental results (for GaAs in this case) show the opposite behavior [23].

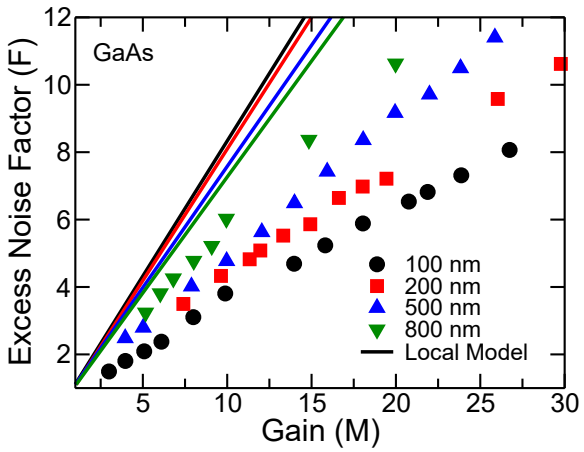

Figure 2.4: Comparison between the measured excess noise factor versus gain curves for GaAs p-i-n diodes [23] and the predictions of the local model using the parameters of [17].

The situation that we will consider for the derivation of the expressions for the gain and the excess noise factor is similar to the one sketched in Fig. 2.1, but now we will denote as x the position where a carrier is generated and as x' the position at which it ionizes.

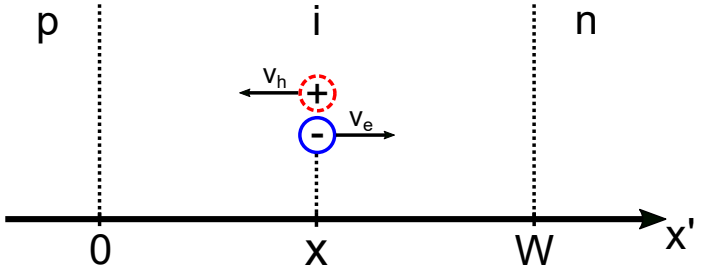

Figure 2.5: Motion of carriers inside a p-i-n junction in the framework of a nonlocal model: x is the position where a carrier is generated (optically or by impact ionization), while x' is the point where impact ionization occurs.

Two main nonlocal models can be found in the literature, namely the *Dead Space* model [35] and the model based on *Effective Fields* by [39]. They differ

in the way they compute the impact ionization coefficients $\alpha(x|x')$ and $\beta(x|x')$, but they share the same set of equations for the derivation of the gain and the excess noise. Hereafter, the equations proposed in [35] will be presented with the notation used in [39].

2.2.1 Gain and Excess Noise Factor

The position dependent impact ionization coefficients ($\alpha(x|x')$ for electrons and $\beta(x|x')$ for holes) are defined as the probability for a carrier generated at x to suffers an impact ionization event at x', within the incremental distance dx', assuming that it travels from x to x' without having other ionizing collisions. Consequently, the electron and hole position dependent impact ionization probabilities are:

$$p_e(x|x')dx' = \alpha(x|x')exp\bigg(- \int_x^{x'} \alpha(x|x'')dx''\bigg)dx' = \alpha(x|x')P_{se}(x|x')dx' \tag{2.42}$$

$$p_h(x|x')dx' = \beta(x|x')exp\bigg(- \int_{x'}^{x} \beta(x|x'')dx''\bigg)dx' = \beta(x|x')P_{sh}(x|x')dx', \tag{2.43}$$

where $P_{se}(x|x')$ and $P_{sh}(x|x')$ are the electron and hole survival probabilities, thus, the probability for a carrier to travel from x to x' without ionizing during its path.

We consider now an electron generated, optically or by impact ionization, at position x that ionizes at position x'. This primary electron will give birth to a secondary electron-hole pair, so that, at the end of the process, we find two electrons and a hole in x' (see Fig. 2.6a). Secondary carriers may, subsequently, suffer impact ionization scattering events and generate more electron-hole pairs. The total number of carriers generated by the ionization in x' of an electron generated in x is

$$n_e(x|x') = n_{e1}(x') + n_{e2}(x') + n_h(x'), \tag{2.44}$$

where $n_{e1}(x')$, $n_{e2}(x')$ and $n_h(x')$ are the number of carriers generated by the ionization of the primary electron, the secondary electron and the secondary hole, respectively. A similar reasoning can be applied for the ionization in x' of a hole that was generated in x. This results in two holes and an electron in x' (Fig. 2.6b) and, thus, we can write

$$n_h(x|x') = n_{h1}(x') + n_{h2}(x') + n_e(x'). \tag{2.45}$$

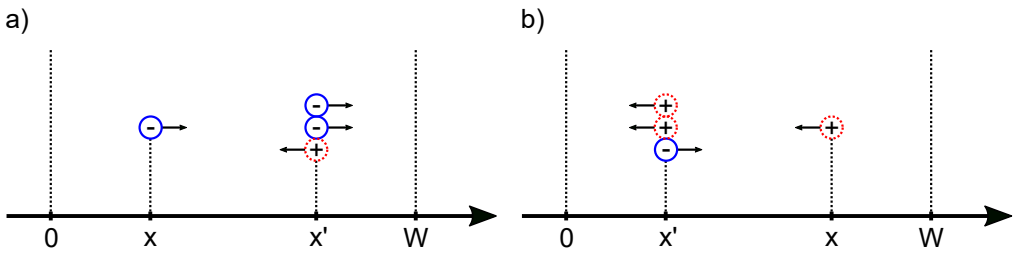

Figure 2.6: a) An electron generated in x ionizes in x'. In x' we find the primary electron and a secondary electron-hole pair. b) A hole generated in x ionizes in x'. In x' we find the primary hole and a secondary electron-hole pair.

If we denote the ensemble averages as

$$N_e(x|x') = \langle n_e(x|x') \rangle \tag{2.46}$$
$$N_h(x|x') = \langle n_h(x|x') \rangle \tag{2.47}$$
$$N_e(x') = \langle n_e(x') \rangle \tag{2.48}$$
$$N_h(x') = \langle n_h(x') \rangle, \tag{2.49}$$

then Eqs. 2.44, 2.45 become

$$N_e(x|x') = 2N_e(x') + N_h(x') \tag{2.50}$$
$$N_h(x|x') = 2N_h(x') + N_e(x') \tag{2.51}$$

The total number of carriers, in x, resulting from the ionization of the primary electron or hole ($N_e(x)$ and $N_h(x)$, respectively) can be found by integrating over x' Eqs. 2.50, 2.51, namely

$$N_e(x) = P_{se}(x|W) + \int_x^W \left[2N_e(x') + N_x(x')\right] p_e(x|x')dx' \tag{2.52}$$
$$N_h(x) = P_{sh}(x|0) + \int_0^x \left[2N_h(x') + N_e(x')\right] p_h(x|x')dx'. \tag{2.53}$$

In Eqs. 2.52, 2.53, the first term is the probability that the primary carrier reaches the boundary of the multiplication region without suffering impact ionization scattering; on the other hand, the second term is the average number of ionizations that result from a first ionization that occurred anywhere between x and W, for electrons, or between 0 and x, for holes [39].

The gain is

$$M(x) = \frac{N_e(x) + N_h(x)}{2} \tag{2.54}$$

The expression for the excess noise factor can by found by substituting Eq. 2.54 into Eq. 1.6, which yields

$$F(x) = \frac{\langle m(x)^2 \rangle}{M(x)^2} = \frac{\langle (n_e(x) + n_h(x))^2 \rangle}{4M(x)^2} = \frac{\langle n_e(x)^2 \rangle + \langle n_h(x)^2 \rangle + 2N_e(x)N_h(x)}{4M(x)^2}. \tag{2.55}$$

$\langle n_e(x)^2\rangle$ and $\langle n_h(x)^2\rangle$ can be derived from Eqs. 2.45-2.53 as follows

$$\begin{aligned}\langle n_e(x)^2\rangle &= P_{se}(x|W) + \int_x^W \langle (n_{e1}(x) + n_{e2}(x) + n_h(x))^2\rangle p_e(x|x')dx' \\ &= P_{se}(x|W) + \int_x^W [2\langle n_e(x')^2\rangle + \langle n_h(x')^2\rangle + 2N_e(x')^2 + 4N_e(x')N_h(x')] \\ &\qquad \times p_e(x|x')dx'\end{aligned} \tag{2.56}$$

$$\begin{aligned}\langle n_h(x)^2\rangle &= P_{sh}(x|0) + \int_0^x \langle (n_{h1}(x) + n_{h2}(x) + n_e(x))^2\rangle p_h(x|x')dx' = \\ &= P_{sh}(x|0) + \int_0^x [2\langle n_h(x')^2\rangle + \langle n_e(x')^2\rangle + 2N_h(x')^2 + 4N_e(x')N_h(x')] \\ &\qquad \times p_h(x|x')dx'.\end{aligned} \tag{2.57}$$

Usually, Eqs 2.52, 2.53, 2.56, 2.57 are solved by successive iterations once that the boundary conditions $N_e(W) = N_h(0) = 1$ are given [35, 39].

2.2.2 Dead Space Model

As stated at the beginning of Section 2.2, a carrier needs to travel across a finite distance, the dead space length ($d_{e,h}$ for electrons and holes, respectively), in order to acquire an energy that is sufficient for its ionization. The Dead Space model, proposed by [35], translates this concept into a threshold behavior for the electron and hole impact ionization probabilities:

$$p_e(x|x') = \begin{cases} 0, & x' < x + d_e(x) \\ \alpha(x')exp(-\int_{x+d_e(x)}^{x'} \alpha(x'')dx''), & x + d_e(x) \le x' \le W \end{cases} \tag{2.58}$$

$$p_h(x|x') = \begin{cases} 0, & x - d_h(x) < x' \\ \beta(x')exp(-\int_{x'}^{x-d_h(x)} \beta(x'')dx''), & 0 \le x' \le x - d_h(x) \end{cases} \tag{2.59}$$

In fact, in Eqs. 2.58, 2.59, we notice that the ionization probability is set to zero if a carrier still has to travel over a distance equal to its dead space length, while it is an exponential decaying function otherwise.

The impact ionization coefficients are computed using Eqs. 2.1, 2.2, while the dead space lengths depend on the reciprocal of the electric field through the following relations:

$$d_e(x) = \frac{E_{th,e}}{qE(x)} \tag{2.60}$$

$$d_h(x) = \frac{E_{th,h}}{qE(x)}, \tag{2.61}$$

where $E_{th,e}$ and $E_{th,h}$ are the threshold energies required to trigger impact ionization in the considered material. The parameters for the computation

of the impact ionization coefficients and the threshold energies are chosen in order to reproduce experimental results for the excess noise factor as a function of the gain in p-i-n APDs [38] (see Tab. 2.1 and Fig. 2.7).

		GaAs	$Al_{0.2}Ga_{0.8}As$	InP	$In_{0.52}Al_{0.48}As$
A_e	$[10^6/\text{cm}]$	6.01	5.39	3.01	4.17
E_{ce}	$[10^6\text{V/cm}]$	2.39	2.71	2.45	2.09
γ_e	-	0.90	0.94	1.08	1.20
$E_{th,e}$	eV	1.90	2.04	2.20	2.00
A_h	$[10^6/\text{cm}]$	3.59	1.28	4.29	2.65
E_{ch}	$[10^6\text{V/cm}]$	2.26	2.06	2.08	2.79
γ_h	-	0.92	0.95	1.12	1.07
$E_{th,h}$	eV	1.55	2.15	2.20	2.00

Table 2.1: Parameters for the computation of the impact ionization coefficients and of the dead space lenghts using the Dead Space model [38].

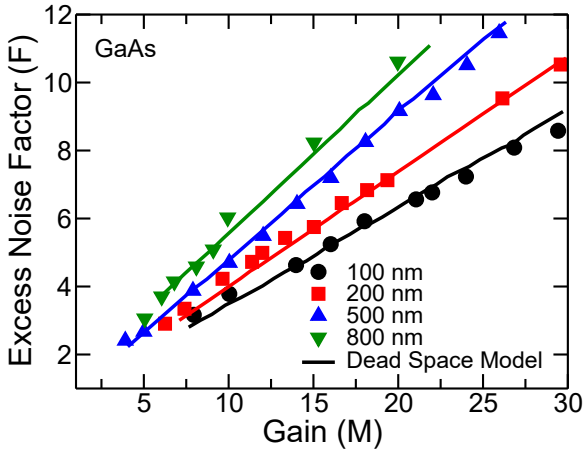

Figure 2.7: Comparison between the excess noise factor versus gain curves measured for GaAs p-i-n diodes of different thicknesses (symbols) and the ones obtained with the Dead Space model using the parameters of Tab. 2.1. Data taken from [38].

In Fig. 2.7 we notice that the Dead Space model correctly predicts the reduction of the excess noise factor for a given gain that is experimentally measured in p-i-n APDs as the diode thickness shortens.

Figure 2.8 compares the electron and holes impact ionization coefficients measured for GaAs and the corresponding α and β computed using the parameters in Tab. 2.1 for the same material [38]. The difference between the experiments and the coefficients used in the model can be explained by looking at the fact that the model coefficients are valid once that a carrier has already traveled over its dead space length. On the other hand, the information on the dead space lengths is somewhat included in the measurements [40].

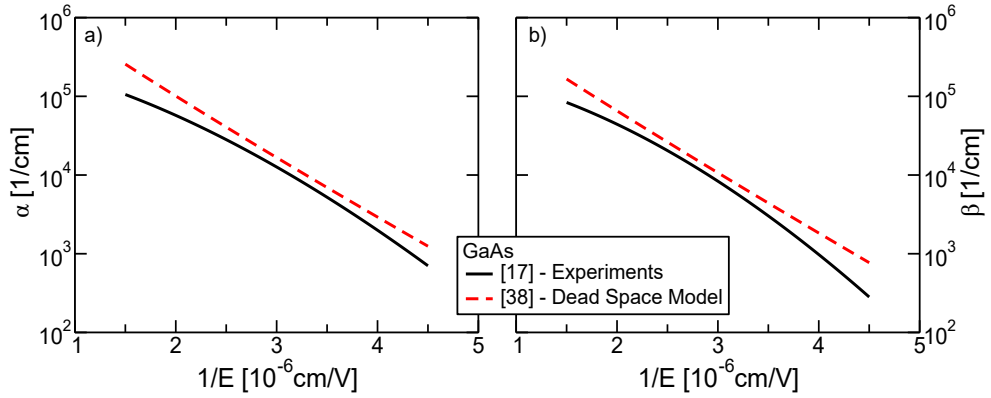

Figure 2.8: Comparison between the experimental impact ionization coefficients for a) electrons and b) holes [17] in GaAs and the ones used in the Dead Space model [38].

In [40], a relation between the experimental impact ionization coefficients (α_m and β_m) and the ones that have to be used in the Dead Space model is proposed, given that the electron and hole ionization threshold energies ($E_{th,e}$ and $E_{th,h}$) are known with accuracy. The probability that an electron travels from x to x' without ionizing can be derived from Eq. 2.58, namely

$$P_{se}(x|x') = \begin{cases} 1, & x' < x + d_e(x) \\ exp\left[-\alpha(x' - x - d_e)\right], & x + d_e(x) \leq x' \leq W. \end{cases} \tag{2.62}$$

If we assume that the electron has been generated by the previous ionization of its parent electron, then we now have two electrons in x that start their motion and the probabilities that they reach x' without suffering an impact ionization scattering event are, respectively $P_{se,1}(x|x')$ and $P_{se,2}(x|x')$. The probability that they both reach x' without ionizing is $P_{se,j}(x|x') = P_{se,1}P_{se,2}$, thus

$$P_{se,j}(x|x') = \begin{cases} 1, & x' < x + d_e(x) \\ exp\left[-2\alpha(x' - x - d_e)\right], & x + d_e(x) \leq x' \leq W. \end{cases} \tag{2.63}$$

The joint impact ionization probability $\partial(1 - P_{se,j})/\partial x'$ is

$$p_{e,j}(x|x') = \begin{cases} 0, & x' < x + d_e(x) \\ 2\alpha exp\left[-2\alpha(x' - x - d_e)\right], & x + d_e(x) \leq x' \leq W. \end{cases} \tag{2.64}$$

From Eq. 2.64 it is possible to extract the mean distance between two consecutive impact ionization events

$$\overline{x}_{ii,e} = \int_0^\infty x' p_{e,j}(0|x')dx' = \frac{1}{2\alpha} + d_e, \tag{2.65}$$

where d_e is computed using Eq. 2.60 once that $E_{th,e}$ is known.

From the experimental measurements, instead, the impact ionization coefficient is related to the mean distance between two consecutive impact ionization events by the relation

$$\alpha_m = \frac{1}{2\overline{x}_{ii,e}}. \tag{2.66}$$

The expression in Eq. 2.66 can be found by using Eq. 2.65, substituting α with α_m and setting $d_e = 0$ in Eq. 2.64.

Finally, by equating Eq. 2.65 and Eq. 2.66 we can derive the relation between α_m and α.

$$\alpha_m = \frac{1}{\frac{1}{\alpha} + 2d_e}. \tag{2.67}$$

A similar relation holds also between β_m and β [40].

Interestingly, [41] demonstrated that, in the framework of the Dead Space model, an expression for the position dependent gain $M(x)$ similar to Eq. 2.10 can be obtained from a first order expansion of the recursive Eqs. 2.52 and 2.53 if α and β in Eq. 2.10 are replaced by suitable effective impact ionization coefficients that include the effects of dead space.

2.2.3 Model Based on Effective Fields

The history dependent model proposed by [39] starts from the same assumptions of the Dead Space model of [35] described in Section 2.2.2, but the hard threshold expressions of the impact ionization probabilities typical of the Dead Space model are substituted by a *soft* threshold behavior that tries to better reproduce the physics of impact ionization [39]. This is achieved by defining suitable *effective fields* for electrons and holes by convolution of the local electric field with Gaussian functions with characteristic lengths λ_e and λ_h, respectively. Hence,

$$E_{eff,e}(x|x') = \int_{x'}^{x} E(x'') \frac{2}{\sqrt{\pi}\lambda_e(x'')} exp\left(-\frac{(x'-x'')^2}{\lambda_e^2(x'')}\right) dx'' \tag{2.68}$$

$$E_{eff,h}(x|x') = \int_{x}^{x'} E(x'') \frac{2}{\sqrt{\pi}\lambda_h(x'')} exp\left(-\frac{(x''-x')^2}{\lambda_h^2(x'')}\right) dx'', \tag{2.69}$$

where

$$\lambda_e(x) = \frac{V_{de}}{E(x)} \tag{2.70}$$

$$\lambda_h(x) = \frac{V_{dh}}{E(x)}. \tag{2.71}$$

V_{de} and V_{dh} represent the voltage drop across the electron and hole dead space lengths [39].

Finally, the nonlocal impact ionization coefficients are computed using the following expressions:

$$\alpha(x|x') = A_e exp\left[-\left(\frac{E_{ce}}{E_{eff,e}(x|x')}\right)^{\gamma_e}\right] \tag{2.72}$$

$$\beta(x|x') = A_h exp\left[-\left(\frac{E_{ch}}{E_{eff,h}(x|x')}\right)^{\gamma_h}\right], \tag{2.73}$$

that are essentially Eqs. 2.1 and 2.2 with the effective fields instead of the local electric field. The model parameters for different materials, $A_{e,h}$, $E_{ce,h}$,

$\gamma_{e,h}$ and $V_{de,h}$, are chosen in order to fit experimental results for the gain as a function of the applied bias voltage and for the excess noise factor versus the gain [36] (see Tab. 2.2 and Fig. 2.9).

		GaAs	$Al_{0.2}Ga_{0.8}As$	InP	$In_{0.52}Al_{0.48}As$
A_e	$[10^6/cm]$	3.30	88.3	2.91	19.9
E_{ce}	$[10^6V/cm]$	1.75	3.74	2.80	3.62
γ_e	-	1.00	1.00	1.00	1.00
V_{de}	V	2.00	2.20	1.90	2.00
A_h	$[10^6/cm]$	0.69	6.47	12.4	3.21
E_{ch}	$[10^6V/cm]$	1.38	2.72	3.05	3.23
γ_h	-	1.00	1.00	1.00	1.00
V_{dh}	V	2.25	2.48	2.14	2.25

Table 2.2: Parameters for the computation of the impact ionization coefficients in the nonlocal model base on effective fields [36].

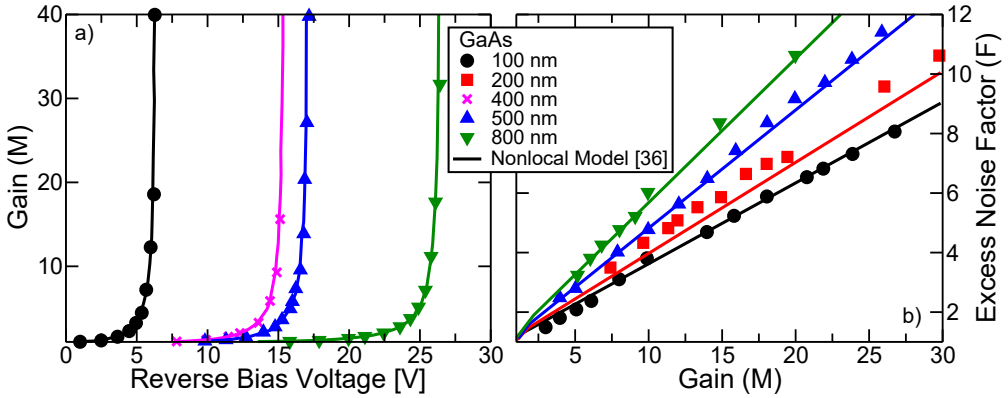

Figure 2.9: Comparison between the a) gain versus applied voltage and b) excess noise factor versus gain curves measured for GaAs p-i-n diodes of different thicknesses (symbols) and the ones obtained with the nonlocal model based on effective fields using the parameters of Tab. 2.2. Data taken from [36].

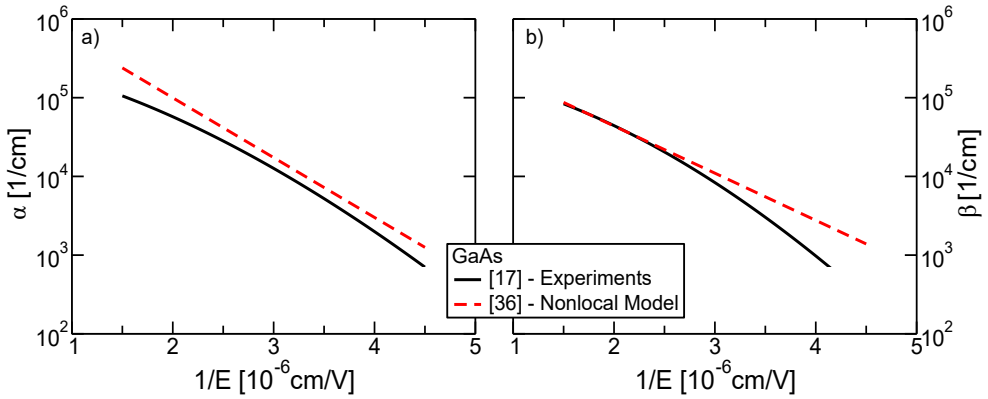

Figure 2.10: Comparison between the experimental impact ionization coefficients for a) electrons and b) holes [17] in GaAs and the ones used in the history dependent model based on effective fields [36].

Figure. 2.9 shows that the nonlocal model based on effective fields well fits the experimental results of thin GaAs p-i-n diodes. In particular, the decrease in the excess noise factor for a given gain as the diode shortens is correctly reproduced.

In Fig. 2.10 we can notice that, for the same reasons explained in Section 2.2.2, the impact ionization coefficients for GaAs computed using the parameters of Tab. 2.2 [36] slightly differ from the ones experimentally measured in [17].

2.2.4 Time and Frequency Response: the Random Path Length Algorithm

Analytic expressions for the derivation of the time and frequency response in the framework of nonlocal models have been proposed in the literature. In [42], for instance, a set of equations to be solved by successive iterations, similar to the one of Section 2.2.1, was developed to compute the evolution in time of number of carriers using the Dead Space model. On the other hand, in [39] the transport equations (Eq. 2.3, 2.4) have been solved in the time domain and rewritten as a function of the nonlocal impact ionization probabilities $p_e(x|x')$ and $p_h(x|x')$.

Interestingly, the problem at hand has been also tackled in [43, 44] using a Monte Carlo approach combined with the view of the Dead Space model, to mimic the motion of the carriers inside the multiplication region of a p-i-n APD. Due to its easy implementation and to its usefullness in the rest of this thesis, in this Section we will review this latter algorithm, called Random Path Length (RPL) as originally proposed in [43, 44].

Firstly, from Eq. 2.62, the distance that an electron travels before its ionization can be computed by equating its survival probability $P_{se}(x|x')$ to a random number r, generated with uniform distribution in the $[0, 1]$ interval, namely

$$r = P_{se}(x|x + l_e) \Rightarrow l_e = d_e - \frac{ln(r)}{\alpha}. \tag{2.74}$$

A similar expression holds also for l_h, the random distance that a hole travels before its ionization.

The RPL algorithm simulates N_{ev} independent trials; each trial corresponds to the absorption of a photon in the APD. For each trial, an electron-hole pair is injected at position $x \in [0, W]$, then, for each carrier:

1. $l_{e,h}$ is computed.

2. If $x' = x + l_e \notin [0, W]$ ($x' = x - l_h$, for holes), the carrier is collected by the contact, otherwise the gain of the trial (m_i) is increased by one and a new electron hole pair is generated in x'.

3. The simulation of a single trial ends when all the carriers have been collected by the contacts.

The mean gain and excess noise factor can be finally computed as

$$M = \frac{1}{N_{ev}} \sum_{i=1}^{N_{ev}} m_i \tag{2.75}$$

$$F = \frac{1}{N_{ev} M^2} \sum_{i=1}^{N_{ev}} m_i^2 \tag{2.76}$$

Assuming constant velocities for electrons and holes [44], v_e and v_h respectively, it is easy to compute the time required for a carrier to travel from x to x' and to keep track, for each trial, also of the number of electrons and holes at time t, $n_{ei}(t)$ and $n_{hi}(t)$. Then, the mean current as a function of the time can be computed using Ramo's Theorem [34]

$$i(t) = \frac{q}{W} \left[v_e N_e(t) + v_h N_h(t) \right], \tag{2.77}$$

where

$$N_{e,h}(t) = \frac{1}{N_{ev}} \sum_{i=1}^{N_{ev}} n_{e,hi}(t). \tag{2.78}$$

The procedure detailed in this Section is valid only for p-i-n APDs, the use of the RPL algorithm in combination with a generic nonlocal model for the study of staircase APDs will be detailed in Chapter 4.

Figure 2.11 shows the current waveforms as a function of the time, in the case of pure electron injection at $x = 0$, computed with the RPL algorithm and the parameters of [43] for GaAs p-i-n APDs with thickness $d = 100, 500, 1000$ nm and at two different gains, $M = 5$ and $M = 10$. We notice that, at a given gain, the duration of the current waveform increases as the thickness of the APD increases. However, the increased duration is compensated by a reduction of the amplitude of the peak, so that, for all the thicknesses, $\int_0^{+\infty} i(t)dt = Mq$.

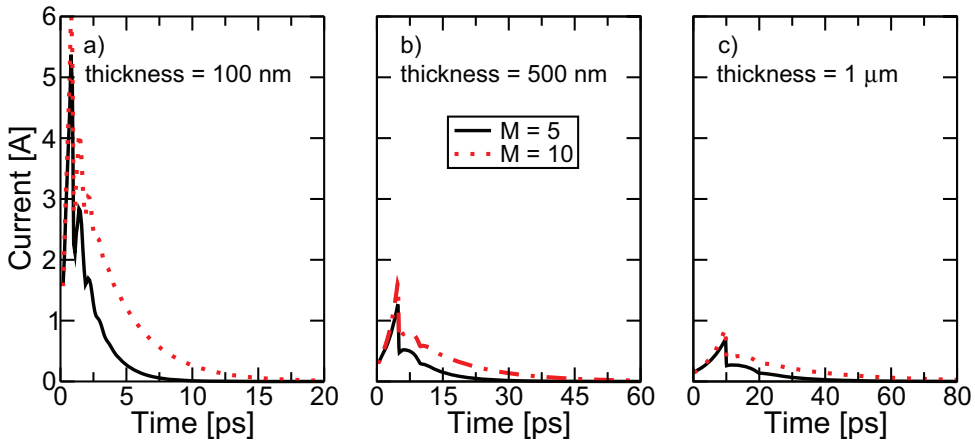

Figure 2.11: Current waveforms as a function of time for GaAs p-i-n APDs at gains $M = 5$ (black solid line) and $M = 10$ (red dotted line). The thickness of the device is a) $d = 100$ nm, b) $d = 500$ nm and c) $d = 1$ μm. The computation has been performed with the RPL algorithm, using the parameters of [43].

The 3dB bandwidth can be easily calculated from the Fourier transforms of the current waveforms computed with the RPL algorithm by using the procedure described in Section 1.3.

2.3 Monte Carlo Models

The Monte Carlo method for the solution of the Boltzmann Transport Equation in semiconductor devices consists of the simulation of the carriers' motion inside the semiconductor crystal taking into account the action of the applied electric field and of scattering mechanisms [45]. The carrier's motion is reproduced by means of successions of free flights interrupted by scattering events. The scattering mechanism responsible for the interruption of the free flight is randomly chosen according to the probability of occurrence of each scattering mechanism [45].

A detailed description of the Monte Carlo method is provided in [45, 46], in this Section, instead, we will review some applications of Monte Carlo simulations for the study of the performance of APDs. In fact, the mean gain, the excess noise factor and the time response of APDs can be computed with Monte Carlo simulations by using Eqs. 2.75, 2.76 and 2.77 introduced in Section 2.2.4 for the RPL algorithm [47]. Moreover, differently to the local and nonlocal models described in Sections 2.1 and 2.2, Monte Carlo models give a full description of the particles' dynamics up to and above the energies required to trigger avalanche multiplication in the considered material [48].

In the following, results of *analytical* and *full band* Monte Carlo simulations will be presented separately.

2.3.1 Analytical Monte Carlo Simulations

In this Section we will review some interesting results concerning analytical Monte Carlo simulations of GaAs and $Al_xGa_{1-x}As$ APDs. In analytical Monte Carlo simulations, the transport is described by means of an effective dispersion relation in the form

$$E_k(1 + \alpha_\varepsilon E_k) = \frac{\hbar^2 k^2}{2m^*} \tag{2.79}$$

where E_k is the kinetic energy, k is the wavevector, α_ε is the nonparabolicity correction factor, m^* is the carrier's effective mass at the valley minima and $\hbar$ is the reduced Planck's constant [49]. α_ε and m^* are usually adjusted to reproduce the shape of the band diagram around a minimum.

Acoustic and optical carrier-phonon scattering rates are described by effective coupling constants that are chosen in order to fit experimental results for the drift velocity as a function of the applied electric field [49, 48]. Figure 2.12 compares the results of the analyticl Monte Carlo simulations of [48] with the experimental results of [50] or with the results of other MC simulations [51], showing a good mutual agreement.

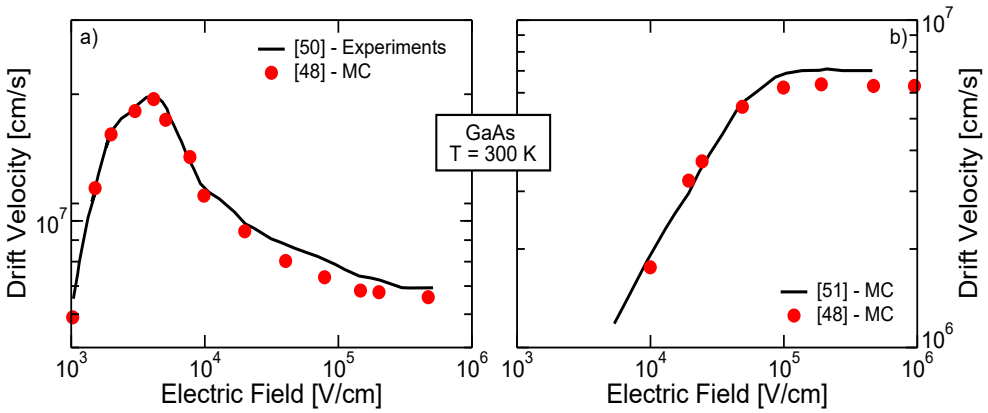

Figure 2.12: a) Electron and b) hole drift velocity as a function of the applied electric field in GaAs at $T = 300$ K. Results obtained with analytical Monte Carlo simulations by [48] (red circles) are compared with the experimental results in [50] or with other MC simulations [51]. Data are taken from [48] (black lines).

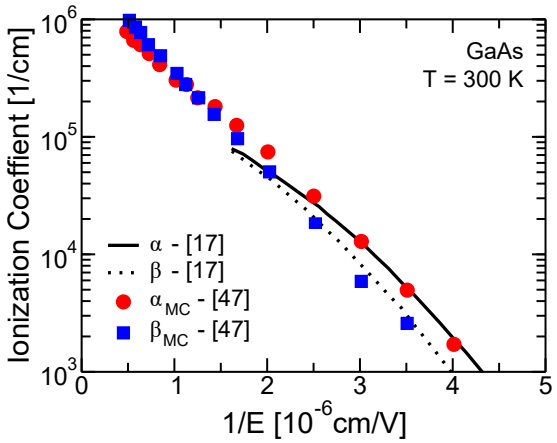

Figure 2.13: Comparison between the experimental electron and hole impact ionization coefficients [17] (black solid and dotted lines) and the ones computed with the analytical Monte Carlo simulations of [47] (red circles and blue squares). Data are taken from [47].

The impact ionization scattering rate as a function of the carrier's kinetic energy E_k is computed using the Keldysh expression [52, 53]

$$SR_{II} = C_{II}\left[\frac{E_k - E_{th}}{E_{th}}\right]^n, \tag{2.80}$$

where C_{II}, E_{th} and n are fitting parameters chosen to reproduce through Monte Carlo simulations the experimental impact ionization coefficients [47] or experimental measurements of gain and excess noise factor in homojunction APDs [54]. Momentum conservation is neglected and the difference between the energy of the primary ionizing carrier and the bandgap is usually equally divided between the three secondary particles [48, 47]. Figure 2.13 compares the electron's and hole's impact ionization coefficients extracted by [47] by using

analytical Monte Carlo simulations with the ones experimentally determined bi [17]. At electric fields below $E = 5 \times 10^5$ V/cm, where a comparison is possible, the agreement is good.

Analytical band Monte Carlo simulations have been exploited by [49] to analyze the dependence on the position of the impact ionization coefficients in GaAs and $Al_xGa_{1-x}As$ APDs of different thickness. To compute $\alpha(x)$, [49] used the expression

$$\alpha(x) = \frac{1}{J_e(x)} \left\{ \left[\frac{dJ_e(x)}{dx} \right]_{\text{electron II}} \right\}, \tag{2.81}$$

where $J_e(x)$ is the electron current flux and $dJ_e(x)/dx$ is the change in $J_e(x)$ in the $[x, x + dx]$ interval caused by electron's impact ionization. A similar expression holds also for $\beta(x)$. Figure 2.14 shows the position dependent impact ionization coefficients computed by [49] for two GaAs p-i-n diodes with thickness $d = 0.1$ μm and $d = 1.0$ μm in the case of electron injection at $x = 0$. We can notice that both $\alpha(x)$ and $\beta(x)$ saturate to a constant value after few tens of nm.

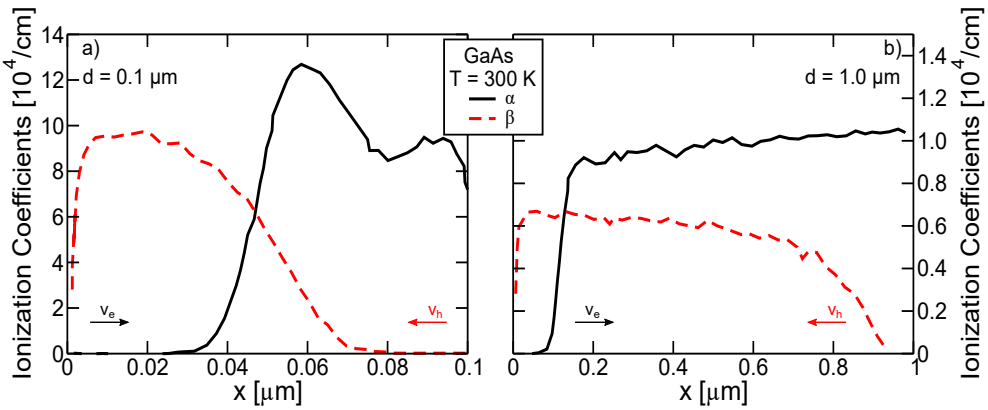

Figure 2.14: Position dependent impact ionization coefficients in GaAs p-i-n diodes of thickness a) $d = 0.1$ μm and b) $d = 1.0$ μm computed by using analytical Monte Carlo simulations. Data are taken from [49].

An interesting application of analytical Monte Carlo simulations is the one proposed in [54]. Using a model similar to the one of [49] and after having calibrated it to reproduce experimental results for the gain and excess noise factor in GaAs, $Al_{0.2}Ga_{0.8}As$ and $Al_{0.6}Ga_{0.4}As$ p-i-n APDs, [54] used Monte Carlo simulations to analyze how the performance of a heterojunction $Al_{0.6}Ga_{0.4}As/GaAs/Al_{0.6}Ga_{0.4}As$ APD are affected by the carrier's initial injection energy and by the thickness of the GaAs layer.

Figure 2.15 points out that when III-V compounds and their alloys with a metal are stacked to form devices such as the heterojunction APD in [54], it exists an optimum thickness for the layer of the quantum well that minimizes the excess noise factor at a given gain. Increasing the thickness of the quantum well from 60 nm to 100 nm translates into an increase of the excess noise factor, since dead space effects become less relevant, while decreasing the thickness of the GaAs layer from 60 nm to 20 nm translates into an increase of the excess

noise factor because the device tends to act as a homojunction alloy APD, that shows a higher noise [54].

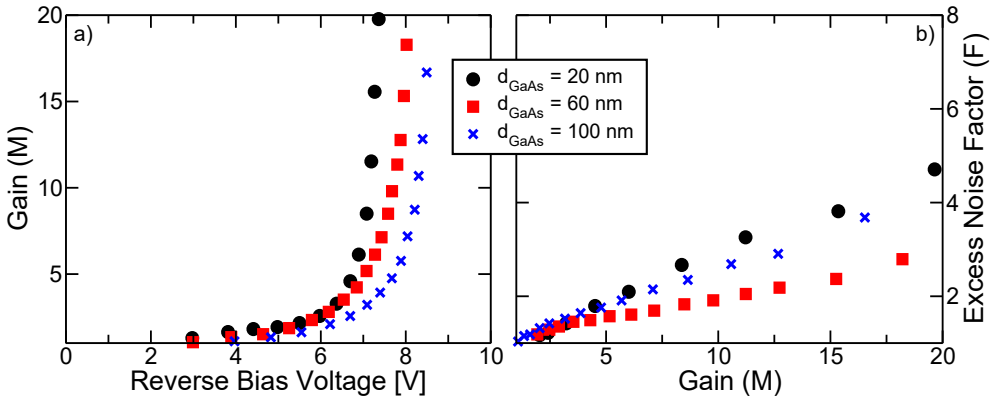

Figure 2.15: Dependence of the a) gain versus applied bias and b) excess noise factor versus gain curves of an $Al_{0.6}Ga_{0.4}As/GaAs/Al_{0.6}Ga_{0.4}As$ APD on the thickness of the GaAs layer. Data are taken from [54].

Finally, analytical Monte Carlo simulations have also been used to compute the time response and the bandwidth of APDs in GaAs [55, 56] and other III-V compound semiconductors [57].

2.3.2 Full Band Monte Carlo Simulations

A detailed description of a Full Band Monte Carlo transport simulator will be given in Chapter 5. In this Section, instead, only the main results concerning the simulation of APDs in III-V compound semiconductors obtained by other authors will be presented.

In Full Band Monte Carlo simulations the band structure and the scattering rates are computed as a function of the wave vector $\vec{k}$ and stored in look-up tables. Since the computation of these quantities in the entire First Brillouin Zone can be very computationally demanding, usually calculations are performed by exploiting the symmetry of the crystal (e. g. diamond and zinc-blende crystals, such as Si and GaAs, have a 48-fold symmetry). A common method for the computation of the band structure in Full Band Monte Carlo simulations is the Empirical Pseudopotential Method (EPM) described in its local and nonlocal implementations in [58] and [59] respectively, while the scattering rates are computed by using the Fermi Golden Rule, that implies momentum and energy conservation. Usually, the expressions reported in [60], for the calculations of the scattering rates, that use effective coupling constants chosen to reproduce the experimental drift velocities as a function of the applied electric field, are employed. Figure 2.16 shows the carrier-phonon and impact ionization scattering rates for electrons and holes used in the Full Band Monte Carlo simulations of [61] and [62]. Since [61] does not report the holes' scattering rates, a comparison is possible only for electrons. We can notice that, even if the results between the two authors for both the electron-phonon and the impact ionization scattering rates are slightly different, the

drift velocities versus applied field curves are in good mutual agreement and correctly reproduce the experimental results of [50] (see Fig. 2.17a). The simulations of [61] and [62] are also able to fit the experimental results for the drift velocity of holes (Fig. 2.17b). It is worth noting that the complete Full Band calculation of the impact ionization scattering rate is so demanding in terms of computational time that often several approximation are adopted even in Full Band Monte Carlo simulators. In [61], for instance, the impact ionization scattering rate is computed only as a function of the carrier energy using, for each band, the expression

$$SR_{II,j} = C_{II,j} \left[E_k - E_{th,j} \right]^{n_j} , \tag{2.82}$$

where E_k is the carrier's energy and j is the band index; [62], instead, used a Full Band approach but neglected the momentum conservation, using the so called *random-k* approximation proposed by [63].

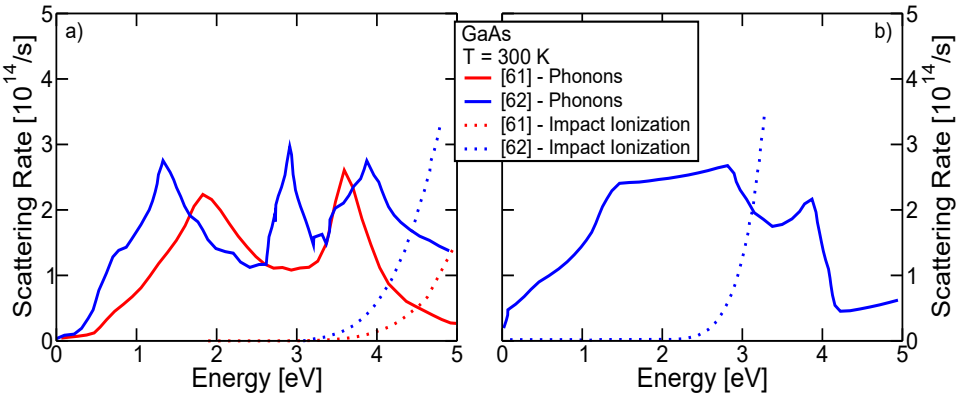

Figure 2.16: Comparison between the a) electron and b) hole scattering rates as a function of the carrier's energy used for GaAs in the Full Band Monte Carlo simulators of [61] (red) and [62] (blue). The solid lines represent the carrier-phonon scattering rates, while the dotted lines are the impact ionization scattering rates.

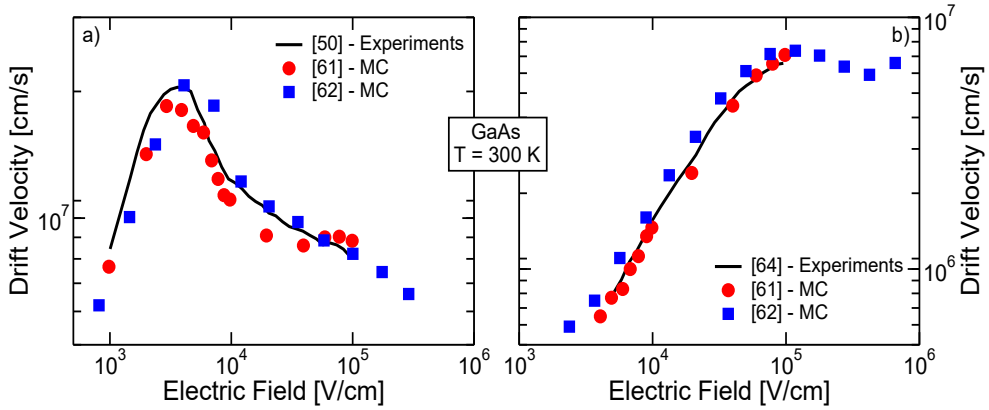

Figure 2.17: a) Electron and b) hole drift velocities as a function of the applied field. The results of the Full Band Monte Carlo simulations of [61] (red circles) and [62] (blue squares) are compared with the experimental results of [50] and [64] (black solid lines).

The electron and hole impact ionization coefficients extracted in [47] and in [62] are compared in Fig. 2.18 with the experimental results of [17] and both the simulators fairly reproduce the measured data.

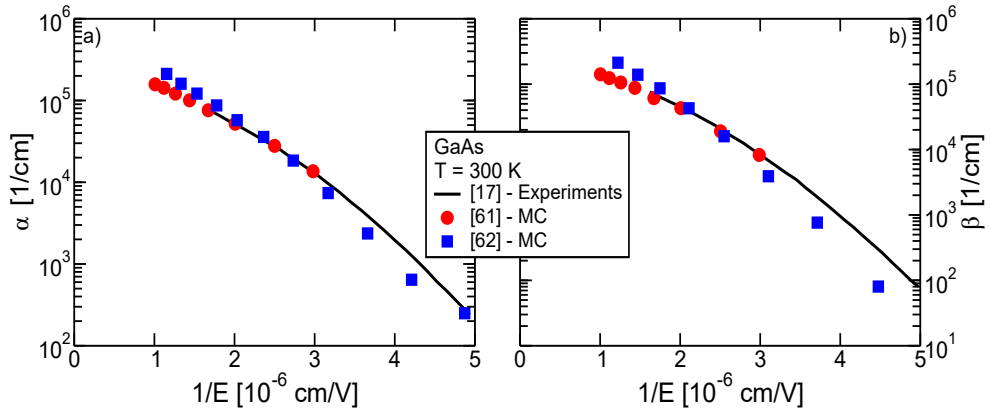

Figure 2.18: a) Electron and b) hole impact ionization coefficients as a function of the reciprocal of the electric field. The results obtained by the Full Band Monte Carlo simulations of [61] (red circles) and [62] (blue squares) are compared with the experimental results of [17] (black solid lines).

Full band Monte Carlo simulations are exploited in [61] to extract the gain and excess noise factor (with Eqs. 2.75 and 2.76) (see Fig. 2.19, the probability of impact ionization as a function of the position inside the multiplication region and also the temporal behavior of GaAs p-i-n APDs in Linear mode [65].

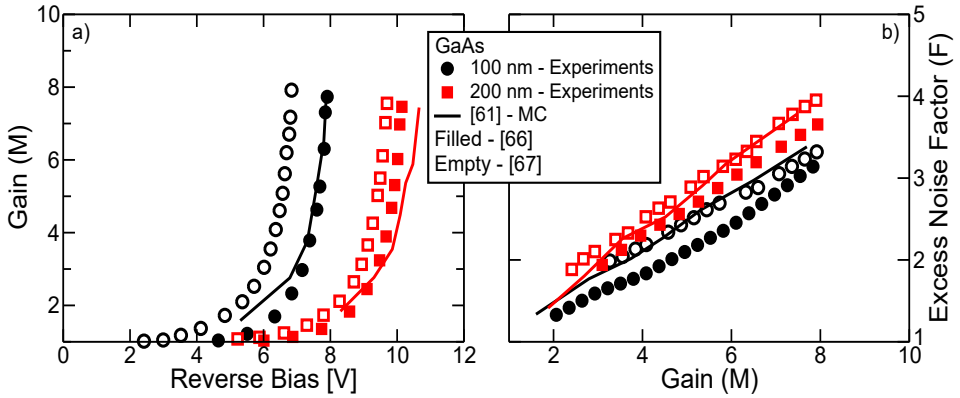

Figure 2.19: a) Gain versus applied bias voltage and b) excess noise factor versus gain curves for GaAs p-i-n diodes with thickness $d = 100$ nm (black) and $d = 200$ nm (red). The experimental results of [66] (filled symbols) and [67] (empty symbols) are compared with the results of the Full Band Monte Carlo simulations of [61] (solid lines).

On the other hand, [62, 68] used Full Band Monte Carlo simulations to study the breakdown probability and the mean time to breakdown as a function

of the applied bias in single photon APDs in GaAs and other III-V compound semiconductors operating in Geiger mode.

Chapter 3

The Energy Balance History Dependent Model

In this Chapter, a new nonlocal model for the computation of the gain and the excess noise factor in p-i-n and staircase APDs, in the following referred to as the Energy Balance History Dependent Model, will be introduced. Our aim is to use the developed model to study, in DC, the figures of merit of complex structures, such as staircase APDs, and to understand how changes in the design of these devices affects their gain and the excess noise factor. The results that will be presented in the following are an extension of the ones published by the author of this thesis in [69, 70, 71, 72].

3.1 Derivation of the Model's Equations

The application of the nonlocal models described in Section 2.2 to staircase APDs (or to APDs that exploit variations in the doping concentration to modulate the electric field in the multiplication region [24]) is not straightforward. For instance, to mimic what happens in the presence of a heterojunction, Ref. [73] used the Dead Space model taking into account the fact that, at a given electric field, the dead space of a *hot* carrier is reduced w. r. t. the one of a *cold* carrier, while [24] introduced the concept of *scattering aware* ionization coefficients, assuming that a carrier becomes cold if it travels for a suitably-defined distance across a region with an electric field below a specific threshold. On the other hand, the nonlocal model based on electric fields proposed by [39], is not applicable to staircase APDs because it relates the parameters λ_e and λ_h to the reciprocal of the electric field, that is singular at conduction or valence band discontinuities (see Eqs. 2.70 and 2.71).

Inspired by [74, 75], to overcome the limitations of the nonlocal models described in Section 2.2, we present an improved nonlocal model applicable to interpret the electrical measures of staircase APDs. The starting point of the derivation of the model's equations is the approximate solution (with the method of moments) of the Boltzmann Transport Equation (BTE) as done in [75]. The derivation of the model's equation will be detailed here for electrons, but the same calculations can be adapted to holes.

The zero-th and second order moments of the BTE, that correspond to charge continuity and energy conservation, are

$$\frac{\partial n_e}{\partial t} + \nabla \cdot (n_e \vec{v}_e) = C_e \tag{3.1}$$

$$n_e \frac{\partial n_e w}{\partial t} + \nabla \cdot \vec{Q} + w\nabla \cdot (n_e \vec{v}_e) + n_e \vec{v}_e \cdot \nabla w + \nabla \cdot (n_e k_B \hat{T} \vec{v}_e) + q n_e \vec{v}_e \cdot \vec{E} = C_W. \tag{3.2}$$

By substituting Eq. 3.1 into Eq. 3.2 we get

$$n_e \frac{\partial w}{\partial t} + \nabla \cdot \vec{Q} + n_e \vec{v}_e \cdot \nabla w + \nabla \cdot (n_e k_B \hat{T} \vec{v}_e) + q n_e \vec{v}_e \cdot \vec{E} = C_W - C_e w, \tag{3.3}$$

where w is the average carrier energy, $\vec{v_e}$ is the average velocity, $\vec{E}$ is the electric field, $\vec{Q} = \int \frac{1}{2} m c^2 \vec{c} f d^3u$ is the heat flux, $f(u_x, u_y, u_z)$ is the distribution function, $\vec{c} = \vec{u} - \vec{v}_e$ is the random component of the carrier velocity, $\hat{T}$ is a tensor defined as: $n k_B T_{ij} = \int m c_i c_j f d^3u$, C_e and C_W are the collision terms. We can then write

$$w = \frac{\int \frac{1}{2} m u^2 f d^3u}{\int f d^3u} = \frac{1}{2} m v_e^2 + \frac{1}{2} k_B (T_{11} + T_{22} + T_{33}). \tag{3.4}$$

We will now use the following approximations:

- Instead of the tensor $\hat{T}$, we use the scalar quantity T_e.
- $C_W - C_e w = -n_e \frac{w - w_0}{\tau_w}$ (relaxation time approximation), $w_0 = \frac{3}{2} k_B T_0$, T_0 is the lattice temperature.
- $\vec{Q} = -k_e \nabla T_e$, k_e is the thermal conductivity.

Assuming steady-state conditions, knowing that $\vec{J}_e = -q n_e \vec{v}_e$ and taking into account continuity equations, it is possible to rewrite Eq. 3.3 as

$$-\nabla \cdot \left[k_e \nabla T_e + \frac{\vec{J}_e}{q} (w + k_B T_e) \right] = \vec{E} \cdot \vec{J}_e - n_e \frac{w - w_0}{\tau_W} - U_e w, \tag{3.5}$$

where $U_e = R - G$ is the recombination-generation function. We now make three additional simplifications:

- $\vec{Q}$ is neglected.
- The kinetic term $\frac{1}{2} m v_e^2$ inside w is neglected.
- $U_e = 0$.

Along the x direction, Eq. 3.5 can be rewritten as

$$-\frac{d}{dx} \left(\frac{J_e(x)}{q} \frac{5}{3} w \right) = J_e E(x) - n_e \frac{w - w_0}{\tau_W}. \tag{3.6}$$

From the continuity equations, in steady-state conditions $U_n = 0$ implies $dJ_e(x)/dx = 0$, hence Eq. 3.6 becomes

$$\frac{d}{dx}\left(\frac{5}{3}w\right) = -qE(x) - \frac{w - w_0}{\tau_W v_e}. \tag{3.7}$$

If the energy relaxation length for electrons is defined as $\lambda_e = \frac{5}{3}v_e\tau_w$ [75], then Eq. 3.7 is equivalent to

$$\frac{dT}{dx} + \frac{T - T_0}{\lambda_e} + \frac{2}{5}\frac{q}{k_B}E(x) = 0. \tag{3.8}$$

The integration of Eq. 3.8 yields the following expression for the carrier's temperature

$$T(x) = T_0 + \frac{2}{5}\frac{q}{k_B}\int_0^x E(x'')exp\left(\frac{x'' - x}{\lambda_e}\right)dx''. \tag{3.9}$$

When we reach the situation $dT/dx = 0$, Eq. 3.8 becomes

$$\lambda_e E(x) = \frac{5}{2}\frac{k_B}{q}\left[T(x) - T_0\right]. \tag{3.10}$$

Equation 3.10 can be now exploited for the definition of an the effective field (that keeps into account the history of a carrier from its generation point x to its ionization point x') by equating it to Eq. 3.9, namely

$$E_{eff,e}(x|x') = \frac{1}{\lambda_e}\int_x^{x'}\frac{dE_C(x'')}{dx''}exp\left(\frac{x'' - x'}{\lambda_e}\right)dx''. \tag{3.11}$$

A similar expression holds also for the hole's effective field:

$$E_{eff,h}(x|x') = \frac{1}{\lambda_h}\int_{x'}^{x}\frac{dE_V(x'')}{dx''}exp\left(\frac{x' - x''}{\lambda_h}\right)dx''. \tag{3.12}$$

It is worth noting that in Eqs. 3.11 and 3.12, the electric field $E(x)$ that appears inside the integral in Eq. 3.9 has been substituted by the conduction and valence band gradients, respectively. This is fundamental for the analysis of staircase APDs, since, as explained in Section 1.4, owing to the configuration of the band diagram of such devices electrons and hole are subjected to different driving forces.

Since Eqs. 3.11 and 3.12 are derived from an energy balance equation (Eq. 3.7), we denoted the developed model *Energy Balance History Dependent Model (EBHDM).*

In the EBHDM, the parameters λ_e for electrons and λ_h for holes are constant (i. e. they neither depend on position nor on the bias) and represent a sort of mean free path: the ionization probability tends to that of the local model after traveling a distance larger than λ from the generation point. Consider for example a region of almost uniform electric field: regardless of the initial conditions at the generation point, the carrier distribution a few mean

free paths from the generation point tends to a unique function of energy well defined by the value of the electric field.

As in the nonlocal model based on effective field of [39], the electron and hole impact ionization coefficients are computed by using Eqs. 2.72 and 2.73, while the gain and the excess noise factor are computed by using Eqs. 2.54, 2.55 and the related equations detailed in Section 2.2.1.

3.2 Numerical Solution

The conduction and valence band profiles $E_C(x)$ and $E_V(x)$ are extracted from TCAD simulations [76] of the devices of interest at the desired bias voltages, assuming that the charge generated by photons or by impact ionization does not affect the polarization of the device. Then, after that the effective fields and the impact ionization coefficients are computed using Eqs. 3.11, 3.12, 2.72 and 2.73, instead of using the iterative procedure proposed in [35, 39], we devised a method to calculate the matrix form for Eqs 2.52, 2.53, 2.56, 2.57. In the following, we will refer to the solution of Eqs. 2.53 and 2.53, but the same method has been used also for Eqs. 2.56 and 2.57.

After discretization on a spatial mesh (see Fig. 3.1), Eqs. 2.52 and 2.53 can be written as products between vectors and matrices:

$$\overline{\mathbf{N_e}} = \overline{\mathbf{A}} + \overline{\overline{\mathbf{B_1}}}\,\overline{\mathbf{N_e}} + \overline{\overline{\mathbf{B_2}}}\,\overline{\mathbf{N_h}} \tag{3.13}$$

$$\overline{\mathbf{N_h}} = \overline{\mathbf{C}} + \overline{\overline{\mathbf{D_2}}}\,\overline{\mathbf{N_h}} + \overline{\overline{\mathbf{D_1}}}\,\overline{\mathbf{N_e}} \tag{3.14}$$

where $\overline{\mathbf{N_e}}$, $\overline{\mathbf{N_h}}$ are column vectors which represent the values of N_e and N_h on the simulation mesh; $\overline{\mathbf{A}}$, $\overline{\mathbf{C}}$ are column vectors that do not contain neither N_e nor N_h, while $\overline{\overline{\mathbf{B_i}}}$ and $\overline{\overline{\mathbf{D_i}}}$, with $i \in \{1, 2\}$, are the constant matrices which will multiply the unknown variables. We can further re-arrange the expressions obtaining the following matrix equation:

$$\begin{pmatrix} \overline{\mathbf{N_e}} \\ \overline{\mathbf{N_h}} \end{pmatrix} = - \begin{pmatrix} \overline{\overline{\mathbf{B_1}}} - \bar{\bar{\mathbf{I}}} & \overline{\overline{\mathbf{B_2}}} \\ \overline{\overline{\mathbf{D_1}}} & \overline{\overline{\mathbf{D_2}}} - \bar{\bar{\mathbf{I}}} \end{pmatrix}^{-1} \cdot \begin{pmatrix} \overline{\mathbf{A}} \\ \overline{\mathbf{C}} \end{pmatrix} \tag{3.15}$$

It has to be observed (see again Fig. 3.1) that $\overline{\mathbf{N_e}}$, $\overline{\mathbf{N_h}}$ include only the unknown samples of N_e and N_h. The values imposed by the boundary conditions $[N_h(0) = 1,\ N_e(W) = 1]$ are not part of these vectors (highlighted in red in Fig. 3.1).

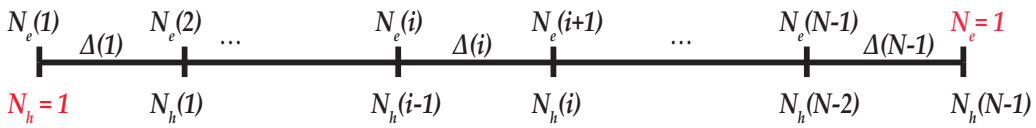

Figure 3.1: Spatial discretization of the variables N_e and N_h and indication of the boundary conditions (in red).

3.3 Model Calibration

As in the Dead Space model [35] and in the nonlocal model based on effective fields of [39], the adjustable model parameters are eight; namely the mean free paths λ_e and λ_h for electrons and holes in Eqs. 3.11 and 3.12, respectively, and A_e, A_h, E_{ce}, E_{ch}, γ_e, γ_h which relate the effective fields with the ionization coefficients (see Eqs. 2.72 and 2.73). As stated in Section 3.2, the model calibration firstly requires a reliable estimate of the conduction and valence band profiles. To this end, we have reproduced with TCAD [76] the same doping concentrations and geometrical structure for the p-i-n diodes reported in [23, 36, 77, 78, 79, 20], simulated them at different bias voltages and then applied the EBHDM in post-processing, taking as input the band profiles from drift-diffusion TCAD simulations. The good agreement at high gains validates the post-processing approach, indicating that the generated charge has little impact on the applied electric field.

Figures 3.2-3.6 compare the model results with the measured gain as a function of bias and excess noise as a function of gain. In both cases, good agreement between simulations and experiments is found over a wide range of intrinsic layer thicknesses with a unique set of material dependent model parameters summarized in Tab. 3.1.

Figures 3.2-3.4 show that in GaAs, $Al_{0.2}Ga_{0.8}As$, $Al_{0.6}Ga_{0.4}As$ the excess noise factor increases proportionally to the gain (plots b) and that it is smaller for thinner intrinsic layers. As pointed out in [23], this behavior is in contrast with the predictions of the local model [1], but it is consistent with the measurements. In fact, when the extension of the intrinsic region becomes comparable to λ_e and λ_h, the ionization probability of the secondary carriers decreases, making the ionization process somewhat more deterministic.

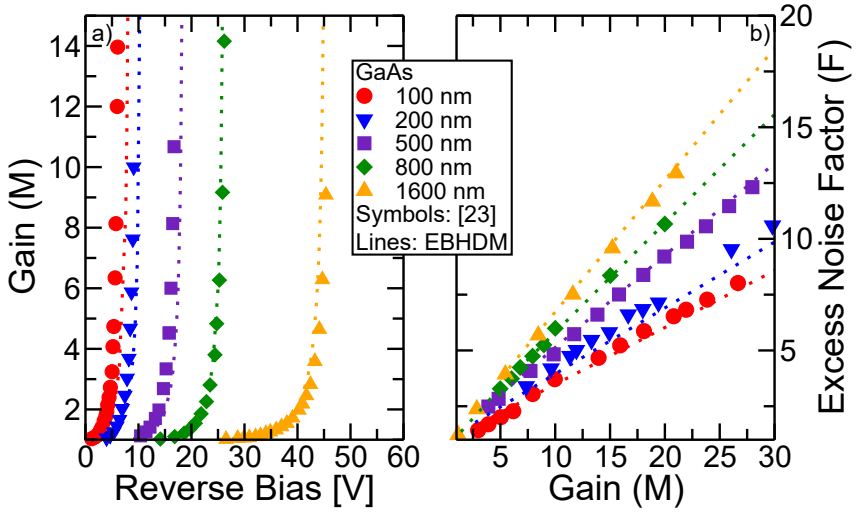

Figure 3.2: a) Gain versus applied bias voltage and b) excess noise factor versus gain curves for GaAs p-i-n diodes with different thickness. The experimental measurements reported in [23] (symbols) are compared with the results of the EBHDM using the parameters of Tab. 3.1 (dotted lines).

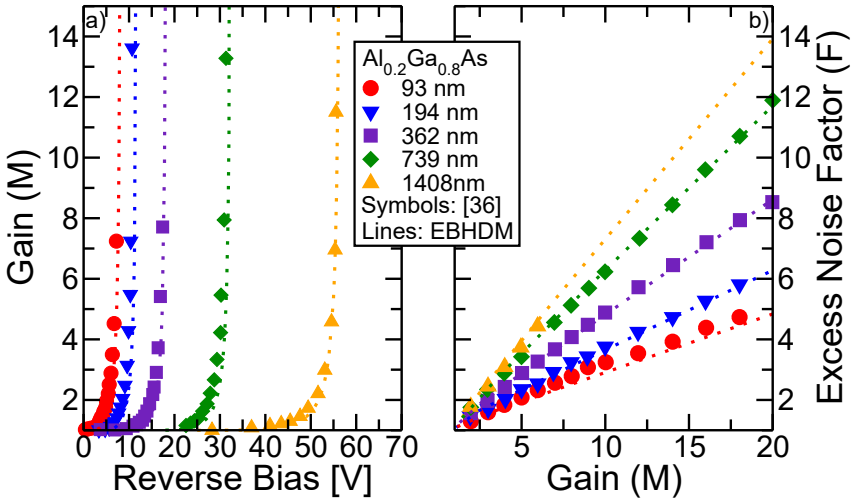

Figure 3.3: Same as Fig. 3.2 but for $Al_{0.2}Ga_{0.8}As$ p-i-n diodes. Experimental data are taken from [36].

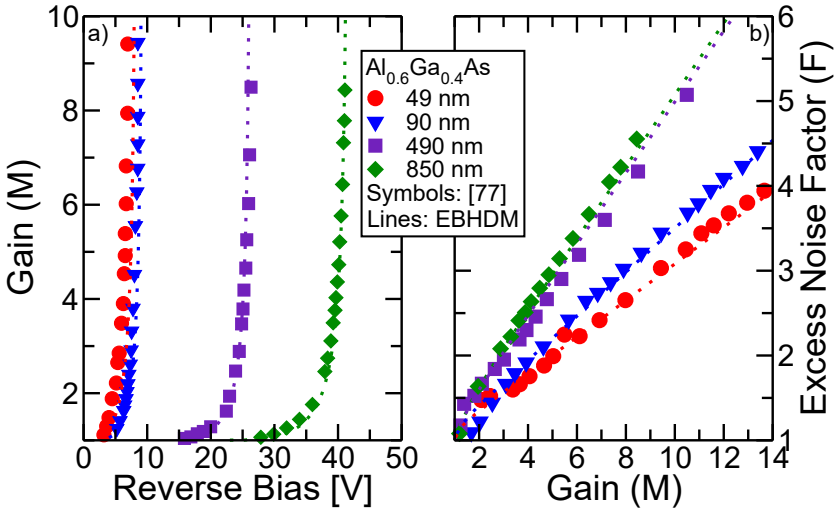

Figure 3.4: Same as Fig. 3.2 but for $Al_{0.6}Ga_{0.4}As$ p-i-n diodes. Experimental data are taken from [77].

The F versus M curves for $Al_{0.8}Ga_{0.2}As$ (Fig. 3.5) put in evidence a more complex non-monotonic trend as a function of the thickness of the intrinsic layer (d); in fact: when d decreases from 1024 nm to 312 nm, F increases for given M, owing to the fact that at high electric field (as in the short diodes) β approaches α [1]. However, as d shortens, nonlocal effects come into play and reduce F as in the other considered materials.

Figure 3.6 shows that the measured excess noise factor for InAs p-i-n diodes is slowly increasing as the gain increases and, for all the considered values of M, $F < 2$. This suggests that InAs is a semiconductor where, for the considered range of applied electric fields, electron's impact ionization is dominant w. r. t. hole's impact ionization. For this reason, consistently with the assumptions of [20], we assumed $\beta(x|x') = 0\ \forall x, x'$ in the EBHDM.

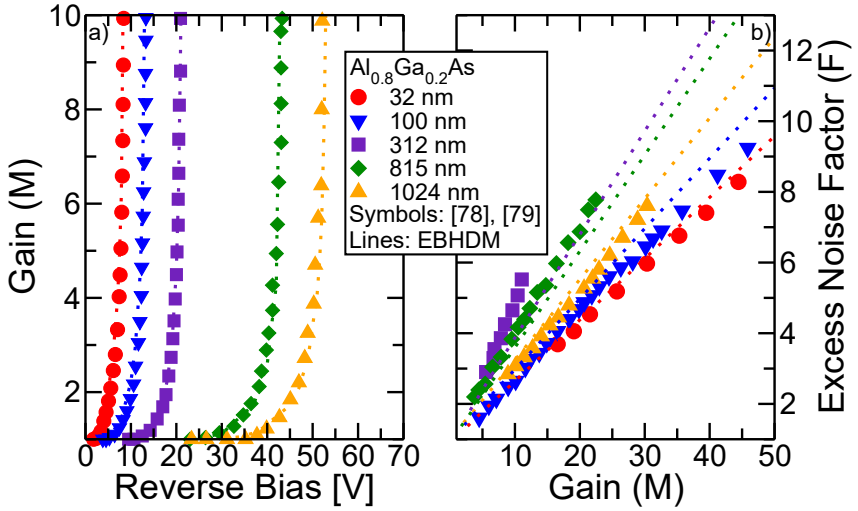

Figure 3.5: Same as Fig. 3.2 but for $Al_{0.8}Ga_{0.2}As$ p-i-n diodes. Experimental data are taken from [78, 79].

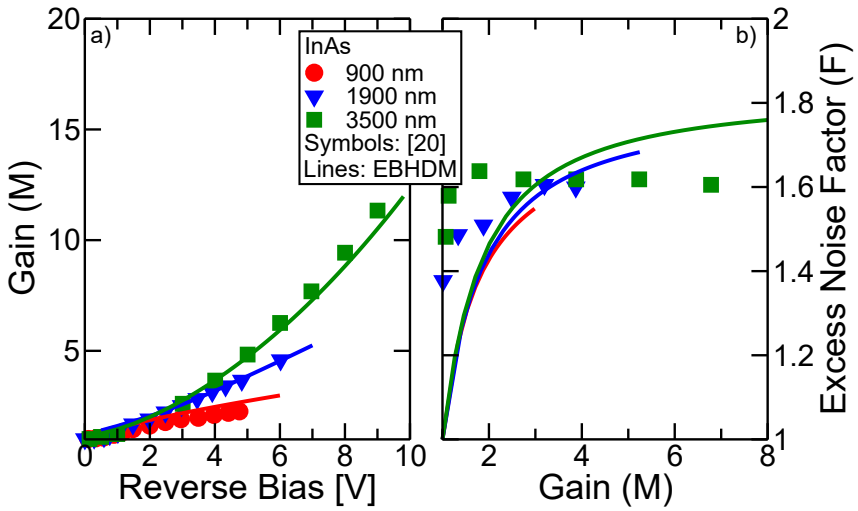

Figure 3.6: Same as Fig. 3.2 but for InAs p-i-n diodes. Experimental data are taken from [20].

		GaAs	$Al_{0.2}Ga_{0.8}As$	$Al_{0.6}Ga_{0.4}As$	$Al_{0.8}Ga_{0.2}As$	InAs
A_e	$[10^6/cm]$	3.30	88.3	88.8	14.8	0.046
E_{ce}	$[10^6V/cm]$	1.75	3.74	4.13	3.53	0.14
γ_e	-	1.00	1.00	1.00	1.00	0.38
λ_e	[nm]	18.0	17.0	18.0	20.0	73.7
A_h	$[10^6/cm]$	0.73	10.8	260	0.14	-
E_{ch}	$[10^6V/cm]$	1.42	2.99	4.99	0.67	-
γ_h	-	1.00	1.00	1.00	5.12	-
λ_h	[nm]	24.0	21.5	16.0	35.0	-

Table 3.1: Model parameters for GaAs, $Al_{0.2}Ga_{0.8}As$, $Al_{0.6}Ga_{0.4}As$, $Al_{0.8}Ga_{0.2}As$ and InAs used in the EBHDM to fit experimental results for the gain versus applied bias and excess noise factor versus gain measurements.

3.4 Gain and Excess Noise Factor of APDs featuring Heterojunctions

In the following, we apply the EBHDM to the two realistic structures already detailed in Section 1.8: the *Separate Absorption and Multiplication* (SAM) GaAs/$Al_{0.8}Ga_{0.2}As$ APD described in [8, 25] (Fig. 1.18a) and the GaAs/$Al_xGa_{1-x}As$ staircase SAM-APD presented in [7] (Fig.1.18b).

3.4.1 GaAs/$Al_{0.8}Ga_{0.2}As$ SAM-APD

The nominal structure of the device reported in [8, 25] (Fig.1.18a) is reproduced with TCAD [76] and the comparison between the simulated and the experimental [8] C-V curves is shown in Fig.3.7. The agreement between measurements and simulations is good, meaning that the TCAD provides a reliable estimate of the electric field profile. Note that the Thermionic Emission Current model for transport at the heterointerfaces has been used [76]. This may be incorrect in indirect-to-direct band gap heterojunctions, as in this case [80]. However, this is expected to have a negligible impact on the device electrostatics. It may however result in a different value of the effective ΔE_C to use in our post-processing model, but this can be assessed only via accurate Monte Carlo simulations.

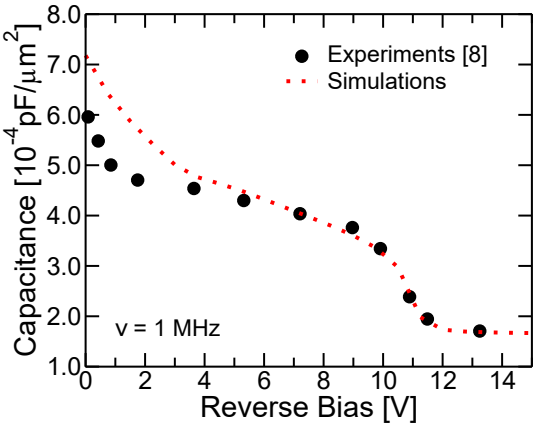

Figure 3.7: Comparison between simulated (dashed line) and experimental (circles) C-V characteristics at $\nu = 1$ MHz of the SAM-APD in [8] (Fig. 1.18a).

The EBHDM is then applied using as inputs the E_C and E_V profiles obtained from TCAD to compute $M(x)$ and $F(x)$. The employed model parameters are the ones listed in Tab. 3.1 for GaAs and $Al_{0.8}Ga_{0.2}As$. The gain and the excess noise factor are shown in Fig. 3.8. The breakdown voltage is slightly underestimated by the model, while the noise from the model is hardly comparable with the experiments in [25]. In such reference only the *FWHM* value is reported. Assuming that the only noise contribution comes from the multiplication noise of the APD, one extracts a $F \simeq 7$ almost constant over a range of gains up to 5 (no data available for higher gains). This suggests

that experiments (at such low gains) are mostly dominated by the noise of the read-out.

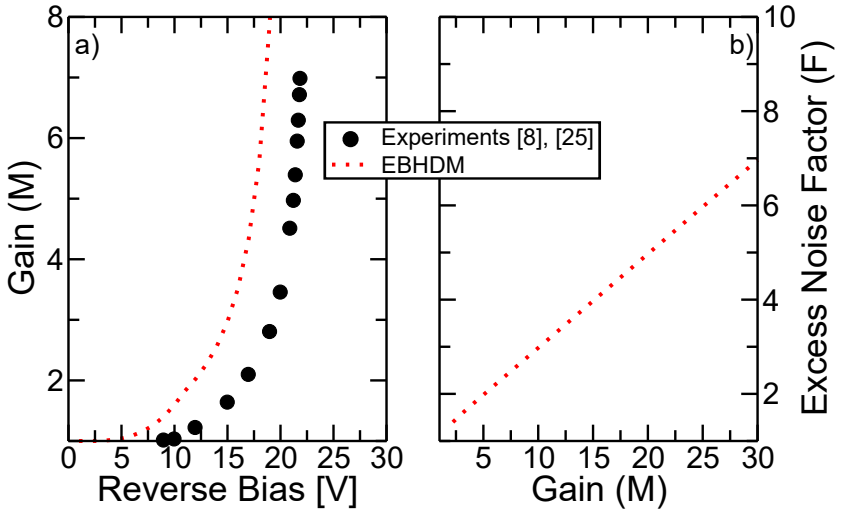

Figure 3.8: a) Simulated (dotted line) and measured (circles) gain versus voltage and b) excess noise factor versus gain for the SAM-APD reported in [8, 25].

3.4.2 GaAs/$Al_xGa_{1-x}As$ Staircase SAM-APD

The structure of the GaAs/$Al_xGa_{1-x}As$ staircase SAM-APD fabricated and measured in [7] is reported in Fig. 1.18b. We recall that the multiplication region of this device consists of twelve identical steps made of a 20 nm-thick graded $Al_xGa_{1-x}As$ layer (x from 0 to 0.45), a 25 nm-thick graded $Al_{0.45}Ga_{0.55}As$ layer and a 35 nm-thick GaAs layer. In principle, the conduction band discontinuities at the $Al_{0.45}Ga_{0.55}As$/GaAs heterojunctions should enhance the impact ionization probability of electrons w. r. t. the impact ionization probability of holes, improving the noise performance of the APD, as described in Section 1.4.

In the TCAD simulations [76], we reproduced the nominal structure, assuming abrupt doping profiles. A sample band structure profile is shown in Fig. 3.9a: we observe the conduction band steps, while the ones in the valence band are very small. Since the energy barriers seen by the electrons are quite thick (45 nm) and include a graded region, tunneling is not accounted for in our model.

Simulated C-V curves (from TCAD), obtained by using default values provided by the simulator [76] for the dielectric constant and the affinity of each material, are reported in Fig. 3.9b. The discrepancy between TCAD simulations and experiments in Fig. 3.9 suggests a possible out-diffusion of dopants from the substrate to the multiplication region [69].

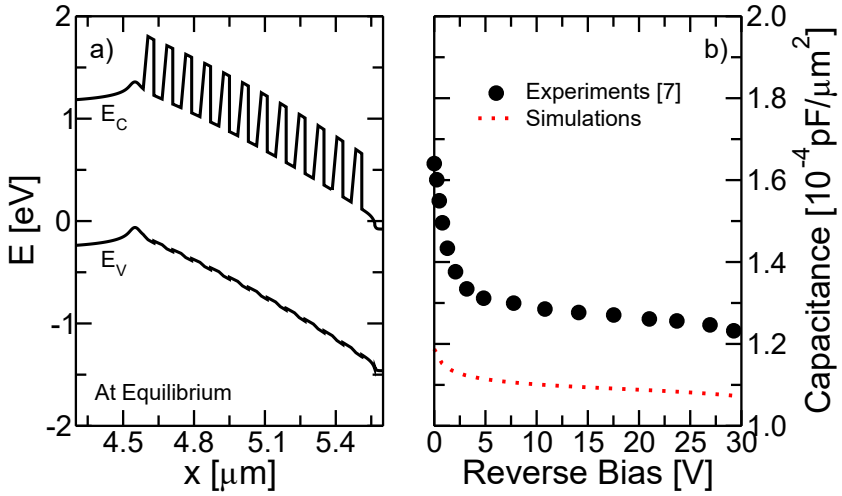

Figure 3.9: a) Band diagram at equilibrium of the multiplication region of the device in [7]. b) Comparison between simulated (dotted line) and experimental (circles) C-V characteristics of the staircase SAM-APD in [7] (Fig. 1.18b).

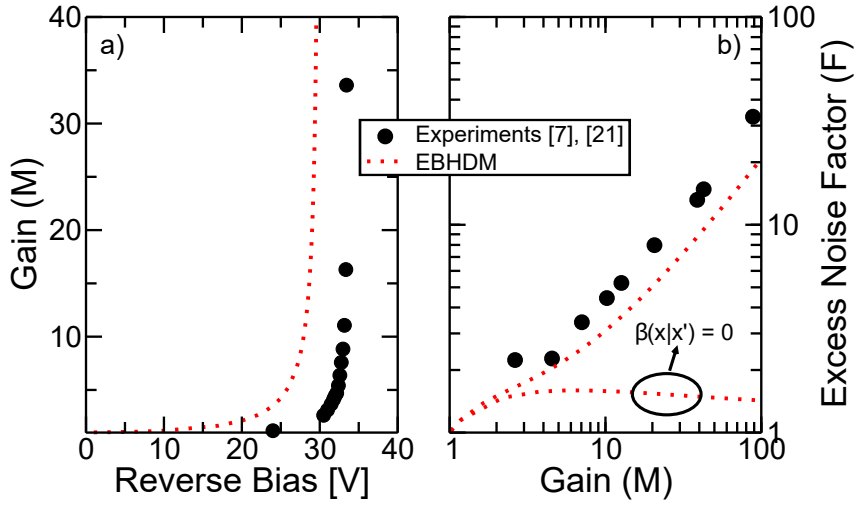

Figure 3.10: Simulated (dotted line) and measured (circles) a) gain versus voltage and b) excess noise factor versus gain for the staircase APD reported in [7]. Experimental results for plot b are taken from [21]. The structure in [21] slightly differs from the one in [7], but the EBHDM, with the model parameters of Tab. 3.1, gives the same $F(M)$ curve for both of these devices.

The EBHDM is applied using as inputs the E_C and E_V profiles obtained from drift-diffusion TCAD simulations activating the Thermionic Emission Current model for the transport at heterojunctions. The model parameters for an arbitrary mole fraction of Al in $Al_xGa_{1-x}As$ have been linearly interpolated from the ones reported in Tab. 3.1. The gain versus voltage and excess noise versus gain curve are shown in Fig.3.10a and b. The agreement between simulated and measured gain versus voltage is not perfect, while the trend of the excess noise versus gain is reproduced quite well.

The strong dependence of the gain on the applied voltage points out that at the electric fields necessary to trigger impact ionization, both carriers ionize also in the regions between consecutive steps and give an important contribution to the multiplication process, more than the energy steps alone, which are only 0.5 eV high [76]. The substantial role of hole's impact ionization on the results is demonstrated in Fig. 3.10b by the comparison of the measured and EBHDM results with the curves obtained with the EBHDM imposing $\beta(x|x') = 0 \ \forall x, x'$. When we turn off hole's impact ionization in the model, we have $F < 2$ also at high gains. These results confirm that low noise performance requires that the energy amplitude of the conduction band discontinuities must be larger than, or at least comparable to, the bandgap of the material where multiplication takes place [10].

3.5 Optimization of the Noise Performance of Single Carrier Avalanche Photodiodes

The detector performance in near infrared optical fiber communication links can be improved by fabricating device in InAs alloys, where α is inherently much larger than β [20] (see Fig. 3.6). A notable example of such a device is the Separate Absorption and Multiplication (SAM) single step staircase APD fabricated and measured in [10].

As reported in Section 1.4, the simple analytical formula in Eq. 1.10 derived in [13] can be used for the computation of the total excess noise factor in a staircase APD with N_{step} identical steps, under the assumption that multiplication is dominated by electron impact ionization (so that hole impact ionization can be neglected). A model accounting for hole's impact ionization due to the electric field *between the steps* has been proposed in [32] based on the theory in [81] and assuming that all the steps have the same amplitude in energy. A large electric field between the steps is needed in AlGaAs/GaAs systems where the conduction band discontinuity is in the order of 0.5 eV and the energy gap is larger than 1 eV [69]. On the other hand, in InAsSb structures [10], steps as large as 0.6 eV can be fabricated, that are more than twice the corresponding energy gap ($\approx$0.25 eV).

Here, we extend previous analyses by deriving a generalization of Eq. 1.10 (namely: Eq. 3.21) valid for single carrier multiplication staircase APDs with arbitrary step gains (M_i) and step excess noise (F_i). The expression is suited to compute the overall M_{TOT} and F_{TOT} and to optimize arbitrary ladders of non uniform layers. Using this generalized formula and accurate numerical models, it is found that for given gain, structures with non uniform energy steps can reduce the overall excess noise factor F_{TOT} if the steps with a large amplitude of the conduction band discontinuity lie ahead along the direction of carrier flow.

The new formula is derived in Section 3.5.1, while the numerical validation of the formula and results obtained with the EBHDM and the analytical expression are reported in Section 3.5.2.

3.5.1 Derivation of the Equation for the Excess Noise Factor

Let us consider, for the sake of simplicity, a two-steps staircase APD with total gain M_{TOT}. By definition the total excess noise factor is given by $F_{TOT} = \langle m_{TOT}^2 \rangle / \langle m_{TOT} \rangle^2$, where m_{TOT} is the random process that represents the multiplication and $\langle m_{TOT} \rangle = M_{TOT}$ is the ensemble average of m_{TOT}. The random process m_1 describes the multiplication of the first step while the random process m_2^k ($k = A, B, ...$ identifies electrons entering the second step) is associated to each electron coming from the first step and multiplying in the second step. We assume that the processes m_2^k are independent and identically distributed $\forall k$. If we use the notation $P_{i,j}$ to express the probability that $m_i = j$ we can write:

$$m_{TOT} = P_{1,1} m_2^A + P_{1,2}(m_2^A + m_2^B) + P_{1,3}(m_2^A + m_2^B + m_2^C) + ... \tag{3.16}$$

It is important to notice that we are considering also $P_{1,j}$ for $j > 2$ to take into account the fact the the first step can be a staircase structure itself and can multiply for more than a factor of 2.

From Eq. 3.16, since $\langle m_2^A \rangle = \langle m_2^B \rangle = ... = M_2$, one can derive:

$$\langle m_{TOT} \rangle = \langle m_2 \rangle \sum_{j=1}^{\infty} j P_{1,j} = \langle m_1 \rangle \langle m_2 \rangle = M_1 M_2 \tag{3.17}$$

It is now possible to compute $\langle m_{TOT}^2 \rangle$:

$$\begin{aligned} \langle m_{TOT}^2 \rangle &= P_{1,1}\langle m_2^2 \rangle + P_{1,2}(2\langle m_2^2 \rangle + 2M_2^2) + P_{1,3}(3\langle m_2^2 \rangle + 6M_2^2) + ... \\ &= \sum_{j=1}^{\infty} P_{1,j}[j\langle m_2^2 \rangle + (j^2 - j)M_2^2] \\ &= \langle m_2^2 \rangle \sum_{j=1}^{\infty} j P_{1,j} + M_2^2 \sum_{j=1}^{\infty} (j^2 - j) P_{1,j} \\ &= \langle m_2 \rangle M_1 + M_2^2(\langle m_1^2 \rangle - M_1) \\ &= \langle m_2^2 \rangle M_1 + M_2^2 \langle m_1^2 \rangle - M_2^2 M_1 \end{aligned} \tag{3.18}$$

Interestingly, Eq. 3.18 can be rewritten as:

$$\begin{aligned} \langle (m_{TOT} - M_{TOT})^2 \rangle = &\langle (m_2 - M_2)^2 \rangle M_1 \\ &+ \langle (m_1 - M_1)^2 \rangle M_2^2 \end{aligned} \tag{3.19}$$

which is consistent with Eq. 2.3 in [82] and with Eq. 38 in [32] for photomultiplier tubes. Equation 3.18 allows then to write the total excess noise factor as:

$$F_{TOT} = F_1 + \frac{F_2 - 1}{M_1} \tag{3.20}$$

The extension of Eq. 3.20 to the case of a N_{step}-steps staircase structure (see Fig. 3.11) is straightforward:

$$F_{TOT} = F_1 + \sum_{i=2}^{N_{step}} \frac{F_i - 1}{\prod_{k=1}^{i-1} M_k} \tag{3.21}$$

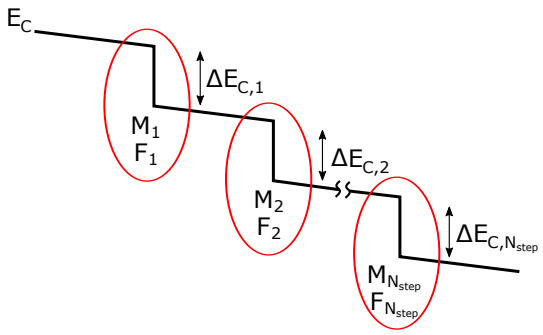

Figure 3.11: Conduction band profile of a staircase structure with N_{step} steps. M_i and F_i are the gain and excess noise factor of each step.

It is easy to show that Eq. 3.21 gives the same result of Eq. 1.10 when all the steps have gain $M_i = 1 + P_e$ and excess noise factor $F_i = 1 + (1 - P_e)\,[1 - (1 + P_e)^{-1}]\,1 + P_e$ as per Eq. 1.10, where P_e is the electron's impact ionization probability at each step. However, differently from Eq. 1.10, Eq. 3.21 is valid also in structures with an arbitrary sequence of decreasing steps and thus useful to optimize arbitrary staircase APDs.

Similarly to the well known Friis formula for the noise figure of cascaded amplifiers [83], Eq. 3.21 tells us that the gain of the first step has a critical role in achieving low noise. The first step must have high gain and low excess noise, two conditions that can be achieved only with large band offsets, as it will be seen in Section 3.5.2.

It is worth noting that Eq. 3.21 keeps its validity also in the more general case where M_1 and F_1 represent the e-h pair generation due to an incoming high-energy photon (e. g. a X-ray) provided that we interpret M_1 as the average number of e-h pairs per photon and $F_1 = 1 + f/M_1$ where f is the so called Fano factor [6]. Under these circumstances, Eq. 3.21 is equivalent to the expression σ_S^2/E_{ehp}^2 in Eq. 1.22 (derived in [6]) for the excess noise of APDs used for X-ray detection.

Compared to existing numerical expressions, Eq. 3.21 can be used as an effective tool to combine simulations of single steps and eventually find the optimum sequence of steps for maximum gain and low noise, as we will see in Section 3.5.2.

3.5.2 Numerical Validation with the EBHDM

Eq. 3.21 must be coupled to an impact ionization model for each step in the ladder suited to compute the gains M_i accurately. To this end we use the nonlocal history dependent model of [69].

Our target is to calibrate the EBHDM on the experiments in [10] for a single step AlInAsSb/InAsSb APD where multiplication takes place in the $InAs_{0.91}Sb_{0.09}$ layer. To this end we start with InAs impact ionization parameters and then adjust them for the small Sb fraction of the multiplication layer.

Having calibrated the model on InAs (Fig. 3.6 in Section 3.3), we can move

to the device of [10], that is a SAM APD made of a 500-nm i-$Al_{0.7}In_{0.3}As_{0.31}Sb_{0.69}$ absorption region followed by a single step multiplication region. The step of the staircase is composed by a 37-nm graded i-$Al_xIn_{1-x}As_ySb_{1-y}$, a 6-nm i-$InAs_{0.91}Sb_{0.09}$ and a 61-nm graded i-$Al_xIn_{1-x}As_ySb_{1-y}$ layers. The diode structure and the band-diagram are reported in Fig. 3.12.

Since multiplication takes place in the $InAs_{0.91}Sb_{0.09}$ film, whose energy gap is 0.25 eV in contrast to the 0.35 eV of InAs [60], the parameter E_{ce} was scaled accordingly by a factor of $0.35/0.25 = 1.4$, following the simple picture that the impact ionization rate depends exponentially on the energy gap of the material. The parameter A_e, instead, has been adjusted to match the measured gain and excess noise at low applied voltage in [10], see Fig. 3.13. Compared to InAs, A_e has been increased by a factor of 6.5.

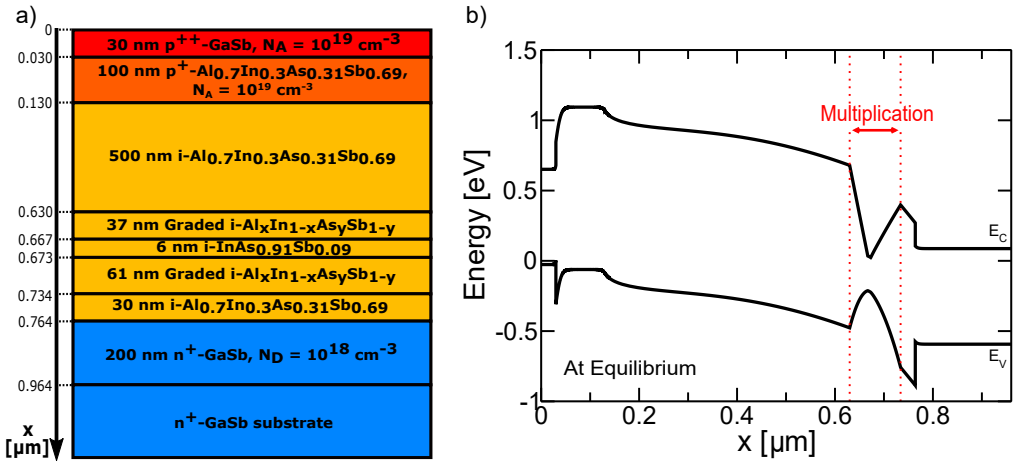

Figure 3.12: a) Sketch and b) band diagram at equilibrium extracted from TCAD simulations [76] of the staircase SAM-APD reported in [10], along the vertical direction.

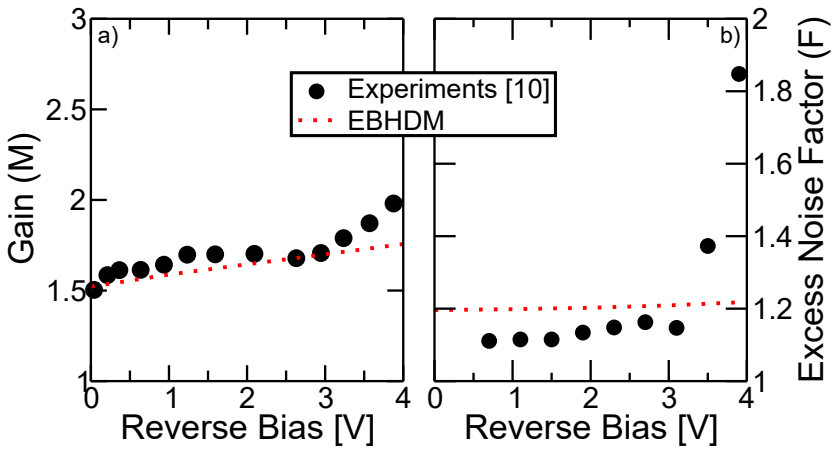

Figure 3.13: a) Gain versus applied voltage and b) excess noise factor versus applied voltage for the staircase SAM-APD reported in [10]. Experimental results from [10] (circles) are compared with the EBHDM (dotted line).

The deviation of the simulation results from experiments visible in Fig. 3.13 for reverse bias higher than 3.0 V is, in fact, due to considering only electron impact ionization in the $InAs_{0.91}Sb_{0.09}$ multiplication layer.

We now use the EBHDM calibrated on $InAs_{0.91}Sb_{0.09}$ to verify the validity of Eq. 3.21. We begin our analysis by simulating single steps with conduction band discontinuities of different amplitude (ΔE_C). In all simulations, we assume that the applied bias is the one that induces the electric field that perfectly compensates the quasi-field due to material grading between the steps, so that the conduction band energy is piecewise constant. As it can be seen in Fig. 3.14, owing to the small gap of the multiplication region, ΔE_C values below 1 eV provide gains that tend to 2. We also see that the relation between the simulated gain and excess noise factor closely matches Eq.1.10 (for $N_{step} = 1$ since we consider only one step here). Note that the local impact ionization model with electron ionization only would provide $F = 2 - 1/M$ (Eq. 2.19 for $k \to 0$), that tends to 2 for large gains instead of the bell shape shown in Fig. 3.14 using the EBHDM. When we have steps with an electric field in between, the $F(M)$ curve obtained using the EBHDM [69], lies between the results obtained using Eq. 1.10 and the ones obtained using the Local Model in Fig. 3.14. This indicates that, regardless of the conduction band profile (strongly nonlocal as in a staircase or as uniform as possible as assumed by local models), if hole impact ionization is negligible, the room for optimization is limited in the $F = 1$ to $F = 2$ range. In Fig. 3.14, the same experimental data from [10], is reported too. We observe that measured values lie very close to the predictions of Eq. 1.10 except for high biases when hole impact ionization comes into play.

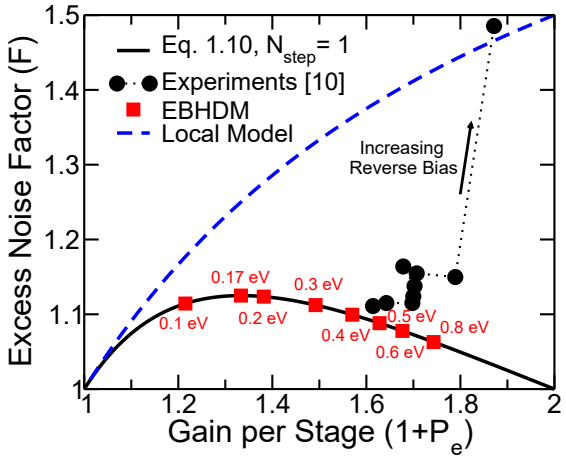

Figure 3.14: Comparison between the excess noise factor versus gain curves predicted by Eq. 1.10 for $N_{step} = 1$ (solid line), by the EBHDM (squares) and by the Local Model (blue dashed line) for single step staircase structures with different amplitude of the conduction band discontinuity. Experimental data from [10] are also reported (circles).

We have then considered staircase structures with different sequences of steps and compared the EBHDM with Eq. 3.21. The results, reported in

Tab. 3.2, demonstrate a very good agreement with Eq. 3.21, with errors well below 1%.

We also see that for a given gain, it is advantageous to locate first the steps with the largest ΔE_C. In fact, consistently with Eq. 3.21, the noise added by each step is divided by the gain of the preceding steps. Since the order of the steps has no effect on the gain, the sequence can be optimized to minimize F. However, due to the small range of F values covered by individual abrupt steps (Fig. 3.14), the reduction of F offered by optimized ordering of the steps is limited, unless the number of steps and the difference among them is large (last two rows of Tab. 3.2).

$\mathbf{N_{step}}$	$\mathbf{\Delta E_C}$ [eV]	M	F	F (Eq.3.21)	% error
5	0.6 (uniform)	13.20	1.179	1.178	0.085
2	0.17, 0.6	2.25	1.180	1.183	0.254
2	0.6, 0.17	2.25	1.150	1.153	0.261
5	0.2, 0.3, 0.4, 0.5, 0.6	8.85	1.293	1.295	0.155
5	0.6, 0.5, 0.4, 0.3, 0.2	8.85	1.211	1.212	0.083
5	0.2, 0.2, 0.2, 0.2, 0.6	6.14	1.342	1.344	0.149
5	0.2, 0.2, 0.6, 0.2, 0.2	6.14	1.317	1.319	0.152
5	0.6, 0.2, 0.2, 0.2, 0.2	6.14	1.268	1.270	0.157
10	5×0.17 and 5×0.6	57.23	1.415	1.420	0.353
10	5×0.6 and 5×0.17	57.23	1.207	1.209	0.166

Table 3.2: Comparison between the excess noise factor obtained with the EBHDM and the one calculated using Eq. 3.21 for staircase structures with different number of steps and conduction band discontinuities with different amplitudes.

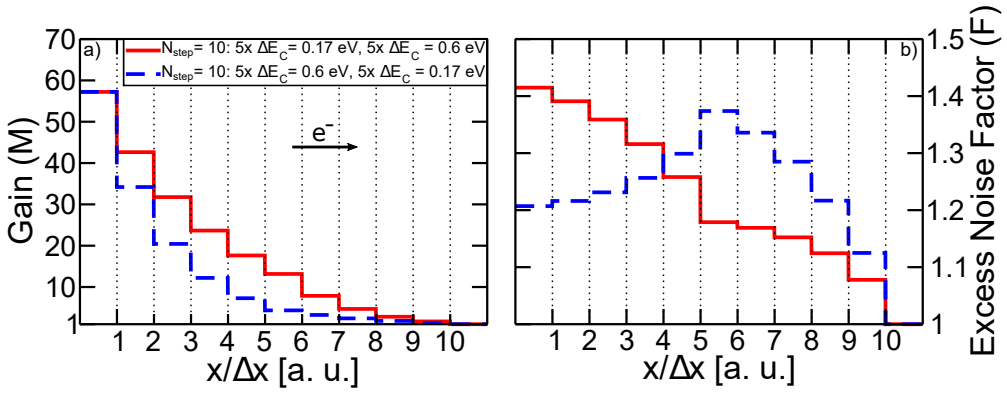

Figure 3.15: Gain (a) and excess noise factor (b) as a function of the normalized position $x/\Delta x$ (Δx being the step's length) at which an electron is generated for two staircase structures with ten steps. Solid red line: five steps with $\Delta E_C = 0.17$ eV are followed by five steps with $\Delta E_C = 0.6$ eV. Dashed blue line: five steps with $\Delta E_C = 0.6$ eV are followed by five steps with $\Delta E_C = 0.17$ eV.

To visualize how the excess noise and gain build up along the structure, we plot $M(x)$ and $F(x)$ in Fig. 3.15 as a function of the position where the initial

carrier is generated. We consider the two cases with identical gain $M = 57.23$ in the last two rows of Tab. 3.2. As expected, the gain decreases moving inside the staircase, i. e. when electrons are generated inside the structures, since one loses the gain associated to the previous steps. As for the excess noise, the spatial distribution changes remarkably with the ordering of the steps. If the steps with larger ΔE_C come first, the excess noise increases while moving inside the multiplication region, since the high noise of the last stages gets divided by a gain which gets lower and lower; thus we do not take advantage of the high gain provided by the initial steps.

3.6 Optimization of the Noise Performance of GaAs/Al_xGa_{1-x}As Staircase APDs for X-Ray Detection

In this Section we report on the optimization of the excess noise factor of GaAs/Al_xGa_{1-x}As Staircase APDs for X-Ray Detection. The results that we present are obtained with the EBHDM described in Section 3.1. Results for staircase structures are compared with experimental data for p-i-n and Multi-Quantum-Well (MQW) APDs. Note that MQW APDs have always abrupt heterojunctions between a low (E_{G1}) and a high (E_{G2}) bandgap material [84, 85], while in staircase APDs each stage is linearly graded from E_{G1} to E_{G2} and the abrupt discontinuity is only between E_{G2} and E_{G1} [13].

As shown in Section 3.3, the EBHDM reproduces a variety of experimental data for APDs with different material and architectures. As a relevant example, Fig. 3.16 reports with filled circles the $F(M)$ curve for a GaAs p-i-n diode [23]: we see that $F \approx 0.75M$, which results in high noise at large M values. This, as stated in Section 1.3, is a consequence of similar electron and hole impact ionization coefficients ($\alpha \simeq \beta$) in GaAs (as well as in many other III-V compounds).

For the staircase APDs in the GaAs/Al_xGa_{1-x}As system in [22], the measured $F(M)$ curves for the devices with mesa diameters of 200 μm and 600 μm are reported in Fig. 3.16. The $F(M)$ curve for the APD with diameter 200 μm is in agreement with the experimental results for the GaAs/AlGaAs MQW APD with 25 steps in [84]: the noise is much lower than for the p-i-n diode and its behavior is predicted also by the EBHDM (that is calibrated on p-i-n diodes without additional model parameter changes when considering staircase structures). The $F(M)$ curve for the device with diameter 600 μm, instead, lies very close to the results reported in [85] for a GaAs/Al_xGa_{1-x}As MWQ APD with 15 steps and to the experimental results for the GaAs p-i-n diode [23]. Concerning the difference between the results for the devices in [22], we think that the architecture with a bigger mesa area may show additional noise sources other than multiplication noise. However, the experimental $F(M)$ curve for the GaAs/Al_xGa_{1-x}As staircase APD of [21], that is similar to the one of [22], indicates that the use of staircase APDs is beneficial in terms of excess noise factor at a given gain w.r.t. p-i-n diodes. In other words, our

nonlocal model (calibrated on GaAs p-i-n diodes, see Fig. 3.2 and Tab. 3.1) seems to support the experiments in [84] as well as the noise measured in [22] for the device with a smaller diameter.

It is important to note that the use of Eq. 1.10 (blue line), using $P_e = M^{1/N_{step}} - 1$, predicts an even lower noise. This can be explained considering that in the GaAs/Al_xGa_{1-x}As system the conduction band energy step is small compared to the bandgap of the material where impact ionization takes place (see the band diagram in Fig. 3.10a). This requires large applied biases to increase the gain, but, due to the large induced electric field, significant electron and hole multiplication takes place between the steps. We thus believe that hole impact ionization between consecutive steps is responsible for the large difference between the experiments (and the EBHDM) and the predictions of Eq. 1.10 which neglects hole impact ionization.

Before continuing, it is worth mentioning that in the EBHDM the sole effect of the heterojunction is to add energy steps equal to the difference in affinity between the materials. Phenomena related to momentum conservation or to disorder at the interface are not included. In practice, in the model the heterojunction provides energy to the carriers over a short distance, making impact ionization more localized and thus with a reduced associated excess noise.

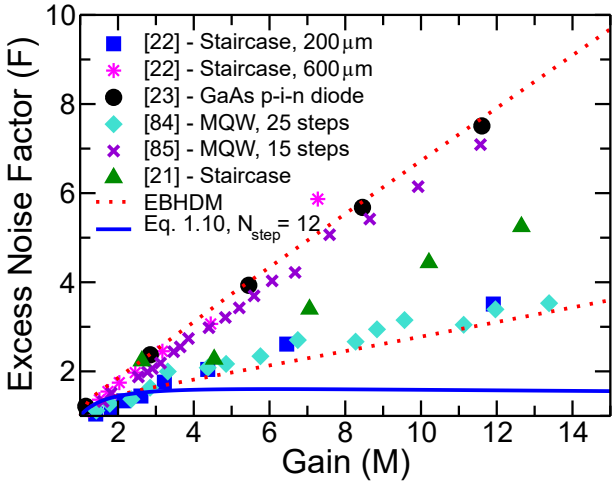

Figure 3.16: Excess noise factor as a function of the gain for different GaAs/AlGaAs APDs: experimental data for a thick ($d = 1.6\ \mu m$) GaAs p-i-n diode from [23] (•), staircase APDs fabricated by our group [22] (■, ⁕ for the 200 μm and the 600 μm mesa diameters, respectively), a MQW APD with 25 steps [84] (⧫), a MQW APD with 15 steps [85] (x) and for the staircase APD of [21] (▲). The dotted lines represent the results obtained with the EBHDM model (same calibration for both devices), while the solid line is Eq. 1.10 [13] (for $N_{step} = 12$ steps).

Experimental and modeling results in Fig. 3.16 point out that staircase structures in GaAs/Al_xGa_{1-x}As perform much better than GaAs p-i-n diodes in terms of noise at given gain. However the excess noise factor is far from what

is expected from Eq. 1.10, the reason being hole impact ionization between the steps due to the large applied electric field, which in turn is necessary to increase the gain because the amplitude of the conduction band discontinuity is small if compared to the bandgap of GaAs. In this section we analyze whether increasing the number of steps lowers the excess noise factor at a given gain.

3.6.1 EBHDM results for different number of steps

We have considered the device structure in Fig. 1.18b, for different values of the number of steps in the multiplication region. Figure 3.17 shows that the excess noise factor for given gain is reduced when the number of steps is increased. Furthermore, by increasing the number of steps we achieve high gain over a larger voltage interval, which in turn makes the external biasing of the device much simpler than in the case with few steps, where high gain can be attained only by biasing the device close to breakdown that is, at the edge of the intended linear regime of operation. Of course, with large number of steps high bias voltages are necessary to obtain high gains, but those voltages do not require a very precise setting as with a small number of steps.

The trend in Fig. 3.17 can be explained by considering that the large number of steps enhances the intrinsic gain that can be achieved without applying an additional electric field. So, for given gain, a structure with more steps entails a lower electric field, as can be seen in Fig. 3.18.

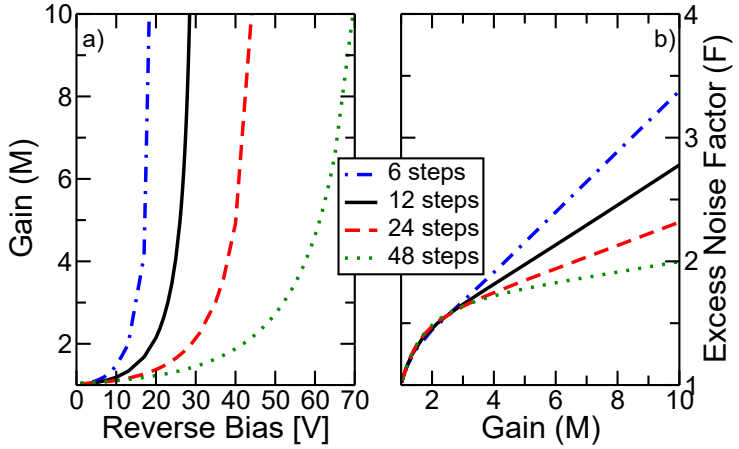

Figure 3.17: a) Simulated (EBHDM) gain as a function of the applied bias and b) excess noise factor as a function of gain for a staircase APD like the one in Fig. 1.18b with $N_{step} = 6, 12, 24, 48$ multiplication steps.

A quantitative interpretation of the results in Fig. 3.17, requires models that go beyond Eq. 1.10 and include hole impact ionization, as described in the next subsection.

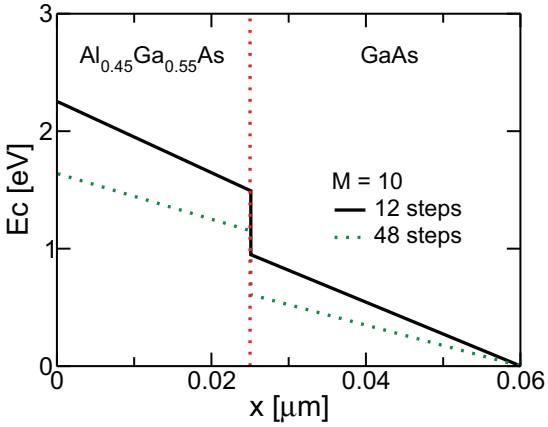

Figure 3.18: Conduction band profile of a 0.55 eV single multiplication step (as for the $Al_{0.45}Ga_{0.55}As$/GaAs [76]) at fixed total gain ($M = 10$) for staircase APDs with 12 (solid line) and 48 steps (dashed line).

3.6.2 Interpretation based on the Electron and Hole Ionization Probabilities per Step

Analytic expressions to compute the overall gain and excess noise factor in staircase APDs when *both* electrons and holes ionize have been proposed in [32] and have been already discussed in Section 2.1.1 (Eqs. 2.20 and 2.21). Here, we recall that P_e and P_h are the electron's and hole's ionization probabilities per step, respectively, and $k_p = P_h/P_e$. Equations 2.20 and 2.21 are valid in the low gain limit of the linear regime, when electron and hole impact ionization events at a single step can be treated separately, as if the two mechanisms were independent. Although this may be correct if impact ionization is localized at the steps, the accuracy is limited when impact ionization events are spread out between the steps.

We have extracted P_e and P_h by simulating electron and hole impact ionization in single or double step structures that include the region with electric field between the steps. In particular, P_e is computed from the gain M obtained simulating a single step structure that includes the step and the electric field region just after the step (up to the next step), by activating only electron impact ionization and writing $P_e = M - 1$ (Fig. 3.19a). Figure 3.19b shows that, when a staircase structure with $N_{step} = 2$ is considered, $\alpha(0|x')$ is the same if we consider an ionization point x' in the first step or the corresponding x' in the second step. To calculate P_h two steps (and not only one) should necessarily be included in the simulation domain, because the distance that holes have to travel in order for the impact ionization coefficient to be in equilibrium with the electric field is larger than the thickness of a single step (see Fig. 3.19c). This interpretation is supported by Fig. 3.19d, in fact we notice that, when we simulate a staircase structure with three steps and we assume the injection of a hole at $x = W$, $\beta(W|x')$ for a point x' belonging to the second step is the same as the one for the corresponding x' in the third step, while it is lower for a point x' in the first step. We then compute P_h using an

expression similar to Eq. 2.22, namely

$$P_h = exp\left(\int_{x_0-L}^{x_0} \beta(x_0|x')dx'\right) \tag{3.22}$$

where $L = d/N_{step}$ is the length of one multiplication step and only hole impact ionization is active in the simulation.

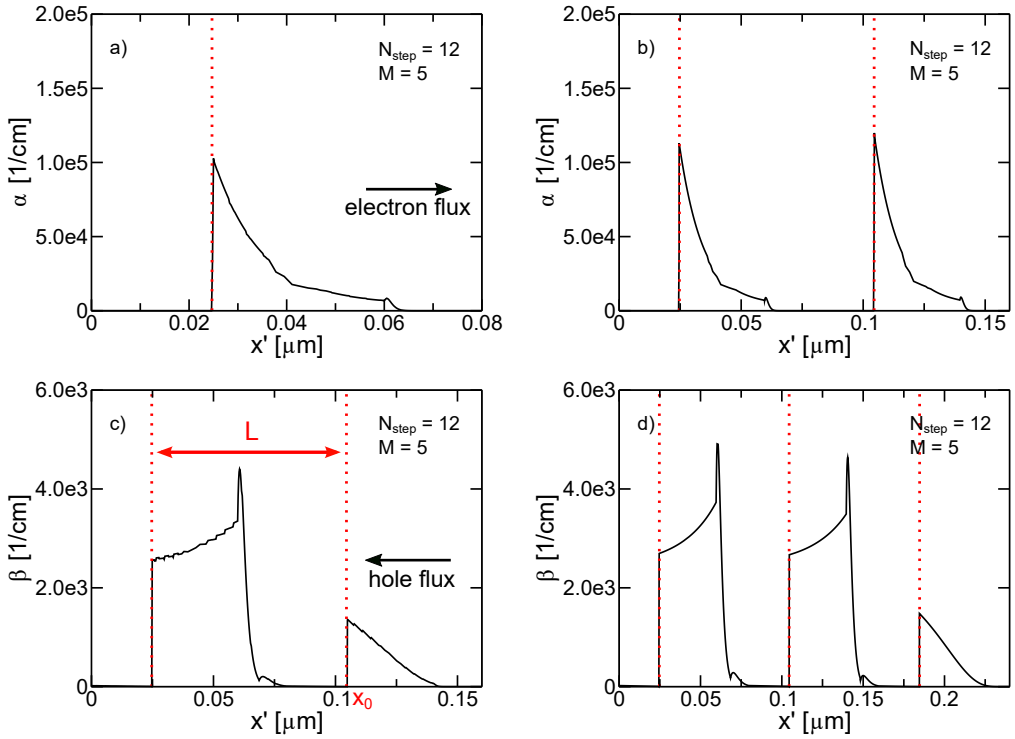

Figure 3.19: a), b) Electron's impact ionization coefficient $\alpha(0|x')$ and c), d) hole's impact ionization coefficient $\beta(d|x')$ as a function of the ionization point x' in one (a), two (b)(c) or three (d) steps of a GaAs/Al_xGa_{1-x}As staircase APD ($N_{step} = 12$, $M = 5$). $x = d$ is the right-most point of the multiplication region. The location of conduction and valence band discontinuities is highlighted by red dashed lines.

Figure 3.20a reports the P_e and P_h obtained with this procedure. P_e and P_h are plotted as a function of N_{step} for different gains, which means that for each N_{step} the electric field between the steps is set to achieve the desired gain in the complete N_{step}-step structure. If we increase the number of steps, the same gain is achieved with a lower electric field between the steps. Thus, both P_e and P_h in Fig. 3.20a decrease when increasing N_{step}. The effect of the reduction of the applied field is much larger on P_h than on P_e (at $M = 10$, from $N_{step} = 6$ to $N_{step} = 48$, P_h is reduced by 98.5%, while P_e is reduced by 80%), since electrons also feel multiplication by the conduction band steps, whereas valence band discontinuities are negligible. As a result $k_p = P_h/P_e$ tends to zero for increasing N_{step} (Fig. 3.20b), leading to a structure essentially dominated by electron impact ionization.

Figure 3.21 compares the EBHDM results of Fig. 3.17 with the results of Eqs. 2.20 and 2.21 using the P_e and P_h values in Fig. 3.20. The mutual agreement is quite good for N_{step}=24 and N_{step}=48, while Eq. 2.21 loses accuracy for a smaller number of steps. In fact, at given gain P_e and P_h are large when N_{step} is small; thus the assumption behind Eqs. 2.20, 2.21 that electron and hole ionization can be treated as independent events becomes less justified. In conclusion, the comparison of the EBHDM and Eqs. 2.20 and 2.21 confirms that the main advantage of using a large number of steps is to reduce the electric field necessary to obtain a given gain, thus reducing hole impact ionization between the steps.

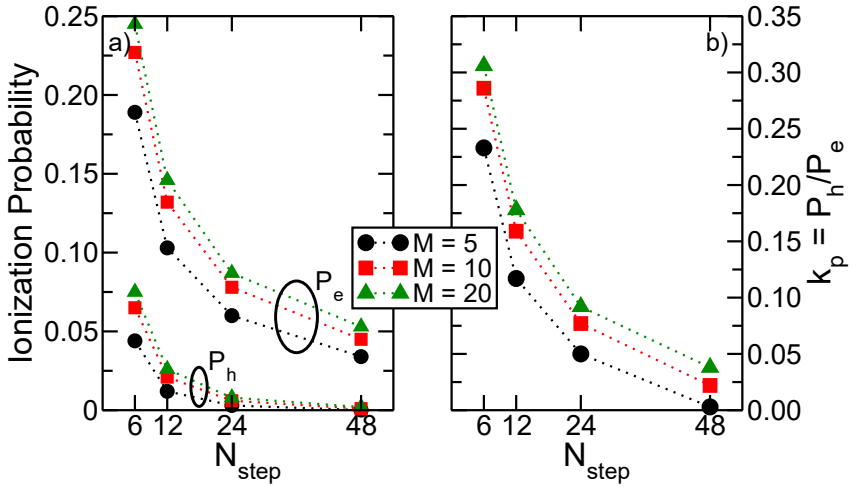

Figure 3.20: Simulated (EBHDM) a) electron's and hole's ionization probabilities and b) ionization ratio $k_p = P_h/P_e$ as a function of the number of steps at given gain $M = 5, 10, 20$.

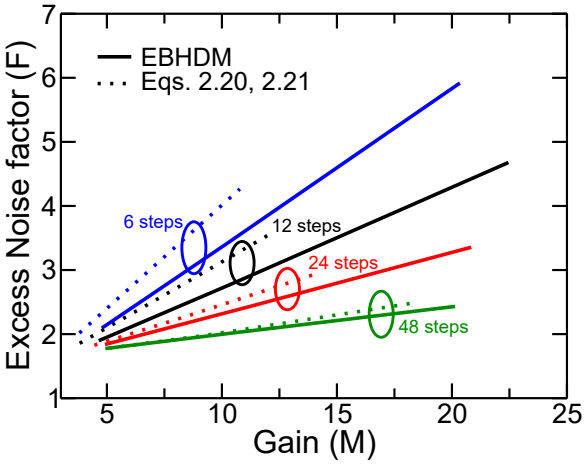

Figure 3.21: Comparison of the excess noise factor as a function of the gain computed by using the EBHDM (solid lines) or by using Eqs. 2.20 and 2.21 with the P_e and P_h from Fig. 3.20a (dashed lines) for a staircase APD like the one in Fig. 1.18 with $N_{step} = 6, 12, 24, 48$ multiplication steps.

3.7 Summary

We have proposed a nonlocal history dependent model (EBHDM) for impact ionization suitable for (but not limited to) APDs with staircase structure in Sections 3.1-3.4. The ionization coefficients for electrons and holes are related to effective field profiles obtained from a first order energy balance equation rather than resorting to the definition of a dead space. This renders the model robust in the presence of abrupt heterojunctions. For a given material, eight parameters are needed. The model has been calibrated against literature experimental data for gain and noise in p-i-n diodes and then applied to more complex APDs based on heterojunctions between III-V compounds. It is found that hole impact ionization still plays a substantial role in these devices and degrades the noise performance.

In Section 3.5 we have derived a simple formula (Eq. 3.21) for the excess noise in staircase APDs with single carrier multiplication that extends the original model in [13] to the case of steps with different amplitude. The results allow technologists to optimize staircase APDs for best F at given M, without need for more computationally demanding numerical models, such as Monte Carlo or history dependent models.

The formula suggests that, for minimum excess noise, larger conduction band steps should come before the small ones along the carrier path, this is consistent with the analysis for photomultiplier tubes reported in [32]. The formula for the excess noise has been validated by numerical simulations using the nonlocal history dependent model for impact ionization of Sections 3.1-3.4. Although we considered here only cases where the effect of the electric field between the steps is negligible, the proposed formula could in principle be used also when this field is not null: essentially the region between two steps has its own gain and excess noise that can be combined with the gain and noise of the steps with Eq. 1.10.

The main limitation of the proposed formula is that it is valid only when hole impact ionization is negligible. However, we would like to point out that the effects of hole impact ionization become relevant when the conduction band discontinuities do not provide electrons with sufficient energy to ionize, as for example in the AlGaAs/GaAs system [69]. When this happens, multiplication in the regions between the steps tends to have similar impact as the one at the steps. In these conditions, the use of different sequences of steps with different amplitudes would likely have less effect on the overall gain and excess noise. Hence, one should either use the Eq. 2.21 to fit experimental data (as in [24]), or should resort to fully numerical models.

in Section 3.6 we have used the EBHDM to study how the gain and the excess noise factor of the staircase SAM-APD of Fig. 1.18b are affected by the number of steps of the multiplication region. The model points out that increasing the number of conduction band steps in these staircase structures reduces the noise at fixed gain, because a lower electric field between the steps (and thus lower hole impact ionization) is required for a given gain. Increasing the value of N_{step} comes at the expense of a longer response time but, as it

will be discussed in Section 4.4.1, for X-ray detection the time constant of the CR-RC shaping circuit (see Section 1.6) is order of magnitudes larger than the duration of the current waveform at the output of the APD, so that changing the value of N_{step} does not affect the duration of the current waveform at the output of the shaping filter.

Chapter 4

The Improved Random Path Length Algorithm

In this Chapter, an improved Random Path Length algorithm (see Section 2.2.4) for the computation of the gain, the excess noise factor and the time response of Avalanche Photodiodes will be presented. Differently from the one presented in [43, 79], the proposed algorithm takes into account both the drift and the diffusion of carriers inside the device and it can be coupled to any nonlocal history dependent impact ionization model. It is thus particularly suited for the simulation of staircase Separate Absorption and Multiplication APDs. The results that will be shown in the following are an extension of the ones published by the author of this thesis in [86, 87].

4.1 Time Response, Bandwidth and Jitter

The usefulness of the Random Path Length algorithm (RPL) for the determination of the gain, the excess noise factor and the time response of Avalanche Photodiodes biased in the Linear regime has already been discussed in Section 2.2.4. In particular, by simulating N_{ev} independent photon-induced generation events (also called *trials*) and mimicking the motion of carriers, at constant velocity, inside the multiplication region of APDs, we can compute M and F by using Eqs. 2.75 and 2.76, but also, thanks to Ramo's theorem [34], the current waveforms associated to carriers' multiplication ($i(t)$, Eq. 2.77) From the Fourier transform of $i(t)$ it is also possible to compute the bandwidth of the APD, by employing the procedure described in Fig. 1.6.

In time of flight applications used for X-ray detection, however, it is important not only to evaluate the average response time, but also the *jitter*, that is defined as the statistical fluctuation of the time interval between the arrival of a photon and the output pulse leading edge [88] (see Section 1.3.1). The jitter results from the stochasticity of carrier multiplication (i. e. at a given bias voltage different carriers can experience different gains [1]) and randomness of processes such as carrier photogeneration and diffusion. Although both analytical [89] and numerical [90] models of jitter have been extensively proposed in the past for Silicon single photon avalanche diodes working in

Geiger mode (Silicon photomultipliers), similar models for APDs working in the linear regime have not been developed to our knowledge.

4.2 Target Application: Staircase SAM-APD for X-ray Detection

In the following we will focus on the dynamic performance (in terms of response time, bandwidth and jitter) of APDs fabricated in high atomic number III-V compound semiconductors and working in the Linear regime. In fact, as stated in Section 1.3, using semiconductors with large atomic number allows to detect photons at energies higher than the ones detectable with Silicon devices, while the self-quenched avalanche of the linear regime provides amplification without an excessively long response time [21].

This simulation study particularly aims at the state of the art GaAs/AlGaAs avalanche photodiodes with separate absorption and multiplication regions (SAM-APD) of Fig. 1.18b, intended for X-ray spectroscopy. The proposed model, however, is quite general and applicable to any SAM-APD, not necessarily fabricated with III-V compound semiconductors. The electric field is confined inside the intrinsic multiplication region where impact ionization occurs (that can be fabricated either with a single material or with a staircase structure) and is separated from the absorption region by a p-doped δ-layer (see Fig. 4.1). The doping profile of the device under study, that features a staircase multiplication region with twelve GaAs/$Al_xGa_{1-x}As$ steps [7, 21, 22], is reported in Fig. 4.1.

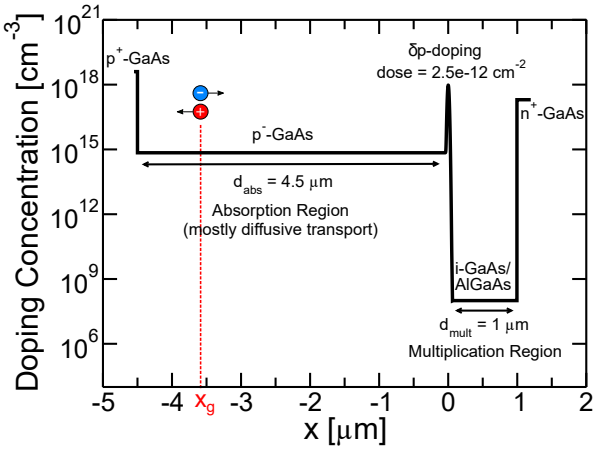

Figure 4.1: Doping profile of the SAM-APD of Fig. 1.18b. The absorption region (thickness $d = d_{abs}$) is separated from the multiplication region ($d = d_{mult}$) by a p-doped δ-layer. The staircase multiplication region of this device features twelve AlGaAs/GaAs steps. In simulations, electron-hole pairs are generated at various x_g points inside the device.

In a SAM-APD like the one in Figs. 1.18b, 4.1, several sources contribute to the jitter: the randomness of the spatial position where electron-hole pairs are

generated (x_g), the number of generated electron-hole pairs per photon, the diffusive transport inside the absorption region and the stochastic nature of electron-hole pairs generation by impact ionization events in the multiplication region.

Since the RPL algorithm mimics the motion of each carrier inside the APD depletion region and, differently from the other model implementations that provide static average quantites, it straightforwardly yields the APD time response to a single photon arrival [79, 86], it allows to study the time response fluctuations and, thus, to extract also the timing jitter. An extension of the original RPL algorithm [43, 79] is necessary, however, to study complex structures: carriers' drift and diffusion in quasi-neutral regions such as the absorption region of SAM-APDs have to be taken into account and, in the case of staircase APDs, the Energy Balance History Dependent Model described in Chapter 3 has to be used to describe impact ionization, instead of the Dead Space model employed in Section 2.2.4.

4.3 Model

The RPL algorithm translates the motion of the carriers into an electric current waveform induced at the terminals. As such, it takes into account the stochastic nature of the diffusive motion in the absorption region and the impact ionization in the multiplication region.

We have assumed a large area device so that edge effects are negligible, and a one-dimensional analysis is sufficient to represent accurately the physical system. We have also assumed that, due to their low number, the photogenerated carriers have a negligible impact on the device electrostatics, so that a fully self-consistent solution of the generation and transport processes is not necessary. Accordingly, the (frozen) electric field is computed with enough accuracy by a drift diffusion or hydrodynamic TCAD model in the absence of photon generation [76]. The ingredients of the model, namely drift and diffusion in the absorption region, drift and impact ionization in the multiplication region and current induced at the terminals are described in details in the following sections.

4.3.1 Carrier Transport in the Absorption Region

The carrier motion in the absorption region have been described by means of a single particle parabolic bands Monte Carlo procedure[1]. A photon generates N electron-hole pairs (where N is an input of our model) with zero velocity and kinetic energy at the location where it is absorbed. These pairs move in a sequence of free flights and scattering events. The free flights have velocity

[1]A multi-valley Monte Carlo procedure that includes non-parabolicity corrections would me more accurate for III-V compound semiconductors. Here, instead, we used a simplified model that allows us to reproduce the mobility extracted with the TCAD simulator.

$v(x)$ and acceleration

$$a(x) = \frac{dv}{dt}(x) = \mp\frac{qE(x)}{m_{eff}}, \tag{4.1}$$

where $E(x)$ is the electric field at position x and m_{eff} is the effective mass of the carrier. They are randomly interrupted by scattering events. The average time that separates two consecutive scattering events is chosen according to the mobility $\mu(x)$, namely

$$\tau_s(x) = \frac{\mu(x) m_{eff}}{q} \tag{4.2}$$

The duration of a free flight starting at position x is then generated according to the standard Monte Carlo method as $t_f(x) = -\tau_s(x) log(r)$ [45], where r is a random number uniformly distributed in the $[0, 1]$ interval. To avoid the repeated lengthy and time consuming exact calculation of the after-scattering state, after a scattering event the carrier velocity is randomized (in magnitude and direction) according to a normal distribution with zero mean and standard deviation equal to a thermal velocity $v_{th} = \sqrt{k_b T/m_{eff}}$, consistently with diffusive transport and the assumption of parabolic bands. Moreover, the duration of each free flight is chosen such that carriers do not travel over distances where steep variations of the electric field occur in the absorption region[2]. If that happens, the free flight is interrupted at a location that satisfies this requirement, a new t_f is computed, but no scattering event occurs, so that the carrier starts the new free flight with the final velocity of the previous one.

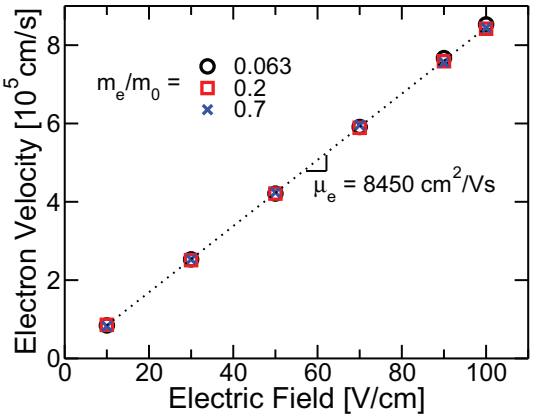

Figure 4.2: Electron's drift velocity in GaAs as a function of the applied electric field for different values of the effective mass m_e, extracted from the RPL algorithm by using the description of carriers' motion reported in Section 4.3.1. The mobility (the slope of the $v(E)$ curve) is insensitive to the choice of m_e, thus $\mu_e = 8450$ cm^2/Vs in all cases, that is the value inserted in Eq. 4.2 to find τ_s when producing the points in this figure.

[2]In our simulations, the maximum variation of electric field that a carrier can experience has been empirically chosen as the 0.1% of the difference between the maximum and the minimum electric field in the absorption region of the APD.

The mobility and the electric field profiles, $\mu(x)$ and $E(x)$ have been extracted from DC analyses with a TCAD software [76], therefore $\mu(x)$ accounts for all scattering mechanisms that were included in the TCAD simulations. The effective masses for electron and hole transport in GaAs are $m_e = 0.063m_0$ and $m_h = 0.51m_0$, respectively [91], where m_0 is the electron rest mass. We have verified that the carriers' mobility and velocity are insensitive to the choice of m_e and m_h (see Fig. 4.2). As a sanity check of the implementation, we have also verified that under uniform electric field, the carriers move according to the mobility μ obtained from TCAD (i.e. the average velocity of the charge ensemble is $v = \mu E$, see Fig. 4.3) and with a diffusion coefficient $D = \mu k_b T/q$ (as verified by simulating the evolution of a Gaussian charge packet, see Fig. 4.4).

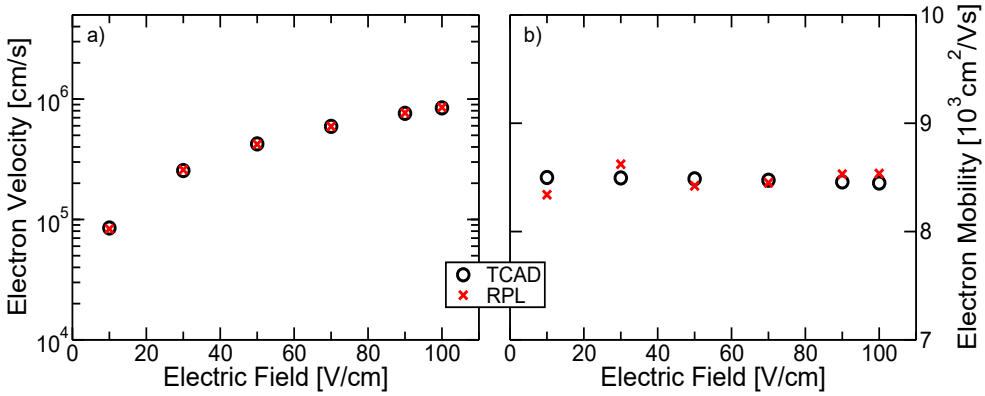

Figure 4.3: a) Electron's drift velocity and b) electron's mobility as functions of the applied electric field in GaAs. The values extracted from TCAD simulations (black circles) are compared with the ones obtained with the RPL algorithm by using $\tau_s \simeq 0.3$ ps, corresponding to $\mu_e = 8450$ cm^2/Vs and $m_e/m_0 = 0.063$ (red crosses).

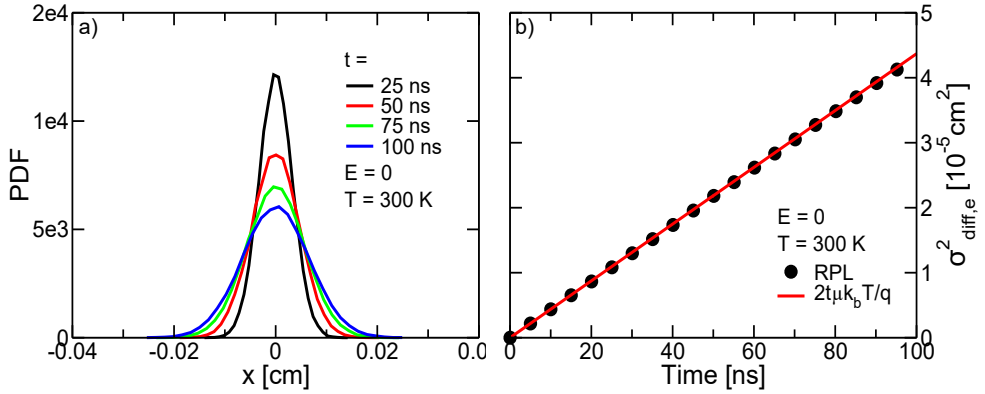

Figure 4.4: a) Evolution in time of the PDF of the electron's position (after simulating an ensemble of 10^5 electrons) when the applied electric field is $E = 0$ and $T = 300$ K. b) Comparison between the time dependence of the variance of the PDF of the electron's position for $E = 0$ and $T = 300$ K (black circles) and the one of a Gaussian bell with variance $\sigma^2_{diff} = 2t\mu_e k_b T/q$ (red line), as given by the solution of the diffusion equation [92].

4.3.2 Carrier Transport in the Multiplication Region

The simulation of carrier transport in the multiplication region makes use of an improved version of the RPL algorithm originally proposed in [43, 79]. The new algorithm can, in fact, be coupled to every nonlocal history-dependent model and not only to the Dead Space model of [35]. In the following, the coupling of the RPL algorithm with the Energy Balance History Dependent Model of Chapter 3 will be discussed.

The History Dependent impact ionization coefficients $\alpha(x|x')$ and $\beta(x|x')$ (i. e. the probabilities per unit length for an electron and a hole generated at position x to ionize at x' [69]) have been computed by using Eqs. 2.72, 2.73 and are functions of suitable effective fields derived from the conduction and the valence band profiles (Eqs. 3.11 and 3.11). According to the definition of the electron's survival probability $P_{se}(x|x')$ in Eq. 2.42, the distance that an electron at position x travels before generating an additional electron-hole pair $(x' - x)$ can be computed by finding the value of x' that satisfies the relation

$$r = P_{se}(x|x') = exp\left(-\int_x^{x'} \alpha(x|x'')dx''\right), \tag{4.3}$$

where r is a random number uniformly distributed in the $[0, 1]$ interval. Equation 4.3 have been solved by storing in a look-up table its right hand side for each value of x and x'. The x and x' spacings are small enough to produce discretization-independent results. Then for a given x and r, a binary search has been performed in the table to find the value of x' that satisfies the relation. A similar methodology has been used to describe the motion of holes. As described in [86], each time a carrier ionizes, the algorithm recursively simulates the motion of the electron and hole originated from the parent carrier, until they are collected by the contacts, then it goes back to the simulation of the parent carrier. The time needed to move a carrier from x to x' is estimated, assuming a constant drift velocity $v_{e,h}$, and computing $(x' - x)/v_{e,h}$.

The parameters of the effective field and of the impact ionization coefficient calculations are reported in Tab. 3.1.

Since the mean gain (M) and the excess noise factor (F) depend only on the transport and impact ionization in the multiplication region, they can be extracted with the RPL algorithm by simulating N_{ev} independent trials (each trial corresponds to a photon-induced generation event) considering the carriers' motion only in the multiplication region of the device. M and F are then computed using Eqs. 2.75 and 2.76, respectively.

4.3.3 Current Induced at the Terminals

A new formulation of Ramo's theorem [34] to compute the current induced at the terminals by carriers moving in a partially depleted device has been proposed in [93]. The contribution of each carrier to the current at time t is given by

$$i(t) = \pm q \int_0^t w[x(t'), t - t']v[x(t'), t']dt', \tag{4.4}$$

where $w(x,t)$ is a weight function and $v(x,t)$ is the carrier's velocity and $t=0$ is the photon's arrival time. Compact formulas for $w(x,t)$ are reported in [93], that assumes two distinct regions in the device: the absorption region with uniform finite conductivity $\sigma = q(\mu_n n + \mu_p p)$, and the multiplication region where σ is approximately zero, since this region is depleted and there are essentially no free carriers (see Fig. 4.1). According to this assumption, the weight functions in the absorption and in the multiplication region are given by

$$w_{abs}(t) = \frac{1}{d_{abs}+d_{mult}}\left(\delta(t) - \frac{1}{\tau}e^{-t/\tau}\right) \tag{4.5}$$

$$w_{mult}(t) = \frac{1}{d_{abs}+d_{mult}}\left(\delta(t) + \frac{1}{\tau}\frac{d_{abs}}{d_{mult}}e^{-t/\tau}\right) \tag{4.6}$$

where

$$\tau = \frac{\varepsilon}{\sigma}\frac{d_{abs}+d_{mult}}{d_{mult}}, \tag{4.7}$$

$\delta(t)$ is the Dirac delta function and ε is the static[3] permittivity of the material [93].

In realistic cases, it is not trivial to make an abrupt distinction, since the values of d_{abs} and d_{mult} do not always correspond to the thickness of the undepleted and depleted regions, respectively. For instance, at high reverse bias voltages the electric field in the device in Fig. 4.1 depletes part of the absorption region and the profile of $\sigma(x)$ becomes highly nonuniform (see Fig. 4.5). For this reason, we have discretized the absorption region in N_d intervals, with nonuniform spacing Δx_i, permettivity ε, conductivity σ_i and weight function $w_i(t)$. We assume $\sigma = 0$ in the multiplication region, that is consistent with the profiles extracted from TCAD (see Fig. 4.5). The $w_i(t)$ have been numerically computed by antitransformation of the corresponding Laplace domain expression. In fact, knowing that in the Laplace domain [93] $W_i(s)$ (Laplace transform of $w_i(t)$) obey to

$$\sum_{i=1}^{N_d} W_i(s)\Delta x_i = 1 \tag{4.8}$$

$$W_{i+1}(s)\left(\varepsilon + \frac{\sigma_{i+1}}{s}\right) = W_i(s)\left(\varepsilon + \frac{\sigma_i}{s}\right) \tag{4.9}$$

one can derive that

$$W_i(s) = \sum_{i=1}^{N_d} \frac{s\varepsilon+\sigma_1}{s\varepsilon+\sigma_i} W_1(s), \tag{4.10}$$

where

$$W_1(s) = \frac{1}{\sum_{i=1}^{N_d} \frac{s\varepsilon+\sigma_1}{s\varepsilon+\sigma_i}\Delta x_i}, \tag{4.11}$$

[3]Note that Eq. 4.7 has been derived in [93] for Silicon. In III-V compound semiconductors, due to their polar nature, the model should include the dependence of ε on the frequency, which would not bring to close-form expressions as Eq. 4.7. In this work we use the static permittivity, since the transverse and longitudinal polar optical frequencies for GaAs are much higher than the frequencies of interest for the computation of the weight functions.

where the index "1" denotes an arbitrary point of the grid, taken as reference. Inverse Fourier transform of the $W_i(s)$ projection on the imaginary axis ($s = j\omega$) yields the desired $w_i(t)$. The integration scheme proposed in [94] was used to this end (the pseudo-code is reported below).

```
nn = [0:2*NFFT-1]; % NFFT = no. of points for FFT comp.
f_max = 1/2/dt;    % dt is the time resolution

w_i(t) = real(ifft(W_i(s)(1:NFFT-1), 2*NFFT) + ...
         ifft(W_i(s)(2:NFFT), 2*NFFT) * ...
         exp(j*2*pi*nn/2/NFFT))/dt;
```

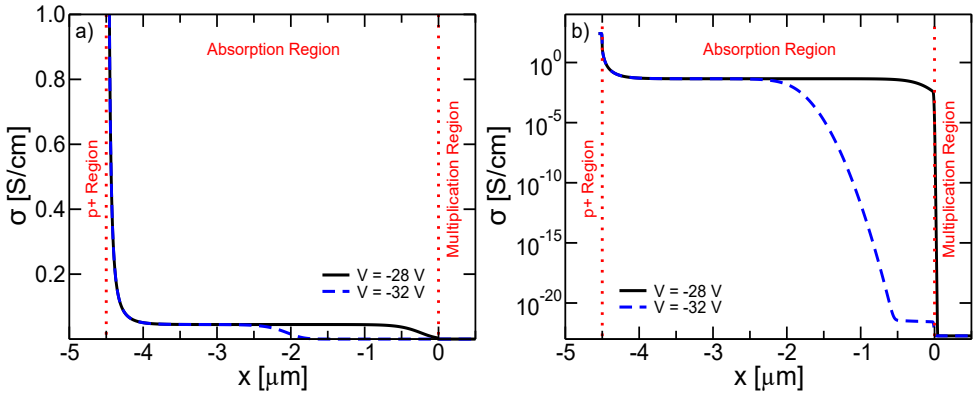

Figure 4.5: Conductivity as a function of the position inside the device of Fig. 4.1 (in linear (a) and logarithmic scales (b)) extracted from TCAD simulations [76]. Two bias voltages lower than the breakdown voltage are considered: $V = -28$ V (black solid line) and $V = -32$ V (blue dashed line).

Figure 4.6 compares, for the same bias voltages of Fig. 4.5, the $w_{abs}(t)$ and $w_{mult}(t)$ computed by using Eqs. 4.5, 4.6 (assuming a constant value of $\sigma(x)$ in the absorption region) and the $w_i(x,t)$ at $x = -2.35$ μm (close to the middle of the absorption region, and at $x = 0$ (where the multiplication region begins) computed numerically by using Eqs. 4.10, 4.11. As expected, the agreement between the two methods is very good only when the electric field is confined inside the multiplication region at (i. e. for $V = -28$ V), but when part of the absorption region is depleted, we get substantially different results, especially at x points close to the multiplication region. However, we also note that the $w_i(t)$ computed by using Eqs. 4.10, 4.11 reported in Fig. 4.6b are similar to those computed by using Eqs. 4.5, 4.6 when, instead of using the nominal values of d_{abs} and d_{mult}, an effective d_{abs} is defined as the distance at which the electric field reaches about 1% of its maximum value inside the multiplication region and an effective value of d_{mult} is also defined consistently.

The contribution of each free flight to the total current waveform is then given by the convolution of $w_i(t)$ with a trapezoidal velocity profile where

the initial velocity is $v(x)$ and increases with constant acceleration $a(x)$ from Eq. 4.1 in the absorption region, while it is equal to v_e (or v_h) in the multiplication region.

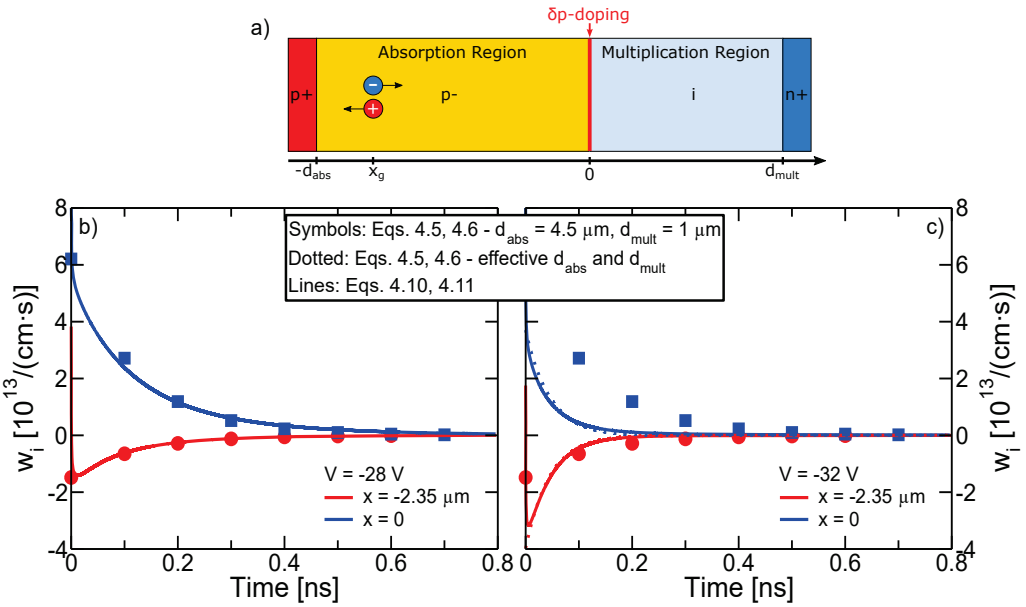

Figure 4.6: a) Sketch of the SAM-APD of Figures 1.18b and 4.1. Electron-hole pairs are generated at position x_g. b), c) Comparison between the weighting functions $w_i(t)$ extracted by using Eqs. 4.5, 4.6 and nominal d_{abs} and d_{mult} values (symbols) and Eqs. 4.10, 4.11 (lines) at two different positions inside the device ($x = -2.35$ μm in red, that corresponds to a point close to the middle of the absorption region, and $x = 0$ in blue, that corresponds to the coordinate where the multiplication region begins) and at b) $V = -28$ V and c) $V = -32$ V. In plot c), the dotted lines represent the $w_i(t)$ computed using Eqs. 4.5, 4.6, but employing effective values of d_{abs} and d_{mult}. When Eqs. 4.5, 4.6 are used, a constant conductivity inside the absorption region, equal to the value of σ at $x = -d_{abs}/2$ in the TCAD simulation, has been assumed.

4.4 Model Verification

The validity of the proposed model has been verified by simulating with the improved Random Path Length algorithm the staircase SAM-APD for X-ray detection of Figures 1.18b and 4.1.

As far as gain and excess noise factor are concerned, the RPL algorithm should give exactly the same results as the *Finite Difference* (FD) implementation described in Section 3.2, since the same parameter values are adopted (Tab. 3.1). This is demonstrated in Fig. 4.7 for p-i-n GaAs APDs and in Fig. 4.8 for the staircase SAM-APD of Fig. 1.18b

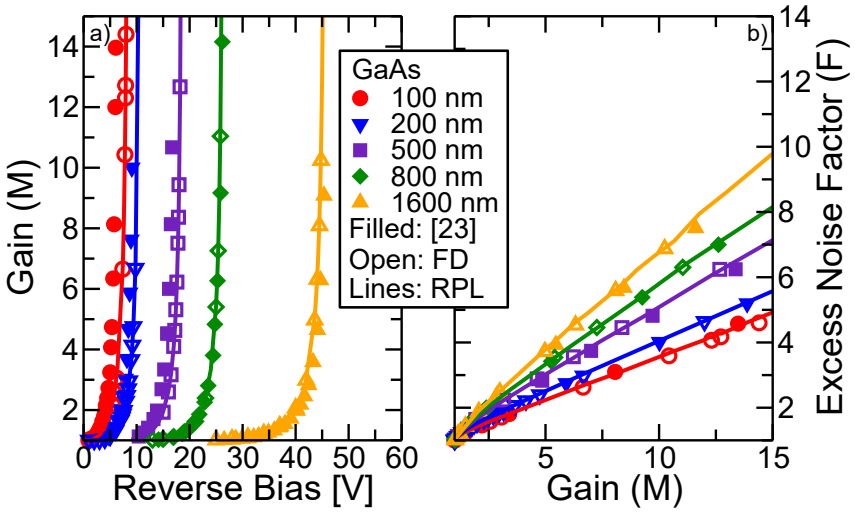

Figure 4.7: a) Gain vs. voltage and b) excess noise factor vs. gain curves for GaAs p-i-n APDs of different thicknesses. The results obtained with the improved RPL algorithm (lines) are compared with the results of the Finite Difference implementation (open symbols, see Section 3.2) and with the experimental data from [23] (filled symbols).

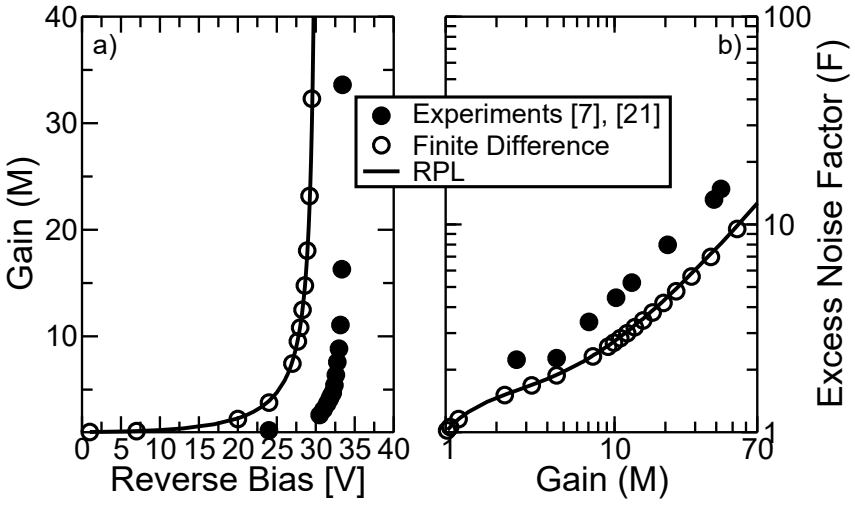

Figure 4.8: Same as Fig. 4.7, but for the staircase SAM-APD of Fig. 1.18b. Experimental data are taken from [7, 21].

To verify the correctness of the current waveforms extracted with our improved RPL algorithm, instead, we have performed DC analyses of the device in Fig. 4.1 at different bias voltages. We haved used the TCAD software [76] to extract the electric field $E(x)$, the field-dependent mobilities $\mu_e(x)$ and $\mu_h(x)$, the concentrations $n(x)$ and $p(x)$, the band profiles, and then we have computed the conductivity $\sigma(x)$ (see Fig. 4.5), the accelerations $a_e(x)$ and $a_h(x)$ (Eq 4.1) and the average times between consecutive scattering events $\tau_{s,e}(x)$ and $\tau_{s,h}(x)$ (Eq. 4.2). Then, the weight functions $w_i(t)$ have been calculated for each point of the absorption region (Eq. 4.10).

Figure 4.9 compares transient simulations with the TCAD software and the calculations with our algorithm after optical generation at different locations in the device. In this case, impact ionization is turned off since the TCAD tool does not include nonlocal models for impact ionization with associated noise comparable to the RPL algorithm [86] in terms of physical content.

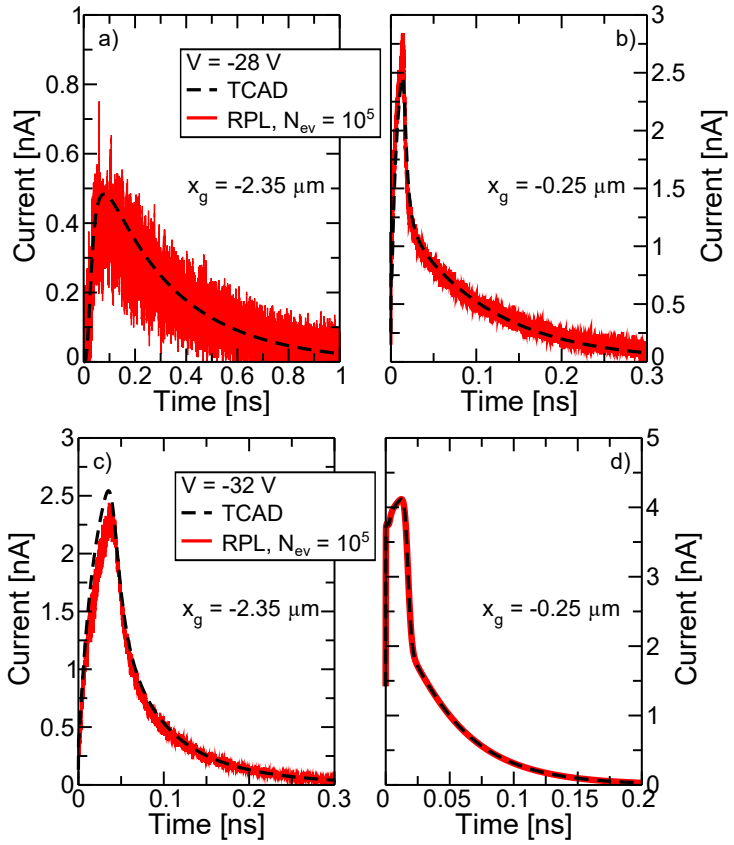

Figure 4.9: Comparison between the current waveforms computed with TCAD [76] (dashed lines) and with our algorithm averaging over 10^5 photon-induced generation events (solid lines). The generation of a single electron-hole pair occurs at $x_g = -2.35$ μm a), c) or at $x_g = -0.25$ μm, b), d) and two different bias voltages have been applied: $V = -28$ V a), b) and $V = -32$ V c), d). In these simulations, impact ionization is turned off. Here and in the next figures, the spatial coordinates are the same as in Fig. 4.1.

The TCAD software is based on the Drift Diffusion equations, works on deterministic ensemble averages and thus provides only a sort of *average* current waveform, obtained by using the doping profile of Fig. 4.1 and solving the Poisson's and continuity equations in the time domain, while our algorithm simulates the random motion of many particles. Hence, the comparison between our approach and TCAD is possible only if the RPL simulations are averaged over many photon-induced generation events (10^5 in this case), starting with randomly chosen generation seeds. As demonstrated in Fig. 4.9, the agreement between the current waveforms computed with TCAD and the RPL,

when we impose that a single electron-hole pair is generated at $x_g = -2.35$ μm or at $x_g = -0.25$ μm, is excellent at both bias points. The average current waveforms extracted with the RPL algorithm in Fig. 4.4 are slightly noisy because we have simulated a finite number of realizations of the stochastic process (trials) of diffusive transport. This noise can be further reduced by simulating (and then averaging) more trials.

4.4.1 Performance Analysis of the Multiplication Region of a Staircase SAM-APD for X-Ray Detection

In this Section, the RPL algorithm will be used to analyze the performance, in terms of gain, excess noise factor, response time and bandwidth, of the multiplication region of the staircase SAM-APD of Fig. 1.18b. The motion of carriers in the absorption region has been neglected on purpose, so that our analysis can highlight how the design of the multiplication region affects the static and dynamic behavior of this device.

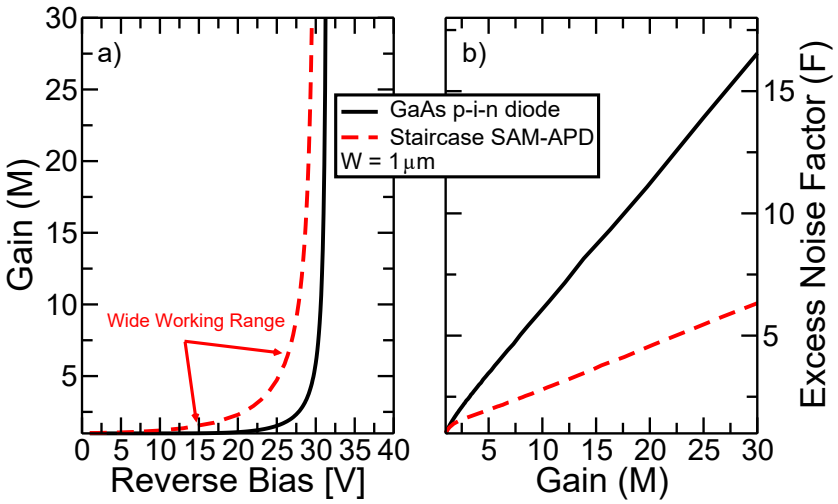

Figure 4.10: a) Gain vs. voltage and b) excess noise factor vs. gain characteristics obtained with the improved RPL algorithm for a 1 μm thick GaAs p-i-n APD and for the staircase SAM-APD reported in Fig.1.18b. In the staircase SAM-APD we have an extended voltage range where a gain significantly larger than one that is achieved by the p-i-n diode.

To better visualize the advantages of a staircase structure compared to a p-i-n diode in terms of a gain/noise perspective, Fig. 4.10 compares the simulated M vs. voltage and F vs. M curves of the device of Fig. 1.18b with a 1 μm thick GaAs p-i-n diode, i.e. same length of the multiplication region for both devices: the staircase structure shows significant gain also below the breakdown voltage and has a much lower associated noise.

Current waveforms after the generation of a single electron-hole pair injected at the left boundary of the multiplication region (i. e. pure electron

injection) are provided in Fig. 4.11. Plots a) and b) consider the staircase structure excluding or including hole impact ionization, respectively; we observe that hole impact ionization induces a long-lasting decaying tail in the current waveform, which becomes longer as the gain increases, whereas the current waveforms obtained when only electrons ionize have the same duration regardless of the gain.

By Fourier transform of the waveforms we determine the 3dB bandwidth (see Fig. 1.6).

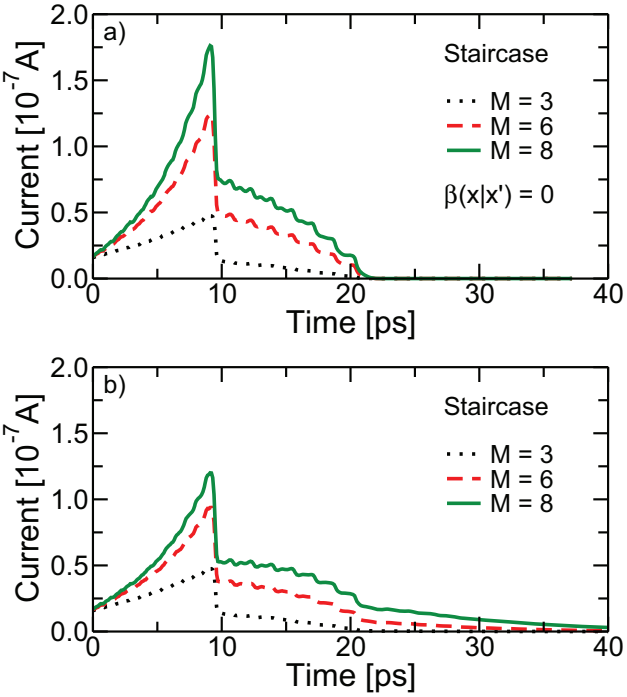

Figure 4.11: Current waveforms at different gains for the multiplication region of the staircase SAM-APD of Fig. 1.18b obtained with the improved RPL algorithm a) without or b) with hole impact ionization. Carriers move at a constant velocity $v_e = v_h = 10^7$ cm/s so that the transit time across the 1-μm multiplication region is $T_R = 10$ ps.

The gain-bandwidth product (GBP, see Fig. 4.12) is almost constant [12] and improves for p-i-n APDs with thin intrinsic region. We can notice that p-i-n and staircase diodes with the same width of the multiplication region have similar GBP. Note that the staircase structure of Fig. 1.18b requires a significant electric field between the steps in order to obtain a significant gain. This results in large hole impact ionization which is detrimental for the bandwidth (see the long tail in Fig. 4.11b, that implies an earlier decay in the frequency domain. This problem does not occur in other material systems (as for example in InAsSb systems [10]), where conduction band discontinuities are large compared to the energy gap of the material in which impact ionization takes place.

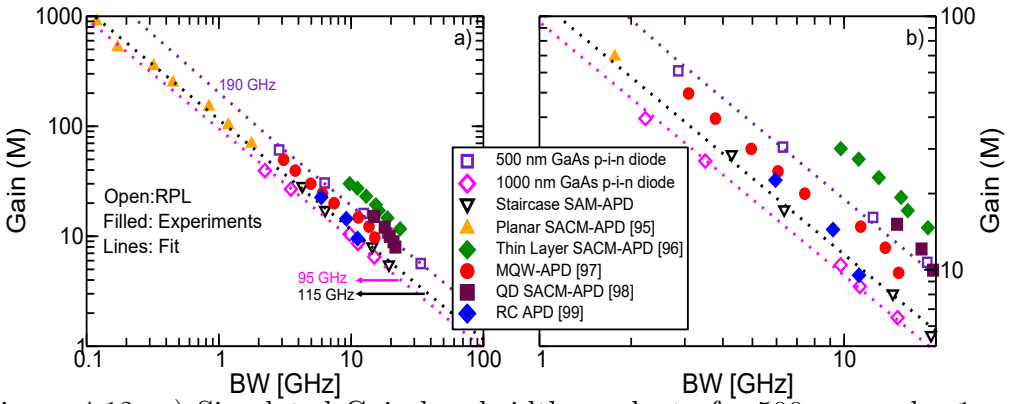

Figure 4.12: a) Simulated Gain-bandwidth product of a 500 nm and a 1 μm-thick GaAs p-i-n diodes and of the multiplication region of the staircase SAM-APD of Fig. 1.18b obtained with the improved RPL agorithm (open symbols). Filled symbols: experimental data for a planar [95] and a thin layer [96] separate, absorption, charge and multiplication (SACM), a Multi Quantum Well (MQW) [97], a quantum dot (QD) SACM [98] and a resonant cavity (RC) APDs [99] based on III-V compound semiconductors. b) Same as plot a) in the range $1 \leq BW \leq 20$ GHz.

The RPL algorithm can now also used to evaluate how changing the number of steps in the multiplication region of the staircase SAM-APD of Fig. 1.18b affects the response time of the device, similarly to what has been done for the gain and the excess noise factor in Section 3.6.

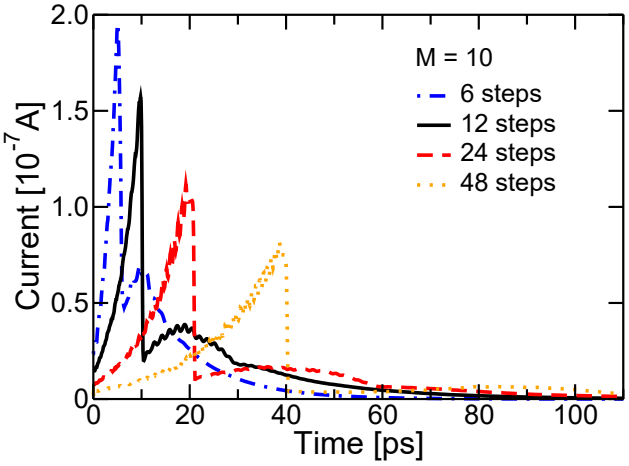

Figure 4.13: Simulated current waveforms for a staircase APD like the one in Fig. 1.18b with $N_{step} = 6, 12, 24, 48$ multiplication steps at fixed gain $M = 10$.

Of course increasing the number of steps results in a longer multiplication region and thus longer time response to single photon absorption. Figure 4.13 reports the resulting current pulses for N_{step}=6, 12, 24 and 48, showing a retarded peak when increasing N_{step}. On the other hand, the smaller hole impact ionization entailed by large N_{step} values reduces the amplitude of the slow current tails w.r.t. the height of the main peak.

However, when considering X-ray spectroscopy as a relevant application for III-V based APDs, one should take into account that the diode current is processed by a leaky integrator followed by an CR-RC shaper, as discussed in Section 1.6. This corresponds to the convolution of the current pulses in Fig. 4.13 with the function in Eq. 1.11. Since the $\tau_s = RC$ time constant is usually in the μs range [25], all the current pulses in Fig. 4.13 result in essentially the same waveform at the output of the shaper (see Fig. 4.14). As a result we can say that, for X-ray spectroscopy, increasing the number of steps is beneficial since it reduces the noise (i.e. improves the energy resolution of the system), as seen in Section 3.6.2, without penalties to the speed of the system.

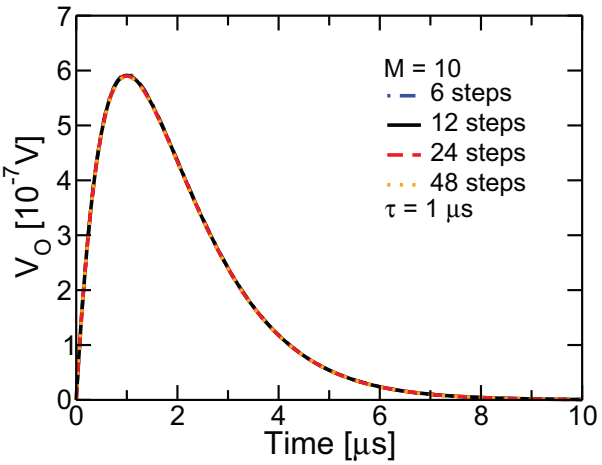

Figure 4.14: Simulated current waveforms, after the convolution with the impulse response function of a CR-RC shaper with time constant $\tau = 1$ μs, for a staircase SAM-APD as the one in Fig. 1.18b with $N_{step} = 6, 12, 24, 48$ multiplication steps at fixed gain $M = 10$.

4.5 Jitter of the Time Response

The random motion of carriers in the absorption region and the stochastic nature of impact ionization events result in random changes of the current waveforms whenever a photon creates electron-hole pairs, thus generating jitter in the APD response. We now want to evaluate this jitter by assuming a realistic architecture of the readout electronics used in time of flight experiments.

In these systems, there is the need for a *trigger* that generates a logic pulse signalling the occurrence of a photon arrival. To this end, different methods can be used, e. g. simple threshold techniques (*Leading Edge Triggering*) or more elaborate *Amplitude and Rise Time Compensated (ARC) Timing* [100]. In the following, we take as reference case the simple *Crossover Timing* (CT) scheme illustrated in the inset of Fig. 4.15a, because: 1) it can be easily implemented as post processing step in the algorithm presented in Section 4.3; 2) it is less affected than leading edge timing by the fact that two pulses with the same

rise time, but different amplitude, reach the same threshold at different times (the so-called "amplitude walk" [100]); 3) it is at the base of other timing methods, such as the *Constant Fraction Discrimination* and ARC Timing. [100]. Following the CT scheme, the (simulated) current waveform generated by the arrival of one photon is subtracted by a delayed version of itself to obtain a bipolar pulse. A trigger signal is generated at the zero-crossing point t^* (see Fig. 4.15). By simulating many photon-induced generation events we can then construct the distribution of t^* (in the following referred to as $PDF(t^*)$) for a given t_D. We call *response time jitter* (t_j) the standard deviation of this distribution; the conceptual scheme in Fig. 4.15 thus gives us an indication of the jitter in a realistic readout for time of flight measurements.

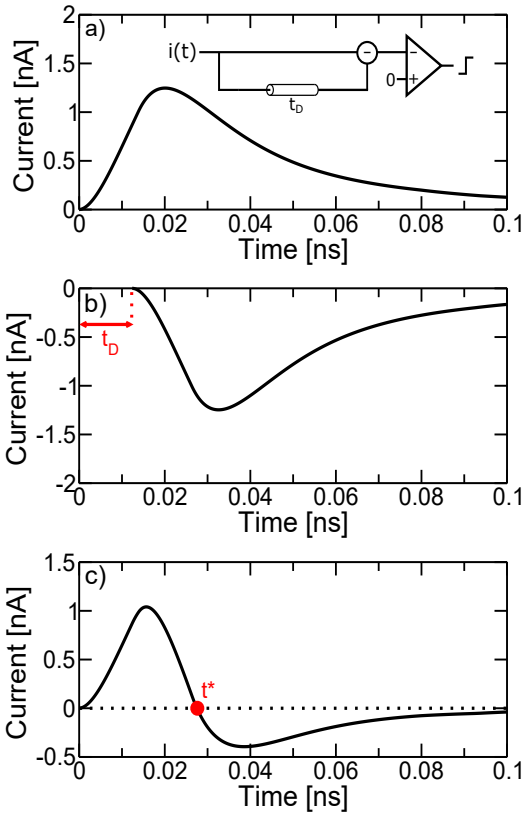

Figure 4.15: Representation of the Crossover Timing method to compute t^*, which is representative of a readout scheme used in time of flight measurements. The original current waveform (a) is subtracted to itself delayed by t_D (b) to obtain a bipolar pulse (c). A trigger is generated at the zero-crossing point t^*. In the inset of panel (a), the procedure is reported in the form of a block diagram.

We have always assumed that the time interval between consecutive photon's arrivals is longer than the time response of the device. Moreover, when simulating the diffusion of the carriers in the absorption region (see Fig. 4.6a), differently from what is explained in Section 4.3, we have set $w_i(x,t) = 0$ for $x < 0$ when the electric field is null in the absorption region, that yields a null current waveform from $t = 0$ to $t = t_{diff}$, where t_{diff} is the random time

needed for the electron generated in the absorption region to diffuse towards the multiplication region (see Fig. 4.16a). In other words, the model considers only the effect of diffusion on the duration of the current waveform, and neglects the contribution of diffusion noise in terms of induced current, since this would result in thermal noise components at high frequency filtered out by any readout circuit. This approximation is supported by Fig. 4.16b that shows the current power spectral densities (PSDs), averaged over $N_{ev} = 10^3$ photon induced generation events, obtained including or not the contribution of carrier diffusion to the induced current. Figure 4.16b has been constructed by assuming random time intervals, generated according to a Poisson distribution with mean frequency $\nu = 0.5$ GHz between consecutive photon arrivals and then performing the Fourier transform of the sequence of current waveforms. The pseudo-code for the computation of the PSD is here reported:

```
T = 0;
PSD = 0;
nu = 0.5e9;

for n = 1:Nev
    i_t = current computed with RPL algorithm;
    T_rnd = -1/nu*log(rand(1, 1));
    T += T_rnd;

    % NFFT = no. of points for FFT computation

    I_fft = fft(i_t, NFFT);
    I_fft2 = abs(I_fft(1:floor(NFFT/2)+1)^2;
    I_fft2(2:end-1) *= 2;
    PSD += I_fft2*dt^2;
end

PSD /= T;
```

We notice that, in the low frequency limit, there is a good agreement between the PSDs computed in the two cases (with or without the contribution of carriers' diffusion to the induced current). The small discrepancy is due to the fact that when the complete model is used, the high frequency white noise associated with carriers' diffusion adds to the shot noise component of the photogenerated current $I_{ph} = q\nu$. So, setting $w_i(x,t) = 0$ for $x < 0$ gives the advantage of getting output waveforms free of additional noise contributions of limited relevance for the considered problem. In addition, to suppress the effect of the residual noise, a zero-crossing point is considered valid only if it occurs when the integration of the original current waveform is larger than 0.1 the electron's elementary charge q. A possibility to further reduce the noise components not relevant to jitter analysis, would be to filter the current waveforms, mimicking the effects of the finite bandwidth of a real readout. When, instead, the absorption region is partially depleted, we compute $w_i(x,t)$

also for $x < 0$ when the carriers move in a region where the electric field is, at least, the 1% of its peak value in the multiplication region.

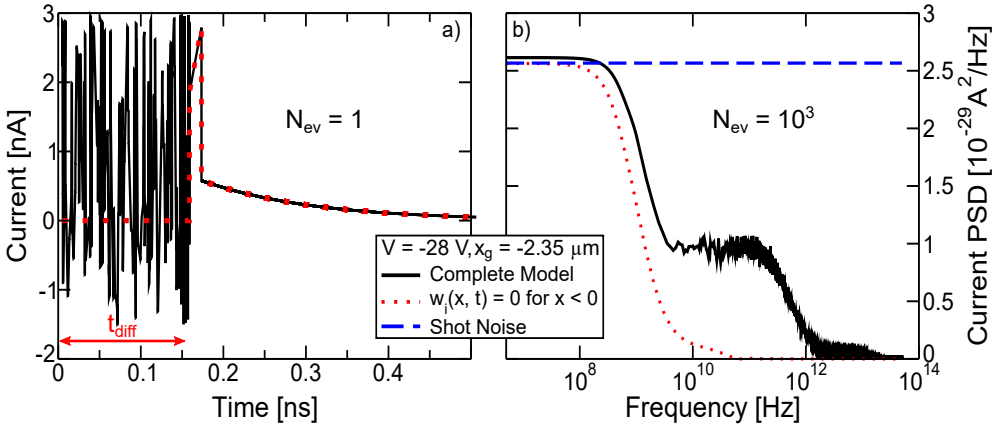

Figure 4.16: a) Sample current waveform for a single generation event and b) the corresponding current power spectral density averaged over $N_{ev} = 10^3$ generation events computed with our algorithm using the complete model described in Section 4.3 (black solid line) or imposing $w_i(x,t) = 0$ for $x < 0$ (red dotted line) for $V = -28$ V and $x_g = -2.35$ μm. A single electron-hole pair is generated per absorbed photon.

Concerning the delay time t_D, this has been set larger than the rise time from 10% to 90% of the peak current of the original waveform and chosen so that the falling edge of the original current pulse crosses the rising edge of the delayed one in a region where small changes of t_D do not affect the jitter. The limitations of this approach are discussed in the following Section 4.5.2. Indeed we have verified that, when all the current waveforms generated by different photons have a similar shape (that is the case when impact ionization is turned off, so that the only difference between the waveforms is t_{diff}, see Fig. 4.16a), then an interval of values exists where the precise t_D does not affect the extracted jitter value (Fig. 4.17).

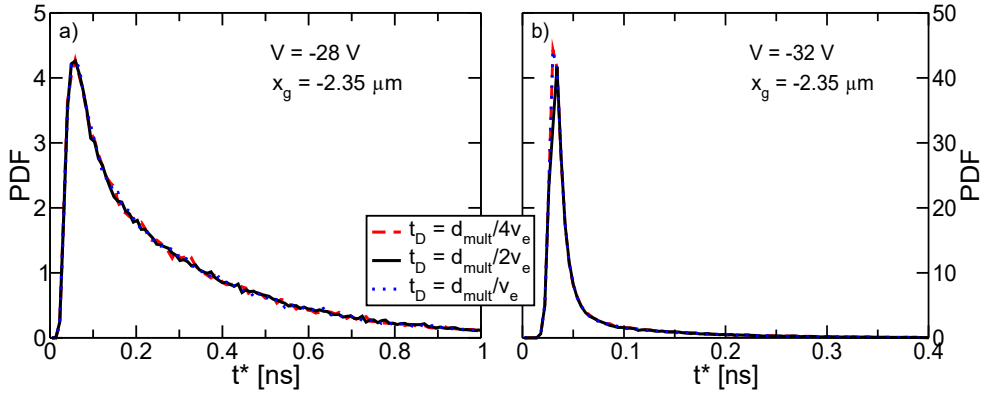

Figure 4.17: Probability Density Functions of t^* for a) $V = -28$ V and b) $V = -32$ V for different t_D. The generation point is x_g = -2.35 μm. $PDF(t^*)$ is the same regardless of the t_D value.

To assist our forthcoming interpretation of the distribution of t^*, we recall that, based on the solution of the diffusion equation [101], for Brownian

motion in a region of constant drift velocity v and diffusion coefficient D, the probability density function of the arrival time t^* necessary to move from a generic photo-generation point x_g in the absorption region to the point where the multiplication region starts ($x = 0$, see Fig. 4.6a), is an inverse Gaussian distribution:

$$f(t^*) = \frac{|x_g|}{\sqrt{4\pi D t^{*3}}} exp\left(-\frac{(-x_g - vt^*)^2}{4Dt^*}\right). \tag{4.12}$$

The standard deviation of the distribution of Eq. 4.12 is a good representation of the jitter of an APD when the multiplication region has a deterministic behavior, i. e. carrier multiplication is negligible and the absorption region is under uniform conditions, so that constant v and D can be assumed along the x direction. In order to examine the validity of these assumptions and their impact on the jitter, different cases will be analyzed in the following subsections.

4.5.1 Case 1: Influence of the Bias Voltage and of the Generation Point

To evaluate how the applied voltage and the location of the generation point affect the distribution of t^*, we have considered two bias points: $V = -28$ V and $V = -32$ V, corresponding to two different configurations for the electric field profile inside the device. In fact, while in the first case the field is entirely confined inside the multiplication region, at $V = -32$ V part of the absorption region is depleted, as also visible from the $\sigma(x)$ profiles in Fig. 4.5. We have considered the deterministic generation of a single electron-hole pair occurring either near the middle of the absorption region ($x_g = -2.35$ μm) or next to the edge of the multiplication region ($x_g = -0.25$ μm). At this stage, we focus on the effect of transport in the absorption region. Therefore, impact ionization is deliberately turned off in the multiplication region, where electrons travel with constant average velocity v_e.

Figure 4.18 shows the $PDF(t^*)$, obtained by simulating $N_{ev} = 10^5$ photon induced generation events for the cases described above. A tentative fit with an inverse Gaussian distribution (Eq. 4.12), where v and D are effective (space independent) fitting parameters, is also reported. We notice that at $V = -28$ V (Fig. 4.18a), when only the multiplication region is depleted and the electron-hole pairs are generated far from the multiplication region, the distribution of t^* is very similar to the inverse Gaussian distribution of Eq. 4.12 (as when transport occurs by drift and diffusion under uniform electric field). However, in the SAM-APD of Fig. 4.1, the assumption of a uniform electric field is not valid at positions close to the p^+-contact and at the boundary between the absorption and the multiplication region. For this reason, Eq. 4.12 holds only if *effective* values of v and D are used instead of the ones that can be extracted from the TCAD analysis; in the case of Fig. 4.18a, for instance, the effective values $v = 7.796 \times 10^5$ cm/s and $D = 1.15 \times 10^2$ cm^2/s have to be used in Eq. 4.12 instead of $v = 680$ cm/s and $D = 221$ cm^2/s, that are the values extracted from TCAD. The resulting jitter, defined as the standard deviation

of the $PDF(t^*)$ computed by the RPL algorithm, is $t_j = 284$ ps. On the other hand, when photons are absorbed close to the multiplication region (Fig. 4.18b) or the reverse bias voltage is increased to $V = -32$ V (Fig. 4.18c and d) and part of the absorption region is depleted, the effect of diffusion is less relevant. Thus, the distribution of t^* is more peaked with respect to the one derived using Eq. 4.12. The jitter is now much smaller: $t_j = 19.2$ ps, 68 ps and 1.8 ps for Fig. 4.18b, c and d, respectively. In particular, in the cases of Fig. 4.18b and c, electron-hole pairs are generated in regions where the conductivity is not constant (see Fig. 4.5a and b) and we are very far from the assumptions of uniform v and D required for the validity of Eq. 4.12. Finally, in Fig. 4.18d, electron-hole pairs are generated in a depletion region with null conductivity, as a result carriers move only by drift and, thus, the extracted $PDF(t^*)$ is essentially a Dirac's delta.

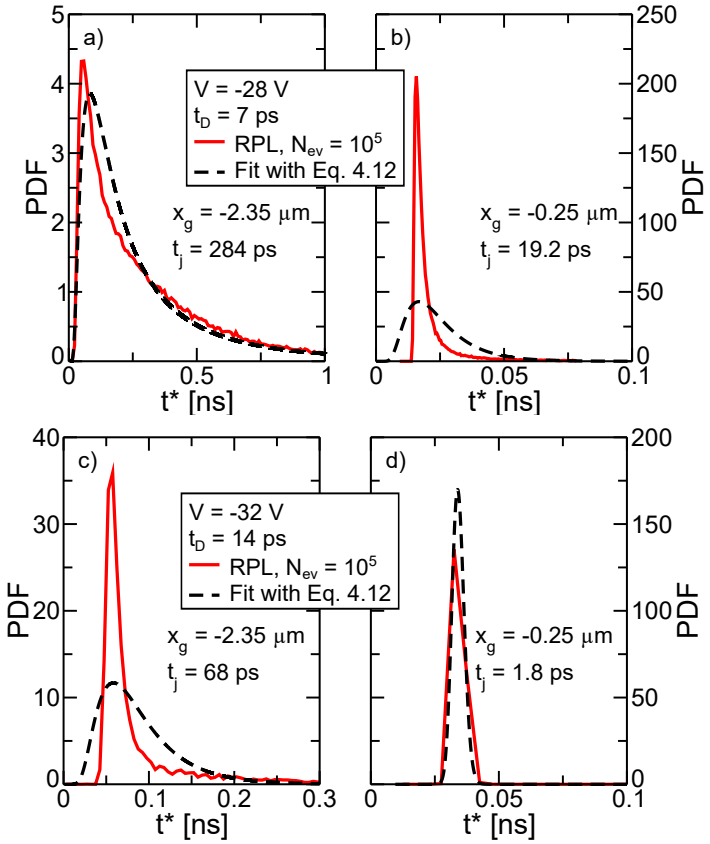

Figure 4.18: Probability Density Functions of t^* at $V = -28$ V a), b) and at $V = -32$ V c), d) when an electron-hole pair is generated at $x_g = -2.35$ μm a), c) or at $x_g = -0.25$ μm b), d). The PDFs extracted with the RPL algorithm (red solid lines) are compared with a fitted inverse Gaussian distribution (Eq. 4.12, black dashed lines). The delay of the readout of Fig. 4.15 is chosen so that the falling edge of the original current waveform crosses the rising edge of the delayed one, thus: $t_D = 0.5 \cdot d_{mult}/v_e = 7$ ps a), b) or $t_D = d_{mult}/v_e = 14$ ps c), d). Note the different scales of the x-axis and the Dirac's delta like shape of the $PDF(t^*)$ in graph d). Impact ionization is turned off.

4.5.2 Case 2: Effect of impact ionization

In avalanche photodiodes, impact ionization plays a fundamental role in amplifying the photogenerated current. The shape of the output current waveforms changes dramatically and this has a significant effect on the $PDF(t^*)$. Moreover, since impact ionization is a stochastic process, at a fixed bias voltage, each carrier triggers multiplication processes with different gain m, and this is an additional source of jitter.

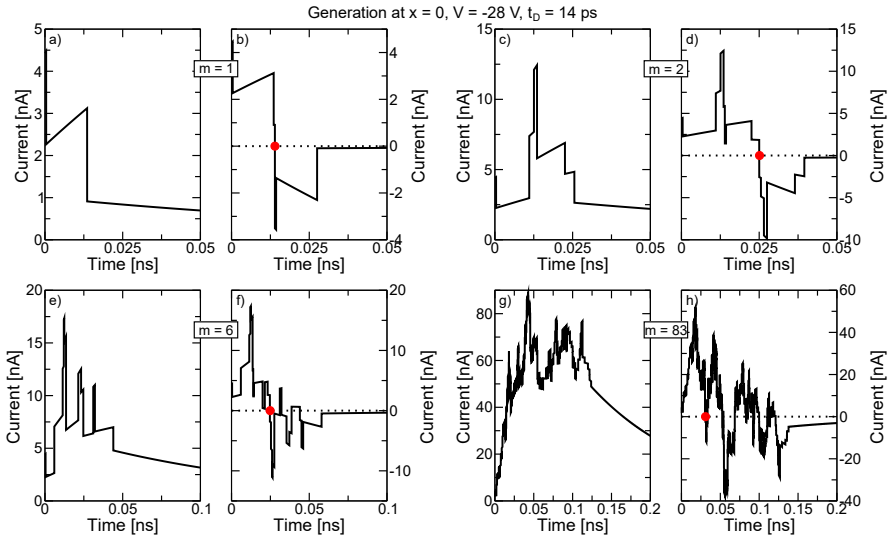

Figure 4.19: a), c), e), g): Sample current waveforms associated to the arrival of a photon that generates one electron-hole pair at $x_g = 0$ when impact ionization is turned on. The applied voltage is $V = -28$ V. Since impact ionization is a stochastic process, the gain m is not the same for all events: $m = 1$ in a) and b), $m = 2$ in c) and d), $m = 6$ in e) and f) and $m = 83$ in g) and h). Plots b), d), f), h) report the difference between the current waveform and its delayed version when the delay is $t_D = d_{mult}/v_e = 14$ ps. The first zero-crossing point is highlighted with a red dot.

Figure 4.19 shows four sample waveforms (plots a, c, e and g) when $V = -28$ V and a single electron-hole pair is generated at $x_g = 0$ (thus excluding the contribution of random diffusive transport in the absorption region). At this bias voltage, the mean gain is $M = \langle m \rangle = 14$. Fig. 4.19b, d, f and h, instead, show the bipolar pulses obtained by adding the current waveform with its inverted version delayed by $t_D = d_{mult}/v_e = 14$ ps. We notice that in Fig. 4.19a and b, when the gain is $m = 1$, the zero-crossing point occurs at $t^* = t_D$, since the delay is longer than the duration of the main lobe of the pulse. In Fig. 4.19c and d instead, the gain is $m = 2$ and the zero-crossing point is at $t^* \simeq 25$ ps. The same happens if the gain is $m = 6$, as shown in Fig. 4.19e and f, although now multiple zero-crossing points are present due to the complex shape of the waveform. Finally, when the gain is $m = 83$ (Fig. 4.19g and h), the first zero-crossing point occurs at $t^* = 30$ ps, that is a time interval smaller than the rise time of the pulse shown in Fig. 4.19g.

Figure 4.20 shows the $PDF(t^*)$ obtained when impact ionization is active.

The jitter (standard deviation of the total $PDF(t^*)$) is $t_j = 5.8$ ps. We notice that the PDF shape is different from those reported in Fig. 4.18. The peak at $t^* = 14$ ps (that is $t^* = t_D$) is due to all those waveforms where the zero-crossing point occurs during or after the falling edge of the current waveform (see Fig. 4.19a and b).

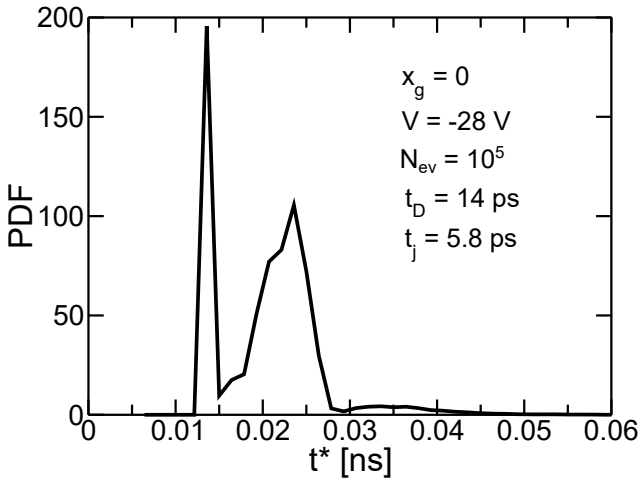

Figure 4.20: Probability Density Function of t^* after the arrival of $N_{ev} = 10^5$ photons, when the bias voltage is $V = -28$ V. Single electron-hole pairs are generated at the beginning of the multiplication region ($x = 0$). $t_D = d_{mult}/v_e = 14$ ps.

The spread in the $PDF(t^*)$ is then caused by the Crossover Timing scheme itself, since the waveforms generated by the arrival of different photons all have different shapes and the duration of the pulses changes dramatically depending on the gain m [100]. The main issue is to calibrate the optimum t_D to be used: if the choice of t_D is based on the duration of the average time response at a given bias voltage, then when m is low the zero crossing might occur during or after the falling edge of the current waveform, while, when m is large the crossing is at the beginning of the rising edge. For this reason, the scheme in Fig. 4.15 is well suited for APDs only if multiple electron-hole pairs are generated by a photon. This happens, for instance, in the detection of X-rays, which is one of the main applications of III-V compound semiconductor APDs. The generation of a single electron-hole pair per photon instead is not representative of our use cases. The discussion of alternative timing methodologies goes beyond the aim of this thesis and, in general, APDs operated in the linear regime may not be the best choice in this case.

4.5.3 Case 3: Generation of Multiple Electron-Hole Pairs

As mentioned above, when avalanche photodiodes are used for the detection of high energy photons (e. g. X-rays), more than one electron-hole pair is generated per absorbed photon. Calibrated generation models predict that the number of generated electron-hole pairs has a Normal distribution with average $\overline{N} = E_{ph}/E_{ehp}$ and standard deviation equal to $\sqrt{\overline{N}f}$, where E_{ph}

is the photon energy, E_{ehp} is the average electron-hole pair creation energy and f is the Fano factor [6]. E_{ehp} and f depend on the material and, for GaAs, their values are $E_{ehp} = 4.21$ eV and $f = 0.12$ [25]. An example of distribution of generated carriers is shown in Fig. 4.21a). Note that, since the number of electron-hole pairs generated for each absorbed photon is a discrete quantity, a Poisson distribution would be more appropriate. However, for the absorption of X-ray photons in GaAs, $\overline{N}$ is as high as 100 and for these numbers the Central Limit Theorem ensures that the Normal distribution is a good approximation of the Poisson's one.

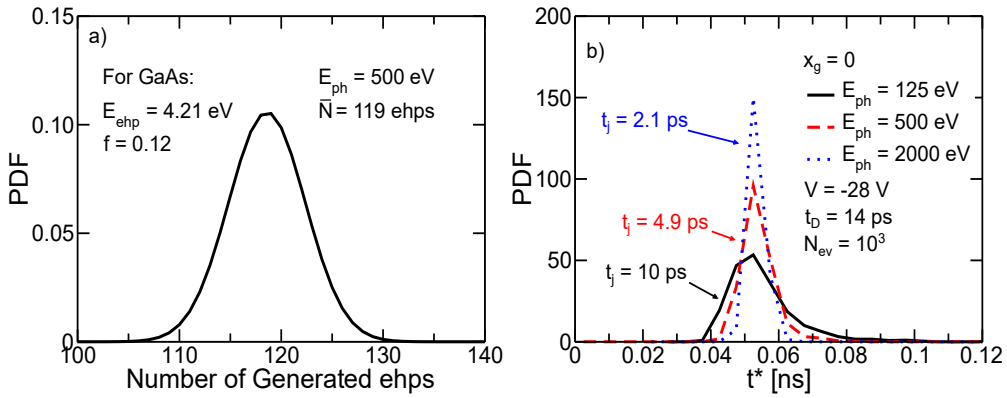

Figure 4.21: a) Distribution of the number of generated electron-hole pairs in GaAs for a photon with energy $E_{ph} = 500$ eV according to [25]. b) Probability Density Functions of t^* considering 10^3 times the process of the arrival of a photon and the random generation of electron-hole pairs, at $x_g = 0$ in the device of Fig. 4.1. $E_{ph} = 125$, 500 or 2000 eV (black solid line, red dashed line and blue dotted line respectively). Impact ionization is turned on, the applied voltage is $V = -28$ V. $t_D = d_{mult}/v_e = 14$ ps.

To evaluate how multiple electron-hole pairs generation affects the jitter of the response time, we have simulated the absorption at $x_g = 0$ of 1000 photons with fixed energy $E_{ph} = 125$, 500 or 2000 eV. This choice is well motivated by the will to highlight only the relative impact of the electron-hole pair generation process on the jitter. As discussed above, each photon generates a random number of electron-hole pairs (N) according to the Normal distribution related to its energy [6, 25]. t^* is then computed with the procedure of Fig. 4.15 on the current waveform generated by the N pairs (i.e. each electron-hole pair is simulated separately, then the waveforms are summed up). The results are shown in Fig. 4.21b. We notice that, as the photon energy increases from 125 to 2000 eV, the distribution of t^* becomes narrower. This happens because the number of electron-hole pairs contributing (statistically) to the current waveforms increases and the curves associated to the arrival of different photons are similar to each other, resulting in a reduced variability with respect to what is shown in Fig. 4.19.

The generation of multiple electron-hole pairs per photon makes the use of the Crossover Timing technique less critical even in the presence of a high gain,

since the current waveform associated to the arrival of a single high energy photon is the sum of all the current waveforms created by each generated electron-hole pair.

4.5.4 Case 4: Distributed Electron-Hole Pair Generation

When the photon flux impinges on the APD, electron-hole pairs generation is not localized but distributed along the x direction according to the Beer-Lambert's law (Eq. 1.8).

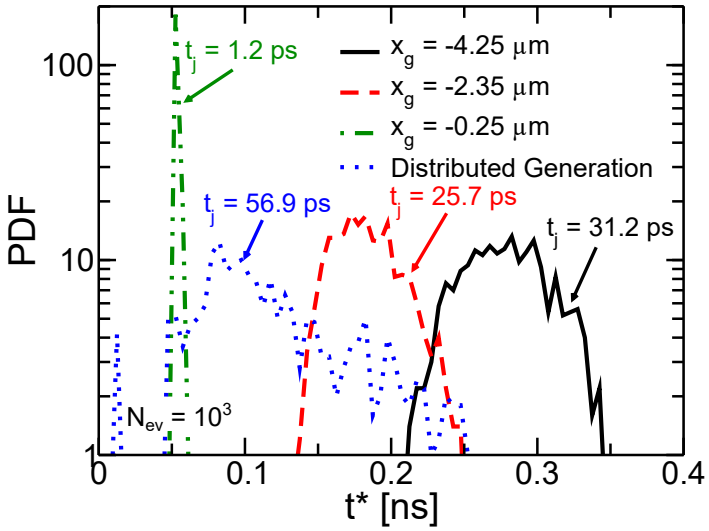

Figure 4.22: Comparison between the Probability Density Functions of t^*, extracted with the extended RPL after the arrival of $N_{ev} = 10^3$ photons, when multiple electron-hole pairs are generated at $x_g = -4.25$ μm (black solid line), $x_g = -2.35$ μm (red dashed line), $x_g = 0$ (green dashed-dotted line) or when the generation follows the profile given by Eq. 1.8 (blue dotted line). The applied bias voltage is $V = -28$ V and impact ionization is turned on. The delay of the readout circuit of Fig. 4.15 is $t_D = d_{mult}/v_e = 14$ ps.

In our simulations, we have considered photons with energy $E_{ph} = 5.89$ keV, typical of ^{55}Fe and we assume a device entirely fabricated in GaAs. The attenuation length is then $L = 11.95$ μm [14]. By using the GaAs parameters reported in Section 4.5.3 [25], each photon generates an average number of 1399 electron-hole pairs.

Fig. 4.22 compares the distribution of t^* when generation of multiple electron-hole pairs is localized at $x_g = -4.25$ μm, $x_g = -2.35$ μm and $x_g = 0$ μm to the case when generation is distributed. We notice that the jitter decreases from $t_j = 31.2$ ps to $t_j = 1.2$ ps as we move the generation point closer to the multiplication region, because carriers have to travel according to the stochastic laws of the diffusive transport over a path of the absorption region that becomes shorter. When the generation is distributed, instead, the jitter is higher than in all previous cases ($t_j = 56.9$ ps), since electron-hole pairs are

generated at random positions inside the device, depending on the point where the photon is absorbed (all the pairs generated by a given photon are, instead, created at the same position, as stated in Section 4.3.1).

4.6 Summary

A new implementation of the Random Path Length algorithm allows us to investigate the stochastic response time of Separate Absorption and Multiplication avalanche photodiodes (SAM-APDs). The model includes an extended version of the Ramo's theorem in order to properly take into account the finite conductivity of the absorption region. The transport model includes both diffusion and drift of carriers as well as impact ionization. Moreover, differently from the RPL algorithm of [43, 79], in our algorithm any nonlocal history dependent model can be used to describe impact ionization, allowing the study of carrier multiplication in complex structures, such as staircase APDs.

It is shown that, as expected, staircase APDs are advantageous over p-i-n in terms of excess noise factor, whereas the advantages in terms of gain-bandwidth product are limited unless hole impact ionization is significantly suppressed.

The model also points out that the when the staircase SAM-APD of Figure 1.18b is used for X-ray spectroscopy, the increase in the number of steps of the multiplication region does not imply any practical drawback in terms of dynamic response of the system, because the shaper usually has a time constant (set to be as close as possible to the optimum case where the combined noise of the input-referred voltage and current sources of the read-out are minimized [26, 15]) much longer than the time delay of the APD.

We validated the model predictions of average current waveforms against TCAD software, and then used them to extract the response time jitter. It has been pointed out that, in cases where impact ionization is vanishingly small (that corresponds to low bias voltages in real scenarios), when electron-hole pairs are generated at the same location in the absorption region, the jitter is higher if the absorption region is quasi neutral (i.e. low electric field as given by a high doping in the δ-p layer). The jitter decreases as the generation of electron-hole pairs occurs closer to the multiplication region.

When impact ionization is relevant, the simple Crossover Timing technique for the estimation of the jitter has limitations, because the line delay t_D has to be fixed but the shapes of the current waveforms created by distinct photons are very different from each other, even at the same bias. However, the situation improves if we consider generation of many electron-hole pairs per photon as for X-ray detection, since several current waveforms are summed together. Consistently, the jitter reduces as the energy of the photon increases (more electron-hole pairs are involved).

Finally, it is important to consider a distributed generation profile due to impinging photons with high energy, since the jitter is higher than in those cases where the generation is localized, due to the random generation position that translates into a different time needed for each electron to diffuse across the absorption layer.

Chapter 5

Full Band Monte Carlo Simulations of GaAs APDs

In this Chapter, the development of a Full Band Monte Carlo simulator and its application to GaAs Avalanche Photodiodes will be presented. The main focus is on using this very accurate modeling approach to assess the limitations of the approaches based on the nonlocal history dependent framework presented in the previous chapters and to improve the calibration of these models by using the results of Full Band Monte Carlo simulations as starting point.

In fact, as discussed in Chapters 2-4, nonlocal history dependent (NL-HD) impact ionization models based either on the Dead Space approximation [35] or on effective fields [39, 23, 69] are often used to estimate the gain (M) and the excess noise factor (F) in APDs. The strength of NL-HD models lies in their low computational burden, when compared with Monte Carlo simulations, that allows to systematically analyze the trade-offs at the basis of APDs design. However, the high computational speed comes at the expense of accuracy. In fact, in NL-HD models impact ionization is described at a macroscopic level: the model parameters have to be empirically chosen to fit experimental gain and excess noise factor as done in Sections 2.2.2, 2.2.3 and 3.3; furthermore, secondary carriers are always generated with zero kinetic energy and can move only in the direction of the applied electric field [35, 39, 23, 69].

The results presented in this Chapter are an extension of the ones published by the author of this thesis in [102].

5.1 Band Structure

GaAs, like many other III-V compound semiconductors, is a crystal with a Zinclblende structure. In the reciprocal space ($\vec{k}$), this corresponds to a Face-Centered Cubic (FCC) lattice, whose First Brillouin Zone (FBZ) can be identified by the $\vec{k}$-points that satisfy the relation

$$\vec{k} \in FBZ \text{ if } \begin{cases} |k_x| \leq 1 \\ |k_y| \leq 1 \\ |k_z| \leq 1 \\ |k_x| + |k_y| + |k_z| \leq 1.5, \end{cases} \tag{5.1}$$

where $|k_x|$, $|k_y|$ and $|k_z|$ are normalized to $2\pi/a_0$ and a_0 is the lattice constant (Fig. 5.1a).

A FCC lattice has a 48-fold symmetry, that means that the energy dispersion relation can be computed on the 1/48th part of the FBZ, the so-called Irreducible Wedge (IW, see Fig. 5.1b), and then derived for the rest of the FBZ by exploiting the symmetry. $\vec{k}$ is part of the IW if

$$\vec{k} \in IW \text{ if } \begin{cases} 1 \geq |k_x| \geq |k_y| \geq |k_z| \geq 0 \\ |k_x| + |k_y| + |k_z| \leq 1.5, \end{cases} \tag{5.2}$$

where, again, $\vec{k}$ is normalized to $2\pi/a_0$.

The symmetry points of the a FCC lattice are highlighted in Fig. 5.1b and are located at (in units of $2\pi/a_0$):

$$\begin{aligned} \Gamma &= (0, 0, 0) \\ X &= (0, 1, 0) \\ L &= (0.5, 0.5, 0.5) \\ W &= (0.5, 1, 0) \\ U &= (0.25, 1, 0.25) \\ K &= (0.75, 0.75, 0). \end{aligned} \tag{5.3}$$

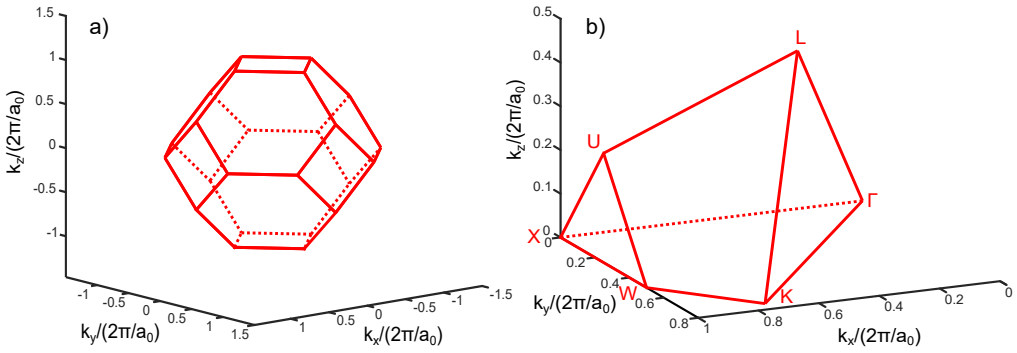

Figure 5.1: a) First Brillouin Zone and b) Irreducible Wedge of the Face-Centered Cubic reciprocal lattice. The symmetry points are indicated in plot b).

Since the electron's effective mass in GaAs is very low ($0.063m_0$ [91]), two cubic meshes have been used to discretize the IW. The parameter used for building the meshes is the number of divisions along the $\Gamma - X$ direction: a fine mesh with $ndiv = 300$ has been built around the Γ valley, from $\vec{k}$ = (0, 0, 0) to $\vec{k}$ = (0.1, 0.1, 0.1). The total number of points in the mesh is 6545; a coarse mesh with $ndiv = 40$, for a total of 6281 $\vec{k}$-points, has been employed to discretize the remaining part of the IW.

Each $\vec{k}$-point inside the IW has an associated weight, that corresponds to the number of identical $\vec{k}$-points in the FBZ: for instance the weight of Γ = (0, 0, 0) is 1, while the weight of L = (0.5, 0.5, 0.5) is 8. The pseudo-code for the computation of the weights is here reported.

```
foreach k in IW
  A = [kx ky kz];
  B = [-kx ky kz];
  C = [kx -ky kz];
  D = [kx ky -kz];
  E = [-kx -ky kz];
  F = [-kx ky -kz];
  G = [kx -ky -kz];
  H = [-kx -ky -kz];

  % perms() computes all the permutations of a vector

  W = [perms(A); perms(B); perms(C); perms(D); ...
       perms(E); perms(F); perms(G); perms(H)];

  Remove duplicate rows from matrix W

  weight = number of rows of matrix W
end
```

It is worth noting that a similar code is used also to reconstruct the dispersion energy of the entire FBZ starting from the one of the IW. Moreover, the above algorithm only provides the weight of each $\vec{k}$-point in the IW, but not the weight of the $\vec{k}$-points at the edges of the FBZ. In principle, this could be a problem when evaluating the transport in a valley located at the edge of the FBZ, such as the L-valley. However, not considering the weight of the $\vec{k}$-points at the edges of the FBZ has been compensated by the fine discretization that we have employed.

The band structure of GaAs (four conduction bands and four valence bands for a total of sixteen bands, since each band is computed for spin up and spin down) has been calculated for $\vec{k}$-points in the IW by using the Local Empirical Pseudopotentials Method (EPM) described by [58]. The EPM Hamiltonian is reported in Eq. 5.4 and its local term is expanded in Eqs. 5.5. In our calculations $V_{NL}(\vec{r}, E) = 0$.

$$\mathbf{H}_{EPM} = -\frac{\hbar^2}{2m_0}\nabla^2 + V_L(\vec{r}) + V_{NL}(\vec{r}, E), \tag{5.4}$$

$$V_L(\vec{r}) = \sum_{\vec{G}} \left[V_S(|\vec{G}|)\cos(\vec{G}\cdot\vec{\tau}) + jV_A(|\vec{G}|)\sin(\vec{G}\cdot\vec{\tau}) \right] e^{-j\vec{G}\cdot\vec{r}}, \tag{5.5}$$

where $\vec{G}$ are the vectors of the reciprocal space and $\vec{\tau} = \frac{a_0}{8}(1,1,1)$ [58]. The summation over $\vec{G}$ in Eq. 5.5 is usually truncated to the first neighbors of the unit cell of the reciprocal lattice, that means that $V_S(|\vec{G}|)$ and $V_A(|\vec{G}|)$ have to be evaluated only on $|\vec{G}| = \sqrt{3}, \sqrt{4}, \sqrt{8}, \sqrt{11}$.

Spin Orbit Interaction has been included in our calculations by using the method proposed by [103]. The Spin Orbit Hamiltonian, that is summed to

the spatial part (Eq. 5.4), is given by

$$\mathbf{H}_{SO}^{ss'}(\vec{K},\vec{K'}) = (\vec{K}\times\vec{K'})\cdot\vec{\sigma_{ss'}}\left(\frac{a_0^2}{2\pi}\right)\left\{-j\lambda_S(\vec{K},\vec{K'})\cos\left[(\vec{K}-\vec{K'})\cdot\tau\right]\right. \\ \left.+\lambda_A(\vec{K},\vec{K'})\sin\left[(\vec{K}-\vec{K'})\cdot\tau\right]\right\}, \tag{5.6}$$

where

$$\lambda_{S,A} = \frac{\lambda_1 \pm \lambda_2}{2}, \tag{5.7}$$

$$\lambda_1(\vec{K},\vec{K'}) = \mu B(\vec{K})B(\vec{K'}), \tag{5.8}$$

$$\lambda_2(\vec{K},\vec{K'}) = \alpha\mu B(\vec{K})B(\vec{K'}), \tag{5.9}$$

$$B(\vec{K}) = \vec{K}\frac{5-k_\zeta^2}{5\left[1+k_\zeta^2\right]^4}, \tag{5.10}$$

$$k_\zeta = \frac{a_B}{\zeta}. \tag{5.11}$$

In Eqs. 5.6-5.11, $\vec{K} = \vec{k} + \vec{G}$, $\vec{K'} = \vec{k} + \vec{G'}$, s and s' are the spin states, $\vec{\sigma}$ are the Pauli matrices and $a_B \simeq 5.29 \times 10^{-11}$ m is the Bohr radius [103].

The code used for the implementation of EPM has been developed by [104] and the parameters that we adopted are listed in Tables 5.1 and 5.2, where the energies of the Form Factors are expressed in Rydberg [Ry] (1 Ry $\simeq$ 13.6 eV).

$V_S(\sqrt{3})$ [Ry]	$V_S(\sqrt{4})$ [Ry]	$V_S(\sqrt{8})$ [Ry]	$V_S(\sqrt{11})$ [Ry]
-0.23	0	0.01	0.055
$V_A(\sqrt{3})$ [Ry]	$V_A(\sqrt{4})$ [Ry]	$V_A(\sqrt{8})$ [Ry]	$V_A(\sqrt{11})$ [Ry]
0.07	0.05	0	0.01

a_0 [m]	E_g [eV]
0.564×10^{-9}	1.424

Table 5.1: Empirical Pseudopotential parameters for GaAs used in the code of [104].

ζ	μ [Ry]	α
5.34	0.0008	1.37

Table 5.2: Spin Orbit Interaction parameters for GaAs used in the code of [104].

It is worth noting that, in principle, Spin Orbit Interaction should be included in the calculations together with the nonlocal corrections for the pseudopotentials, as described in [59, 103]. Since in our calculations we have set $V_{NL}(\vec{r},E) = 0$ in Eq. 5.5, we treat the bandgap (E_g) as a free parameter: a rigid shift in energy of the eigenvalues has been imposed so that the difference between the minimum of the first conduction band and the maximum of the last valence band is equal to the desired E_g (see Tab. 5.1).

The band structure of GaAs is stored into two bi-dimensional matrices (one for the fine mesh and one for the coarse mesh), where the row number is the band index and the column number is the index of the $\vec{k}$-point in the mesh.

Figure 5.2 compares the band diagram computed by using our algorithm with the one calculated by [105], showing an excellent mutual agreement.

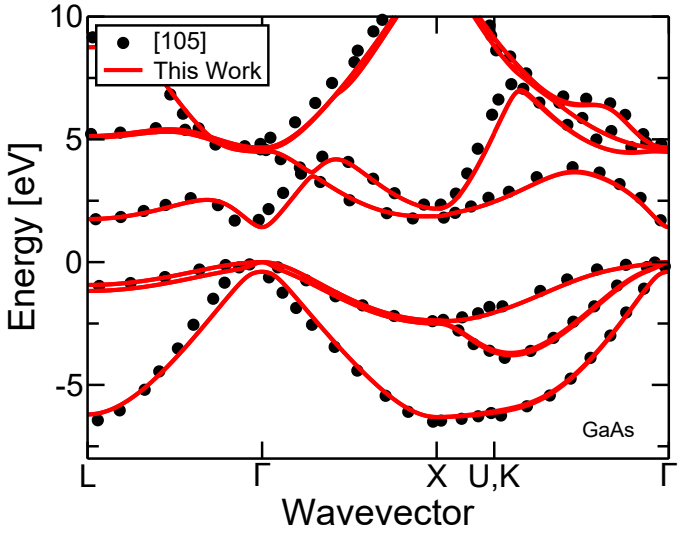

Figure 5.2: Comparison between the Band Structure of GaAs computed by employing the Empirical Pseudopotential Method, including Spin Orbit Interaction, by using the code of [104] with the parameters of Tabs. 5.1 and 5.2 (red lines), and the one calculated by [105] (black circles).

Finally, once that the band structure is computed in the IW, the dispersion relation is reconstructed for the entire FBZ and a centered finite difference scheme is employed to compute the first and second derivative of the energy with respect to $\vec{k}$. The results, for each direction, are stored in a bi-dimensional matrix with the same convention used to store the energies.

Some useful band structure parameters for bulk GaAs, namely the electron's effective mass ($m_{e,\Gamma}$) and the nonparabolicity coefficient (α_Γ in the Γ valley and the energy distances $\Gamma - L$ and $\Gamma - X$, have been extracted from our calculations and are compared in Tab. 5.3 with the results obtained by other authors [106, 107, 108], reporting a good mutual agreement, in particular with [106]. This result is expected, since in this work we have used the same parameters of [106] for the EPM (see Tab. 5.1).

Ref.	Method	$m_{e,\Gamma}$ $[m_0]$	α_Γ $[\text{eV}^{-1}]$	$\Gamma - L$ [eV]	$\Gamma - X$ [eV]
This Work	EPM	0.060	0.84	0.329	0.444
[106]	EPM	0.063	0.834	0.323	0.457
[107]	DFT	0.083	0.75	0.12	0.52
[107]	TB	0.067	0.73	0.288	0.49
[107]	$\mathbf{k}\cdot\mathbf{p}$	0.067	0.65	-	-
[108]	-	0.067	-	0.28	0.48

Table 5.3: Band structure parameters for bulk GaAs.

Figure 5.3 compares the dispersion relation of the Γ valley of GaAs computed in this work with the analytical dispersion relation of Eq. 2.79.

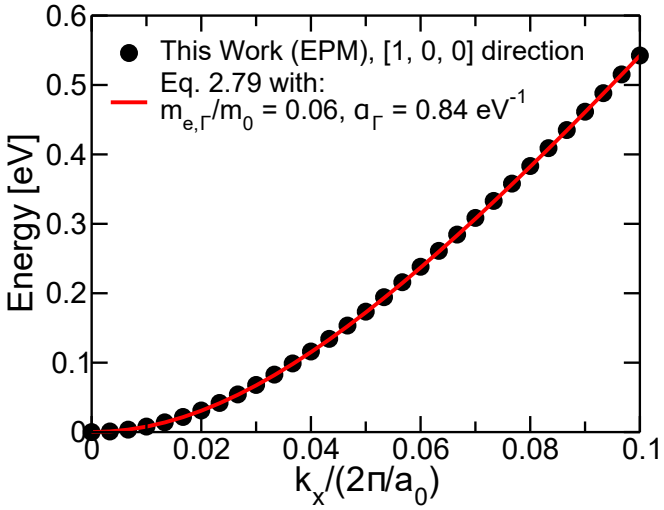

Figure 5.3: Comparison between the Γ valley of GaAs, along the $[1, 0, 0]$ direction, computed in this work by using the EPM with the parameters of Tabs. 5.1 and 5.2 and the analytical dispersion relation of Eq. 2.79 with the parameters of Tab. 5.3.

5.1.1 Density of States

From the band structure, the Density of States (DoS) as a function of energy can be computed by

$$DoS(E) = \sum_{\vec{k} \in FBZ} \sum_{n} \delta(E - E(n, \vec{k})), \tag{5.12}$$

where n denotes the band index. Note that, since we have included Spin Orbit Interaction in our calculations, the multiplication factor 2, usually employed in the expressions for the DoS, is not present in Eq. 5.12.

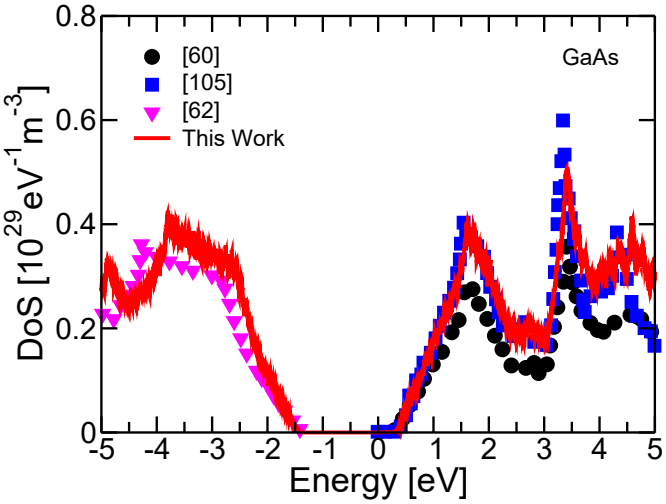

Figure 5.4: Comparison between the GaAs Density of States computed by using our code (red line) and the ones calculated by [60] (black circles), [105] (blue squares) and [62] (magenta triangle-downs).

Figure 5.4 compares the DoS of GaAs computed in this thesis with results from other authors [60, 105, 62] highlighting the mutual agreement.

While computing the DoS, it is useful also to create, for each band, a list of states at a given energy (or better, inside an energy bin centered around a given energy). As it will be shown in Section 5.4, these lists are needed to compute the initial state of the injected particles and final state after a scattering event. The pseudo-code for the creation of the lists is reported below.

```
foreach ie in Energy
  foreach k⃗ in FBZ
    foreach n
      if (|Energy(ie) − E(n, k⃗)| ≤ ΔE/2)
        list_n(ie) = [list_n(ie); (n, k⃗)];
      end
    end
  end
end
```

In our code, the Dirac's delta function has been approximated by a BOX function of width ΔE; we have set $\Delta E = 1$ meV and each state $(n, \vec{k})$ is encoded in the list with a single number by using the following convention

$$(n, \vec{k}) = k \times OFFSET + n, \tag{5.13}$$

where k is the index of the wavevector $\vec{k}$ in the mesh and $OFFSET = 10$ if less than 10 bands are computed, while $OFFSET = 100$ otherwise.

5.2 Carrier-Phonon Scattering Rates

The approach followed to compute the carrier-phonon scattering rates is the one proposed in [60]. Note that, in all the following expressions, the upper signs corresponds to phonon emission, while the lower sign stands for phonon absorption.

5.2.1 Acoustic and Nonpolar Optical Phonons

The carrier-phonon scattering rate, $SR_\eta(\vec{k_1}, n_1)$, between a carrier with wavevector $\vec{k_1}$ in the n_1-th band and acoustic or nonpolar optical phonons with polarization η (LA = Longitudinal Acoustic, TA = Transverse Acoustic, TO = Transverse Optical) with different wavevector $\vec{q}$ has been computed by using the Fermi golden rule, namely

$$\begin{aligned} SR_\eta(\vec{k_1}, n_1) = \sum_{\vec{q}} \frac{\pi}{\rho\omega_{\eta,\vec{q}}} \Delta_{\eta,n_2}(\vec{q})^2 |\mathcal{I}(n_1, n_2; \vec{k_1}, \vec{k_2})|^2 \cdot \\ \cdot \delta(E(n_1, \vec{k_1}) - E(n_2, \vec{k_2}) \mp \hbar\omega_{\eta,\vec{q}}) \left(n_{\eta,\vec{q}} + \frac{1}{2} \pm \frac{1}{2} \right) \end{aligned} \tag{5.14}$$

where $(n_2, \vec{k_2})$ is final state, ρ is the density of the semiconductor, $\omega_{\eta,\vec{q}}$ is the angular frequency of the phonon with polarization η and wavevector $\vec{q}$, $\mathcal{I}(n_1, n_2; \vec{k_1}, \vec{k_2})$ is the overlap integral between the wavefunctions of the initial and final states [45], $\varphi_{n_1,\vec{k_1}}(\vec{r})$ and $\varphi_{n_2,\vec{k_2}}(\vec{r})$, respectively

$$\mathcal{I}(n_1, n_2; \vec{k_1}, \vec{k_2}) = \int_{cell} \varphi^*_{n_2,\vec{k_2}}(\vec{r}) \varphi_{n_1,\vec{k_1}}(\vec{r}) e^{j\vec{G}\cdot\vec{r}} d\vec{r} \tag{5.15}$$

and $n_{\eta,\vec{q}}$ is the phonon occupation number, which can be computed through the Bose-Einstein relation

$$n_{\eta,\vec{q}} = \left[exp\left(\frac{\hbar\omega_{\eta,\vec{q}}}{k_b T} \right) - 1 \right]^{-1}. \tag{5.16}$$

Momentum conservation implies:

$$\vec{q} = \vec{k_1} \mp \vec{k_2} + \vec{G}_0, \tag{5.17}$$

where $\vec{G}_0$ is a reciprocal lattice vector which translates, when necessary, $\vec{q}$ to the first Brillouin zone (*umklapp processes* [45]).

Consistently with [60], for acoustic phonons the coupling constant has been approximated as $\Delta_{\eta,n_2}(\vec{q}) = \Delta_{ac}|\vec{q}|$ and the following dispersion relation was used:

$$\hbar\omega_{\eta,\vec{q}}(\vec{q}) = \begin{cases} \hbar\omega_{\eta,max} \left[1 - cos\left(\frac{|\vec{q}|a_0}{4} \right) \right]^{\frac{1}{2}}, & \text{if } |\vec{q}| \leq 2\pi/a_0 \\ \hbar\omega_{\eta,max}, & \text{if } |\vec{q}| > 2\pi/a_0 \end{cases} \tag{5.18}$$

where $\omega_{\eta,max} = 4c_\eta/a_0$ (c_η is the sound velocity of a phonon with polarization η).

For optical phonons the coupling constant has been approximated as $\Delta_{\eta,n_2}(\vec{q}) = \Delta K_{op}$ and the dispersion relation has been ignored by setting $\hbar\omega_{\eta,\vec{q}}(\vec{q}) = \hbar\omega_{op}$ regardless of $\vec{q}$.

The sum over $\vec{q}$ of Eq. 5.14 has been then translated into an integral over $\vec{k_2}$, namely

$$\begin{aligned} SR_\eta(\vec{k_1}, n_1) = & \frac{1}{(2\pi)^3} \int_{\vec{k_2}\in 1BZ} \sum_{n_2} \frac{\pi}{\rho\omega_{\eta,\vec{q}}} \Delta_{\eta,n_2}(\vec{q})^2 |\mathcal{I}(n_1, n_2; \vec{k_1}, \vec{k_2})|^2 \cdot \\ & \cdot \delta(E(\vec{k_1}, n_1) - E(\vec{k_2}, n_2) \mp \hbar\omega_{\eta,\vec{q}}) \left(n_{\eta,\vec{q}} + \frac{1}{2} \pm \frac{1}{2} \right), \end{aligned} \tag{5.19}$$

where $\vec{q}$ is determined by the momentum conservation (Eq. 5.17).

It is worth noting that, following [46], for acoustic phonons in the $|\vec{q}| \to 0$ limit, the elastic and energy equipartition approximation has been used and Eq. 5.19 becomes

$$\begin{aligned} SR_{LA,TA}(\vec{k_1}, n_1) = & \frac{1}{(2\pi)^3} \frac{2\pi k_b T \Delta_{ac}^2}{\rho\hbar c_\eta} \int_{\vec{k_2}\in 1BZ} \sum_{n_2} |\mathcal{I}(n_1, n_2; \vec{k_1}, \vec{k_2})|^2 \cdot \\ & \cdot \delta(E(n_1, \vec{k_1}) - E(n_2, \vec{k_2}, n_2)) \end{aligned} \tag{5.20}$$

The pseudo-code for the computation of $SR_\eta(\vec{k_1}, n_1)$ for all $\vec{k_1} \in$ IW (Eqs. 5.19 and 5.20) in the case of phonon emission is here reported.

```
foreach k1⃗ in IW
  foreach n1
    foreach k2⃗ in FBZ
      foreach n2

        q⃗ = k1⃗ − k2⃗;

        if (q⃗ is not in the FBZ)
          Compute G0⃗ so that
          q⃗ = q⃗ + G0⃗ ∈ FBZ
        end

        if (η == LA || TA)
          Compute phonon angular frequency ω_{η,q⃗} and
          energy E(q⃗) from dispersion relation;
        else
          E(q⃗) = ħω_op;
        end

        if (|E(n1, k1⃗) − E(n2, k2⃗) − E(q⃗)| ≤ ΔE/2)
          if (η = LA || TA)
            if (|q⃗| != 0)
              SR_{em,LA,TA}(k1⃗, n1) += C1 * |q⃗|²/ω(q⃗) * (n_{η,q⃗} + 1) * |I|²;
            else
              % Use elastic and energy
              % equipartition approximation
              SR_{em,LA,TA}(k1⃗, n1) += C2 * |I|²;
            end
          else
              SR_{em,TO}(k1⃗, n1) += C3 * (n_{η,q⃗} + 1) * |I|²;
          end
        end
      end
    end
  end
end
```

C_1 is the constant for LA and TA phonons and it is equal to:

$$C_1 = \frac{1}{(2\pi)^3}\frac{1}{q\Delta E}\left(\frac{2\pi}{a_0 ndiv}\right)^3 \frac{\pi}{\rho}\left(\frac{2\pi}{a_0}\right)^2 (q\Delta_{ac})^2 \tag{5.21}$$

C_2 is the constant for LA and TA phonons in the $|\vec{q}| \to 0$ limit and it is equal to:

$$C_2 = \frac{1}{(2\pi)^3}\frac{1}{q\Delta E}\left(\frac{2\pi}{a_0 ndiv}\right)^3 \frac{2\pi}{\hbar}\frac{k_b T}{\rho c_\eta}(q\Delta_{ac})^2 \tag{5.22}$$

C_3 is a constant for nonpolar and TO phonons and it is equal to:

$$C_3 = \frac{1}{(2\pi)^3}\frac{1}{q\Delta E}\left(\frac{2\pi}{a_0 ndiv}\right)^3 \frac{\pi}{\rho}(q\Delta K_{op})^2 \frac{1}{\hbar\omega_{op}} \tag{5.23}$$

In Eqs. 5.21-5.23, all the energies are expressed in eV and, since the IW is dicretized by using two cubic meshes with different $ndiv$, we point out that the value of $ndiv$ to use in these equations is the one of the mesh where the final state $(n_2, \vec{k}_2)$ lies. The constants C_1, C_2 and C_3 derive from the transformation of the integral over $\vec{k}_2$ in Eq. 5.19 into a sum over the $\vec{k}_2$-points in the mesh that we have built.

Carrier-phonon scattering rates with acoustic or nonpolar optical phonons are stored in four bi-dimensional matrices (acoustic phonon emission, acoustic phonon absorption, nonpolar optical phonon absorption, nonpolar optical phonon emission), where the row index corresponds to the index of the $\vec{k}$-point in the IW and the column index is associated to the band index. During the computation, for each initial state $(n_1, \vec{k}_1)$ and for each of the four categories used to store the scattering rates, the maximum value of the argument of the summation over n_2 in Eq. 5.19 is stored. This values will be used for the selection of the final state after the scattering event, as it will be described in Section 5.4.2.

5.2.2 Polar Optical Phonons

In GaAs and other III-V compound semiconductors, the carrier-phonon scattering with Longitudinal Optical (LO) phonons has to be take into account the polar nature of these crystals. Therefore, following [60], the scattering rate, $SR_{po}(\vec{k}_1, n_1)$, for a carrier with wavevector $\vec{k}_1$ in the band n_1 and a polar optical phonon is computed as

$$\begin{aligned} SR_{po}(\vec{k}_1, n_1) =& \frac{2\pi}{\hbar}\sum_{\vec{q}} \frac{q^2 F_{po}^2}{|\vec{q}|^2}\Delta_{\eta,n_2}(\vec{q})^2 |\mathcal{I}(n_1, n_2; \vec{k}_1, \vec{k}_2)|^2 \cdot \\ & \cdot\delta(E(n_1, \vec{k}_1) - E(n_2, \vec{k}_2) \mp \hbar\omega_{op})\left(n_{op} + \frac{1}{2} \pm \frac{1}{2}\right). \end{aligned} \tag{5.24}$$

F_{po} is the polar coupling constant which is given by

$$F_{po}^2 = \frac{\hbar\omega_{op}}{4}\left(\frac{1}{\epsilon_\infty} - \frac{1}{\epsilon_0}\right), \tag{5.25}$$

where ϵ_∞ and ϵ_0 are the optical and static dielectric functions, respectively.

Similarly to what we have done for Eq. 5.14 in Section 5.2.1, the implementation of Eq. 5.24 is based on the transformation of the sum over $\vec{q}$ in an integral over the wavevector of the final state $\vec{k}_2$ and then to a sum over the discretized states. The pseudo-code for the case of phonon emission is reported below.

```
foreach k1⃗ in IW
  foreach n1
    foreach k2⃗ in FBZ
      foreach n2

        E(q⃗) = ħω_op ;
        q⃗ = k1⃗ − k2⃗ ;

        if (q⃗ is not in the FBZ)
          Compute G0⃗ so that
          q⃗ = q⃗ + G0⃗ ∈ FBZ
        end

        if (|E(n1, k1⃗) − E(n2, k2⃗) − E(q⃗)|) ≤ ΔE/2)
          SR_em,po(k1⃗, n1)+ = C4/|q⃗|²/ω_op ∗ (n_η,q⃗ + 1) ∗ |I|² ;
        end

      end
    end
  end
end
```

where

$$C_4 = \frac{1}{(2\pi)^3}\frac{1}{q\Delta E}\left(\frac{2\pi}{a_0 ndiv}\right)^3 \frac{2\pi}{\hbar} q^2 F_{op}^2 \left(\frac{2\pi}{a_0}\right)^{-2}. \tag{5.26}$$

The value of $ndiv$ to use in Eq. 5.26 is the one of the mesh of the final state.

It is worth noting that, even if in this work we have computed the scattering rate with polar optical phonons for all the $(n, \vec{k})$ states in the IW, this scattering mechanism usually affects the transport only at low energy states [106].

Carrier-phonon scattering rates with polar optical phonons are saved in two bi-dimensional matrices (for phonon emission and absorption, respectively), where the row index corresponds to the index of the $\vec{k}$-point in the IW and the column index is associated to the band index. During the computation, for each initial state $(n_1, \vec{k}_1)$ and for both phonon emission and absorption, the maximum value of the scattering rate between the initial state and every possible final state is saved. This values will be used for the selection of the state after scattering, as it will be described in Section 5.4.2.

5.2.3 Results

The total carrier-phonon scattering rate for each initial state $n_1, \vec{k}_1)$ can be computes as

$$SR_{phonon}(\vec{k}_1, n_1) = \sum_{\eta=LA,TA,TO} SR_\eta(\vec{k}_1, n_1) + SR_{po}(\vec{k}_1, n_1). \tag{5.27}$$

The carrier-phonon scattering rate as a function of energy can then be found by integrating over all the possible initial states

$$SR_{phonon}(E) = \frac{1}{DoS(E)} \int_{\vec{k_1} \in FBZ} \sum_{n_1} SR_{phonon}(\vec{k_1}, n_1) \delta(E - E(n_1, \vec{k_1}) d\vec{k_1}). \tag{5.28}$$

For the computation of the overlap integrals in Eqs. 5.19 and 5.24 we have employed the Rigid Ion approximation [60] for both electrons and holes (Eq. 5.29).

$$\mathcal{I}(n_1, n_2; \vec{k}_1, \vec{k}_2) = \mathcal{I}(|\vec{q}|) = \frac{3}{(R_s|\vec{q}|)^3} \left[\sin(R_s|\vec{q}|) - R_s|\vec{q}| \cos(R_s|\vec{q}|)\right], \tag{5.29}$$

where $R_s = 2\pi \sqrt[3]{3/16\pi}$. Moreover, scattering events conserve the spin and, for holes, we have imposed that the final state of a carrier-phonon scattering event is in the same band of the initial state [109] (see Appendix B). Figure 5.5 compares the carrier-phonon scattering rates as functions of energy computed by us by using the parameters in Tab. 5.4 and $\Delta E = 4$ meV with the calculations of other authors [60, 105, 61, 62]. Results are not always coincident but, as it will be shown in Section 5.4.3, these scattering rates all yield similar drift velocities as a function of the applied electric field.

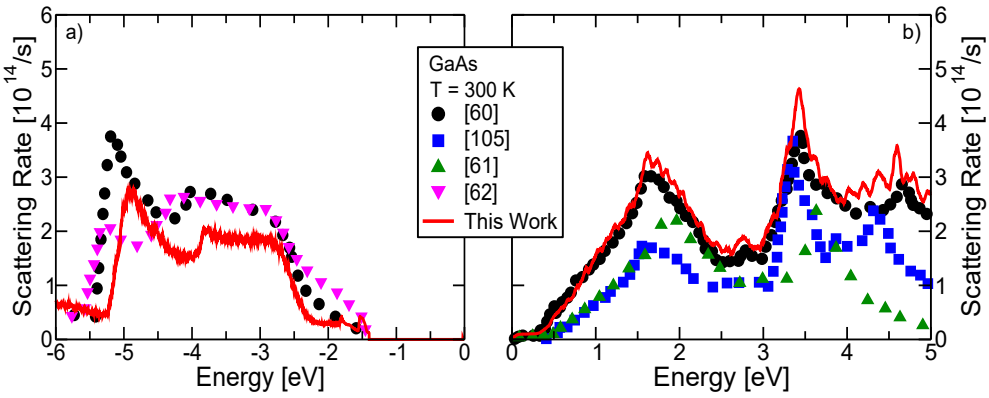

Figure 5.5: Carrier-phonon scattering rates for a) holes and b) electrons as functions of energy. Our results (red lines), obtained by using the parameters in Tab. 5.4 and $\Delta E = 4$ meV, are compared with the calculations of [60] (black circles), [105] (blue squares), [61] (green triangle-ups) and [62] (magenta triangle-downs).

ρ [kg/m^3]	c_l [m/s]	c_t [m/s]	ϵ_0	ϵ_∞
5360	5240	3340	12.9	10.92

$D_{ac,h}$ [eV]	$\Delta K_{op,h}$ [eV/m]	$D_{ac,e}$ [eV]	$\Delta K_{op,e}$ [eV/m]
4.5	8×10^{10}	$5\sqrt{2}$	2.1×10^{10}

Table 5.4: Deformation potentials and other parameters used for the computation of the carrier-phonon scattering rates in GaAs.

5.3 Impact Ionization

The impact ionization mechanisms (see Fig. 5.6) consists of a Coulomb interaction between two electrons: one in the conduction band (1) and one in the valence band (4). The energy exchange promotes the electron in the valence band to the conduction band (3), thus generating one electron-hole pair, while the primary electron falls to a less energetic state (2).

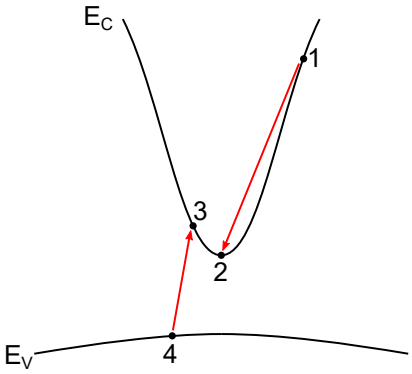

Figure 5.6: Schematic representation of the impact ionization mechanism for a *hot* electron in a direct bandgap semiconductor. The primary electron (1) in the conduction band interacts with an electron in the valence band (4). The process ends with two secondary electrons in the conduction band (2, 3) and a secondary hole in the valence band (4).

During these transitions, both energy and momentum have to be conserved, that implies

$$\vec{k}_1 + \vec{k}_4 + \vec{G}_0 = \vec{k}_2 + \vec{k}_3, \tag{5.30}$$

where $\vec{G}_0$ is a reciprocal lattice vector that translates a $\vec{k}$-point into the corresponding point inside the FBZ.

The impact ionization scattering rate for a carrier in the state $(n_1, \vec{k}_1)$ can be found by using the Fermi golden rule [110]

$$\begin{aligned} SR_{ii}(\vec{k}_1, n_1) =& 2\frac{2\pi}{\hbar}\frac{\Omega^2}{(2\pi)^6}\int\int \sum_{n_2,n_3,n_4} T_{ii}(n_1,\vec{k}_1,n_2,\vec{k}_2,n_3,\vec{k}_3,n_4,\vec{k}_4)\cdot \\ & \cdot \delta(E_1 + E_4 - E_2 - E_3)d\vec{k}_2 d\vec{k}_3, \end{aligned} \tag{5.31}$$

where Ω is the crystal volume, $E_1 = E(n_1, \vec{k}_1)$, $E_2 = E(n_2, \vec{k}_2)$, $E_3 = E(n_3, \vec{k}_3)$, $E_4 = E(n_4, \vec{k}_4)$ and $T_{ii}(n_1, \vec{k}_1, n_2, \vec{k}_2, n_3, \vec{k}_3, n_4, \vec{k}_4)$ is the so-called *matrix element*. The integral over $\vec{k}_4$ in Eq. 5.31 is eliminated by the momentum, conservation, namely

$$\vec{k}_4 = \vec{k}_2 + \vec{k}_3 - \vec{k}_1 - \vec{G}_0. \tag{5.32}$$

In principle, T_{ii} depends on the wavefunctions of the initial and final states and on the screened Coulomb potential between states 1-4 and 2-3 [110, 111]. In this work, we have decided to exploit the isotropic nature of GaAs and to embrace the *Constant Matrix Element approximation* [112]. Therefore, the

matrix element $T_{ii}(n_1, \vec{k}_1, n_2, \vec{k}_2, n_3, \vec{k}_3, n_4, \vec{k}_4)$ has been substituted by the constants $T_{ii,h}$ and $T_{ii,e}$ for the computation of the hole's and electron's impact ionization scattering rates, respectively.

The pseudo-code for the computation of the impact ionization scattering rate for an electron in the state $(n_1, \vec{k}_1)$ is

```
foreach k1 in IW
  foreach n1 in CB
    foreach k2 in FBZ
      foreach n2 in CB
        foreach k3 in FBZ
          foreach n3 in CB

            k4 = k2 + k3 - k1 ;

            if (k4 is not in the FBZ)
              Compute G0 so that
              k4 = k4 - G0 ∈ FBZ
            end

            foreach n4 in VB
              if (|E1 + E4 - E2 - E3)| ≤ ΔE/2)
                SRii(k1, n1)+ = Cii * Tii,e ;
              end
            end

          end
        end
      end
    end
  end
end
```

It is worth noting that the quantity that we denote as T_{ii} in the above algorithm are not simply the matrix elements, but they also include all the constants of Eq. 5.31 that do not scale with the mesh parameters nor with the ΔE that is chosen for the BOX function that approximates the Dirac's delta function. On the other hand. the constant C_{ii} depends on ΔE and on $ndiv$, namely

$$C_{ii} = \frac{1}{ndiv^6} \frac{1}{q\Delta E}. \tag{5.33}$$

To reduce the time needed for the computation of the impact ionization scattering rates, we have discretized the FBZ with a third mesh with $ndiv = 20$ and calculated SR_{ii} only for the $\vec{k}$-points that belong to this mesh. Then, we associated to the $\vec{k}$-points of the fine and coarse meshes described in Section 5.1 the impact ionization scattering rate of the closest $\vec{k}$-point in the mesh with $ndiv = 20$.

The impact ionization scattering rates as functions of the energy of the primary carrier (E_i) can be found by integrating over all the possible initial states

$$SR_{ii}(E_i) = \frac{\sum_{n_1} \int SR(\vec{k}_1, n_1)\delta(E_i - E(\vec{k}_1, n_1))d\vec{k}_1}{\sum_{n_1} \int \delta(E_i - E(\vec{k}_1, n_1))d\vec{k}_1}. \tag{5.34}$$

Figure 5.7 compares $SR_{ii,e}(E_i)$ and $SR_{ii,h}(E_i)$ obtained by using our code ($\Delta E = 4$ meV) with the results of other authors [105, 113, 114], confirming the validity of the proposed algorithm.

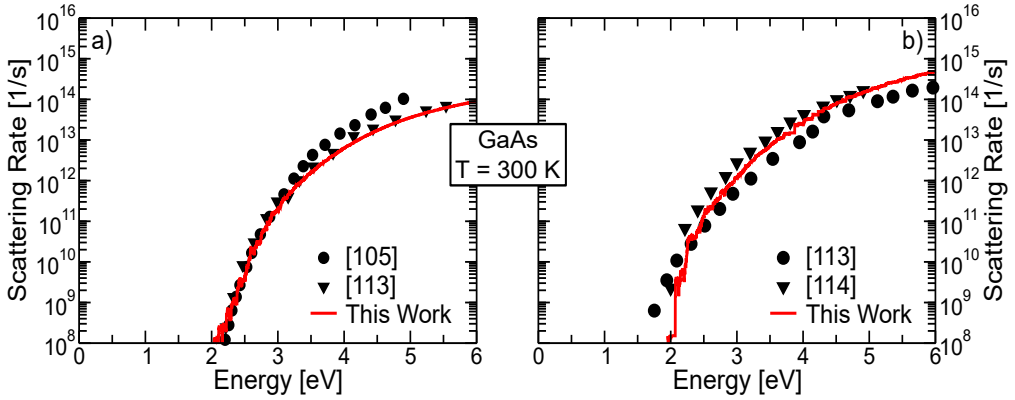

Figure 5.7: a) Electron and b) hole impact ionization scattering rates in GaAs as a function of energy. Our results (red lines), obtained by using the Constant Matrix Element approximation [112], are compared with the scattering rates computed by other authors [105, 113, 114].

The matrix elements that we have employed for the calculation of the hole's and electron's impact ionization scattering rates, to reproduce the results of other authors [105, 113, 114], are reported in Tab. 5.5.

$T_{ii,h}$ [J/s]	$T_{ii,e}$ [J/s]
4.5×10^{-6}	8.0×10^{-7}

Table 5.5: Constant Matrix Elements used for the computation of the hole's and electron's impact ionization scattering rates in GaAs.

Together with the scattering rates, we have computed also the energy distribution of the secondary electrons $E_{e2}(E_i, E_f)$ and holes ($E_{h4}(E_i, E_f)$), that are needed to assign to the generated particles the appropriate energy (E_f) by using the expressions

$$E_{e2}(E_i, E_f) = \frac{\sum_{n_1,n_2,n_3,n_4} \int\int\int T_{ii,e}\delta(E_i - E_1)\delta(E_1 + E_4 - E_2 - E_3)\delta(E_f - E_2)d\vec{k}_1 d\vec{k}_2 d\vec{k}_3}{\sum_{n_1,n_2,n_3,n_4} \int\int\int T_{ii,e}\delta(E_i - E_1)\delta(E_1 + E_4 - E_2 - E_3)d\vec{k}_1 d\vec{k}_2 d\vec{k}_3}, \tag{5.35}$$

$$E_{h4}(E_i, E_f) = \frac{\sum_{n1,n_2,n_3,n_4} \int\int\int T_{ii,e}\delta(E_i - E_1)\delta(E_1 + E_4 - E_2 - E_3)\delta(E_f - E_4)d\vec{k}_1 d\vec{k}_2 d\vec{k}_3}{\sum_{n1,n_2,n_3,n_4} \int\int\int T_{ii,e}\delta(E_i - E_1)\delta(E_1 + E_4 - E_2 - E_3)d\vec{k}_1 d\vec{k}_2 d\vec{k}_3}. \tag{5.36}$$

Sample results for an ionizing primary electron with kinetic energy 4 eV and 6 eV are shown in Fig 5.8. Similar expressions hold also for the computation of the energy distribution of secondary carriers, $E_{h2}(E_i, E_f)$ and $E_{e4}(E_i, E_f)$ in the case of hole-initiated impact ionization (Fig. 5.9).

E_{e2}, E_{h4}, E_{h2} and E_{e4} are stored in bi-dimensional matrices where the row number corresponds to the index of the initial energy, while the column number is the index of the final energy.

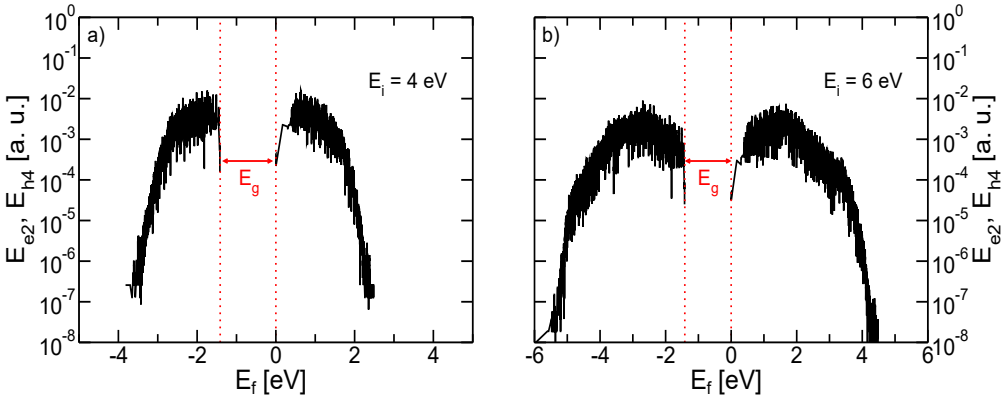

Figure 5.8: Secondary carriers' energy distributions for a ionizing electron with kinetic energy (a) 4 eV or (b) 6 eV. Positive energy refers to electrons and negative energies to holes. The computation has been performed by using Eqs. 5.35 and 5.36 with the constant matrix elements of Tab. 5.4. $\Delta E = 4$ meV and $ndiv = 20$.

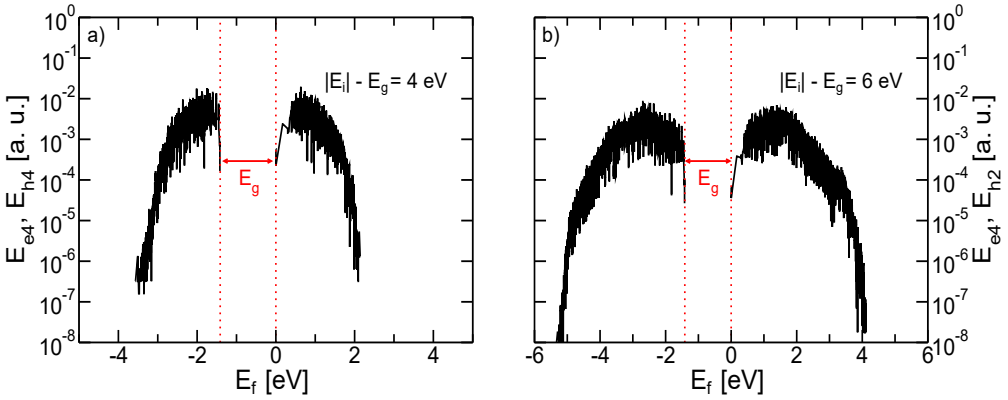

Figure 5.9: Same as Fig. 5.8 but for hole-initiated impact ionization.

5.4 The Full Band Monte Carlo Simulator

In this Section, the single particle Full Band Monte Carlo (FBMC) simulator for carriers' transport under uniform electric fields will be described. In the following Sections, no discretization is applied to the real space in order to extract the features of bulk GaAs.

5.4.1 Carriers' Injection and Motion

Each simulation begins by specifying the initial energy of carrier. For convention, negative energies are associated to holes, while positive energies to electrons.

The program then looks for all the states in the FBZ at that energy inside the lists created while computing the DoS (see Section 5.1.1) and one of these states is chosen randomly.

The equation of motion

$$\frac{d\vec{r}}{dt} = \frac{1}{\hbar}\nabla_{\vec{k}} E(n,\vec{k}) \tag{5.37}$$

$$\frac{d\vec{k}}{dt} = -\frac{q}{\hbar}\vec{E}(\vec{r}) \tag{5.38}$$

are solved by means of a self-scattering algorithm [45] where free flights alternate with scattering events. The duration of each free flight (t_{ff}) is determined according to the expression

$$t_{ff} = -\frac{1}{\Gamma_{ff}} ln(r), \tag{5.39}$$

where r is a random number uniformly distributed in the $[0,1]$ interval and

$$\Gamma_{ff} = max\left\{SR_{phonon}(\vec{k},n) + SR_{ii}(\vec{k},n)\right\}. \tag{5.40}$$

After each free flight, the updated $\vec{k}$-vector is brought back to the FBZ, if necessary, and the eight points ($\vec{k}_\lambda,\ \lambda = 1,...,8$) of the mesh that form the cube that contains the $\vec{k}$-vector are identified. The energy of the state after the free flight is then computed by using the expressions reported in [106], namely

$$E_\lambda(n,\vec{k}) = E(n,\vec{k}_\lambda) + \sum_{i=x,y,z} \frac{\partial E(n,\vec{k}_\lambda)}{\partial k_i}(k_i - k_{i,\lambda}) + \sum_{i,j=x,y,z} \frac{1}{2}\frac{\partial^2 E(n,\vec{k}_\lambda)}{\partial k_i \partial k_j}(k_i - k_{i,\lambda})(k_j - k_{j,\lambda}) \tag{5.41}$$

$$E(n,\vec{k}) = \sum_{\lambda=1}^{8} P_\lambda E_\lambda(n,\vec{k}) \tag{5.42}$$

$$P_\lambda = \left[1 - \frac{k_x - k_{x,\lambda}}{l}\right]\left[1 - \frac{k_y - k_{y,\lambda}}{l}\right]\left[1 - \frac{k_z - k_{z,\lambda}}{l}\right], \tag{5.43}$$

where l is the length of the side element of the cube. A similar procedure is done also to compute the velocity in the $\vec{k}$-point after the free flight, but a linear interpolation around each corner of the cubic mesh is performed instead of the quadratic expansion of Eq. 5.41.

Finally, during carriers' motion, the possibility of band crossing has been taken into account by checking, at the end of each free flight, energy of the states that are in the bands $n-1$ and $n+1$. When $|E(n,\vec{k}) - E(n \pm 1,\vec{k})| < 0.25$ eV, the band index after the free flight is the one of the state that minimizes the difference between the velocity of the initial state and the one of the final state.

5.4.2 Selection of the Scattering Mechanism and State After Scattering

At the end of each free flight, a scattering event occurs. The scattering mechanism (carrier-phonon, impact ionization or self-scattering) is randomly chosen according to the relative impact of a given scattering mechanisms to the total scattering rate for the initial state $(n, \vec{k})$. The program does not interpolate the scattering rates, but it associates to the state $(n, \vec{k})$ the scattering rates of the closest mesh point.

Once that the scattering mechanism is fixed, the selection of the state after scattering is performed according to the chosen scattering mechanism:

- **Acoustic Phonons**.
  Storing all the possible final states in the FBZ for all the initial states in the IW would be very demanding in terms of memory occupation, hence we have decided to apply a rejection method for the determination of the final state in the case of scattering with acoustic phonons. A candidate final state $(n_f, \vec{k_f})$ is randomly selected, by searching in the lists created in Section 5.1.1, within the energy range $[E(n, \vec{k}) - E_{\eta,max}]$ for phonon emission or within the range $[E(n, \vec{k}) + E_{\eta,max}]$ for phonon absorption, where $E_{\eta,max}$ is the maximum energy of a phonon with polarization η, according to Eq. 5.18.
  The scattering rate $SR(n, \vec{k}, n_f, \vec{k_f})$ between $(n, \vec{k})$ and $(n_f, \vec{k_f})$ is computed (Eq. 5.19).
  The final state is accepted if $r \cdot SR_{\eta,max} \leq SR(n, \vec{k}, n_f, \vec{k_f})$, where r is a random number with uniform distribution in $[0, 1]$ and $SR_{\eta,max}$ is the maximum scattering rate between the initial state and all the possible final states in the case of acoustic phonon emission or absorption (see Section 5.2.1 and the sketch in Fig. 5.10). If the final state is not accepted, a new candidate final state $(n'_f, \vec{k'_f})$ is randomly chosen and evaluated and the procedure is repeated.

- **Nonpolar and Polar Optical Phonons**.
  For the same reasoning done for acoustic phonons regarding the memory occupation of a look-up table where all the possible final states in the FBZ are stored for all the initial states in the IW, a rejection method similar to the one discussed above is adopted also for the determination of the final state in the case of scattering with optical phonons. A candidate final state $(n_f, \vec{k_f})$ is randomly selected, by searching in the lists created in Section 5.1.1, at energy $E(n, \vec{k}) - \hbar\omega_{op}$ for phonon emission or $E(n, \vec{k}) + \hbar\omega_{op}$ for phonon absorption, since optical phonons have fixed energy. The scattering rate $SR(n, \vec{k}, n_f, \vec{k_f})$ between $(n, \vec{k})$ and $(n_f, \vec{k_f})$ is computed by using Eq. 5.19 for nonpolar or Eq. 5.24 for polar optical phonons.
  The final state is accepted if $r \cdot SR_{max} \leq SR(n, \vec{k}, n_f, \vec{k_f})$, where SR_{max} is the maximum scattering rate between two states in the case of nonpolar (Section 5.2.1) or polar optical phonon (Section 5.2.2) emission or

absorption (see the sketch in Fig. 5.10). If the final state is not accepted, a new candidate final state $(n'_f, \vec{k'_f})$ is randomly chosen and evaluated and the procedure is repeated.

- **Impact ionization**. Given the energy E_i of the initial state $(n, \vec{k})$, the new state is chosen randomly according to the energy distributions of secondary carrier computed in Section 5.3. For instance, in the case of electron's impact ionization, the probability for a primary carrier with energy E_i to generate a secondary electron with energy E_f is

$$p(E_i, E_f) = \frac{E_{e2}(E_i, E_f)}{\sum_{E_f} E_{e2}(E_i, E_f)}. \tag{5.44}$$

  Cumulative probabilities are computed for all the possible final energies and the generation of a random number $r \in [0, 1]$ is used to determine E_f. A final state at energy E_f is randomly selected by searching in the lists created in Section 5.1.1. No rejection mechanism is employed and momentum conservation is neglected in the selection of the final state.

- **Self-scattering**. The final state is the initial state.

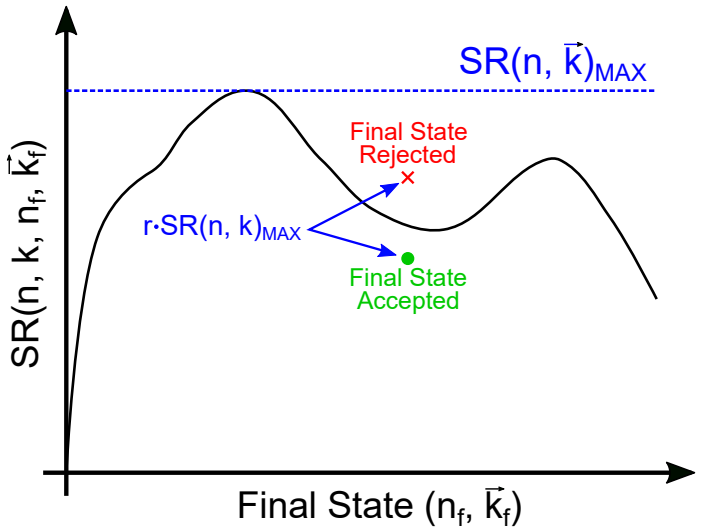

Figure 5.10: Schematic representation of the selection of the state after scattering with the rejection algorithm.

5.4.3 Results

In this Section, we present the results of Full Band Monte Carlo simulations under uniform electric field conditions for bulk GaAs. All the carriers have been injected with energy $3/2k_bT$ and the statistics (drift velocities, average energies, occupation functions and impact ionization coefficients) have been collected over $10^6 \div 10^7$ scattering events.

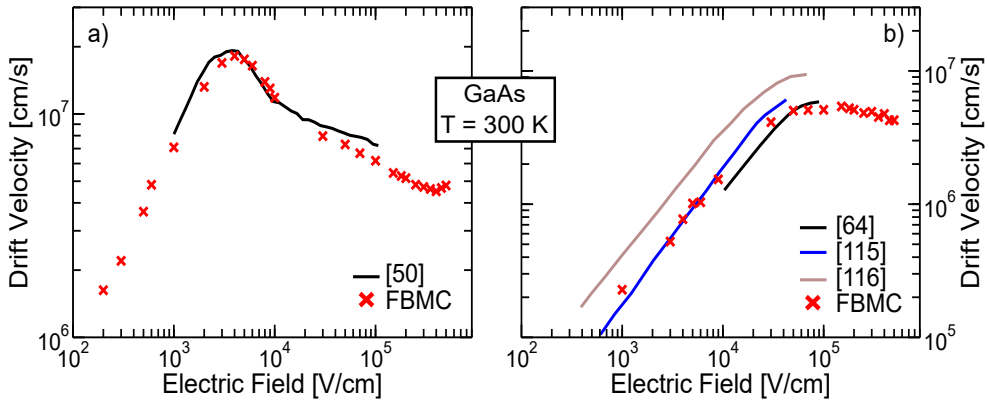

Figure 5.11: a) Electron velocity v_e and b) hole velocity v_h versus electric field (E) curves in GaAs at $T = 300$ K. FBMC results (red crosses) are compared with experimental data [50, 64, 115, 116] (solid lines).

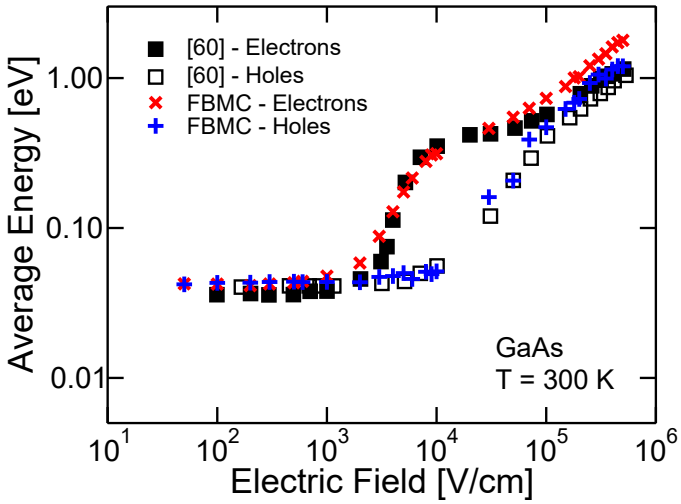

Figure 5.12: Electron's and hole's average energies as functions of the applied electric field. Results of our FBMC simulations (red crosses and (blue plus signs) are compared with the results of [60] (black filled and open squares).

Figure 5.11 compares the drift velocities of electron and holes as functions of the applied electric field extracted with our FBMC simulations with the experimental results of [50, 64, 115, 116], confirming the validity of the implementation described in Sections 5.4.1 and 5.4.2 and the choice of parameters for the computation of the band structure (Tabs. 5.1, 5.2) and of the scattering rates (Tabs. 5.4, 5.5).

Figure 5.12 compares the average energies for electrons and holes as functions of the applied electric field extracted with our FBMC simulations with the results of FBMC simulations by [60]. The agreement between the two models is satisfactory.

The impact ionization coefficients corresponding to the scattering rates in Fig. 5.7 are extracted from FBMC simulations with two different methods: namely, either as the reciprocal of the average distance $\langle l \rangle$ between consecutive

impact ionization events

$$\alpha = \frac{1}{\langle l_e \rangle}, \tag{5.45}$$

or by using the expression (valid for electrons)

$$\alpha = \frac{\int_0^{+\infty} SR_{II,e}(E) F_{occ}(E) dE}{v_e \int_0^{+\infty} F_{occ}(E) dE}, \tag{5.46}$$

where $SR_{II,e}(E)$ and $F_{occ}(E)$ are, respectively, the electron's impact ionization scattering rate and the occupation function as a function of the energy W, while v_e is the drift velocity. Similar equations are used also for the hole impact ionization coefficient β. The two methods are compared in Fig. 5.13 and give similar results that are in an overall good agreement with experimental data [17], and with the impact ionization coefficients used in the EBHDM described in Chapter 3 [69].

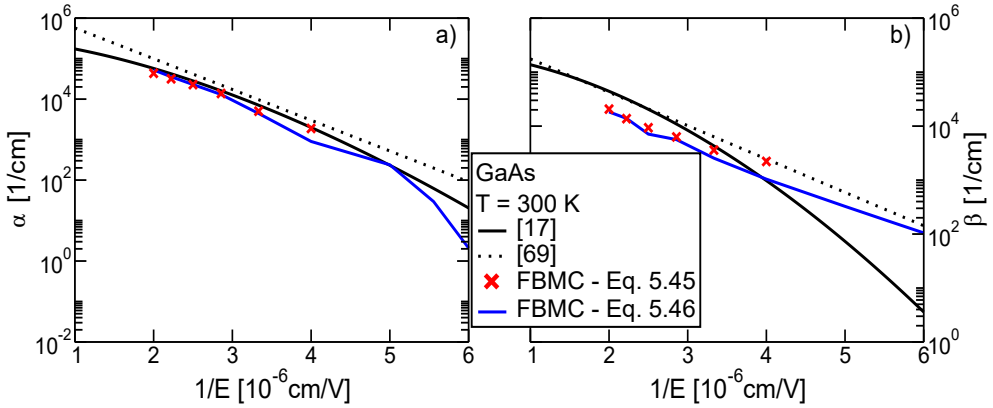

Figure 5.13: a) α and b) β versus the reciprocal of the electric field in GaAs at $T = 300$ K. FBMC (Eq. 5.45 (red crosses) or Eq. 5.46 (blue solid line)) is compared with experiments [17] (black solid) and with α and β used in [69] (black dotted line).

Figure 5.14 shows the histograms of the distance between consecutive electron's ionizations (l_e). Similarly to what has been done in [61], the histograms have been normalized to extract the probability density functions of l_e ($PDF(l_e)$). The $PDF(l_e)$ has been computed at different electric fields with the same FBMC simulations used for the extraction of α in bulk GaAs (Fig. 5.13).

In the framework of the local model [1], the analytical expression for $PDF(l_e)$ is

$$PDF(l_e) = \alpha \cdot exp\left(-\alpha l_e\right), \tag{5.47}$$

since $exp\left(-\alpha l_e\right)$ is the probability for an electron to travel across a distance equal to l_e without ionizing, while αdl_e is the impact ionization probability in the incremental distance dl_e that is after l_e.

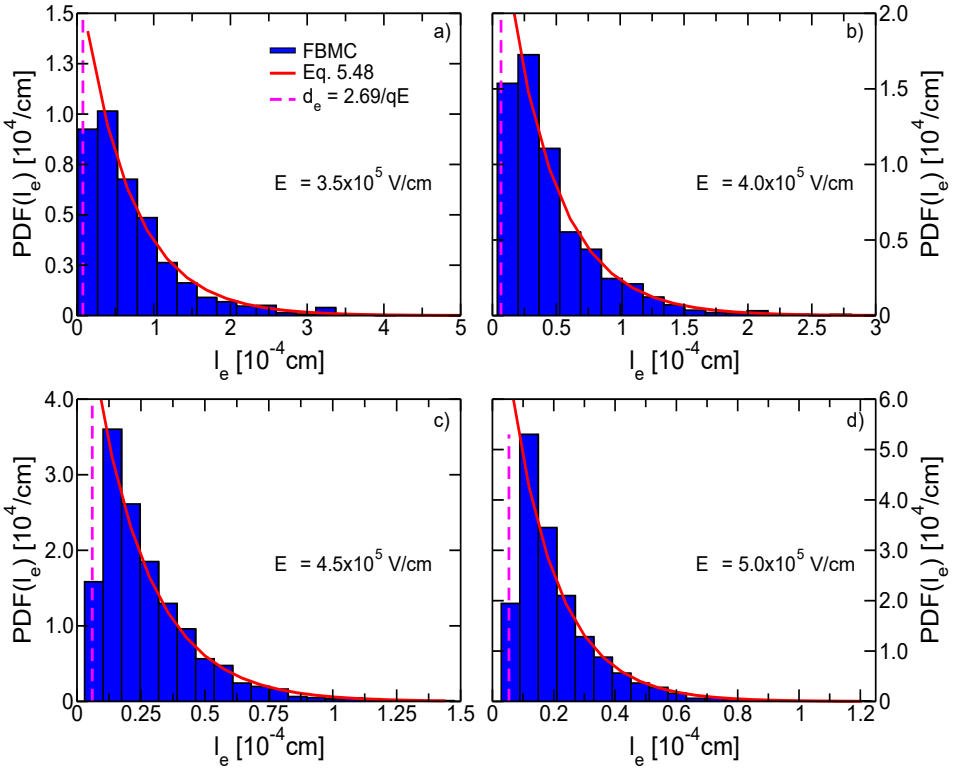

Figure 5.14: $PDF(l_e)$ at different electric fields. The red solid lines represent Eq. 5.48. The magenta dashed line is the electron's dead space (d_e) computed by using Eq. 2.60 with $E_{th,e} = 2.69$ eV (see Fig. 5.22b).

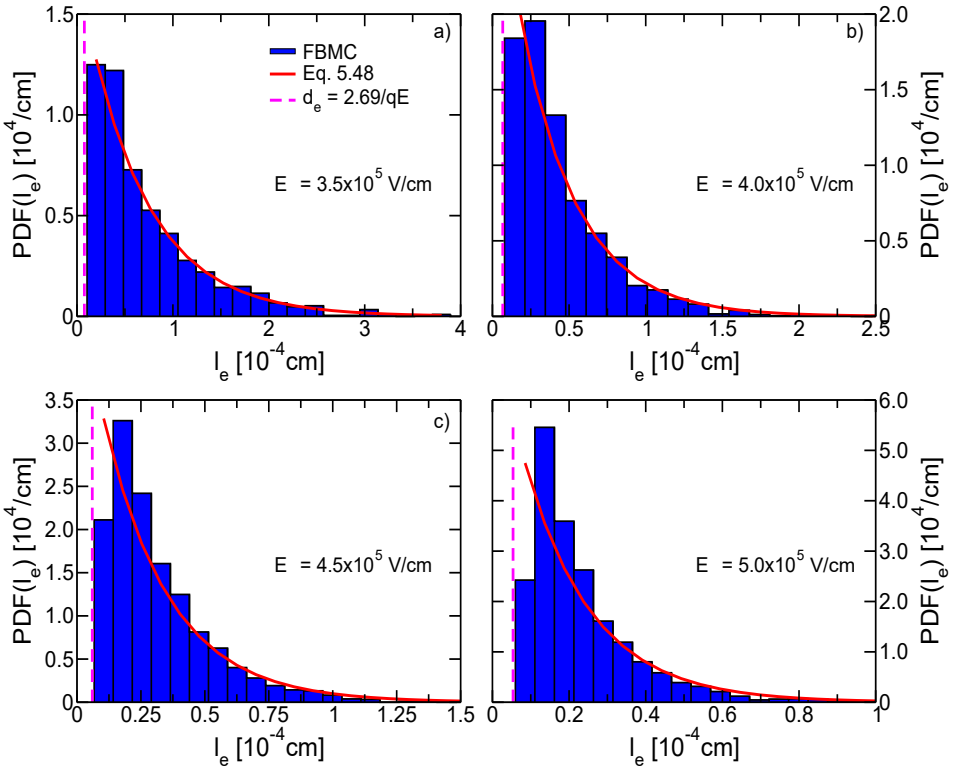

Figure 5.15: Same as Fig. 5.14, but secondary electrons are generated with null kinetic energy in FBMC simulations.

In Fig. 5.14 we immediately notice that Eq. 5.47 is not suited to reproduce the $PDF(l_e)$ computed with FBMC simulations. In fact, the first bin of the histograms is always partially filled, indicating the presence of a dead space (d_e). The effects of d_e on the $PDF(l_e)$ are even more evident in Fig. 5.15, that shows the $PDF(l_e)$ extracted for the same electric field values of Fig. 5.14 when, after an impact ionization event, the initial energy of secondary carriers has been set to zero instead of being computed by using the selection rules described in Section 5.4.2.

We have then compared, in Figs. 5.14 and 5.15, the $PDF(l_e)$ computed with the FBMC with the $PDF(l_e)$ predicted by the Dead Space model [35]. In the case of a uniform electric field, we can write

$$PDF(l_e) = \begin{cases} 0, & l_e < d_e \\ \alpha^* exp\left[-\alpha^*(l_e - d_e)\right], & l_e \geq d_e \end{cases}, \tag{5.48}$$

where d_e has been computed by using Eq. 2.60 with $E_{th,e} = 2.69$ eV (the choice of this value will be discussed in Section 5.6, see Fig. 5.22b). The value of α^* differs from the α obtained in Fig. 5.13 by using Eqs. 5.45 and 5.46. In fact, as explained in [40], α^* is the impact ionization coefficient for an electron which has already traveled over its dead space d_e. By combining Eqs. 5.45 and 5.48, we can write

$$\frac{1}{\alpha} = \langle l_e \rangle = \int_{d_e}^{\infty} l_e \alpha^* exp\left[-\alpha^*(l_e - d_e)\right] dl_e \Rightarrow \frac{1}{\alpha} = d_e + \frac{1}{\alpha^*}. \tag{5.49}$$

The agreement between Eq. 5.48 and FBMC results in Figs. 5.14 and 5.15 is good, in particular in the case of Fig. 5.14. This result is expected, since, as it will be discussed in Section 5.6, the value of $E_{th,e}$ used in Eq. 2.60 has been extracted from FBMC simulations where the energy of secondary carriers are chosen with the selection rules described in Section 5.4.2, once that its distribution is known (see Eq. 5.35).

Similarly to what done for electrons, we have also extracted the probability density functions of the distance between consecutive hole's impact ionization events at different electric fields ($PDF(l_h)$). Figure 5.16 shows the $PDF(l_h)$ when secondary holes are generated with the selection rules described in Section 5.4.2, while Fig. 5.17 shows the $PDF(l_h)$ when, after an impact ionization event, secondary holes are generated with null kinetic energy. The values of d_h extracted by using Eq. 2.61 with $E_{th,h} = 3.12$ eV (see Fig. 5.24b later in Section 5.6) are compared with the histograms that we have computed with FBMC simulations. We notice that, both in Figs. 5.16 and 5.17, the first filled bin in the histograms is always the one after d_h, indicating that, in GaAs and for these electric fields, hole's impact ionization is less sensitive than electron's impact ionization to the initial energy of the carrier. The $PDF(l_h)$ in Figs. 5.16 and 5.17 are also compared with the analytical $PDF(l_h)$ predicted by the Dead Space model of [35] (Eq. 5.48 substituting α^* with β^* and d_e with d_h) and a good mutual agreement has been obtained.

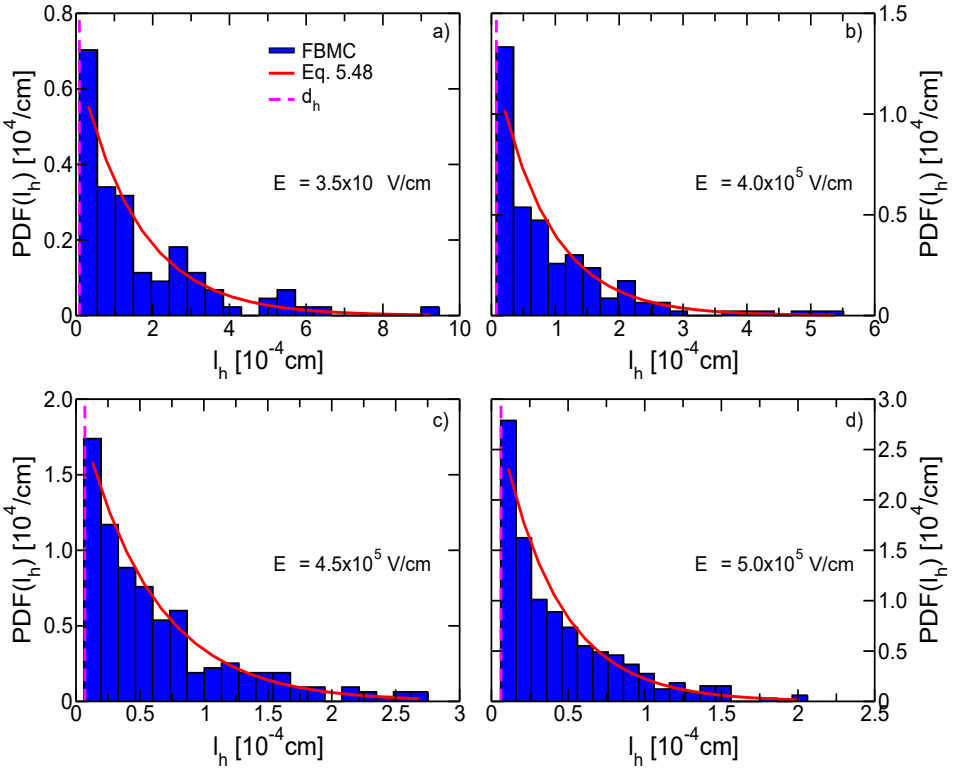

Figure 5.16: $PDF(l_h)$ at different electric fields. The red solid lines represent Eq. 5.48. The magenta dashed line is the hole's dead space (d_h) computed by using Eq. 2.61 with $E_{th,h} = 3.12$ eV (see Fig. 5.24b).

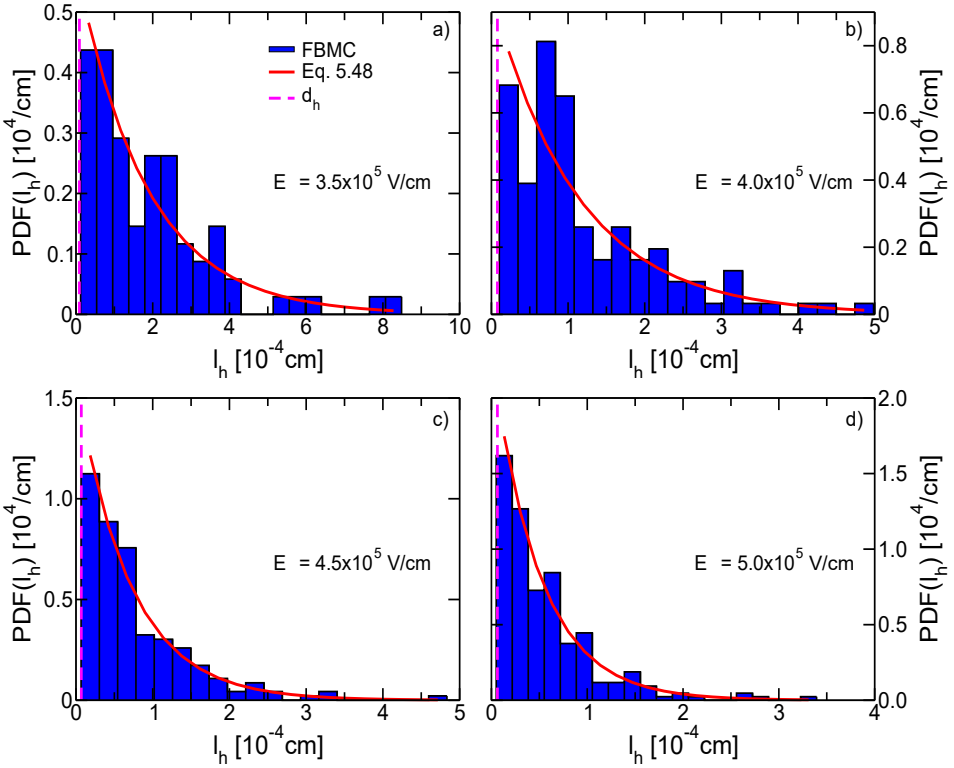

Figure 5.17: Same as Fig. 5.16, but secondary holes are generated with null kinetic energy in FBMC simulations.

5.5 Gain and Excess Noise Factor of Thin GaAs p-i-n APDs

To validate the FBMC transport model described in Sec. 5.4, we have computed the gain and the excess noise factor are computed of thin GaAs p-i-n diodes. We have assumed that:

1. The intrinsic region of the p-i-n APD is fully depleted.

2. The electric field is entirely confined inside the intrinsic region.

3. The electric field is uniform in the intrinsic region.

4. The built-in voltage is the same for all the devices that we have simulated and it is equal to $\Psi_0 = 1.2$ V [117].

Therefore, the simulation domain coincides with the intrinsic region of the APD and it extends from $x = 0$ to $x = d$ (see Fig. 5.18).

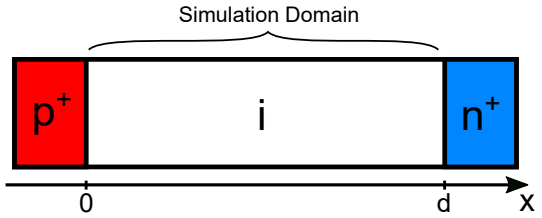

Figure 5.18: Sketch of the simulation domain employed in this work to compute the gain and the excess noise factor in thin GaAs APDs.

The algorithm that we have employed is similar to the one described in Sec. 2.2.4 for the RPL: we have simulated many trials starting from a single electron injected at $x = 0$. Carriers move following the rules presented in Sec. 5.4 and when impact ionization occurs at position x', an electron-hole pairs is generated in x' and recursion is used to handle the increasing number of carriers in the simulation. A trial ends when all the carriers exit from the simulation domain and the simulation ends when all the trials are completed. Since the trials are independent, we have exploited parallel execution of the code to reduce the CPU time needed to simulate a single bias point. The gain (M) and the excess noise factor (F) have been computed by using Eqs. 2.75 and 2.76, respectively.

Figure 5.19 compares the experimental $M(V_{rev})$ and $F(M)$ curves for GaAs p-i-n diodes of different thicknesses [23] with the results of FBMC. The agreement between experiments and simulations is good with no further parameter adjustments with respect to the calibration of the carrier-phonon deformation potentials and of the matrix elements for the computation of the impact ionization scattering rates discussed in Sections 5.2.3 and 5.3.

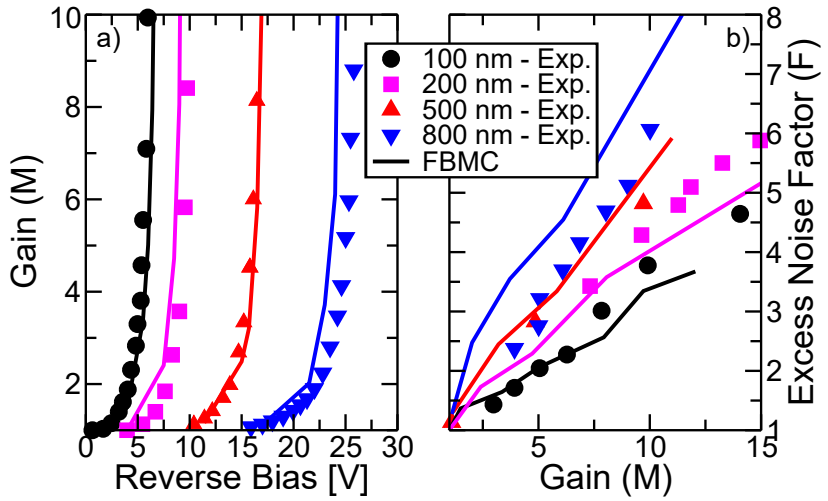

Figure 5.19: a) M versus V_{rev} and b) F versus M curves for GaAs p-i-n APDs. FBMC (solid lines) is compared with experiments [23] (symbols). A built-in voltage $\Psi_0 = 1.2$ V has been assumed [117].

5.6 Extraction of the History Dependent Impact Ionization Coefficients with Full Band Monte Carlo Simulations

In nonlocal history dependent (NL-HD) models α and β are functions of the generation (x) and the ionization (x') points (see Fig. 5.20) and they have a nonlocal dependence on the complete electric field profile between x and x'. In other words α and β are not given solely by the local electric field, hence it is also necessary an alternative procedure to extract α and β from Full Band Monte Carlo (FBMC) simulations, thus going beyond Eqs. 5.45 and 5.46 used for Fig. 5.13.

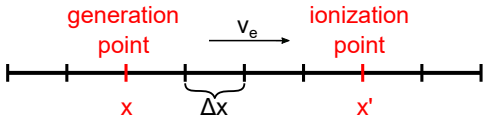

Figure 5.20: Discretization of the intrinsic region of a p-i-n diode with a mesh with uniform spacing Δx. x is the point where a carrier is generated, optically or by impact ionization, and x' is the point where it ionizes. Electrons move from left to right with average velocity v_e (while holes move from right to left with average velocity v_h and x and x' are inverted).

To this purpose, we have derived Eq. 5.53 to extract $\alpha(x|x')$ (and $\beta(x|x')$) from FBMC simulations. In fact, following [39, 69], the electron's impact

ionization probability is

$$p(x|x')\Delta x = \frac{\textit{No. of electrons generated in x that ionize in x' } \pm \Delta x/2}{\textit{No. of electrons generated in x}} = \alpha(x|x')\exp\left(-\int_x^{x'} \alpha(x|x''')dx'''\right)\Delta x. \tag{5.50}$$

With a similar reasoning, we can also find the probability for an electron to ionize before reaching x', namely:

$$\begin{aligned} p(x|x'' < x') &= \frac{\textit{No. of electrons generated in x that ionize before x'}}{\textit{No. of electrons generated in x}} \\ &= \int_x^{x'} \alpha(x|x'')\exp\left(-\int_x^{x''} \alpha(x|x''')dx'''\right)dx'' \\ &= 1 - \exp\left(-\int_x^{x'} \alpha(x|x'')dx''\right). \end{aligned} \tag{5.51}$$

Combining Eqs. 5.50 and 5.51, the expression for $\alpha(x|x')$ is found by writing

$$\alpha(x|x') = \frac{p(x|x')}{[1 - p(x|x'' < x')]}, \tag{5.52}$$

which is equivalent to

$$\alpha(x|x') = \frac{\textit{No. of electrons generated in x (by II or a photon) that ionize in } x' \pm \Delta x/2}{\Delta x \cdot (\textit{No. of electrons generated in x} - \textit{No. of electrons generated in x that ionize in } [0, x' - \Delta x/2))} \tag{5.53}$$

It is worth noting that at the denominator of Eq. 5.53 we look for all the electrons generated in x that ionize in $[0, x' - \Delta x/2)$, instead of $[x, x' - \Delta x/2)$, to account for those electrons that, due to a scattering event, travel with negative velocity and ionize at points lying before (along the field direction) the location where the carrier was generated.

Sample results are shown in Fig. 5.21 for an electron generated at $x = 0$ or at $x = 50$ nm in a 100 nm thick device. As it can be seen, $\alpha(x|x')$ saturates to a constant value (denoted as α^*, consistently with Eq. 5.48) after few tens of nm.

Figure 5.22a compares $\alpha(1/E)$ from Eq. 5.45 and $\alpha^*(1/E)$ from Eq. 5.53 when $x' \gg x$ and shows that they can be related by using Eq. 5.49 with $d_e = E_{th,e}/qE$ (Eq. 2.60), where $E_{th,e}$ is the threshold energy for electron's ionization (see Fig. 5.22b). We have extracted $E_{th,e} = 2.69$ eV, which is consistent with the value computed by [40] (3.0 eV). In Fig. 5.21b, we notice that at high reverse bias voltages (namely at high gains) $\alpha(x|x') > 0$ also for $x' < x$. In fact, in FBMC secondary carriers are generated with nonzero kinetic energy and in some cases with a velocity going leftward, which is a case neglected by NL-HD models. Such left going electrons can undergo impact ionization events even for $x' < x$.

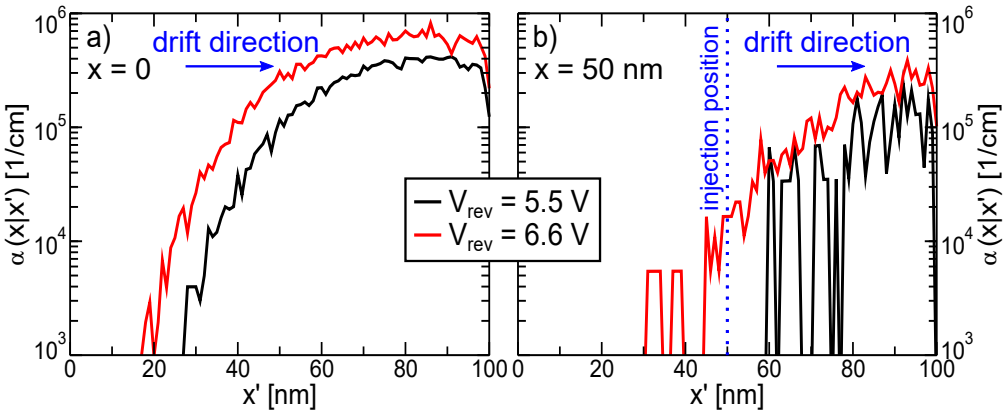

Figure 5.21: $\alpha(x|x')$ extracted from FBMC simulations by using Eq. 5.53 in a 100 nm-thick GaAs p-i-n APD with electron injection from the left side at $V_{rev} = 5.5$ V (black) and $V_{rev} = 6.6$ V (red). a) $x = 0$, b) $x = 50$ nm. A built-in voltage $\Psi_0 = 1.2$ V has been assumed [117].

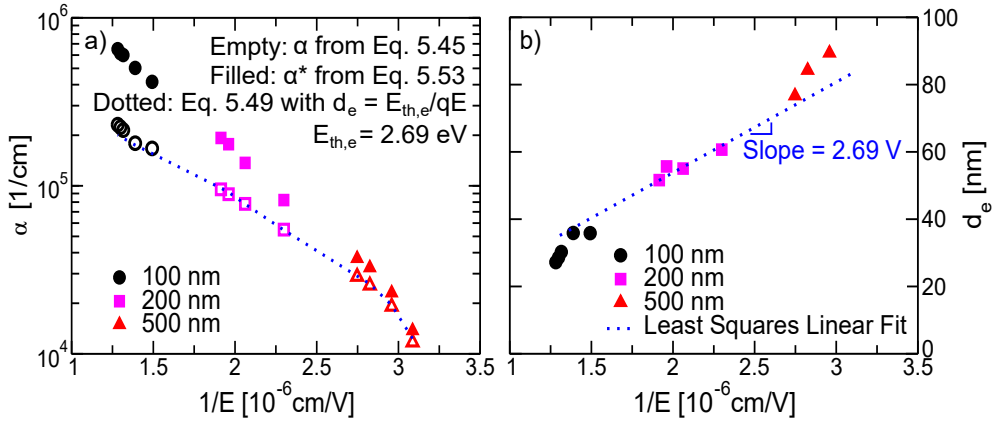

Figure 5.22: a) α (empty symbols) and α^* (filled symbols) versus $1/E$ extracted from FBMC simulations of GaAs p-i-n diodes by using Eq. 5.45 and Eq. 5.53 (plateau for $x' \gg x$), respectively. b) Electron's dead space d_e versus $1/E$ extracted, point by point, with Eq. 5.49 from the α and α^* of Fig. 5.22a with Eq. 5.49. The blue dotted line in plot b is the least squares linear fit of the d_e values, giving a slope $E_{th,e}/q = 2.69$ V. The same parameter inserted in Eq. 5.49 gives the blue dotted line in plot a.

Figure 5.23 shows $\beta(x|x')$ for holes extracted from FBMC: also $\beta(x|x')$ saturates to a constant value β^* after few tens of nm. Differently from the case of electrons, the saturation of $\beta(x|x')$ for secondary holes (plot b) takes place after an overshoot that is not present in the NL-HD models. After that overshoot, $\beta(x|x')$ stabilizes to a value independent of x', as long as $x' \ll x$.

Similarly to what has been done for electrons in Fig. 5.22, Fig. 5.24a compares $\beta(1/E)$ from Eq. 5.45 with $\beta^*(1/E)$ from Eq. 5.53 when $x' \ll x$. From Fig. 5.24b, we extract a value for the threshold energy for hole's impact ionization in GaAs equal to $E_{th,h} = 3.12$ eV, which is consistent with the value computed by [40] (3.3 eV).

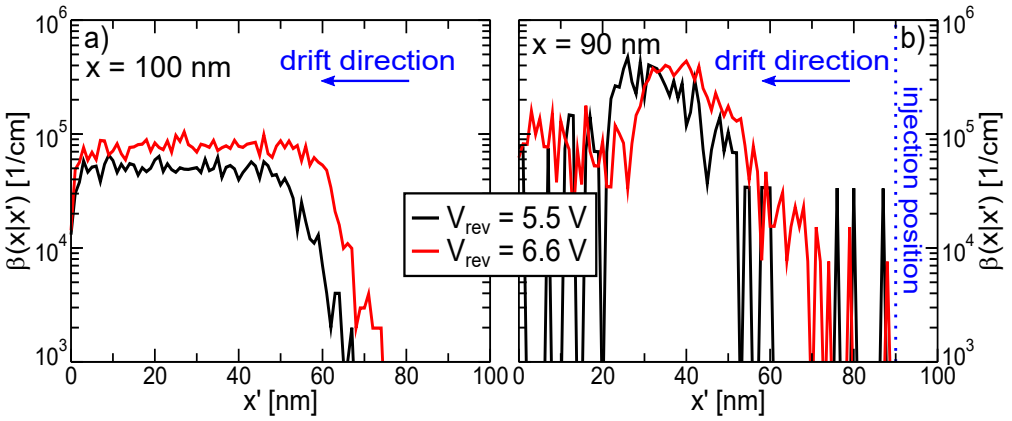

Figure 5.23: $\beta(x|x')$ extracted from FBMC simulations by using Eq. 5.53 in a 100 nm-thick GaAs p-i-n APD with hole injection from the right side at $V_{rev} = 5.5$ V (black) and $V_{rev} = 6.6$ V (red). a) $x = 100$ nm, b) $x = 90$ nm. A built-in voltage $\Psi_0 = 1.2$ V has been assumed [117].

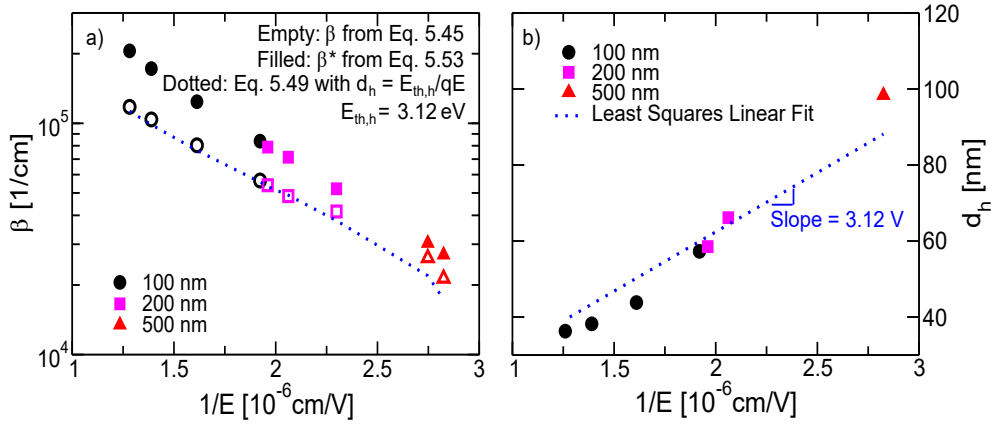

Figure 5.24: Same as Fig. 5.22, but for the hole's impact ionoization coefficient β. The the least squares linear fit of the d_h values in plot b) (blue dotted line) has slope $E_{th,h}/q = 3.12$ V.

5.6.1 Using $\alpha(x|x')$ and $\beta(x|x')$ from FBMC in the NL-HD Model's Equations

Figure 5.25 compares the $M(V_{rev})$ and $F(V_{rev})$ curves for GaAs p-i-n diodes extracted with FBMC simulations and those obtained with the numerical implementation of NL-HD model's equations described in Section 3.2 by using as input the impact ionization coefficients extracted from the FBMC with Eq. 5.53. The agreement between the two algorithms for $M(V_{rev})$ is good at low gains and for long diodes. The larger discrepancies at high gains in short devices are due to the fact that the NL-HD model's equations neglects electron impact ionization for $x' < x$ and hole impact ionization for $x' > x$; in fact, such contributions become more relevant as the reverse bias in short devices increases. We also observe that the NL-HD model's equations underestimates $F(V_{rev})$ for short diodes and overestimates $F(V_{rev})$ for long ones.

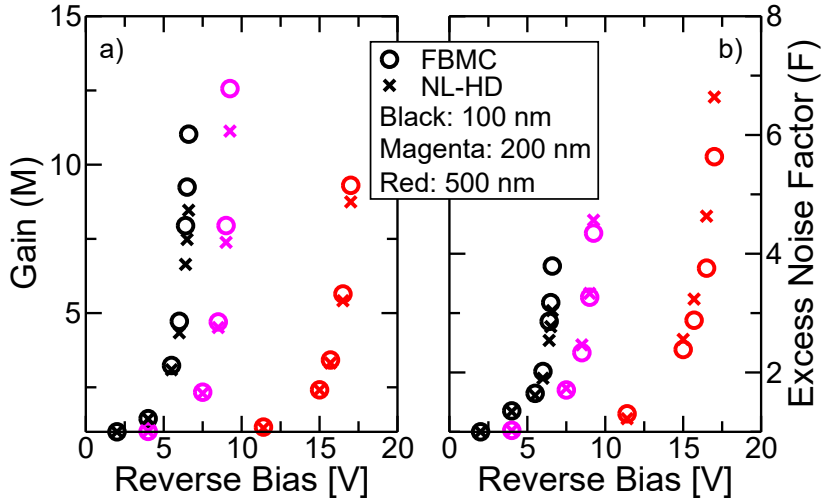

Figure 5.25: Comparison between the a) M and b) F versus V_{rev} curves for GaAs p-i-n diodes obtained with the FBMC (circles) or by using the NL-HD model's equations described in Section 3.2 with $\alpha(x|x')$ and $\beta(x|x')$ extracted from FBMC simulations as inputs (crosses). A built-in voltage $\Psi_0 = 1.2$ V has been assumed [117].

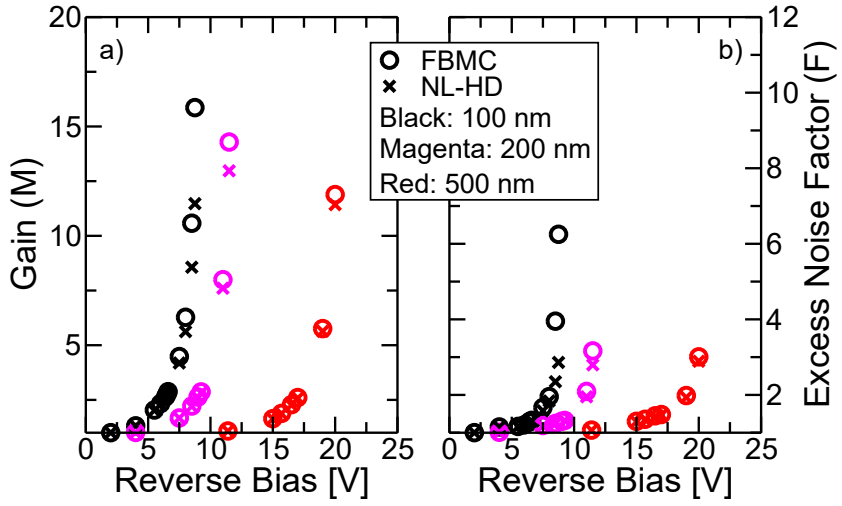

Figure 5.26: Same as Fig. 5.25 but, after an impact ionization event, secondary electrons and holes are generated with null kinetic energy.

To understand how the gain and the excess noise factor of p-i-n GaAs APDs are affected by the initial energy of secondary carriers, we have computed M and F after having imposed in FBMC simulations that, after each impact ionization event, secondary electrons and holes are generated with null kinetic energy. The results are reported in Fig. 5.26, that also compares the results of the FBMC with the NL-HD model's equations when $\alpha(x|x')$ and $\beta(x|x')$ extracted from FBMC simulations are taken as input. We notice that, given the device's thickness, higher applied bias voltages are necessary to obtain the same gain achieved in Fig. 5.25. Moreover, the agreement between the FBMC and the NL-HD model's equations is improved, in particular for the $d = 500$ nm device, where F is no longer overestimated. The underestimation

of the M and the M at a given bias voltage obtained with the NL-HD model's equations is due to those hot carriers that, due to a backscattering event, ionize at position $x' < x$.

Finally, Fig. 5.27 compares the $F(M)$ curves computed with the FBMC with the ones obtained with the NL-HD model's equations for the cases of FIgs. 5.25 and 5.26. We notice that, when secondary carriers are generated according to the selection rules of Section 5.4.2, the $F(M)$ curve obtained with the NL-HD model's equations (again with $\alpha(x|x')$ and $\beta(x|x')$ profiles computed with the FBMC) reproduces the one of the FBMC for the shorter devices, but it is overestimated for the $d = 500$ nm APD. On the other hand, when secondary carriers are generated with null kinetic energy, the NL-HD model's equations always agree with FBMC simulations, even though the extracted $F(M)$ curves are dramatically different from the ones reported in Fig. 5.19 that match the experimental results of [23].

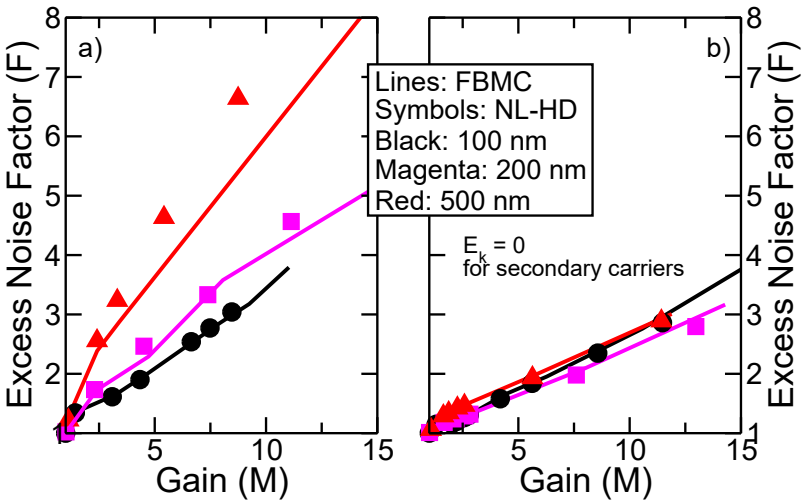

Figure 5.27: Comparison of the excess noise factor as a function of the gain computed with FBMC simulations (solid lines) or by using the NL-HD model's equations described in Section 3.2 with $\alpha(x|x')$ and $\beta(x|x')$ extracted from FBMC simulations as input (symbols) for GaAs p-i-n APDs of different thickness. a) Secondary carriers are generated with an inital energy determed with the selectrion rules described in Section 5.4.2. b) Secondary carriers are generated with null kinetic energy. The values of M and F in plots a) and b) are the same reported in Figs. 5.25 and 5.26, respectively. A built-in voltage $\Psi_0 = 1.2$ V has been assumed [117].

5.7 Calibration of the EBHDM based on the Results of FBMC Transport Simulations

In this Section, we show how the results for the electron's and hole's impact ionization coefficients, $\alpha(x|x')$ and $\beta(x|x')$, obtained with FBMC simulations have been used to improve the calibration for GaAs of the nonlocal history dependent impact ionization model described in Chapter 3 (the EBHDM).

Our final goal is to model the impact ionization coefficients in the presence of a conduction band discontinuity in biasing configurations that involve low applied electric fields, to evaluate the performance of a single step of GaAs-based staircase APDs.

We have started the calibration by finding the values of the parameters A_e, A_h, E_{ce}, E_{ch}, γ_e and γ_h to insert into Eqs. 2.72 and 2.73 to fit the curves of α^* and β^* as a function of the reciprocal of the electric field reported in Figs. 5.22a and 5.24a (see Fig. 5.28). The new values are reported in Tab. 5.6.

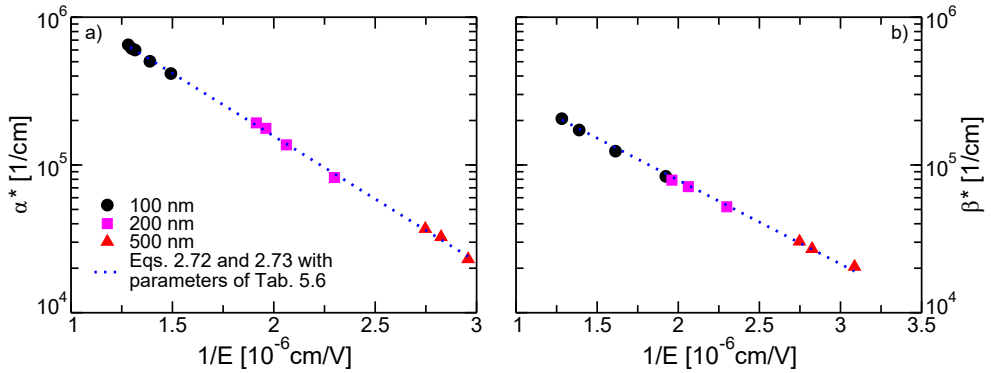

Figure 5.28: Fitting of the values of a) α^* and b) β^* as a function of the reciprocal of the electric field extracted from FBMC simulations (and reported in Figs. 5.22a and 5.24a) by using Eqs. 2.72 and 2.73, respectively, with the parameters of Tab. 5.6.

A_e [10^6/cm]	E_{ce} [10^6V/cm]	γ_e
7.856	1.957	1.0

A_h [10^6/cm]	E_{ch} [10^6V/cm]	γ_h
1.080	1.308	1.0

Table 5.6: EBHDM model parameters for GaAs calibrated on the results of FBMC simulations.

The EBHDM described in Chapter 3 is based on an energy balance equation with a constant energy relaxation lengths λ_e and λ_h. To improve the agreement between the impact ionization coefficients calculated with FBMC simulations and the one used in the EBHDM model, we have proposed the following relation between $\lambda_{e,h}$ and the energy (i.e. the effective field)

$$\lambda_{e,h}(x|x') = \frac{A_{\lambda e,h}}{B_{\lambda e,h} + E_{eff,e,h}(x|x')}, \tag{5.54}$$

where the expressions for the computation of the effective field in Eqs. 3.11 and 3.12 have been modified as follows

$$E_{eff,e}(x|x') = \int_x^{x'} \frac{1}{\lambda_e(x|x'')} \frac{dE_C}{dx''} \exp\left(\frac{x''-x'}{\lambda_e(x|x'')}\right) dx'', \tag{5.55}$$

$$E_{eff,h}(x|x') = \int_{x'}^{x} \frac{1}{\lambda_h(x|x')} \frac{dE_V(x'')}{dx''} exp\left(\frac{x'-x''}{\lambda_h(x|x')}\right) dx''.. \tag{5.56}$$

The parameters $A_{\lambda e,h}$ and $B_{\lambda e,h}$ to insert into Eq. 5.54 are reported in Tab. 5.7 and have been chosen so that, for each bias point, the $\alpha(0|x')$ and $\beta(d|x')$ computed with the EBHDM and $\lambda_{e,h}(x|x')$ from Eq. 5.54 could reproduce fairly well the $\alpha(0|x')$ and $\beta(d|x')$ extracted from FBMC simulations (see Figs. 5.29 and 5.30).

$A_{\lambda e}$ [V]	$B_{\lambda e}$ [10^5 V/cm]
1.4142	1.3188

$A_{\lambda h}$ [V]	$B_{\lambda h}$ [10^5 V/cm]
0.6149	0.1465

Table 5.7: Values of the parameters A_λ and B_λ to insert into Eq. 5.54 to compute the electron's energy dependent relaxation length $\lambda_e(x|x')$.

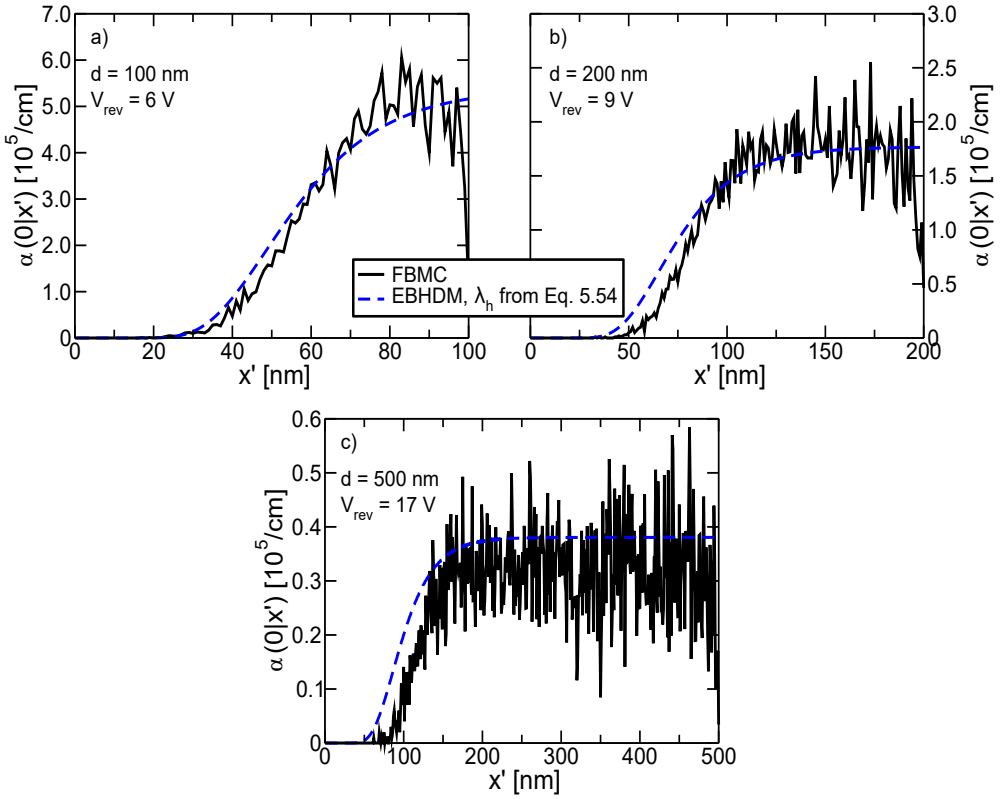

Figure 5.29: Comparison of the electron's impact ionization coefficient $\alpha(0|x')$ extracted from FBMC simulations (black solid line) with the one computed using the EBHDM (Eq. 2.72) with an energy dependent relaxation length $\lambda_e(x|x')$ (Eq. 5.54, blue dashed line) for devices with different thickness and at different bias voltages: a) $d = 100$ nm, $V_{rev} = 6$ V; b) $d = 200$ nm, $V_{rev} = 9$ V; c) $d = 500$ nm, $V_{rev} = 17$ V. The built-in voltage is $\Psi_0 = 1.2$ V [117].

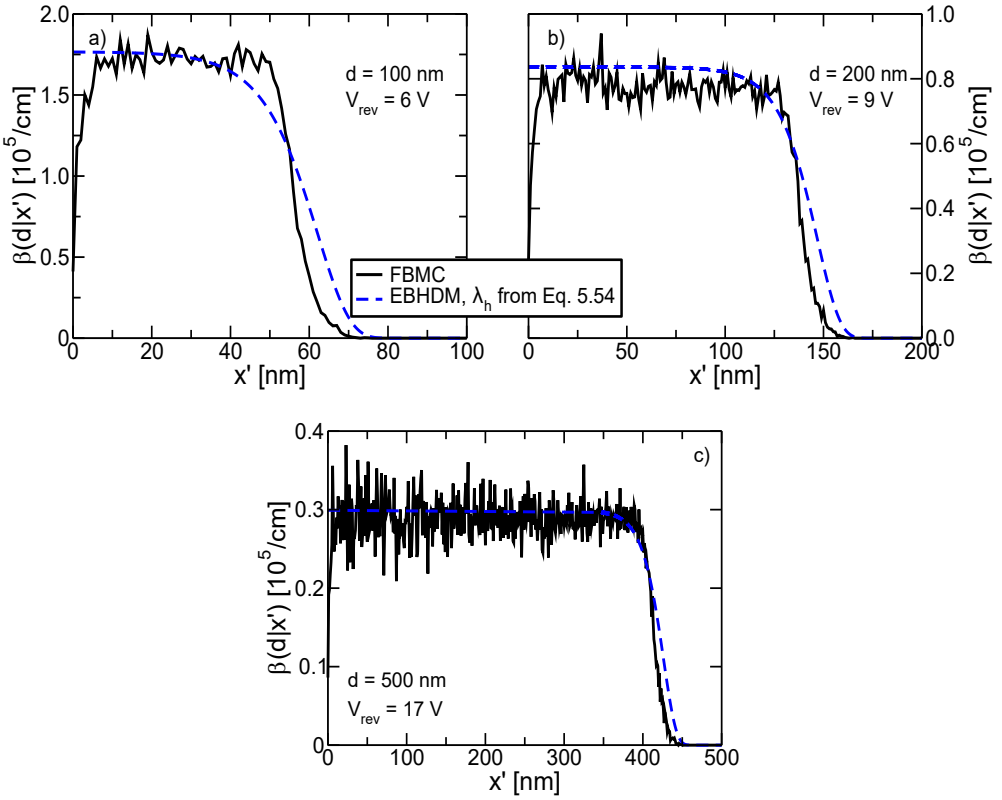

Figure 5.30: Same as Fig. 5.29, but for the hole's history dependent impact ionization coefficient $\beta(d|x')$.

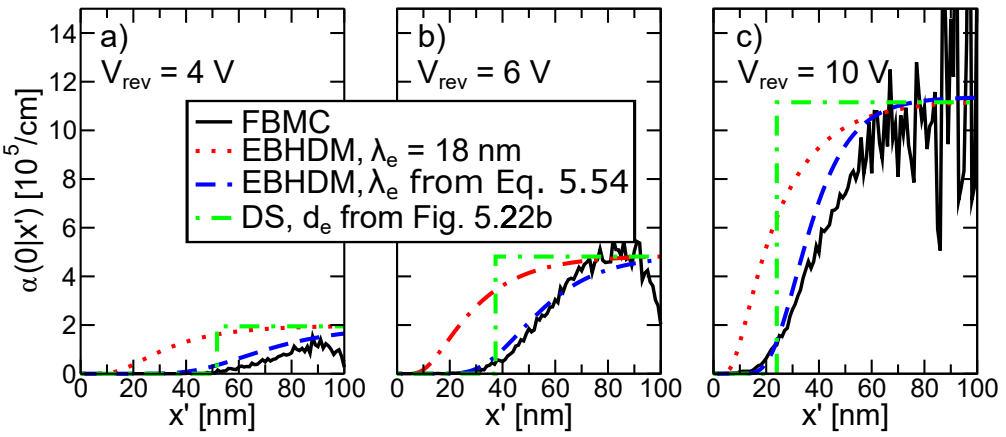

Figure 5.31: $\alpha(0|x')$ for a 100 nm-thick GaAs p-i-n diode when hole impact ionization is turned off. FBMC (black solid line) is compared with the EBHDM described in Chapter 3 either with $\lambda_e = 18$ nm (red dotted line) or λ_e from Eq. 5.54 (blue dashed line) and with the Dead Space model (DS) [35], when d_e is taken from Fig. 5.22b (green dashed-dotted line). A built-in voltage $\Psi_0 = 1.2$ V has been assumed [117].

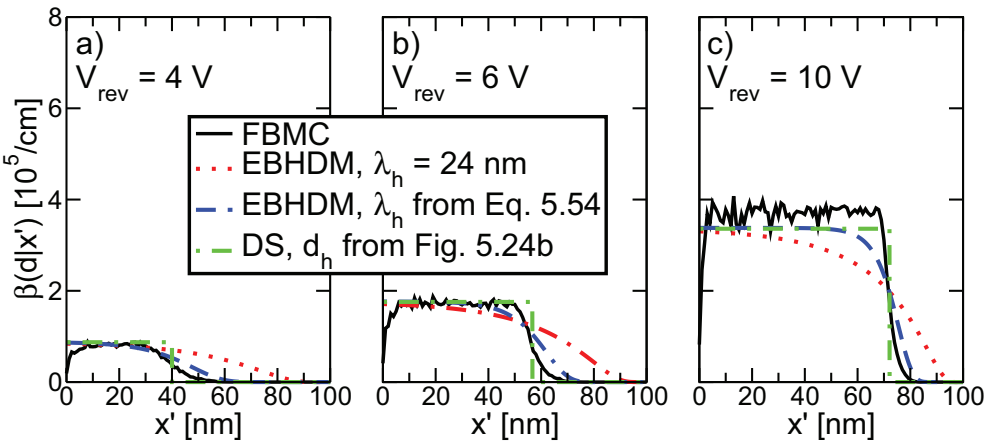

Figure 5.32: Same as Fig. 5.31, but for $\beta(d|x')$. Electron's impact ionization is turned off.

Figures 5.31 and 5.32 compare $\alpha(0|x')$ and $\beta(d|x')$, respectively, for a 100 nm thick GaAs p-i-n diode from FBMC, with the NL-HD impact ionization coefficients corresponding to different approximations. The NL-HD results are shown for the Dead Space model [35] (d_e is taken from Fig. 5.22b and d_h from Fig. 5.24b) and for the EBHDM using the effective fields from Eqs. 5.55, 5.56 with $\lambda_e = 18$ nm and $\lambda_h = 24$ nm (Tab. 3.1) or with $\lambda_{e,h}(x|x')$ from Eq. 5.54 and the parameters in Tab. 5.7. Good agreement is obtained between FBMC results and the impact ionization coefficients of the EBHDM when an energy dependent $\lambda_e(x|x')$ and $\lambda_h(x|x')$ have been used (Eq. 5.54). The Dead Space model and the EBHDM model with constant λ_e and λ_h are instead found to be less accurate. It is worth nothing that, when constant λ_e and λ_h are used, the parameters A_e, A_h, E_{ce}, E_{ch}, γ_e and γ_h to insert into Eqs. 2.72 and 2.73 are the ones of Tab. 5.6 and not the ones extracted from the calibration of the EBHDM on GaAs p-i-n diodes (see Chapter 3) and reported in Tab. 3.1, since our goal in this Section is to match the saturation value, α^* or β^*, of FBMC simulations. Finally, the validity of the parameters in Tabs. 5.6 and 5.7 is limited to the range of electric field over which they have been tested (from 324 kV/cm to 1.12 MV/cm).

5.8 Simulation of Conduction Band Steps in GaAs APDs

Finally, the Full Band Monte Carlo simulator has been used to study the behavior of a single conduction band step of amplitude ΔE_C in a GaAs APD, mimicking the effects of a AlGaAs/GaAs heterojunction in a staircase APD. In principle, an accurate description of carrier transport across the heterojunction, involving energy and momentum conservation, should be employed but, to capture the essential features of the process, in this work we have described the conduction band step as a contribution to the initial energy of the electron that is injected at $x = 0$ to start the simulation (i. e. the initial energy of the injected electron is ΔE_C, see Fig. 5.33).

We have simulated devices with two different thicknesses, $d = 50$ nm and $d = 100$ nm, for three different values of ΔE_C, namely $\Delta E_C = 0$, 0.3 eV, 0.5 eV. Moreover, we have always applied an electric field along the x direction, to ensure that all the carriers exit from the simulation domain. Therefore, the gain and the excess noise factor of the aforementioned devices have been computed for $E = 400$, 500 and 600 kV/cm.

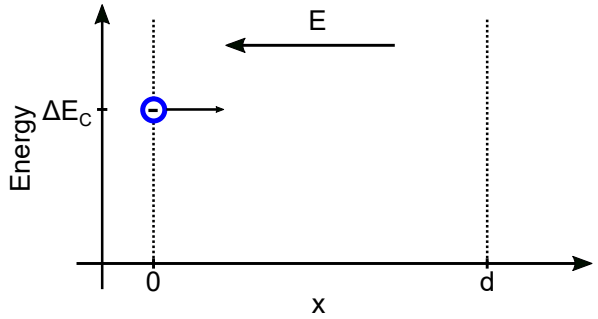

Figure 5.33: Schematic representation of how conduction band steps have been simulated in this thesis. The initial electron is injected with energy ΔE_C in the simulation domain, that extends from $x = 0$ to $x = d$. An electric field is applied along the x direction, to ensure that all the carriers exit from the simulation domain.

Figures 5.34 and 5.35 compare the gain and the excess noise factor as functions of the applied electric field obtained with FBMC simulations with the results of the numerical implementation of the NL-HD model's equations described in Section 3.2 when the $\alpha(x|x')$ and $\beta(x|x')$ extracted from the FBMC are taken as input, for the 50 nm thick and the 100 thick devices, respectively. For each applied electric field, M and F are evaluated for the three different values of ΔE_C. For the 50 nm thick device we notice that both the gain and the excess noise factor increase as either the applied field or ΔE_C increase (Fig. 5.34) However, in all cases, $M \simeq F \simeq 1$, that indicates that, for a device with this thickness, these values of the applied electric field are not high enough to trigger impact ionization events and also that an increase in the conduction band step amplitude alone is not sufficient to achieve a significant gain. For the 100 nm thick device (Fig. 5.35), instead, we notice that the gain increases with the value of ΔE_C, but the major contribution to M is given by the applied electric field. On the other hand, at $E = 600$ kV/cm we notice that $F(\Delta E_C = 0.5 \text{ eV}) < F(\Delta E_C = 0) < F(\Delta E_C = 0.3 \text{ eV})$. This non-monotonic behavior of the excess noise factor seems to be consistent with what predicted by Eq. 1.10 by [13], where an increase in the electron's impact ionization probability due to a conduction band step is associated with a reduction of the excess noise factor. For both the device thicknesses, we notice that the FBMC simulator and the NL-HD model's equations that we have developed give similar results when the $\alpha(x|x')$ and $\beta(x|x')$ extracted from the FBMC are taken as input; this indicates that, differently from what discussed in Section 5.6, at this biasing configurations, secondary carriers are generated at low energies, so that impact ionization of electrons at $x' < x$ is negligible,

so that the assumptions at the base of nonlocal impact ionization models are verified and these models could, in principle, be used to compute M and F in these operating scenarios.

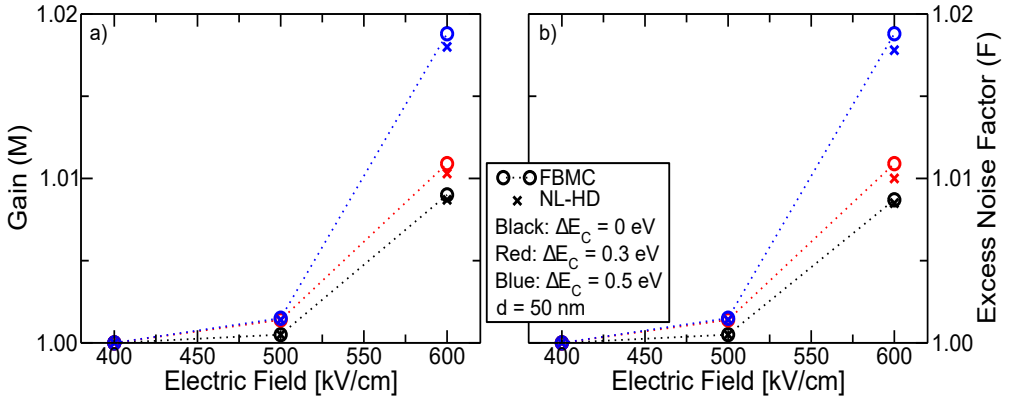

Figure 5.34: a) Gain and b) excess noise factor as functions of the applied electric field in a 50 nm thick device when an electron with initial $\Delta E_C = 0$ eV (black), 0.3 eV (red) or 0.5 eV (blue) is injected at $x = 0$. The results obtained with FBMC simulations (circles) are compared with the results of the NL-HD model's equations described in Section 3.2 when $\alpha(x|x')$ and $\beta(x|x')$ extracted from FBMC simulations are taken as input.

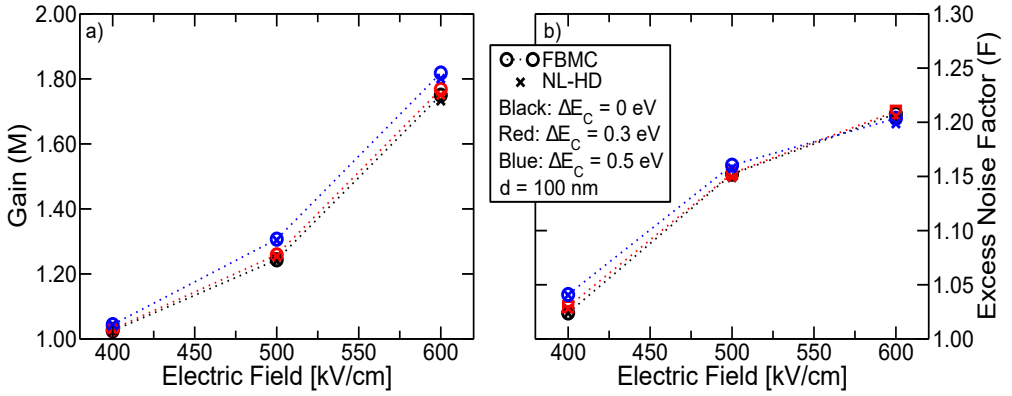

Figure 5.35: Same as Fig. 5.34, but for a 100 nm thick device.

Figure 5.36 shows, for a given electric field, the variation of the gain $\Delta M = M(\Delta E_C) - M(\Delta E_C = 0)$ as a function of ΔE_C for the 50 nm and the 100 nm GaAs APDs. We notice that ΔM increases with the field and with ΔE_c and it is higher in the thicker device, since in this device, w. r. t. to the thinner one, electrons can travel over longer distances, and thus acquire sufficient energy for ionization, without exiting from the simulation domain. However, we also notice that the values of ΔM are low, this indicates that in GaAs-based APDs conduction band discontinuities up to 0.5 eV are not enough to achieve a significant improvement of the gain (and thus a reduction of the excess noise factor), since these values of ΔE_C are small if compared to the threshold energy to trigger impact ionization in this material (we have extracted $E_{th,e} = 2.69$ eV from FBMC simulations in Section 5.6).

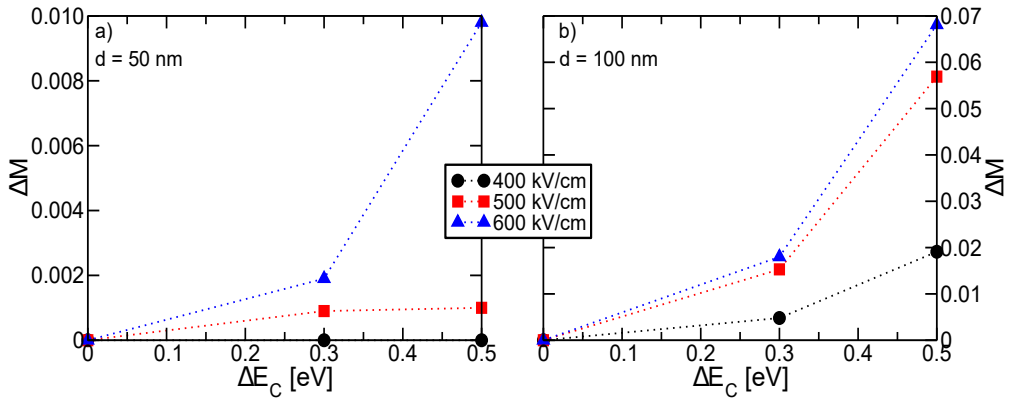

Figure 5.36: Gain variation (ΔM) as a function to the electron's injection energy (ΔE_C) w. r. t the case $\Delta E_C = 0$ eV in a a) 50 nm or in a b) 100 nm thick device.

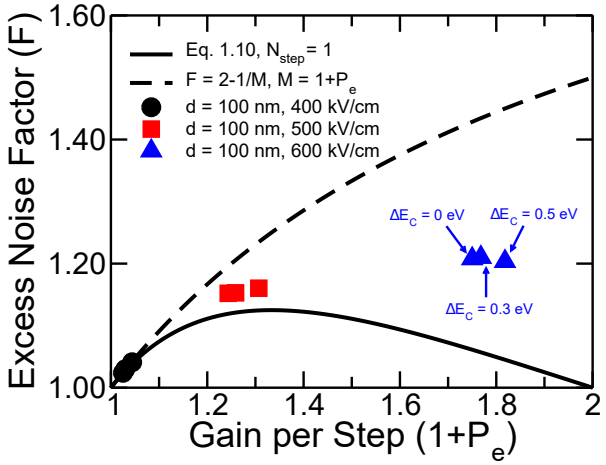

Figure 5.37: Comparison between the excess noise factor as a function of the gain per step calculated by using Eq. 1.10 with $N_{step} = 1$ (black solid line), $F = 2 - 1/M$ (black dashed line), which is Eq. 2.19 in the $k = \beta/\alpha \to 0$ limit, and the results of FBMC simulations of 100 nm thick GaAs conduction band steps at different applied electric fields (symbols). For a given electric field, the increase of the gain is achieved by increasing the electron's injection energy.

Figure 5.37 compares the excess noise factor as a function of the gain computed at different electric fields with the FBMC for the 100 nm thick device with the predictions of Eq. 1.10 by [13] for F in a single step staricase APD when only electrons ionize and $F = 2 - 1/M$, which is Eq. 2.19 for the excess noise factor computed with the local model in the $k = \beta/\alpha \to 0$ limit (i. e. hole's impact ionization is neglected). We notice that when $E = 400$ V/cm FBMC results are in agreement with Eq. 1.10, then, as the electric field increases, the excess noise compute with the FBMC deviates from the theory proposed by [13], indicating that the electric field is the major responsible for the increase of the gain in the GaAs device that we have analyzed). On the other hand, the excess noise factor is always lower than the predictions of the local model, that means that nonlocal effects (i. e. the fact that a carrier as to travel over a certain distance to acquire sufficient energy for its ionization) still play a significant role.

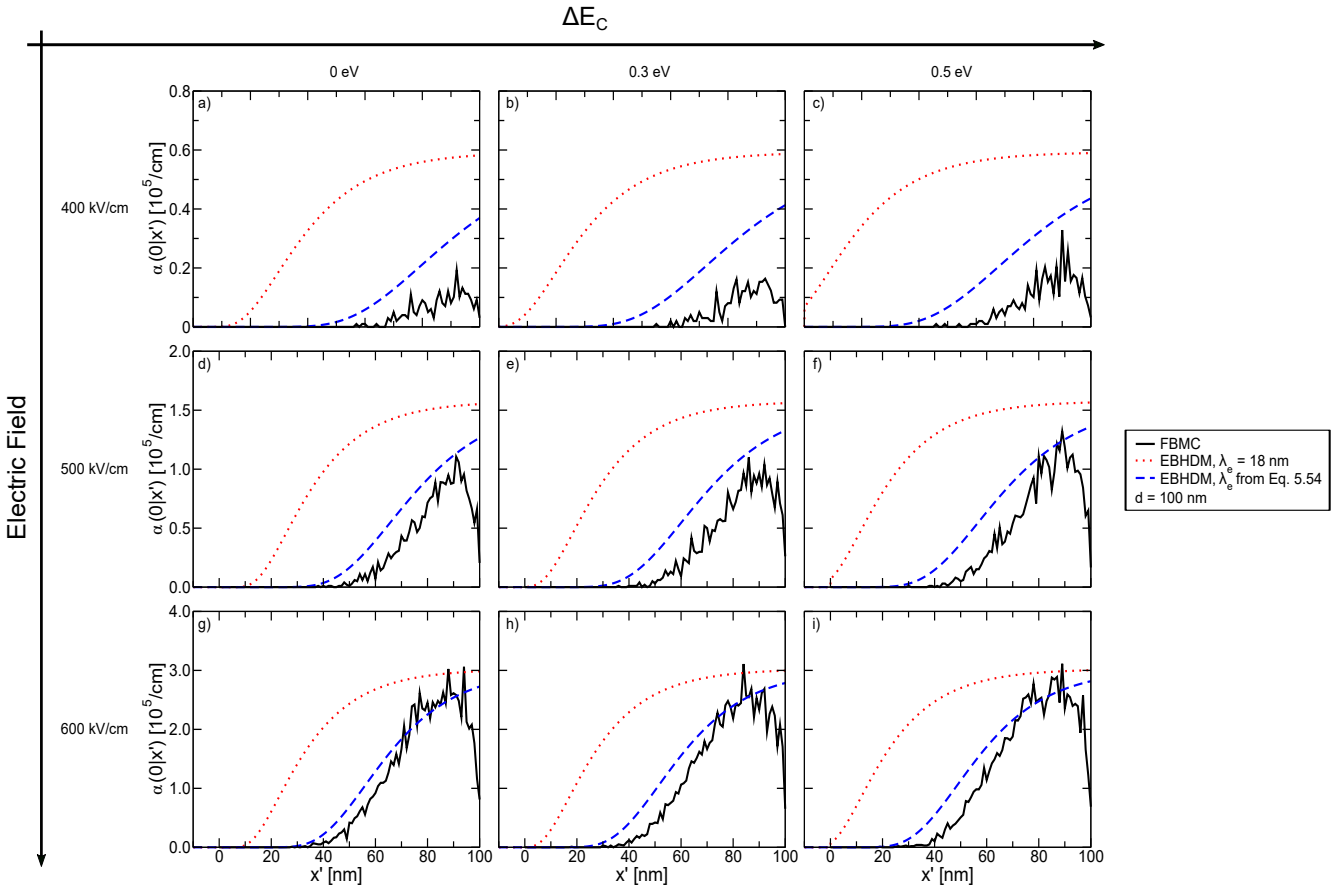

Figure 5.38: $\alpha(0|x')$ for a 100 nm-thick GaAs conduction band steps of different amplitude and at different values of the applied electric field. FBMC (black solid line) is compared with the EBHDM either with $\lambda_e = 18$ nm (red dotted line) or λ_e from Eq. 5.54 (blue dashed line).

Figure 5.38 compares the profiles of $\alpha(0|x')$ obtained with the FBMC simulator for the 100 nm thick device with the ones used in the EBHDM when λ_e is constant (18 nm, Tab. 3.1) or depends on $E_{eff,e}$ through Eq. 5.54. We notice that in all the analyzed cases, the peak value of the electron's impact ionization coefficient increases as either ΔE_C or the electric field. From Fig. 5.38 it is also clear that the largest variations of $\alpha(0|x')$ are achieved by increasing the applied electric field. Moreover the use of the EBHDM with constant λ_e always overestimates the $\alpha(0|x')$ extracted from FBMC simulations, that are, however, in good agreement with the EBHDM when an energy dependent relaxation length is used.

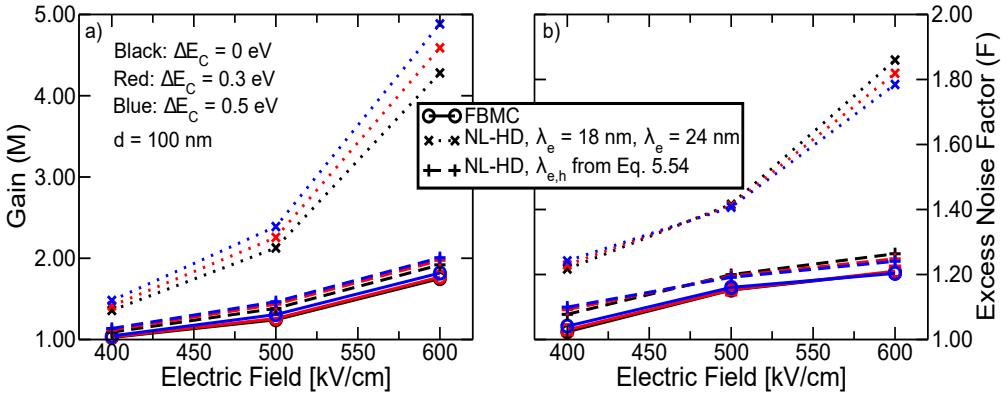

Figure 5.39: Comparison between a) the gain and b) the excess noise factor as a function of the applied electric field and for different values of ΔE_C computed with the FBMC simulator (circles and solid lines) and with the EBHDM by using constant λ_e and λ_h (crosses and dotted lines) or $\lambda_e(x|x')$ and $\lambda_h(x|x')$ from Eq. 5.54 (plus signs and dashed lines).

As a sanity check of the improved calibration of the electron's and hole's impact ionization coefficients in the EBHDM discussed in Section 5.7, we have computed the gain and the excess noise factor as a function of the applied electric field, for different values of ΔE_C, by using the FBMC and the EBHDM either with $\lambda_e = 18$ nm and $\lambda_h = 24$ nm or with $\lambda_e(x|x')$ and $\lambda_h(x|x')$ from Eq. 5.54 (as stated in Section 5.7, the parameters A_e, A_h, E_{ce}, E_{ch}, γ_e and γ_h to insert into Eqs. 2.72 and 2.73 are the ones of Tab. 5.6). The results are compared in Fig. 5.39. We notice that, with respect to FBMC simulations, the EBHDM overestimates both the gain and the excess noise factor when constant λ_e and λ_h are used, while the results of the EBHDM with energy dependent relaxation lengths are almost coincident with the ones of the FBMC, in the entire range of electric field values that we have simulated. This indicates that the improved calibration of the EBHDM, based on the results of FBMC simulation, that we have proposed in Section 5.7 can be safely used to study the performance, in terms of gain and excess noise factor, of GaAs-based APDs featuring conduction band discontinuities.

5.9 Summary

We have developed a Full Band Monte Carlo simulator (FBMC) to study carrier transport and impact ionization at high energies. We have calibrated the FBMC to match the experimental results for the drift velocities and the impact ionization coefficients of electrons and holes.

We have proposed a new expression to compute the position dependent impact ionization coefficients from FBMC simulations (Eq. 5.53) and we have used it to identify some major limitations of nonlocal history dependent models (NL-HD), that mainly stem from the assumption that secondary carriers are generated with zero kinetic energy and can move only in the direction of the electric field, resulting in impact ionization events only at $x' > x$ for electrons ($x' < x$ for holes). The FBMC simulations point out the role of backscattering that may lead to impact ionization at positions preceding the generation point along the field direction, in particular at high gains in short devices.

The FBMC has been used to compute the probability density functions of the distance between consecutive electron's or hole's impact ionization events and to extract the threshold energies for impact ionization in GaAs: $E_{th,e} = 2.69$ eV for electrons and $E_{th,h} = 3.12$ eV. These values are consistent with the ones determined in [40].

Starting from FBMC results, we have proposed an improved calibration of the electron's and hole's impact ionization coefficients for the EBHDM, based on energy dependent relaxation lengths λ_e and λ_h. The $\alpha(0|x')$ and $\beta(d|x')$ computed by using the improved calibration is in better agreement with FBMC results, if compared to the Dead Space model or the EBHDM with constant λ_e and λ_h.

Finally, the FBMC has been used to study impact ionization in GaAs-based APDs that feature conduction band discontinuities. Even though we have neglected energy and momentum conservation at the heterojunction, we have found that conduction band discontinuities up to $\Delta E_C = 0.5$ eV in GaAs are not sufficient to considerably improve the performance of the APD, in terms of gain and excess noise factor, and that high gains can be achieved only if impact ionization is triggered also by the applied electric field. However, the improved calibration of the EBHDM reproduces with a satisfactory agreement the gain and the excess noise factor as a function of the electric field, and for different values of ΔE_C, computed with the FBMC.

Chapter 6

TCAD Simulations and Comparison with Experiments

In the previous chapters we have focused on the description of impact ionization, on multiplication phenomena in APDs and on the photogenerated current noise. In this framework, comparison between our models and experiments has been already shown in Figs. 3.2-3.6, 3.8, 3.10, 3.13, 3.14, 3.16, 4.7 and 4.8. However, M and F are not the only relevant parameters to describe an APD. In this Chapter, we show how experimental characterization and TCAD simulation analysis [76] have been used to study the dark current and the differential capacitance as functions of the applied reverse bias voltage of the staircase SAM-APD for X-ray detection of Fig. 1.18b.

As mentioned in Sections 1.3 and 1.7, the dark current (I_{dark}) is a major concern in APDs, since it limits the energy resolution of the device. I_{dark} originates from generation/recombination processes that also reduce the number of photo-generated carriers able to reach the multiplication region, thus further reducing the signal-to-noise ratio. In the following, the dark current of GaAs/AlGaAs based APDs will be characterized over temperature (T), aiming to investigate its origin and to extract relevant parameters related to the carrier generation/recombination process. Comparison with TCAD simulations allowed us to extract the carrier lifetimes and to predict the collection efficiency of the photogenerated carriers.

The results shown in the following extend the ones published by the author of this thesis in [118, 119, 120].

6.1 Dark Current

Staircase SAM-APDs with the structure sketched in Fig. 1.18b have been fabricated at the IOM-CNR (Trieste, Italy) by using Molecular Beam Epitaxy and experimentally characterized to study the dependence of the dark current on temperature. TCAD simulations have been run to extract the the carriers' lifetimes and to evaluate the collection efficiency of these devices.

6.1.1 Experimental Characterization

The static characteristics of several APDs have been measured as a function of the applied reverse bias voltage (V_{rev}). Figure 6.1 reports the current-voltage (IV) curves of a subset of the measured APDs that can be considered as representative of the fabrication process. It is worth mentioning that the currents scale with the device area (not shown), which proves that edge effects give a small contribution to the measured current. A one dimensional model is thus adequ

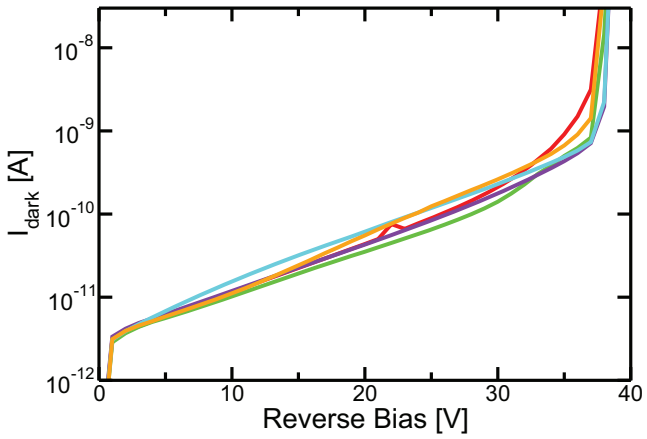

Figure 6.1: Dark current as a function of the applied reverse bias voltage V_{rev} for a subset of APDs. The breakdown voltage of the devices (V_{br}) is around 38 V. The APD active area is circular, with diameter 400 μm.

Then the IV curves of the APDs have measured at different temperatures, as shown in Fig. 6.2. We can notice that the dark current is largely modulated by temperature. The breakdown voltage (V_{br}) for different values of T is reported in Fig. 6.3). V_{br} increases as the temperature increases and this is a signature of the avalanche multiplication process at the base of the APD operation [12[1]

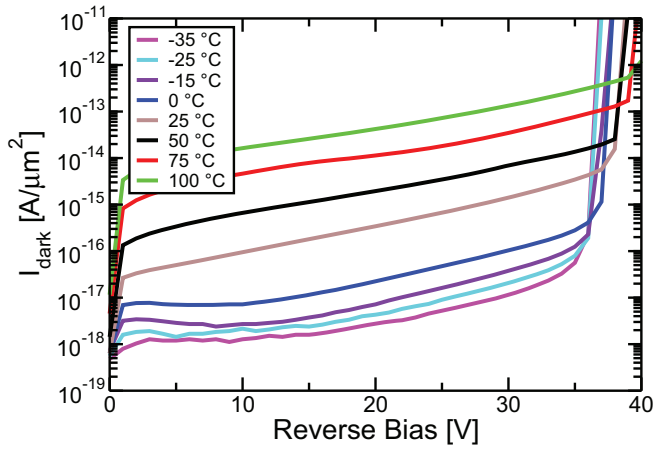

Figure 6.2: Experimental IV curves of a representative APD for different operating temperatures T.

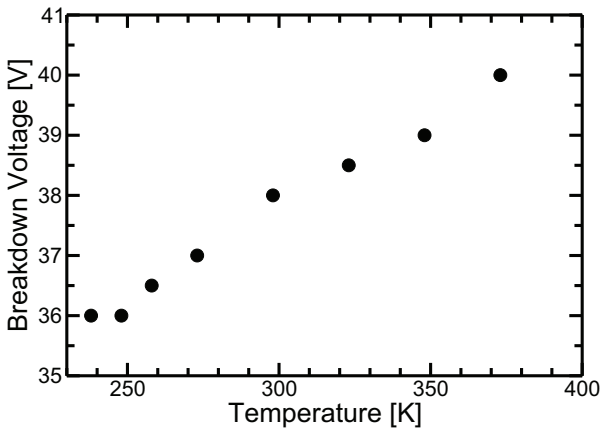

Figure 6.3: Breakdown voltage as a function of temperature. The positive temperature coefficient is a signature of the avalanche multiplication process.

Figure 6.4 reports the Arrhenius plots of the current for different values of V_{rev}. All curves essentially follow the exponential Arrhenius law

$$I = A \exp\left(-\frac{E_A}{k_b T}\right), \tag{6.1}$$

where A is a constant and E_A is the activation energy. The data in Fig. 6.4 have been used to extract the activation energy E_A (see Fig. 6.5), which turned out to be quite independent of V_{rev}, with a value of about 0.55 eV. This suggests that the dark current is related to traps in the bandgap of the III-V alloy, and that the midgap trap assisted Shockley Read Hall (SRH) generation/recombination process is mainly responsible for the dark current. Furthermore, since E_A does not depend on the bias (i.e. on the applied electric field), the presence of recombination processes that strongly depend on the applied field, like the band

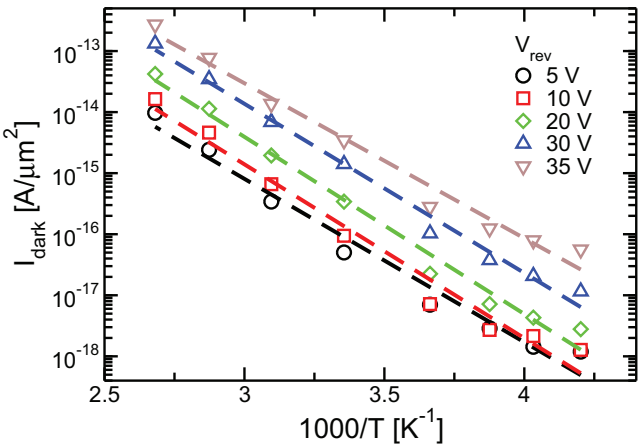

Figure 6.4: Arrhenius plots of the dark current for several V_{rev} values. Curves show the expected exponential behavior down to low temperatures where they start to deviate from Eq. 6.1 likely because a temperature independent dark current component enters into play.

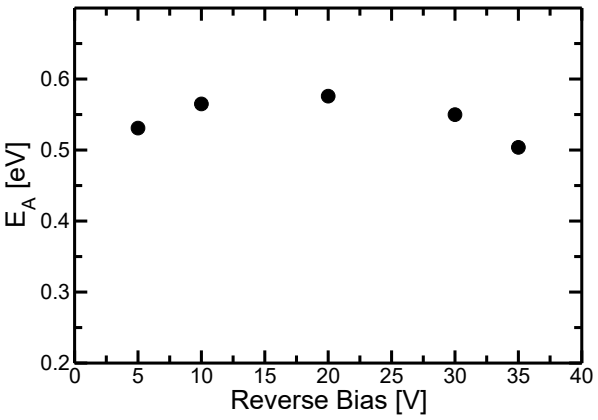

Figure 6.5: Activation energy as a function of the appiled reverse bias voltage, V_{rev}, extracted from the Arrhenius plots in Fig. 6.4. E_A is rather independent of the V_{rev} value and close to $E_g/2$.

It is worth noting that, if the carrier lifetimes were independent of temperature, a trap energy with a ΔE energy offset with respect to $\frac{E_g}{2}$, would result in an activation energy (extracted from the Arrhenius plots as in Fig. 6.5) that is the smallest value between $\frac{E_g}{2} + \Delta E$ and $\frac{E_g}{2} - \Delta E$.

6.1.2 TCAD Simulations

TCAD simulations [76] have been used to reproduce the dependence of the APD current-voltage characteristics on temperature and reverse bias voltage. The SRH generation/recombination rate (U_{SRH}) is modeled through the following set of equations:

$$U_{SRH} = R - G = \frac{np - n_i^2}{\tau_p(n + n_1) + \tau_n(p + p_1)}, \tag{6.2}$$

$$n_1 = n_i \exp\left(\frac{E_T - E_i}{k_b T}\right), \tag{6.3}$$

$$p_1 = n_i \exp\left(-\frac{E_T - E_i}{k_b T}\right), \tag{6.4}$$

where τ_n, τ_p and E_i are the electron's and hole's lifetimes and the Fermi level, respectively. The electron's density of the intrinsic semiconductor, n_i, is given by

$$n_i = \sqrt{N_C(T) N_V(T)} exp\left(-\frac{E_g(T)}{2k_b T}\right), \tag{6.5}$$

where the bandgap E_g and the effective conduction and valence band density of states (N_C and N_V, respectively) as a function of temperature are

$$E_g = E_g(0) - \frac{\alpha_{bg} T^2}{T + \beta_{bg}}, \tag{6.6}$$

$$N_{C,V} = N_{C,V}(300K) \left(\frac{T}{300K}\right)^{\frac{3}{2}}. \tag{6.7}$$

In the following concerning the parameters $E_A(0)$, α_L, β_L, and $N_{C,V}(300K)$, the default se d.

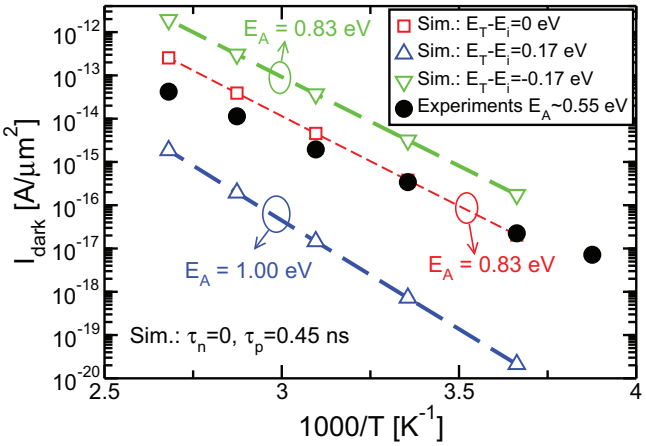

Figure 6.6: Arrhenius plots simulated for $V_{rev} = 20$ V assuming constant τ_n and τ_p and variable trap energy depth E_T.

Figure 6.6 reports the simulation analysis we performed on the current versus temperature data at $V_{rev} = 20$ V. We can reproduce the experiments at $T = 300$ K (i.e. $1000/T = 3.33$ K^{-1}) by setting $\tau_n = 0$ and $\tau_p = 0.45$ ns and by assuming $E_T = E_i$ (red dashed line). As it can be seen, we extract $E_A = 0.83$ eV (red curve) that is larger than in the experiments (black circles).

With $\tau_n = 0$, the slope of the Arrhenius plot can be modulated by changing E_T with respect to E_i (see Eqs. 6.2-6.4). Indeed, for $(E_T - E_i) > 0$, the slope of the simulated curve actually changes (Fig. 6.6, blue line), but E_A increases. Instead, for $(E_T - E_i) < 0$, E_A does not change (green line). This is because, in the generation/recombination function (Eq. 6.2), n_1 becomes negligible with respect to the electron density n (see Eq. 6.3). A similar behavior is observed with $\tau_n \neq 0$ and $\tau_p = 0$ or $\tau_n = \tau_p$: the U_{SRH} value required to reproduce the experiments always leads to $E_A \geq 0.83$ eV, hence to E_A values much larger than experimentally observed.

In summary, Fig. 6.6 indicates that the experiments can be reproduced only by assuming temperature dependent carrier lifetimes. Therefore, we assume $E_T = E_i$ and equal τ_n and τ_p values with a power–law dependence on T as in [76, 122, 123]:

$$\tau_n = \tau_p = \tau_{300K} \cdot \left(\frac{T}{300}\right)^{\alpha}, \tag{6.8}$$

where τ_{300K} is the carrier lifetime at $T = 300$ K.

Now, by using $\tau_{300K} = 0.39$ ns and $\alpha = 6.06$ in Eq. 6.8, the simulations in Fig. 6.7 reproduce well the experimental Arrhenius plots at different V_{rev}, for E_A values close to those in Fig. 6.5. Even though a positive value of α is reported also in [122], the fact that carrier lifetimes increase with temperature is hard to support and may indicate that other physical mechanisms, whose description is missing, are playing a role. However, to continue our analysis with the purpose of validating our methodology for the extraction of the collection efficiency (see Sec. 6.1.3), we kept $\alpha = 6.06$ in the following. Notice

that, in the simulations, the absorption region is always at equilibrium, thus we are only able to extract the lifetimes for the GaAs layers in the multiplication region, where [illegible] (see Fig. 6.8).

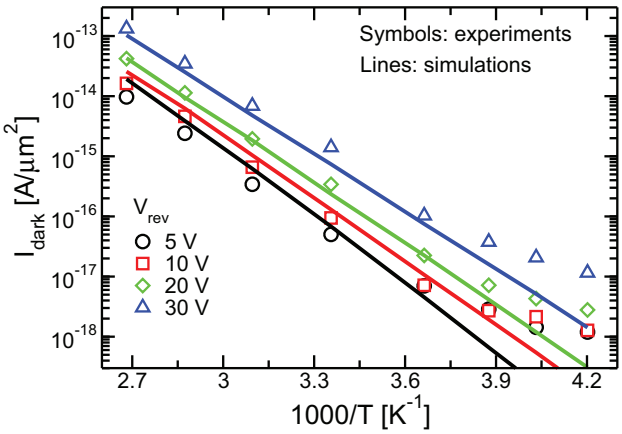

Figure 6.7: Arrhenius plots simulated with $\tau_n = \tau_p$ as in Eq. 6.8, and with $E_T = E_i$. Simulations now reproduce the experiments for different V_{rev}. A power-law temperature dependence is assumed to model the lifetimes (Eq. 6.8, $\tau_{300K} = 0.39$ ns, $\alpha = 6.06$). At low T, the experiments deviate from the linear behavior most likely because of a temperature-independent component not included in simulations.

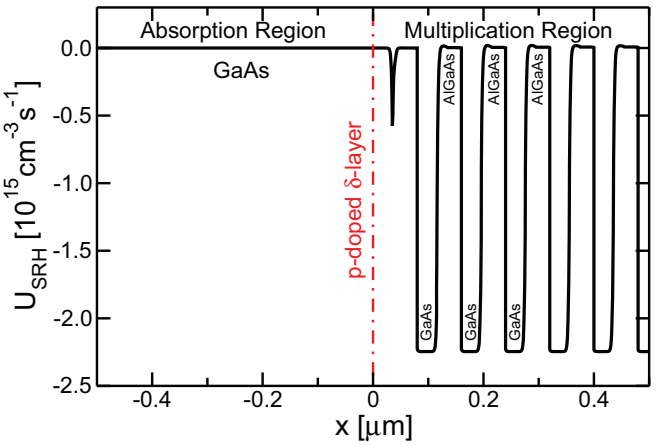

Figure 6.8: SRH generation/recombination function along the device depth. $x = 0$ corresponds to the p-doped δ-layer position that separates the absorption and multiplication regions. Note that carrier generation ($U_{SRH} < 0$) occurs in the small bandgap GaAs layers of the multiplication region. $V_{rev} = 20$ V. $\tau_n = \tau_p = \tau_{300K} = 0.39$ ns, $\alpha = 6.06$.

This parameter set allows us to fit the IV curves at different temperature (Fig. 6.9). The agreement between experiments and simulations is good down to $T = -15$ °C. At lower temperatures, a temperature-independent component of the current may arise in the measurements. Furthermore, the limited agreement for very small V_{rev} is most likely due to the fact that in the simulations

we consider the idealized APD structure, which neglects the presence of defects and on uniform trap density (i.e. uniform lifetimes along the multiplication region) in spite of the superlattice compositional changes over distance. In the simulations reported in Fig. 6.9, the dependence of τ_n and τ_p on the electric field is included by activating the Schenk model[76], that improves the match of the exponential increase of the IV curves for $V_{rev} > 20$ V observed in the experiments.

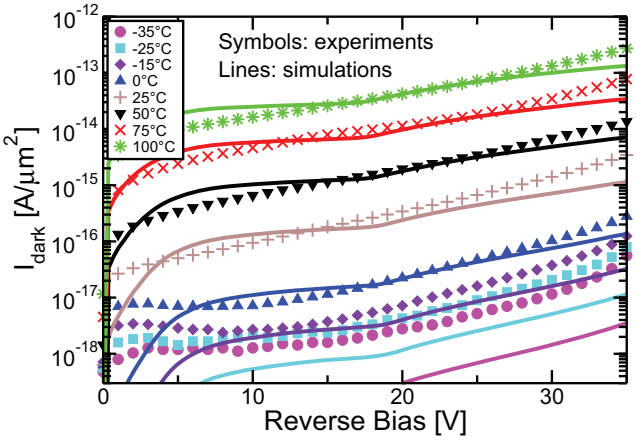

Figure 6.9: Simulated IV curves with $\tau_n = \tau_p$ as in Eq. 6.8. Simulations well reproduce the experiments, except at low T, when a temperature independent leakage com

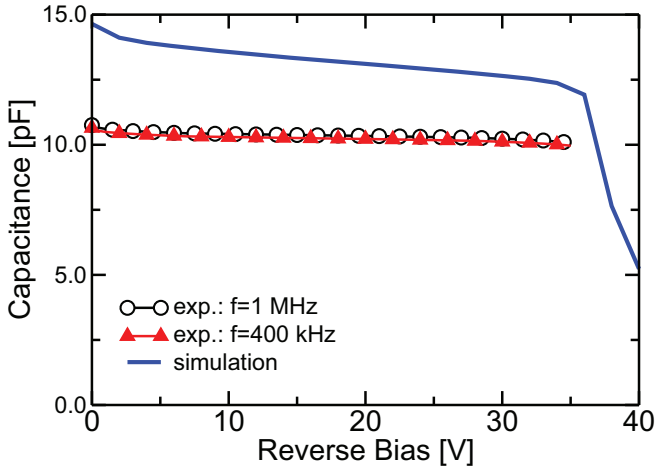

Figure 6.10: Typical experimental capacitance–voltage curves (symbols) of the measured APDs. The TCAD simulation for nominal parameter values (line) is reported for comparison.

Concerning the first point, Fig. 6.10 reports the experimental capacitance–voltage (CV) curves of a fabricated APD (symbols) and the CV calculated considering nominal dimensions and nominal parameters for the materials. The mismatch between simulated and measured CV curves suggests that better agreement between the model and the experiments in both Figs. 6.9 and 6.10 may be obtained by tuning the simulated APD geometry/composition. Moreover, a large trap density near the δ-layer (whose high doping may also

be source of defects) can induce an extra leakage current component also when the multiplication region is not fully depleted, thus resulting in a larger dark current at low V_{rev}. Finally, the simulation predicts that the depletion of the absorption region occurs for $V_{rev} > 35$ V, thus suggesting an interpretation for the capacitance drop above this voltage value (see Section 6.2).

6.1.3 Simulation of the Collection Efficiency

We also run TCAD simulations [76] of the APD's response to the photo–generation of an electron–hole pair in a position corresponding to the middle of the absorption layer. In this simulation, we applied $V_{rev} = 28$ V, a voltage large enough to ensure carrier multiplication in the APD, but not sufficient to make the electric field penetrate into the absorption region [118]. This is confirmed by the CV curves in Fig. 6.10, showing that up to $V_{rev} = 35$ V, the δ-p layer confines the voltage drop into the multiplication region and no capacitance drop is seen [118]. Indeed, only for $V_{rev} > 35$ V the simulation predicts that the electric field penetrates also into the absorption region causing the capacitance to drop (Fig. 6.10, dashed line).

In this respect, Fig. 6.11 shows how, after the generation of the electron-hole pair in the middle of the absorption layer, the charge diffuses all over the region because of the negligible electric field in the layer, leading to a rather flat electron density (n) after some time (t). Then, without considering the SRH generation recombination (Fig. 6.11(a)), electrons can exit the device only through the multiplication layer that is located at the right of the absorption layer ($x > 4.5$ μm).

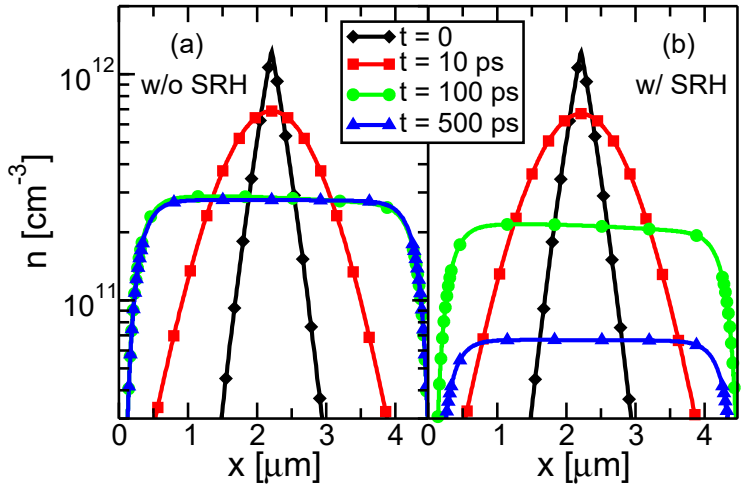

Figure 6.11: Electron density n calculated in absorption layer at different instants (t) after the generation of an electron-hole pair (in the middle). After the generation, carrier diffuse all over the absorption layer, due to the negligible electric field in the region. Then, without the SRH process (a), electrons can exit the region only through the multiplication layer on the right. With SRH (b), instead, electrons partly recombine before reaching the multiplication layer. Area of the device is 1 μm^2.

Figure 6.11(b) shows, instead, that when including the SRH process, electrons may recombine inside the absorption layer before reaching the multiplication region (compare circle and triangles), thus reducing the number of carriers that are finally collected at the n-type contact of the device and, hence, lowering the sensitivity of the APD to the electron-hole pair generation event.

To better illustrate this point, Fig. 6.12 reports the simulated current waveform at the n-type contact after the electron–hole pair generation: without the SRH recombination all the charge exits the device (black line), and the current integral over time gives exactly the photo-generated charge. Instead, when SRH is active inside the device, only the 55% of the charge reaches the contact (red line); therefore the SRH recombination causes the loss of about the 45% of photo–generated charge. Note that, for this calculations, we assumed the same carrier lifetimes in the GaAs absorption region and in the GaAs layers of the multiplication region.

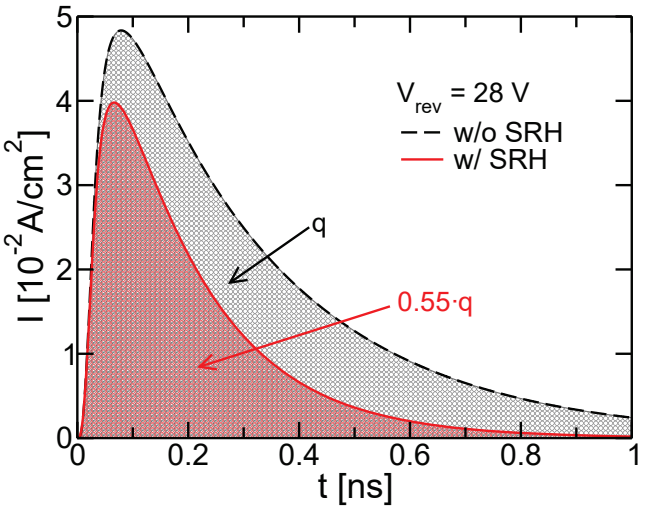

Figure 6.12: Simulated current collected at the n-type contact as a function of time after the generation of an electron-hole pair in the middle of the absorption layer. The current is simulated including (red) or not (black) the SRH generation/recombination. At $V_{rev} = 28$ V, the SRH process causes the loss of 45% of the photo–generated charge.

Of course, the probability to recombine for a photo–generated electron depends also on the distance to reach the APD contact; hence on the position at which it is generated inside the absorption region. To verify this, in Fig. 6.13, we report the calculated collection efficiency as a function of the photo–generation position. As expected, the closer to the multiplication region the photo–generation is, the larger the collection efficiency of the APD is, because of the reduction of the recombination probability. The collection efficiency is 42% when electrons are generated near the p–contact (left), while it is 92% for a generation close to the δ-layer (right).

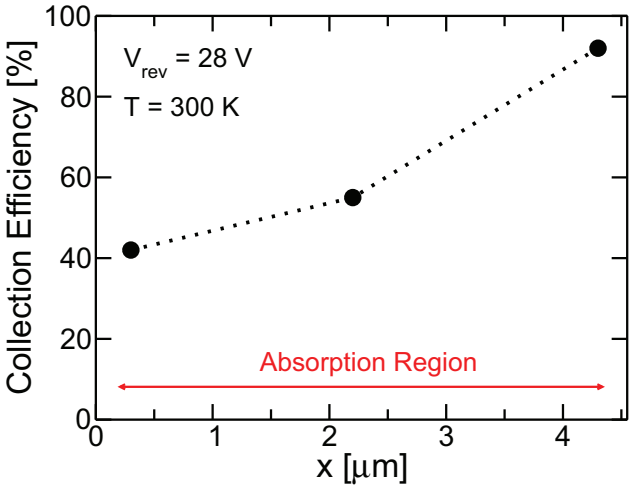

Figure 6.13: Collection efficiency as a function of the position inside the absorption layer where the photo–generation takes place. If the electron–hole pair is generated closer to the multiplication region ($x > 4.5$ μm), the collection efficiency is larger.

6.2 Simulation of the CV Characteristics

We have performed AC TCAD simulations [76] of the staircase SAM-APD of Fig. 1.18b to compute the CV characteristics of the device when the dose of the p-doped δ-layer that separates the absorption and the multiplication region varies from its nominal value (2.5×10^{12} cm^{-2}). CV measurements are a useful mean to inspect the extension of the depletion region inside the device. This analysis thus allowed us to investigate how, depending on the value of the dose, the applied voltage falls across the multiplication region alone or also on a portion of the absorption region. As stated in Sections 1.3 and 1.7, being able to determine the detector's capacitance at a given operating voltage is important also to compute the energy resolution of the APD at that specific bias point (Eq. 1.28).

The p-doped δ-layer has been reproduced with TCAD by assuming a Gaussian doping profile. According to this assumption, the dose is the area under the Gaussian bell and it is given by

$$Dose = \frac{Peak \cdot FWHM \cdot \sqrt{2\pi}}{2\sqrt{2ln(2)}}, \tag{6.9}$$

where $Peak$ is the peak value of the Gaussian and $FWHM$ is the full width at the half of the maximum (see Fig. 6.14).

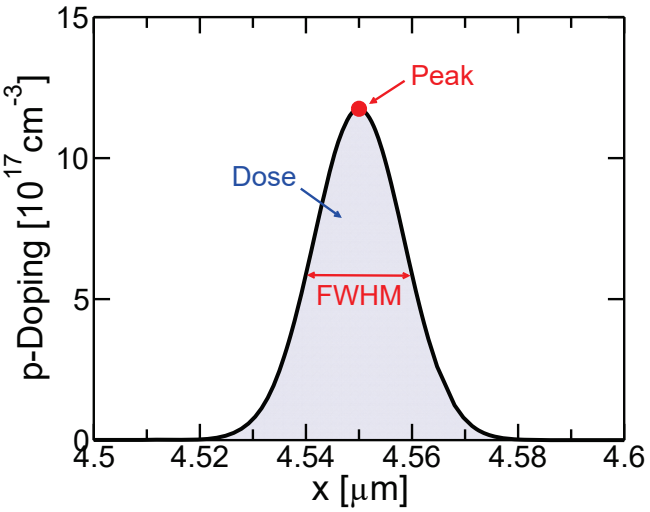

Figure 6.14: Dose of the p-doped δ-layer that separates the absorption and the multiplication region of the staircase SAM-APD of Fig. 1.18b. The dose is computed with Eq. 6.9 since a Gaussian doping profile has been assumed in the TCAD simulations [76].

Figure 6.15 reports the simulated capacitance as a function of the applied reverse bias voltage for the staircase SAM-APD of Fig. 1.18b with $Dose = 2.5{\times}10^{12}$ cm^{-2} for different values of $FWHM$. It is worth noting that the simulated CV characteristic is insensitive to the value of $FWHM$ that we set, thus, in the following, we have always assumed $FWHM = 20$ nm, which is a realistic value based on processing conditions.

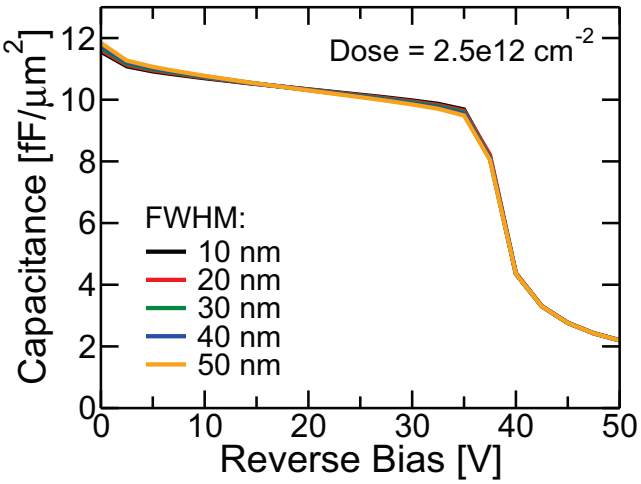

Figure 6.15: Capacitance as a function of the reverse bias voltage obtained with TCAD simulations [76] for different $FWHM$ values of the dose of the p-doped δ-layer (see Fig. 6.14).

From Fig. 6.15 we also notice that, for the simulated dose, the CV characteristic is constant for V_{rev} up to 33 V, then it rapidly decreases to a lower value. In fact, at first the applied bias voltage falls on the multiplication region

and the electric field is confined therein. When V_{rev} increases, the p-doped δ-layer is no more able to contain the electric field in the multiplication region and part of the absorption region is also depleted. Then, the differential capacitance of the absorption region is in series to the one of the multiplication region, as sketched in Fig. 6.16, and the total capacitance is given by

$$C = \left(\frac{1}{C_{abs}} + \frac{1}{C_{mult}} \right)^{-1}, \tag{6.10}$$

where C_{abs} and C_{mult} are the differential capacitances of the absorption and the multiplication regions, respectively, and are computed by using the parallel plate capacitor approximation, consistently with our assumption that edge effects should be negligible in our samples.

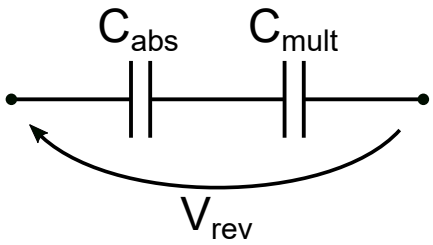

Figure 6.16: Schematic representation of the absorption and multiplication regions' contributions to the total capacitance of the staircase SAM-APD of Fig. 1.18b.

Figure 6.17 compares the experimental and simulated CV characteristics of the staircase SAM-APD of Fig. 1.18b for different values of the dose of the p-doped δ-layer. The agreement between simulations and measurements is excellent and we notice that, as the dose decreases, the reverse bias voltage that can be applied without depleting part of the absorption region also decreases.

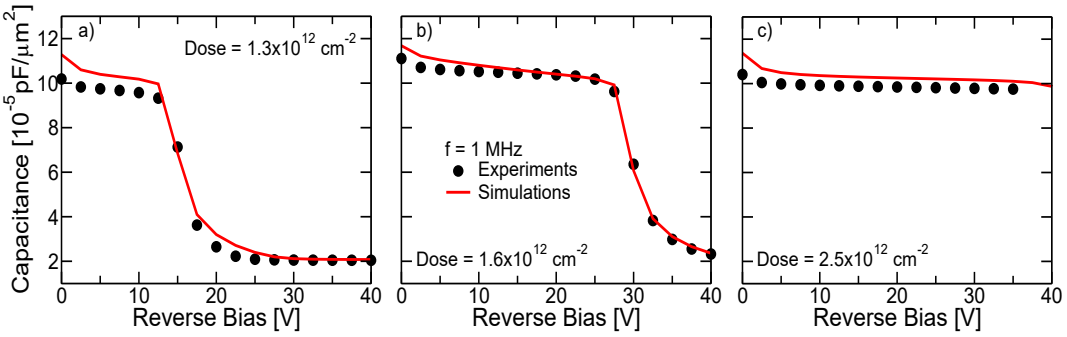

Figure 6.17: Experimental (symbols) and simulated (red lines) capacitance versus applied reverse bias voltage curves of the staircase SAM-APD of Fig. 1.18b for different doses of the p-doped δ-layer. The dose is a) 1.3×10^{12} cm^{-2}, b) 1.6×10^{12} cm^{-2} and c) 2.5×10^{12} cm^{-2}.

The behavior of the CV characteristics of Fig. 6.17 is reflected by the conduction band profiles reported in Fig. 6.18 for different bias voltages. In fact,

a higher dose translates into a higher energy barrier for electrons between the absorption and the multiplication region. A high barrier ensures that impact ionization occurs only in the multiplication region of the device, lowering the excess noise factor, but it also limits the velocity of the carrier in the absorption region (see the flat conduction band profile for the higher dose in Fig. 6.18).

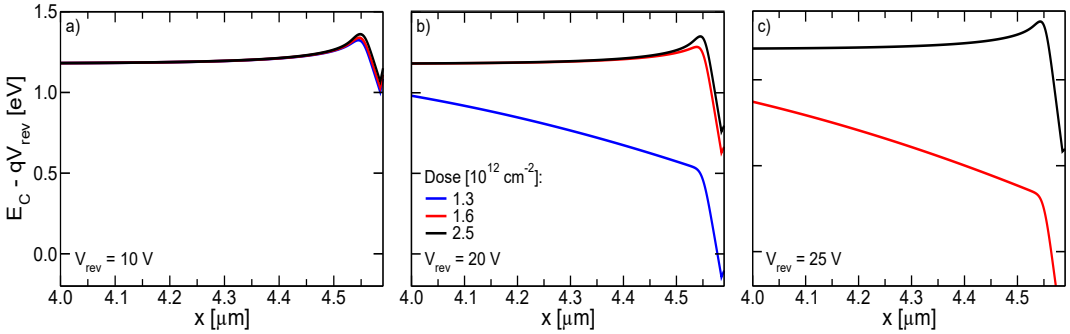

Figure 6.18: Conduction band profiles near the end of the absorption region extracted from TCAD simulations [76] of the staircase SAM-APD of Fig. 6.18 at differnt bias voltages: a) $V_{rev} = 10$ V, b) $V_{rev} = 20$ V, c) $V_{rev} = 25$ V. The dose of the p-doped δ-layer is $1.3{\times}10^{12}$ cm^{-2} (blue), $1.6{\times}10^{12}$ cm^{-2} (red) or $2.5{\times}10^{12}$ cm^{-2}. Notice that in plot c) the blue curve is not visible beacuse it is out of scale.

6.3 Summary

Experiments and TCAD simulations allowed us to extract the SRH carrier lifetimes in GaAs/AlGaAs APDs and to evaluate the CV characteristics of these devices for different values of the dose of the p-doped δ-layer.

The extracted lifetimes were used for calibrated simulations of the collection efficiency of the photo–generated current under realistic operating conditions.

The results show that the collection efficiency goes from a minimum of 42%, for a photo–generation near the top contact of the device, to a maximum value of 92% when the electron–hole pair is generated at the end of the absorption layer, hence near the multiplication layer.

These collection efficiency is in general quite high, thus reassuring on the sensitivity of the studied APDs. However, the large collection efficiency dependence on the position inside the absorption layer of the photo–generation rises questions concerning the potential energy resolution of these photo–detectors. It is of course a fact that, to collect high energy particles, absorption layers with not very small thickness are required and, thus, the distribution of the photo–generation events along the device may become a concern for these APDs.

Concerning the CV characteristics, we have noticed that the nominal dose for the p-doped δ-layer ($2.5{\times}10^{12}$ cm^{-2} [7, 118, 22]) ensures that carrier multiplication occurs only in the multiplication region and this is beneficial in terms of noise. However, as stated also in Section 4.5.1, having part of the absorption region depleted increases the speed of the device and reduces the jitter. This

trade-off between the excess noise factor and the carrier's velocity inside the absorption region has to be taken into account during the design of the APD.

Chapter 7

Conclusions and Future Work

We have developed a suite of simulation tools to accurately describe impact ionization and study the figures of merit of Avalanche Photodiodes (APDs) and, in particular, GaAs/AlGaAs staircase Separate Absorption and Multiplication (SAM) APDs. These tools include:

1. A nonlocal history dependent model, the EBHDM, implemented with a Finite Difference (FD) scheme, to compute the gain (M) and the excess noise factor (F) of APDs. Compared to state of the art, our approach includes a different definition of the effective field based on the energy balance equation and provides an improved trade-off between accuracy and efficiency.

2. A Random Path Length (RPL) implementation of the EBHDM, that, in addition to M and F, provides also the time response, the bandwidth and the jitter of APDs. Compared to other RPL approaches, the one presented in this thesis is based on the effective field definition given by the EBHDM and, beside impact ionization, the model also describes carriers' drift and diffusion in the absorption region. To our knowledge, the RPL algorithm that we have developed is the only one in the literature that is based on generic nonlocal history dependent impact ionization models, not only on the Dead Space model, and it is the first one to include an accurate description of carriers' motion in regions where the electric field is not sufficient to trigger impact ionization events, not only in the multiplication region.

3. A Full Band Monte Carlo simulator (FBMC), to describe carrier transport and the scattering mechanisms, including impact ionization, at a microscopic level. Compared with other FBMCs employed in the literature for the study of p-i-n APDs, we use a $\vec{k}$-dependent description of impact ionization based on the Constant Matrix Element approximation, instead of an energy-dependent Keldysh expression, which improves the accuracy of our results.

Each model has been validated by comparison with experimental data for the gain and the excess noise factor of different APD structures or with the results of TCAD simulations.

The FBMC is the most accurate tool, but, as sketched in Fig. 7.1, this accuracy comes with an associated computational burden that limits the use of the FBMC to the study of short devices and for short time scales. On the other hand, the RPL and FD implementations of the EBHDM are faster and allow handling larger detector structures, but they rely on several approximations (the kinetic energy of secondary carriers after an impact ionization event is always null and carriers can move only in the direction of the electric field), that may not always be valid. To give a reference, considering a server with 48 cores and 252 GB of RAM, the computation of the gain, the excess noise factor and the history dependent impact ionization coefficients for a given bias point with the FBMC takes, on average, from 8 hours for a 100 nm thick p-i-n APD to 2 weeks for a 800 nm thick device, while it takes from 15 to 30 and from 30 to 60 minutes with the FD and the RPL implementations of the EBHDM, respectively. On the other hand, the computation of the jitter with the RPL algorithm for a SAM-APD with a 4.5 μm and a 1 μm thick absorption and multiplication regions takes from 2 to 10 hours, according to the bias point (longer simulation times are required for bias voltages close to the breakdown) and to the number of waveforms that have to be computed, which depends on the photon's energy. This kind of analysis can be performed only with the RPL so we cannot compare this computation time with that of the FBMC.

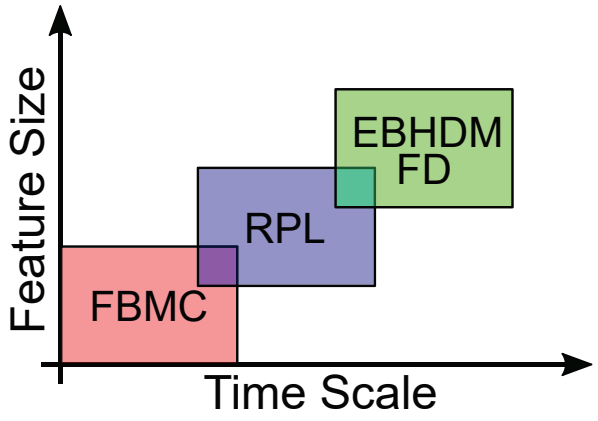

Figure 7.1: Schematic representation of the simulation tools developed in this thesis. Each model is suited to analyze different feature sizes and times scales.

We have found that, in a GaAs/AlGaAs staircase APD used for X-Ray detection:

- Hole's impact ionization plays a substantial role and degrades the noise performance. However, increasing the number of conduction band steps reduces the noise at fixed gain but comes at the expense of a longer response time.

- The increase in the number of steps of the multiplication region does not imply any practical drawback in terms of dynamic response of the system, because the following shaper circuit usually has an optimized time constant much longer than the time delay of the APD.

- The jitter is higher if the absorption region is quasi-neutral. Therefore, the δ-p layer that separates the absorption and the multiplication regions should be designed so that, at the desired operating voltages, the electric field in the absorption region is not null. This field has to be small enough to prevent triggering of unwanted impact ionization events.

- Conduction band discontinuities up to $\Delta E_C = 0.5$ eV in GaAs/AlGaAs are not sufficient to considerably improve the performance of the APD, in terms of gain and excess noise factor, and the required high gains can be achieved only if impact ionization is triggered also by the applied electric field.

In addition, we have also performed experimental characterization and DC, AC and time-dependent analyses with a TCAD simulator of GaAs/AlGaAs staircase APDs that allowed us to extract the SRH carrier lifetimes and to estimate the dark current and the collection efficiency of these devices.

7.1 Future Work

The variety of applications where Avalanche Photodiodes are used and the flexibility of the simulation tools that we have developed pave the way to many exploitation paths and open the possibility of several different improvements to our work.

On the modeling side and with reference to the EBHDM, a further improvement could by achieved by developing model's equation that include the possibility of impact ionization events at positions that are before, along the field direction, the carrier's generation position, namely $x' < x$ for electrons and $x' > x$ for holes.

As for the Full Band Monte Carlo transport simulator, its calibration for InAs-based materials would allow to understand at a microscopic level the working principle of APDs used for optical fiber communication links and working in the infrared wavelength range. More in general, the calibration for other materials of all the developed simulation tools could be exploited to improve the design and the performance of APDs. Regarding, staircase APDs for instance, optimized sequences of steps could be created by placing the largest conduction band discontinuity (the one with largest associated gain and lowest excess noise factor) as the first step.

Finally, another interesting option is to extend the model's equations of the EBHDM for studying the figures of merit of APDs operating in Geiger mode. Interestingly, also the FBMC could be used to this aim.

Bibliography

[1] R. J. McIntyre, "Multiplication noise in uniform avalanche diodes," *IEEE Transactions on Electron Devices*, vol. ED-13, no. 1, pp. 164–168, Jan. 1966. doi: 10.1109/T-ED.1966.15651

[2] V. C. Spanoudaki and C. S. Levin, "Photo-detectors for time of flight positron emission tomography (ToF-PET)," *Sensors*, vol. 10, no. 11, pp. 10 484–10 505, Nov. 2010. doi: 10.3390/s101110484

[3] F. Powolny, E. Auffray, S. E. Brunner, E. Garutti, M. Goettlich, H. Hillemanns, P. Jarron, P. Lecoq, T. Meyer, H. C. Schultz-Coulon, W. Shen, and M. C. S. Williams, "Time-based readout of a silicon photomultiplier (SiPM) for time of flight positron emission tomography (TOF-PET)," *IEEE Transactions on Nuclear Science*, vol. 58, no. 3, pp. 597–604, 2011.

[4] R. Agishev, A. Comeron, J. Bach, A. Rodriguez, M. Sicard, J. Riu, and S. Royo, "Lidar with SiPM: Some capabilities and limitations in real environment," *Optics and Laser Technology*, vol. 49, pp. 86 – 90, 2013. doi: 10.1016/j.optlastec.2012.12.024

[5] M. Akiba, K. Inagaki, and K. Tsujino, "Photon number resolving SiPM detector with 1 GHz count rate," *Opt. Express*, vol. 20, no. 3, pp. 2779–2788, Jan 2012. doi: 10.1364/OE.20.002779

[6] C. H. Tan, R. B. Gomes, J. P. R. David, A. M. Barnett, D. J. Bassford, J. E. Lees, and J. S. Ng, "Avalanche gain and energy resolution of semiconductor X-ray detectors," *IEEE Transactions on Electron Devices*, vol. 58, no. 6, pp. 1696–1701, Jun. 2011. doi: 10.1109/TED.2011.2121915

[7] J. Lauter, D. Protic, A. Forster, and H. Luth, "AlGaAs/GaAs SAM-avalanche photodiode: An X-ray detector for low energy photons," *Nuclear Instruments and Methods in Physics Research Section A: Accelerators, Spectrometers, Detectors and Associated Equipment*, vol. 356, no. 2, pp. 324–329, 1995. doi: 10.1016/0168-9002(94)01237-7

[8] R. B. Gomes, C. H. Tan, J. E. Lees, J. P. R. David, and J. S. Ng, "Effects of dead space on avalanche gain distribution of X-ray avalanche photodiodes," *IEEE Transactions on Electron Devices*, vol. 59, no. 4, pp. 1063–1067, Apr. 2012. doi: 10.1109/TED.2012.2182674

[9] J. C. Campbell, "Recent advances in avalanche photodiodes," *Journal of Lightwave Technology*, vol. 34, no. 2, pp. 278–285, Jan. 2016. doi: 10.1109/JLT.2015.2453092

[10] M. Ren, S. Maddox, Y. Chen, M. Woodson, J. C. Campbell, and S. Bank, "AlInAsSb/GaSb staircase avalanche photodiode," *Applied Physics Letters*, vol. 108, no. 8, pp. 1–4, 2016. doi: 10.1063/1.4942370

[11] A. Vilà, A. Arbat, E. Vilella, and A. Dieguez, *Geiger-Mode Avalanche Photodiodes in Standard CMOS Technologies*, 03 2012. ISBN 978-953-51-0358-5

[12] R. B. Emmons, "Avalanche-photodiode frequency response," *Journal of Applied Physics*, vol. 38, no. 9, pp. 3705–3714, 1967. doi: 10.1063/1.1710199

[13] F. Capasso, Won-Tien Tsang, and G. F. Williams, "Staircase solid-state photomultipliers and avalanche photodiodes with enhanced ionization rates ratio," *IEEE Transactions on Electron Devices*, vol. 30, no. 4, pp. 381–390, Apr. 1983. doi: 10.1109/T-ED.1983.21132

[14] B. Henke, E. Gullikson, and J. Davis, "X-ray interactions: Photoabsorption, scattering, transmission, and reflection at E = 50-30,000 eV, Z = 1-92," *Atomic Data and Nuclear Data Tables*, vol. 54, no. 2, pp. 181 – 342, 1993. doi: 10.1006/adnd.1993.1013

[15] L. M. P. Fernandes, F. D. Amaro, A. Antognini, J. M. R. Cardoso, C. A. N. Conde, O. Huot, P. E. Knowles, F. Kottmann, J. A. M. Lopes, L. Ludhova, C. M. B. Monteiro, F. Mulhauser, R. Pohl, J. M. F. dos Santos, L. A. Schaller, D. Taqqu, and J. F. C. A. Veloso, "Characterization of large area avalanche photodiodes in X-ray and VUV-light detection," *Journal of Instrumentation*, vol. 2, no. 8, pp. 1–30, Aug. 2007. doi: 10.1088/1748-0221/2/08/p08005

[16] R. Van Overstraeten and H. De Man, "Measurement of the ionization rates in diffused silicon p- n junctions," *Solid State Electronics*, vol. 13, no. 5, pp. 583–608, May 1970. doi: 10.1016/0038-1101(70)90139-5

[17] G. E. Bulman, V. M. Robbins, K. F. Brennan, K. Hess, and G. E. Stillman, "Experimental determination of impact ionization coefficients in (100) GaAs," *IEEE Electron Device Letters*, vol. 4, no. 6, pp. 181–185, Jun. 1983. doi: 10.1109/EDL.1983.25697

[18] A. Barnett, D. Bassford, J. Lees, J. Ng, C. Tan, and J. David, "Temperature dependence of AlGaAs soft X-ray detectors," *Nuclear Instruments and Methods in Physics Research Section A: Accelerators, Spectrometers, Detectors and Associated Equipment*, vol. 621, no. 1, pp. 453 – 455, 2010. doi: 10.1016/j.nima.2010.06.089

[19] S. Adachi, *GaAs and Related Materials: Bulk Semiconducting and Superlattice Properties*. World Scientific, 1994. ISBN 9789810219253

[20] A. R. J. Marshall, J. P. R. David, and C. H. Tan, "Impact ionization in InAs electron avalanche photodiodes," *IEEE Transactions on Electron Devices*, vol. 57, no. 10, pp. 2631–2638, Oct. 2010. doi: 10.1109/TED.2010.2058330

[21] J. Lauter, A. Forster, H. Luth, K. D. Muller, and R. Reinartz, "AlGaAs/GaAs avalanche detector array-1 GBit/s X-ray receiver for timing measurements," *IEEE Transactions on Nuclear Science*, vol. 43, no. 3, pp. 1446–1451, Jun. 1996. doi: 10.1109/23.507080

[22] C. Nichetti, T. Steinhartova, M. Antonelli, G. Cautero, R. Menk, A. Pilotto, F. Driussi, P. Palestri, L. Selmi, F. Arfelli, and G. Biasiol, "Gain and noise in GaAs/AlGaAs avalanche photodiodes with thin multiplication regions," *Journal of Instrumentation*, vol. 14, no. 01, pp. 1–8, Jan. 2019. doi: 10.1088/1748-0221/14/01/c01003

[23] P. Yuan, K. A. Anselm, C. Hu, H. Nie, C. Lenox, A. L. Holmes, B. G. Streetman, J. C. Campbell, and R. J. McIntyre, "A new look at impact ionization-part II: Gain and noise in short avalanche photodiodes," *IEEE Transactions on Electron Devices*, vol. 46, no. 8, pp. 1632–1639, Aug. 1999. doi: 10.1109/16.777151

[24] G. M. Williams, M. Compton, D. A. Ramirez, M. M. Hayat, and A. S. Huntington, "Multi-Gain-Stage InGaAs avalanche photodiode with enhanced gain and reduced excess noise," *IEEE Journal of the Electron Devices Society*, vol. 1, no. 2, pp. 54–65, Feb. 2013. doi: 10.1109/JEDS.2013.2258072

[25] R. Gomes, C. Tan, X. Meng, J. David, and J. Ng, "GaAs/$Al_{0.8}Ga_{0.2}As$ avalanche photodiodes for soft X-ray spectroscopy," *Journal of Instrumentation*, vol. 9, no. 3, pp. 1–10, March 2014. doi: 10.1088/1748-0221/9/03/p03014

[26] E. Gatti and P. F. Manfredi, "Processing the signals from solid-state detectors in elementary-particle physics," *La Rivista del Nuovo Cimento (1978-1999)*, vol. 9, no. 1, pp. 1–146, Jan. 1986. doi: 10.1007/BF02822156

[27] *Courtesy of P. Palestri*. University of Udine, Udine (Italy).

[28] J. Lees, D. Bassford, J. Ng, C. Tan, and J. David, "AlGaAs diodes for X-ray spectroscopy," *Nuclear Instruments and Methods in Physics Research Section A: Accelerators, Spectrometers, Detectors and Associated Equipment*, vol. 594, no. 2, pp. 202 – 205, 2008. doi: 10.1016/j.nima.2008.06.038

[29] J. E. Lees, A. M. Barnett, D. J. Bassford, J. S. Ng, C. H. Tan, N. Babazadeh, R. B. Gomes, P. Vines, J. P. R. David, R. D. McKeag, and D. Boe, "Development of high temperature AlGaAs soft X-ray photon counting detectors," *Journal of Instrumentation*, vol. 6, no. 12, pp. C12 007–C12 007, Dec 2011. doi: 10.1088/1748-0221/6/12/c12007

[30] A. Barnett, J. Lees, D. Bassford, J. Ng, C. Tan, and R. Gomez, "Modelling results of avalanche multiplication in AlGaAs soft X-ray APDs," *Nuclear Instruments and Methods in Physics Research Section A: Accelerators, Spectrometers, Detectors and Associated Equipment*, vol. 626-627, pp. 25 – 30, 2011. doi: 10.1016/j.nima.2010.10.022

[31] A. G. Chynoweth, "Ionization rates for electrons and holes in silicon," *Phys. Rev.*, vol. 109, pp. 1537–1540, Mar. 1958. doi: 10.1103/PhysRev.109.1537

[32] M. Teich, K. Matsuo, and B. Saleh, "Excess noise factors for conventional and superlattice avalanche photodiodes and photomultiplier tubes," *IEEE Journal of Quantum Electronics*, vol. 22, no. 8, pp. 1184–1193, Aug. 1986. doi: 10.1109/JQE.1986.1073137

[33] G. Kahraman, B. E. A. Saleh, W. L. Sargeant, and M. C. Teich, "Time and frequency response of avalanche photodiodes with arbitrary structure," *IEEE Transactions on Electron Devices*, vol. 39, no. 3, pp. 553–560, 1992. doi: 10.1109/16.123477

[34] L.-A. Hamel and M. Julien, "Generalized demonstration of Ramo's theorem with space charge and polarization effects," *Nuclear Instruments and Methods in Physics Research Section A: Accelerators, Spectrometers, Detectors and Associated Equipment*, vol. 597, no. 2, pp. 207–211, 2008. doi: 10.1016/j.nima.2008.09.008

[35] M. M. Hayat, W. L. Sargeant, and B. E. A. Saleh, "Effect of dead space on gain and noise in Si and GaAs avalanche photodiodes," *IEEE Journal of Quantum Electronics*, vol. 28, no. 5, pp. 1360–1365, May 1992. doi: 10.1109/3.135278

[36] P. Yuan, C. C. Hansing, K. A. Anselm, C. V. Lenox, H. Nie, A. L. Holmes, B. G. Streetman, and J. C. Campbell, "Impact ionization characteristics of III-V semiconductors for a wide range of multiplication region thicknesses," *IEEE Journal of Quantum Electronics*, vol. 36, no. 2, pp. 198–204, Feb. 2000. doi: 10.1109/3.823466

[37] M. A. Saleh, M. M. Hayat, B. E. A. Saleh, and M. C. Teich, "Dead-space-based theory correctly predicts excess noise factor for thin GaAs and AlGaAs avalanche photodiodes," *IEEE Transactions on Electron Devices*, vol. 47, no. 3, pp. 625–633, Mar. 2000. doi: 10.1109/16.824739

[38] M. A. Saleh, M. M. Hayat, P. P. Sotirelis, A. L. Holmes, J. C. Campbell, B. E. A. Saleh, and M. C. Teich, "Impact-ionization and noise characteristics of thin III-V avalanche photodiodes," *IEEE Transactions on Electron Devices*, vol. 48, no. 12, pp. 2722–2731, Dec. 2001. doi: 10.1109/16.974696

[39] R. J. McIntyre, "A new look at impact ionization-part I: A theory of gain, noise, breakdown probability, and frequency response," *IEEE Transactions on Electron Devices*, vol. 46, no. 8, pp. 1623–1631, Aug. 1999. doi: 10.1109/16.777150

[40] J. S. Cheong, M. M. Hayat, X. Zhou, and J. P. R. David, "Relating the experimental ionization coefficients in semiconductors to the nonlocal ionization coefficients," *IEEE Transactions on Electron Devices*, vol. 62, no. 6, pp. 1946–1952, 2015. doi: 10.1109/TED.2015.2422789

[41] A. Spinelli and A. L. Lacaita, "Mean gain of avalanche photodiodes in a dead space model," *IEEE Transactions on Electron Devices*, vol. 43, no. 1, pp. 23–30, 1996. doi: 10.1109/16.477589

[42] M. M. Hayat and B. E. A. Saleh, "Statistical properties of the impulse response function of double-carrier multiplication avalanche photodiodes including the effect of dead space," *Journal of Lightwave Technology*, vol. 10, no. 10, pp. 1415–1425, Oct. 1992. doi: 10.1109/50.166785

[43] D. S. Ong, K. F. Li, G. J. Rees, J. P. R. David, and P. N. Robson, "A simple model to determine multiplication and noise in avalanche photodiodes," *Journal of Applied Physics*, vol. 83, no. 6, pp. 3426–3428, 1998. doi: 10.1063/1.367111

[44] J. S. Ng, C. H. Tan, B. K. Ng, P. J. Hambleton, J. P. R. David, G. J. Rees, A. H. You, and D. S. Ong, "Effect of dead space on avalanche speed [apds]," *IEEE Transactions on Electron Devices*, vol. 49, no. 4, pp. 544–549, Apr. 2002. doi: 10.1109/16.992860

[45] C. Jacoboni and L. Reggiani, "The Monte Carlo method for the solution of charge transport in semiconductors with applications to covalent materials," *Rev. Mod. Phys.*, vol. 55, pp. 645–705, Jul. 1983. doi: 10.1103/RevModPhys.55.645

[46] D. Esseni, P. Palestri, and L. Selmi, *Nanoscale MOS Transistors: Semi-Classical Transport and Applications*. Cambridge University Press, 2011.

[47] D. S. Ong, K. F. Li, G. J. Rees, G. M. Dunn, J. P. R. David, and P. N. Robson, "A Monte Carlo investigation of multiplication noise in thin p^+-i-n^+ GaAs avalanche photodiodes," *IEEE Transactions on Electron Devices*, vol. 45, no. 8, pp. 1804–1810, Aug. 1998. doi: 10.1109/16.704382

[48] G. M. Dunn, G. J. Rees, J. P. R. David, S. A. Plimmer, and D. C. Herbert, "Monte carlo simulation of impact ionization and current multiplication in short GaAs diodes," *Semiconductor Science and Technology*, vol. 12, no. 1, pp. 111–120, jan 1997. doi: 10.1088/0268-1242/12/1/019

[49] S. A. Plimmer, J. P. R. David, R. Grey, and G. J. Rees, "Avalanche multiplication in $Al_xGa_{1-x}As$ (x=0 to 0.60)," *IEEE Transactions on Electron Devices*, vol. 47, no. 5, pp. 1089–1097, 2000. doi: 10.1109/16.841245

[50] P. Houston and A. Evans, "Electron drift velocity in n-GaAs at high electric fields," *Solid-State Electronics*, vol. 20, no. 3, pp. 197 – 204, 1977. doi: https://doi.org/10.1016/0038-1101(77)90184-8

[51] K. Brennan and K. Hess, "High field transport in GaAs, InP and InAs," *Solid-State Electronics*, vol. 27, no. 4, pp. 347 – 357, 1984. doi: https://doi.org/10.1016/0038-1101(84)90168-0

[52] L. V. Keldysh, "Kinetic theory of impact ionization in semiconductors," *Soviet Physics JETP*, vol. 37, no. 3, pp. 509 – 518, 1960.

[53] M. Stobbe, R. Redmer, and W. Schattke, "Impact ionization rate in gaas," *Phys. Rev. B*, vol. 49, pp. 4494–4500, Feb 1994. doi: 10.1103/PhysRevB.49.4494

[54] F. Ma, S. Wang, X. Li, K. A. Anselm, X. G. Zheng, A. L. Holmes, and J. C. Campbell, "Monte Carlo simulation of low-noise avalanche photodiodes with heterojunctions," *Journal of Applied Physics*, vol. 92, no. 8, pp. 4791–4795, 2002. doi: 10.1063/1.1505987

[55] P. J. Hambleton, S. A. Plimmer, and G. J. Rees, "Limitations of the saturated drift velocity approximation for time domain modelling," *Semiconductor Science and Technology*, vol. 17, no. 2, pp. 124–128, jan 2002. doi: 10.1088/0268-1242/17/2/306

[56] P. J. Hambleton, B. K. Ng, S. A. Plimmer, J. P. R. David, and G. J. Rees, "The effects of nonlocal impact ionization on the speed of avalanche photodiodes," *IEEE Transactions on Electron Devices*, vol. 50, no. 2, pp. 347–351, 2003. doi: 10.1109/TED.2002.808523

[57] Feng Ma, Ning Li, and J. C. Campbell, "Monte Carlo simulations of the bandwidth of InAlAs avalanche photodiodes," *IEEE Transactions on Electron Devices*, vol. 50, no. 11, pp. 2291–2294, 2003. doi: 10.1109/TED.2003.818149

[58] M. L. Cohen and T. K. Bergstresser, "Band structures and pseudopotential form factors for fourteen semiconductors of the diamond and zincblende structures," *Phys. Rev.*, vol. 141, pp. 789–796, Jan 1966. doi: 10.1103/PhysRev.141.789

[59] J. R. Chelikowsky and M. L. Cohen, "Nonlocal pseudopotential calculations for the electronic structure of eleven diamond and zinc-blende semiconductors," *Phys. Rev. B*, vol. 14, pp. 556–582, Jul 1976. doi: 10.1103/PhysRevB.14.556

[60] M. V. Fischetti, "Monte Carlo simulation of transport in technologically significant semiconductors of the diamond and zinc-blende structures. I. homogeneous transport," *IEEE Transactions on Electron Devices*, vol. 38, no. 3, pp. 634–649, Mar. 1991. doi: 10.1109/16.75176

[61] D. S. Ong, K. F. Li, S. A. Plimmer, G. J. Rees, J. P. R. David, and P. N. Robson, "Full band Monte Carlo modeling of impact ionization, avalanche multiplication, and noise in submicron GaAs p^+-i-n^+ diodes," *Journal of Applied Physics*, vol. 87, no. 11, pp. 7885–7891, 2000. doi: 10.1063/1.373472

[62] D. Dolgos, H. Meier, A. Schenk, and B. Witzigmann, "Full-band Monte Carlo simulation of high-energy carrier transport in single photon avalanche diodes: Computation of breakdown probability, time to avalanche breakdown, and jitter," *Journal of Applied Physics*, vol. 110, no. 8, p. 084507, 2011. doi: 10.1063/1.3652844

[63] E. O. Kane, "Electron scattering by pair production in Silicon," *Phys. Rev.*, vol. 159, pp. 624–631, Jul 1967. doi: 10.1103/PhysRev.159.624

[64] L. H. Holway, S. R. Steele, and M. G. Alderstein, *Proceedings of the 7th Biennial Cornell Electrical Engineering Conference*, p. 199, 1979.

[65] D. S. Ong, G. J. Rees, and J. P. R. David, "Avalanche speed in thin avalanche photodiodes," *Journal of Applied Physics*, vol. 93, no. 7, pp. 4232–4239, 2003. doi: 10.1063/1.1557785

[66] C. Hu, K. A. Anselm, B. G. Streetman, and J. C. Campbell, "Noise characteristics of thin multiplication region GaAs avalanche photodiodes," *Applied Physics Letters*, vol. 69, no. 24, pp. 3734–3736, 1996. doi: 10.1063/1.117205

[67] K. F. Li, D. S. Ong, J. P. R. David, G. J. Rees, R. C. Tozer, P. N. Robson, and R. Grey, "Avalanche multiplication noise characteristics in thin GaAs p^+-i-n^+ diodes," *IEEE Transactions on Electron Devices*, vol. 45, no. 10, pp. 2102–2107, 1998. doi: 10.1109/16.725242

[68] D. Dolgos, H. Meier, A. Schenk, and B. Witzigmann, "Full-band Monte Carlo simulation of high-energy carrier transport in single photon avalanche diodes with multiplication layers made of InP, InAlAs, and GaAs," *Journal of Applied Physics*, vol. 111, no. 10, p. 104508, 2012. doi: 10.1063/1.4717729

[69] C. Nichetti, A. Pilotto, P. Palestri, L. Selmi, M. Antonelli, F. Arfelli, G. Biasiol, G. Cautero, F. Driussi, N. Y. Klein, R. H. Menk, and T. Steinhartova, "An improved nonlocal history-dependent model for gain and noise in avalanche photodiodes based on energy balance equation," *IEEE Transactions on Electron Devices*, vol. 65, no. 5, pp. 1823–1829, May 2018. doi: 10.1109/TED.2018.2817509

[70] A. Pilotto, P. Palestri, L. Selmi, M. Antonelli, F. Arfelli, G. Biasiol, G. Cautero, F. Driussi, R. H. Menk, C. Nichetti, and T. Steinhartova, "A new expression for the gain-noise relation of single-carrier avalanche photodiodes with arbitrary staircase multiplication regions," *IEEE Transactions on Electron Devices*, vol. 66, no. 4, pp. 1810–1814, 2019. doi: 10.1109/TED.2019.2900743

[71] A. Pilotto, C. Nichetti, P. Palestri, L. Selmi, M. Antonelli, F. Arfelli, G. Biasiol, G. Cautero, F. Driussi, D. Esseni, R. H. Menk, and T. Steinhartova, "Optimizing the number of steps and the noise in staircase APDs with ternary III-V semiconductor alloys," in *2019 Joint International EUROSOI Workshop and International Conference on Ultimate Integration on Silicon (EUROSOI-ULIS)*, pp. 1–4, 2019. doi: 10.1109/EUROSOI-ULIS45800.2019.9041888

[72] A. Pilotto, C. Nichetti, P. Palestri, L. Selmi, M. Antonelli, F. Arfelli, G. Biasiol, G. Cautero, F. Driussi, D. Esseni, R. Menk, and T. Steinhartova, "Optimization of GaAs/AlGaAs staircase avalanche photodiodes accounting for both electron and hole impact ionization," *Solid-State Electronics*, vol. 168, p. 107728, 2020. doi: https://doi.org/10.1016/j.sse.2019.107728 Special Issue of Solid-State Electronics, dedicated to EUROSOI-ULIS 2019.

[73] Oh-Hyun Kwon, M. M. Hayat, J. C. Campbell, B. E. A. Saleh, and M. C. Teich, "Gain-bandwidth product optimization of heterostructure avalanche photodiodes," *Journal of Lightwave Technology*, vol. 23, no. 5, pp. 1896–1906, 2005. doi: 10.1109/JLT.2005.846911

[74] P. Palestri, L. Selmi, G. A. M. Hurkx, J. W. Slotboom, and E. Sangiorgi, "Energy dependent electron and hole impact ionization in Si bipolar transistors," in *International Electron Devices Meeting 1998. Technical Digest (Cat. No.98CH36217)*, pp. 885–888, Dec. 1998. doi: 10.1109/IEDM.1998.746496

[75] J. W. Slotboom, G. Streutker, M. J. van Dort, P. H. Woerlee, A. Pruijmboom, and D. J. Gravesteijn, "Non-local impact ionization in silicon devices," in *International Electron Devices Meeting 1991 [Technical Digest]*, pp. 127–130, Dec. 1991. doi: 10.1109/IEDM.1991.235484

[76] *Sentaurus Device User Guide, Version L-2016.03*. Synopsys, Mountain View, CA, USA, 2016.

[77] C. H. Tan, J. P. R. David, S. A. Plimmer, G. J. Rees, R. C. Tozer, and R. Grey, "Low multiplication noise thin $Al_{0.6}Ga_{0.4}As$ avalanche photodiodes," *IEEE Transactions on Electron Devices*, vol. 48, no. 7, pp. 1310–1317, Jul. 2001. doi: 10.1109/16.930644

[78] B. K. Ng, J. P. R. David, S. A. Plimmer, G. J. Rees, R. C. Tozer, M. Hopkinson, and G. Hill, "Avalanche multiplication characteristics of $Al_{0.8}Ga_{0.2}As$ diodes," *IEEE Transactions on Electron Devices*, vol. 48, no. 10, pp. 2198–2204, Oct. 2001. doi: 10.1109/16.954454

[79] B. K. Ng, J. P. R. David, R. C. Tozer, M. Hopkinson, G. Hill, and G. J. Rees, "Excess noise characteristics of $al_{0.8}ga_{0.2}as$ avalanche photodiodes," *IEEE Photonics Technology Letters*, vol. 14, no. 4, pp. 522–524, 2002. doi: 10.1109/68.992598

[80] M. Calciati, A. Tibaldi, F. Bertazzi, M. Goano, and P. Debernardi, "Many-valley electron transport in AlGaAs VCSELs," *Semiconductor Science and Technology*, vol. 32, no. 5, pp. 1–6, Apr. 2017. doi: 10.1088/1361-6641/aa66bb

[81] K. M. van Vliet, A. Friedmann, and L. M. Rucker, "Theory of carrier multiplication and noise in avalanche devices - part II: Two-carrier processes," *IEEE Transactions on Electron Devices*, vol. 26, no. 5, pp. 752–764, May 1979. doi: 10.1109/T-ED.1979.19490

[82] R. Burgess, "Some topics in the fluctuations of photo-processes in solids," *Journal of Physics and Chemistry of Solids*, vol. 22, pp. 371 – 377, 1961. doi: 10.1016/0022-3697(61)90284-0

[83] B. Razavi, *RF Microelectronics*, ser. Prentice Hall communications engineering and emerging technologies series. Prentice Hall, 2012. ISBN 9780137134731

[84] T. Kagawa, H. Iwamura, and O. Mikami, "Dependence of the GaAs/AlGaAs superlattice ionization rate on Al content," *Applied Physics Letters*, vol. 54, no. 1, pp. 33–35, 1989. doi: 10.1063/1.100825

[85] C. K. Chia, B. K. Ng, J. P. R. David, G. J. Rees, R. C. Tozer, M. Hopkinson, R. J. Airey, and P. N. Robson, "Multiplication and excess noise in $Al_xGa_{1-x}As$/GaAs multilayer avalanche photodiodes," *Journal of Applied Physics*, vol. 94, no. 4, pp. 2631–2637, 2003. doi: 10.1063/1.1593217

[86] A. Pilotto, P. Palestri, L. Selmi, M. Antonelli, F. Arfelli, G. Biasiol, G. Cautero, F. Driussi, R. H. Menk, C. Nichetti, and T. Steinhartova, "An improved random path length algorithm for p-i-n and staircase avalanche photodiodes," in *2018 International Conference on Simulation of Semiconductor Processes and Devices (SISPAD)*, pp. 26–30, Sep. 2018. doi: 10.1109/SISPAD.2018.8551751

[87] F. Rosset, A. Pilotto, L. Selmi, M. Antonelli, F. Arfelli, G. Biasiol, G. Cautero, D. De Angelis, F. Driussi, R. Menk, C. Nichetti, T. Steinhartova, and P. Palestri, "A model for the jitter of avalanche photodiodes with separate absorption and multiplication regions," *Nuclear Instruments and Methods in Physics Research Section A: Accelerators, Spectrometers, Detectors and Associated Equipment*, vol. 977, p. 164346, 2020. doi: https://doi.org/10.1016/j.nima.2020.164346

[88] C. Niclass, A. Rochas, P. . Besse, and E. Charbon, "Design and characterization of a cmos 3-d image sensor based on single photon avalanche diodes," *IEEE Journal of Solid-State Circuits*, vol. 40, no. 9, pp. 1847–1854, 2005. doi: 10.1109/JSSC.2005.848173

[89] F. Sun, Y. Xu, Z. Wu, and J. Zhang, "A simple analytic modeling method for spad timing jitter prediction," *IEEE Journal of the Electron Devices Society*, vol. 7, pp. 261–267, 2019. doi: 10.1109/JEDS.2019.2895151

[90] A. Ingargiola, M. Assanelli, A. Gallivanoni, I. Rech, M. Ghioni, and S. Cova, "Avalanche buildup and propagation effects on photon-timing jitter in Si-SPAD with non-uniform electric field," in *Advanced Photon Counting Techniques III*, M. A. Itzler and J. C. Campbell, Eds., vol. 7320, pp. 103 – 114, International Society for Optics and Photonics. SPIE, 2009. doi: 10.1117/12.818521

[91] W. Nakwaski, "Effective masses of electrons and heavy holes in GaAs, InAs, AlAs and their ternary compounds," *Physica B: Condensed Matter*, vol. 210, no. 1, pp. 1 – 25, 1995. doi: https://doi.org/10.1016/0921-4526(94)00921-H

[92] G. Pinaroli, P. Palestri, A. Pilotto, and L. Selmi, "Modeling charge collection in X-ray imagers," in *Radiation Detectors in Medicine, Industry, and National Security XVIII*, G. P. Grim, L. R. Furenlid, and H. B. Barber, Eds., vol. 10393, pp. 103 – 113, International Society for Optics and Photonics. SPIE, 2017. doi: 10.1117/12.2273923

[93] W. Riegler, "An application of extensions of the Ramo-Shockley theorem to signals in silicon sensors," *Nuclear Instruments and Methods in Physics Research Section A: Accelerators, Spectrometers, Detectors and Associated Equipment*, vol. 940, pp. 453 – 461, 2019. doi: 10.1016/j.nima.2019.06.056

[94] T. J. Brazil, "Causal-convolution - a new method for the transient analysis of linear systems at microwave frequencies," *IEEE Transactions on Microwave Theory and Techniques*, vol. 43, no. 2, pp. 315–323, Feb. 1995. doi: 10.1109/22.348090

[95] L. E. Tarof, J. Yu, R. Bruce, D. G. Knight, T. Baird, and B. Oosterbrink, "High-frequency performance of separate absorption grading, charge, and multiplication InP/InGaAs avalanche photodiodes," *IEEE*

Photonics Technology Letters, vol. 5, no. 6, pp. 672–674, Jun. 1993. doi: 10.1109/68.219706

[96] K. A. Anselm, H. Nie, C. Hu, C. Lenox, P. Yuan, G. Kinsey, J. C. Campbell, and B. G. Streetman, "Performance of thin separate absorption, charge, and multiplication avalanche photodiodes," *IEEE Journal of Quantum Electronics*, vol. 34, no. 3, pp. 482–490, Mar. 1998. doi: 10.1109/3.661456

[97] K. Makita, I. Watanabe, M. Tsuji, and K. Taguchi, "150 GHz GB-product and low dark current InAlGaAs quaternary well superlattice avalanche photodiodes," in *Proceedings IOOC-95*, p. 36, 1995.

[98] P. Yuan, O. Baklenov, H. Nie, A. L. Holmes, B. G. Streetman, and J. C. Campbell, "High-speed and low-noise avalanche photodiode operating at 1.06 μm," *IEEE Journal of Selected Topics in Quantum Electronics*, vol. 6, no. 3, pp. 422–425, May 2000. doi: 10.1109/2944.865097

[99] H. Nie, K. A. Anselm, C. Hu, B. G. Streetman, and J. C. Campbell, "High-speed, low-noise resonant-cavity avalanche photodiodes," in *Conference Proceedings LEOS'96 9th Annual Meeting IEEE Lasers and Electro-Optics Society*, vol. 1, pp. 392–393, Nov. 1996. doi: 10.1109/LEOS.1996.565298

[100] G. F. Knoll, *Radiation detection and measurement*. John Wiley & Sons, 2010.

[101] A. Molini, P. Talkner, G. Katul, and A. Porporato, "First passage time statistics of Brownian motion with purely time dependent drift and diffusion," *Physica A: Statistical Mechanics and its Applications*, vol. 390, no. 11, pp. 1841 – 1852, 2011. doi: 10.1016/j.physa.2011.01.024

[102] A. Pilotto, F. Driussi, D. Esseni, L. Selmi, M. Antonelli, F. Arfelli, G. Biasiol, S. Carrato, G. Cautero, D. D. Angelis, R. H. Menk, C. Nichetti, T. Steinhartova, and P. Palestri, "Full-Band Monte Carlo simulations of GaAs p-i-n avalanche photodiodes: What are the limits of nonlocal impact ionization models?" in *2020 International Conference on Simulation of Semiconductor Processes and Devices (SISPAD)*, Sep. 2020 (in publication).

[103] W. Pötz and P. Vogl, "Theory of optical-phonon deformation potentials in tetrahedral semiconductors," *Phys. Rev. B*, vol. 24, pp. 2025–2037, Aug 1981. doi: 10.1103/PhysRevB.24.2025

[104] *Courtesy of M. Pala.* University of Paris-Saclay, Palaiseau (France).

[105] H. K. Jung, K. Taniguchi, and C. Hamaguchi, "Impact ionization model for full band monte carlo simulation in GaAs," *Journal of Applied Physics*, vol. 79, no. 5, pp. 2473–2480, 1996. doi: 10.1063/1.361176

[106] M. V. Fischetti and S. E. Laux, "Monte carlo analysis of electron transport in small semiconductor devices including band-structure and space-charge effects," *Phys. Rev. B*, vol. 38, pp. 9721–9745, Nov 1988. doi: 10.1103/PhysRevB.38.9721

[107] G. Zerveas, E. Caruso, G. Baccarani, L. Czornomaz, N. Daix, D. Esseni, E. Gnani, A. Gnudi, R. Grassi, M. Luisier, T. Markussen, P. Osgnach, P. Palestri, A. Schenk, L. Selmi, M. Sousa, K. Stokbro, and M. Visciarelli, "Comprehensive comparison and experimental validation of band-structure calculation methods in III-V semiconductor quantum wells," *Solid-State Electronics*, vol. 115, pp. 92 – 102, 2016. doi: https://doi.org/10.1016/j.sse.2015.09.005 Selected papers from the EUROSOI-ULIS conference.

[108] I. Vurgaftman, J. R. Meyer, and L. R. Ram-Mohan, "Band parameters for III-V compound semiconductors and their alloys," *Journal of Applied Physics*, vol. 89, no. 11, pp. 5815–5875, 2001. doi: 10.1063/1.1368156

[109] M. De Michielis, D. Esseni, P. Palestri, and L. Selmi, "Semiclassical modeling of quasi-ballistic hole transport in nanoscale pMOSFETs based on a multi-subband Monte Carlo approach," *IEEE Transactions on Electron Devices*, vol. 56, no. 9, pp. 2081–2091, 2009. doi: 10.1109/TED.2009.2026388

[110] T. Kunikiyo, M. Takenaka, Y. Kamakura, M. Yamaji, H. Mizuno, M. Morifuji, K. Taniguchi, and C. Hamaguchi, "A Monte Carlo simulation of anisotropic electron transport in silicon including full band structure and anisotropic impact-ionization model," *Journal of Applied Physics*, vol. 75, no. 1, pp. 297–312, 1994. doi: 10.1063/1.355849

[111] P. Palestri, *Monte-Carlo simulations of hot carrier effects and photoemission in MOS devices*. PhD Thesis, University of Udine, Udine (Italy), 2004.

[112] N. Sano and A. Yoshii, "Impact-ionization model consistent with the band structure of semiconductors," *Journal of Applied Physics*, vol. 77, no. 5, pp. 2020–2025, 1995. doi: 10.1063/1.358839

[113] D. Harrison, R. A. Abram, and S. Brand, "Impact ionization rate calculations in wide band gap semiconductors," *Journal of Applied Physics*, vol. 85, no. 12, pp. 8178–8185, 1999. doi: 10.1063/1.370657

[114] M. Fischetti, N. Sano, S. Laux, and K. Natori, "Full-band-structure theory of high-field transport and impact ionization of electrons and holes in Ge, Si, GaAs, InAs, and InGaAs," Aug. 2015. doi: 10.13140/RG.2.1.5004.2088

[115] V. L. Dalal, "Hole velocity in p-GaAs," *Applied Physics Letters*, vol. 16, no. 12, pp. 489–491, 1970. doi: 10.1063/1.1653077

[116] V. L. Dalal, A. B. Dreeben, and A. Triano, "Temperature dependence of hole velocity in p-GaAs," *Journal of Applied Physics*, vol. 42, no. 7, pp. 2864–2867, 1971. doi: 10.1063/1.1660641

[117] S. A. Plimmer, J. P. R. David, D. S. Ong, and K. F. Li, "A simple model for avalanche multiplication including deadspace effects," *IEEE Transactions on Electron Devices*, vol. 46, no. 4, pp. 769–775, 1999. doi: 10.1109/16.753712

[118] T. Steinhartova, C. Nichetti, M. Antonelli, G. Cautero, R. Menk, A. Pilotto, F. Driussi, P. Palestri, L. Selmi, K. Koshmak, S. Nannarone, F. Arfelli, S. D. Zilio, and G. Biasiol, "Influence of δ p-doping on the behaviour of GaAs/AlGaAs SAM-APDs for synchrotron radiation," *Journal of Instrumentation*, vol. 12, no. 11, pp. C11 017–C11 017, Nov. 2017. doi: 10.1088/1748-0221/12/11/c11017

[119] F. Driussi, A. Pilotto, D. De Belli, M. Antonelli, F. Arfelli, G. Biasiol, G. Cautero, R. H. Menk, C. Nichetti, L. Selmi, T. Steinhartova, and P. Palestri, "Experimental and simulation analysis of carrier lifetimes in GaAs/AlGaAs Avalanche Photo-Diodes," in *2020 IEEE 33rd International Conference on Microelectronic Test Structures (ICMTS)*, pp. 1–6, 2020. doi: 10.1109/ICMTS48187.2020.9107920

[120] C. Nichetti, T. Steinhartova, M. Antonelli, G. Biasiol, G. Cautero, D. D. Angelis, A. Pilotto, F. Driussi, P. Palestri, L. Selmi, F. Arfelli, M. Danailov, and R. Menk, "Effects of p doping on GaAs/AlGaAs SAM-APDs for X-rays detection," *Journal of Instrumentation*, vol. 15, no. 02, pp. C02 013–C02 013, feb 2020. doi: 10.1088/1748-0221/15/02/c02013

[121] S. Sze and K. Ng, *Physics of Semiconductor Devices*. Wiley, 2006. ISBN 9780470068304

[122] H. Goebel and K. Hoffmann, "Full dynamic power diode model including temperature behavior for use in circuit simulators," in *Proceedings of the 4th International Symposium on Power Semiconductor Devices and Ics*, pp. 130–135, 1992. doi: 10.1109/ISPSD.1992.991249

[123] A. Schenk, "A model for the field and temperature dependence of Shockley-Read-Hall lifetimes in silicon," *Solid-State Electronics*, vol. 35, no. 11, pp. 1585 – 1596, 1992. doi: https://doi.org/10.1016/0038-1101(92)90184-E

[124] M. V. Fischetti and S. E. Laux, "Band structure, deformation potentials, and carrier mobility in strained Si, Ge, and SiGe alloys," *Journal of Applied Physics*, vol. 80, no. 4, pp. 2234–2252, 1996. doi: 10.1063/1.363052

Acknowledgments

I would like to express my sincere gratitude to Prof. Pierpaolo Palestri for his supervision, guidance, encouragement, and assistance over the past four years. He gave me the opportunity to work on interesting and challenging topics and he taught me how a good researcher acts when approaching a new theme. I really admire him as a teacher, as a researcher, and as a person.

Special thanks go to Prof. Luca Selmi for his continuous support and for the careful and critical reading of all the work that I have done.

I want to acknowledge for the useful and fruitful discussion Prof. David Esseni, Prof. Francesco Driussi, and all the professors and researchers with whom I collaborated during my PhD, in particular Matias Antonelli, Fulvia Arfelli, Giorgio Biasiol, Giuseppe Cautero, Ralf H. Menk, Camilla Nichetti, Giovanni Pinaroli, Francesca Rosset and Tereza Steinhartova.

I would also like to thank my former and present colleagues, in particular Leandro Julian Mele, for creating a stimulating work environment. Special thanks go also to my friends and to all the PhD students from other research groups that I met at the University of Udine for all the fun that we had during lunch breaks, classes, or during our free time.

Last but not least, I want to thank my parents, my sister, my grandmother, and all the members of my family: everything that I have ever achieved in my life would not have been possible without their support.

Finally, the last thank is for Alessandra, for the support, for existing, and for being part of my life.

Appendices

Appendix A

Solution of the Integral in Eq. 2.15

In this Appendix, the detailed solution of the integral in Eq. 2.15 (Section 2.1.1) is provided.

We start by rewriting Eq. 2.15

$$S_i = 2q^2 \int_0^W \frac{d\phi_e(x)}{dx} M^2(x) dx.$$

We notice that the argument of the integral is the product between the first derivative of ϕ_e and $M^2(x)$: the integral can be thus solved by parts

$$\begin{aligned} S_i &= 2q^2 \left\{ \left[\phi_e(x) M^2(x)\right]_0^W - \int_0^W \phi_e(x) \frac{d^2 M(x)}{dx^2} dx \right\} \\ &= 2q^2 \left\{ \phi M^2(W) - 2 \int_0^W \phi_e(x) M(x) \frac{dM(x)}{dx} dx \right\}, \end{aligned} \tag{A.1}$$

where we considered that due to total flux conservation (Eq. 2.5), $\phi_e(W) = \phi$ and $\phi_e(0) = 0$.

The expression of the first derivative of $M(x)$ can be easily found from Eq. 2.13, namely

$$\frac{dM(x)}{dx} = -\left[\alpha(x) - \beta(x)\right] M(x). \tag{A.2}$$

By substituting Eq. A.2 in Eq. A.1, we get

$$S_i = 2q^2 \left\{ \phi M^2(W) + 2 \int_0^W \left[\alpha(x) - \beta(x)\right] \phi_e(x) M^2(x) dx \right\}. \tag{A.3}$$

From Eq. 2.7, we derive

$$\left[\alpha(x) - \beta(x)\right] \phi_e(x) = \frac{d\phi_e(x)}{dx} - \beta(x)\phi - G_{opt}(x). \tag{A.4}$$

Substitution of Eq. A.4 in Eq. A.5 yields

$$\begin{aligned} S_i = 2q^2 \Bigg\{ & \phi M^2(W) + 2 \int_0^W \frac{d\phi_e(x)}{dx} M^2(x) dx - 2 \int_0^W \beta(x) \phi M^2(x) dx \\ & -2 \int_0^W G_{opt}(x) M^2(x) dx \Bigg\}. \end{aligned} \tag{A.5}$$

By comparing Eqs. 2.15 and A.5, we get

$$\int_0^W \frac{d\phi_e(x)}{dx}dx = 2\phi \int_0^W \beta(x)M^2(x)dx + 2\int_0^W G_{opt}(x)M^2(x)dx - \phi M^2(W). \tag{A.6}$$

Eq. A.6 is then substituted into Eq. 2.15 and, rewriting the total flux ϕ with the expression reported in Eq. 2.9, we obtain

$$\begin{aligned} S_i = 2q^2 \Bigg\{ & 2\int_0^W G_{opt}M^2(x)dx + 2\int_0^W G_{opt}(x)M(x)dx \int_0^W \beta(x)M^2(x)dx \\ & - M^2(W)\int_0^W G_{opt}(x)M(x)dx \Bigg\}, \end{aligned} \tag{A.7}$$

which is equivalent to the solution reported in Eq. 2.16, namely

$$\begin{aligned} S_i &= 2q^2 \left\{ \int_0^W G_{opt}(x)M^2(x) \left[2 + \frac{2\int_0^W \beta(x')M^2(x')dx'}{M(x)} - \frac{M^2(W)}{M(x)} \right] dx \right\} \\ &= 2q^2 \int_0^W G_{opt}(x)M^2(x)F(x)dx. \end{aligned}$$

Appendix B

Hole's Overlap Integrals

As stated in Section 5.2.3, in our FBMC, since storing the wavefunctions for all the states in the Irreducible Wedge and using Eq. 5.15 would be very demanding in terms of memory usage, in the case of hole-phonon scattering event, the overlap integral between the initial state $(n_1, \vec{k_1})$ and the final state $(n_2, \vec{k_2})$ has been substituted by the $\vec{q}$-dependent Rigid Ion expression (Eq. 5.29), where $\vec{q} = \vec{k_2} - \vec{k_1}$ is the exchanged momentum, and we have imposed that the final state can be identified only in the same band of the initial one, thus suppressing interband scattering: namely $n_1 = n_2$ for all the hole-phonon scattering events.

In this Appendix, we will discuss the choice that we have made by comparing it to the results that we have obtained by using the expressions for the hole's overlap integrals reported in [124]. In fact, following [124], the squared modulus of the hole's overlap integral ($|\mathcal{I}|^2$) is approximately equal to 1/2 for all interband processes and for intraband collisions within the two topmost bands and to unity for intraband transitions within the split-off band.

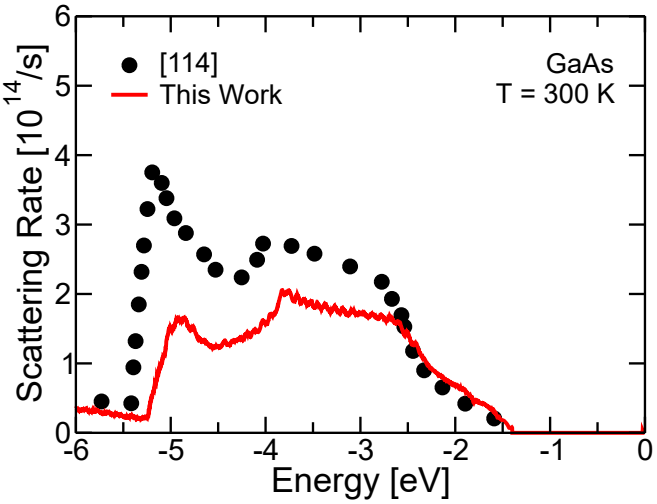

Figure B.1: Hole-phonon scattering rate as a function of the carrier energy. The deformation potentials of Tab. B.1 have been used and the hole's overlap integrals have been computed as in [124]. Our results (red solid line) have been compared with the results of [114] (black circles).

Figure B.1 shows the hole-phonon scattering computed by using the expressions reported in [124] and compares it to the results of [114]. The acoustic and nonpolar optical phonon deformation potentials of Tab. B.1 have been used: the choice of these values has been made to make the FBMC simulations match the experimental results for the drift velocity as a function of the applied electric field [64, 115, 116] (see Fig. B.2).

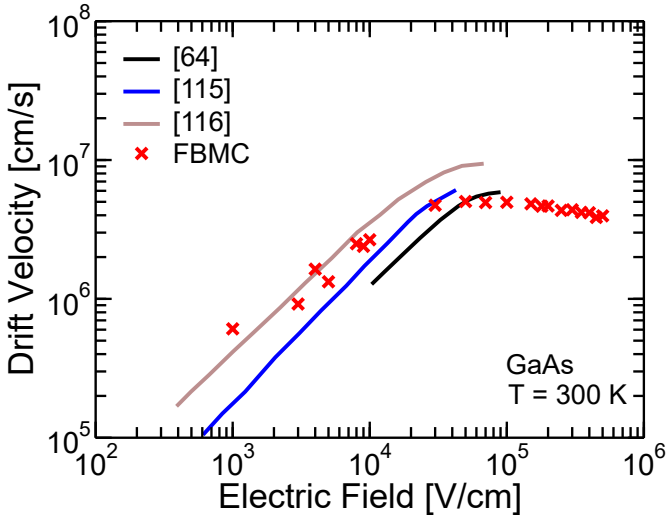

Figure B.2: Hole's drift velocity as a function of the applied electric field in bulk GaAs at $T = 300$ K when the hole-phonon scattering rate is the one of Fig. B.1. FBMC results have been compared with the experimental results of [64, 115, 116] (black, blue and brown solid lines, respectively).

$D_{ac,h}$ [eV]	$\Delta K_{op,h}$ [eV/m]
4.0	4.8×10^{10}

Table B.1: Deformation potentials used for the computation of the hole-phonon scattering rates in GaAs when the hole's overlap integrals have been computed as in [124].

Figure B.3a compares the hole's impact ionization scattering rate used to match the experiments in [17] for the impact ionization coefficient as a function of the reciprocal of the electric field (Fig. B.3b) with the results of [113, 114]. The matrix element $T_{ii,h}$ has been set three times bigger with respect to the one in Tab. 5.5 to reproduce the same set of experimental data. It is also worth noting that the value of the deformation potential for acoustic phonons used to match the experimental $v(E)$ curves and reported in Tab. B.1 is similar to the one reported in Tab. 5.4 (4.5 eV), while the value of $\Delta K_{op,h}$ is quite different (8.0×10^{10} eV/m). These differences of the matrix element and of the phonon deformation potentials with respect to the values discussed in Chapter 5 points out the role of interband scattering for holes. In fact, the presence of interband scattering increases the hole-phonon scattering rate for a given initial state $(n_1, \vec{k_1})$ and, thus reduces the velocity and the impact ionization probability

at a given field. Thus, when interband scattering is allowed, the FBMC gives the same results presented in Chapter 5 only if the deformation potentials for hole phonon scattering are reduced and if $T_{ii,h}$ is increased.

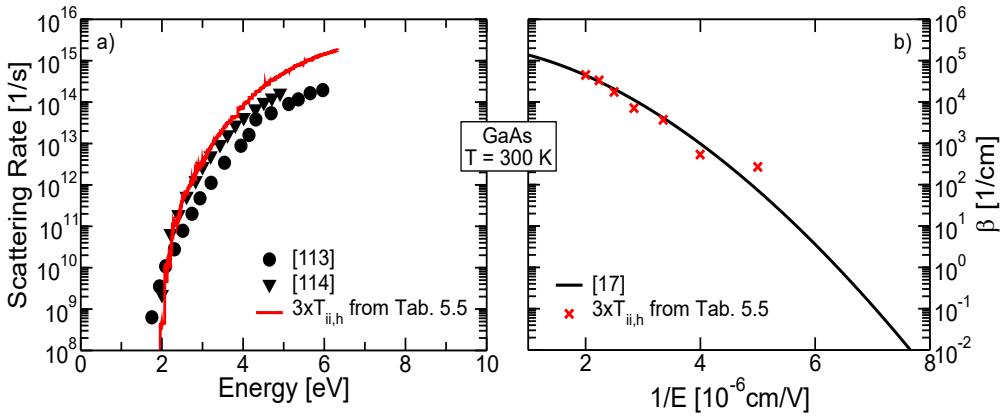

Figure B.3: Hole's impact ionization a) scattering rate as a function of the carrier energy and b) impact ionization coefficient as a function of the reciprocal of the electric field. The results have been obtained by multiplying by 3 the matrix element $T_{ii,h}$ of Tab. 5.5. In plot a) our results (red solid line) have been compared with the computations of [113, 114] (black circles and triangles, respectively), while in plot b) FBMC results (red crosses) have been compared with experiments (black solid line)[17].

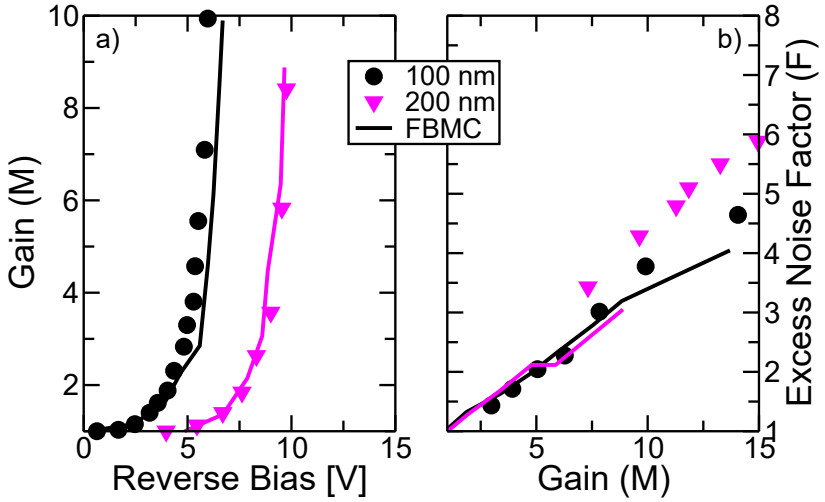

Figure B.4: a) M versus V_{rev} and b) F versus M curves for GaAs p-i-n APDs when the hole's overlap integrals have been compued as in [124] and the matrix element $T_{ii,h}$ of Tab. 5.5 has been multiplied by 3. FBMC (solid lines) is compared with experiments [23] (symbols). A built-in voltage $\Psi_0 = 1.2$ V has been assumed [117].

Figure B.4 compares the gain as a function of the applied bias voltage and the excess noise factor as a function of the gain computed with the FBMC, by

using the hole-phonon and impact ionization scattering rates of Figs. B.1 and B.3a, with the experimental results of [23] for a 100 nm and a 200 nm thick GaAs p-i-n APDs. We notice that the $M(V_{rev})$ curves are in mutual agreement, while the excess noise factor for the 200 nm thick diode is underestimated.

To solve the problem, we have increased the matrix element for the computation of the hole's impact ionization scattering rate $T_{ii,h}$ until FBMC simulations were able to reproduce the experimental data of [23] (Fig. B.5). In fact, we have noticed that, differently from the gain at a given voltage, the excess noise factor at a given gain strongly depends on the value of $T_{ii,h}$.

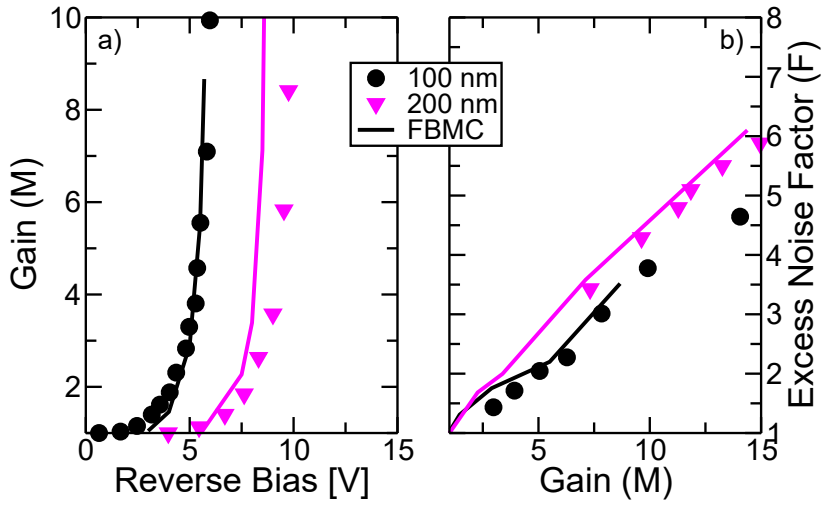

Figure B.5: Same as Fig. B.4, but the matrix element $T_{ii,h}$ of Tab. 5.5 has been multiplied by 50.

We have found that, in order to match the experiments of [23], a value of $T_{ii,h}$ fifty times larger than the one used in Tab. 5.5 to obtain the results presented in Chapter 5 have to be used. The results for the hole's impact ionization scattering rate and impact ionization coefficient are shown in Fig B.6 and compared with the one of Fig. B.3.

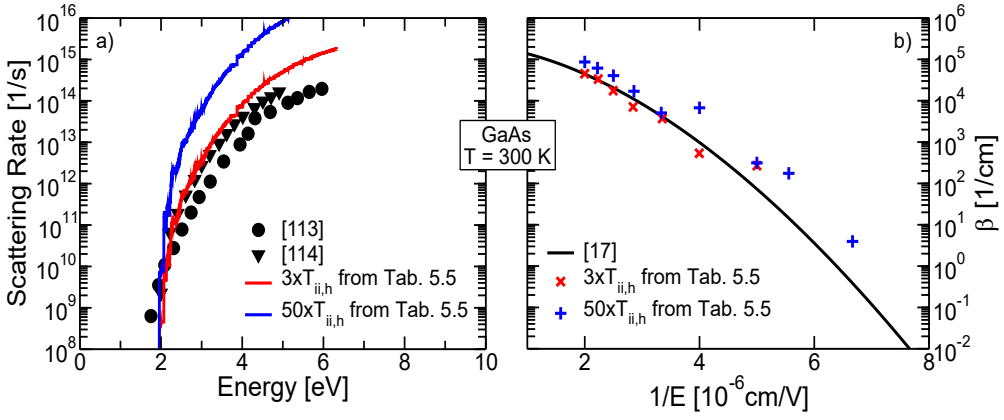

Figure B.6: Same as Fig. B.3, but the results for when the matrix element $T_{ii,h}$ of Tab. 5.5 is multiplied by 50 are also reported (blue solid line).

Since the results for the hole's impact ionization scattering rate obtained with the new value of $T_{ii,h}$ are largely different from the ones reported by [113, 114] and the impact ionization coefficient differs from the experiments of [17], in the case of hole-phonon intraband scattering events we have decided to compute the overlap integral between the initial state $(n_1, \vec{k_1})$ and the final state $(n_2, \vec{k_2})$ by using the Rigid Ion approximation of Eq. 5.29, while, consistently with [109], interband scattering has been ignored.

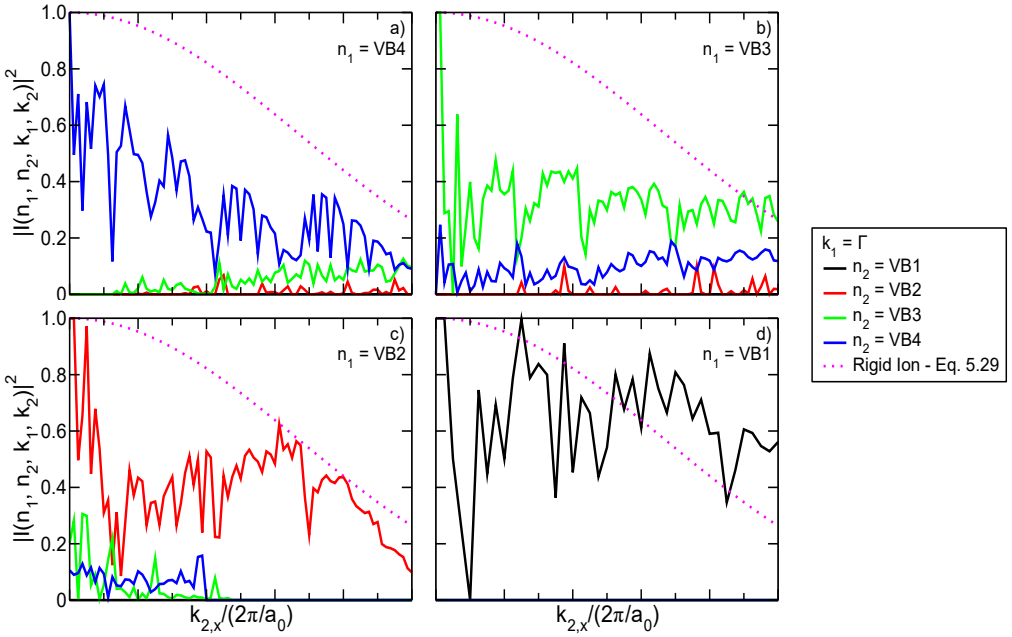

Figure B.7: Squared modulus of the hole's overlap integrals $\mathcal{I}(n_1, n_2; \vec{k_1}, \vec{k_2})$ by using Eq. 5.15, with the wavefunctions given as output of the solution of the EPM Hamiltonian (Eq. 5.4). For each plot, the wavevector of the initial state is fixed ($\vec{k_1} = \Gamma$), while the band index n_1 goes from the highest valence band ($VB4$) in plot a) to the lowest one ($VB1$) in plot d). The final state $(n_2, \vec{k_2})$ is chosen along the $[1, 0, 0]$ direction and the overlap integral is computed only if $|E(n_2, \vec{k_2}) - E(n_1, \vec{k_1})| \leq 33$ meV, which is the maximum phonon energy in GaAs (Eq. 5.18 with the parameters in Tab. 5.4). The dotted magenta line is the result of the Rigid Ion approximation (Eq. 5.29).

Finally, Figure B.7 shows the squared modulus overlap integrals, computed by using Eq. 5.15 and the wavefunctions obtained by the solution of the EPM hamiltonian (Eq. 5.4), between the state $(n_1 = VB4 \div VB1, \vec{k_1} = \Gamma)$, where $VB1$ and $VB4$ are, respectively, the lowest and the highest valence band, and final states $(n_2, \vec{k_2})$ along the $[1, 0, 0]$. The overlap integrals are computed only if $|E(n_2, \vec{k_2}) - E(n_1, \vec{k_1})| \leq 33$ meV, which is the maximum phonon energy in GaAs (Eq. 5.18 with the parameters in Tab. 5.4). The results are also compared with the Rigid Ion expression (Eq. 5.29). We notice that, in all the

plots, the squared modulus of the overlap integral for interband transitions is negligible, if compared to the one for intraband scattering events. On the other hand, the Rigid Ion expression does not match the values obtained by using Eq. 5.15, but this difference can be compensated by the choice of the deformation potentials for acoustic and nonpolar optical phonons.

In conclusion, as shown in Chapter 5, the use of the Rigid Ion approximation for the computation of the hole's overlap integral, associated with an adequate choice of the deformation potentials for the scattering with acoustic and nonpolar optical phonons, allows to obtain results for the hole's impact ionization scattering rate, the impact ionization coefficient and for the $M(V_{rev})$ and $F(M)$ curves that are consistent with experiments and/or with the results obtained by other authors. However, we think that, in the future, further investigation on the hole's overlap integrals is necessary to achieve a closer approximation of the ones computed with Eq. 5.15 and the wavefunctions obtained by solving the EPM hamiltonian.

Appendix C

Short Biography

Alessandro Pilotto was born in Pordenone, Italy, on March 13, 1992. He received the Bachelor's Degree and the Master's Degree (*summa cum laude*) in Electronic Engineering from the University of Udine, Udine, Italy, in 2014 and 2017, respectively. From May 2014 to September 2014, for his Bachelor's thesis, he worked in Card Tech s.r.l, Udine, Italy, on the development of the firmware for NFC applications on fingerprint-enabled smart cards. From January 2016 to June 2016 he was a Master's student at the Institut National Polytechnique de Grenoble, Grenoble, France, in the framework of the Erasmus project. In May 2017 he joined the Polytechnic Department of Engineering and Architecture at the University of Udine, Udine, Italy, where he is currently working on the modeling and simulation of Avalanche Photodiodes for the detection of X-rays.

Appendix D

List of Author's Publications

International Journals

1. T. Steinhartova, C. Nichetti, M. Antonelli, G. Cautero, R. Menk, A. Pilotto, F. Driussi, P. Palestri, L. Selmi, K. Koshmak, S. Nannarone, F. Arfelli, S. D. Zilio, and G. Biasiol, "Inuence of δ p-doping on the behaviour of GaAs/AlGaAs SAM-APDs for synchrotron radiation," *Journal of Instrumentation*, vol. 12, no. 11, C11017, Nov. 2017. doi: 10.1088/1748-0221/12/11/c11017

2. C. Nichetti, A. Pilotto, P. Palestri, L. Selmi, M. Antonelli, F. Arfelli, G. Biasiol, G. Cautero, F. Driussi, N. Y. Klein, R. H. Menk, and T. Steinhartova, "An improved nonlocal history-dependent model for gain and noise in avalanche photodiodes based on energy balance equation," *IEEE Transactions on Electron Devices*, vol. 65, no. 5, pp. 1823-1829, May 2018. doi: 10.1109/TED.2018.2817509

3. C. Nichetti, T. Steinhartova, M. Antonelli, G. Cautero, R. Menk, A. Pilotto, F. Driussi, P. Palestri, L. Selmi, F. Arfelli, and G. Biasiol, "Gain and noise in GaAs/AlGaAs avalanche photodiodes with thin multiplication regions," *Journal of Instrumentation*, vol. 14, no. 01, C01003, Jan.2019. doi: 10.1088/1748-0221/14/01/c01003

4. A. Pilotto, P. Palestri, L. Selmi, M. Antonelli, F. Arfelli, G. Biasiol, G. Cautero, F. Driussi, R. H. Menk, C. Nichetti, and T. Steinhartova, "A new expression for the gain-noise relation of single-carrier avalanche photodiodes with arbitrary staircase multiplication regions," *IEEE Transactions on Electron Devices*, vol. 66, no. 4, pp. 1810-1814, 2019. doi: 10.1109/TED.2019.2900743

5. A. Pilotto, C. Nichetti, P. Palestri, L. Selmi, M. Antonelli, F. Arfelli, G. Biasiol, G. Cautero, F. Driussi, D. Esseni, R. Menk, and T. Steinhartova, "Optimization of GaAs/AlGaAs staircase avalanche photodiodes accounting for both electron and hole impact ionization," *Solid-State Electronics*, vol. 168, p. 107728, 2020. doi: 10.1016/j.sse.2019.107728

Special Issue of Solid-State Electronics, dedicated to EUROSOI-ULIS 2019.

6. C. Nichetti, T. Steinhartova, M. Antonelli, G. Biasiol, G. Cautero, D. De Angelis, A. Pilotto, F. Driussi, P. Palestri, L. Selmi, F. Arfelli, M. Danailov and R.H. Menk, "Effects of p doping on GaAs/AlGaAs SAM-APDs for X-rays detection," *Journal of instrumentation*, vol. 5, no. 02, C02013, Feb. 2020. doi: 10.1088/1748-0221/15/02/c02013

7. F. Rosset, A. Pilotto, L. Selmi, M. Antonelli, F. Arfelli, G. Biasiol, G. Cautero, D. De Angelis, F. Driussi, R. Menk, C. Nichetti, T. Steinhartova, and P. Palestri, "A model for the jitter of avalanche photodiodes with separate absorption and multiplication regions," *Nuclear Instruments and Methods in Physics Research Section A: Accelerators, Spectrometers, Detectors and Associated Equipment*, vol. 977, p. 164346, 2020. doi: 10.1016/j.nima.2020.164346

Conference Proceedings

1. G. Pinaroli, P. Palestri, A. Pilotto, L. Selmi, "Modeling charge collection in X-ray imagers," *Proceedings of SPIE 2017*, vol. 10393, pp. 103930D-1-103930D-11, San Diego, CA, USA, 2017. doi: 10.1117/12.2273923

2. A. Pilotto, P. Palestri, L. Selmi, M. Antonelli, F. Arfelli, G. Biasiol, G. Cautero, F. Driussi, R. H. Menk, C. Nichetti, and T. Steinhartova, "An improved random path length algorithm for p-i-n and staircase avalanche photodiodes," in *2018 International Conference on Simulation of Semiconductor Processes and Devices (SISPAD)*, pp. 26-30, Sep. 2018. doi: 10.1109/SISPAD.2018.8551751

3. C. Nichetti, T. Steinhartova, M. Antonelli, G. Cautero, R. H. Menk, A. Pilotto, F. Driussi, P. Palestri, L. Selmi, F. Arfelli, G. Biasiol, "Investigation of the behaviour of GaAs/AlGaAs SAM-APDs for synchrotron radiation," *AIP Conference Proceedings*, vol. 2054, pp. 060064-1-060064-6, 2019. doi: 10.1063/1.5084695

4. A. Pilotto, C. Nichetti, P. Palestri, L. Selmi, M. Antonelli, F. Arfelli, G. Biasiol, G. Cautero, F. Driussi, D. Esseni, R. H. Menk, and T. Steinhartova, "Optimizing the number of steps and the noise in staircase APDs with ternary III-V semiconductor alloys," in *2019 Joint International EUROSOI Workshop and International Conference on Ultimate Integration on Silicon (EUROSOI-ULIS)*, pp. 1-4, 2019. doi: 10.1109/EUROSOI-ULIS45800.2019.9041888

5. F. Driussi, A. Pilotto, D. De Belli, M. Antonelli, F. Arfelli, G. Biasiol, G. Cautero, R. H. Menk, C. Nichetti, L. Selmi, T. Steinhartova, and P. Palestri, "Experimental and simulation analysis of carrier lifetimes in

GaAs/AlGaAs Avalanche Photo-Diodes," in *2020 IEEE 33rd International Conference on Microelectronic Test Structures (ICMTS)*, pp. 1-6, 2020. doi: 10.1109/ICMTS48187.2020.9107920

6. A. Pilotto, F. Driussi, D. Esseni, L. Selmi, M. Antonelli, F. Arfelli, G. Biasiol, S. Carrato, G. Cautero, D. De Angelis, R. H. Menk, C. Nichetti, T. Steinhartova and P. Palestri, "Full-Band Monte Carlo simulations of GaAs p-i-n Avalanche PhotoDiodes: What Are the Limits of Nonlocal Impact Ionization Models?" in *2020 International Conference on Simulation of Semiconductor Processes and Devices (SISPAD)*, Sep. 2020 (in publication).

Presentations at National Conferences

1. A. Pilotto, F. Driussi, D. Esseni, P. Palestri, L. Selmi, M. Antonelli, F. Arfelli, G. Biasiol, G. Cautero, R. H. Menk, C. Nichetti and T. Steinhartova, "Modeling speed and noise in III-V based Avalanche Photo-diodes" in *51st Meeting Società Italiana di Elettronica*, Rome, Jun. 2019.